Department of Pure and Applied Chemistry

Hollow Gold Nanoshells as Unique Near Infrared Optical Materials for Surface Enhanced Raman Scattering

by

Hayleigh Kearns

A thesis presented to the Department of Pure and Applied Chemistry, University of Strathclyde, in fulfilment of the requirements for the degree of Doctor of Philosophy.

2016

This thesis is the result of the author's original research. It has been composed by the author and has not been previously submitted for examination which has led to the award of a degree.

Signed: Date:

Acknowledgements

Firstly, I'd like to take this opportunity to thank my supervisors Professor Duncan Graham and Dr Karen Faulds for the opportunity to carry out this research and also for their continued help and support throughout the course of my PhD.

A lot of this research was conducted through collaborations with other academics, universities and industrial partners. Firstly, I would like to express my gratitude to Prof. W. Ewen Smith for his invaluable help, and numerous discussions. I would also like to thank my industrial funders DSTL and in particular Prof. Neil Shand, for all his help and advice and for supplying (mostly fixing) all the Raman instruments required to carry out this research. Thank you to Prof. Michael Detty and Matthew Bedics from the University at Buffalo for supplying ~30 chalcogenopyrylium dyes for me to analyse. It was worth it though! Furthermore, I would like to thank Ivan Ramos-Sasselli for all his help with the computational studies, to Dr Samuel Mabbott for his continued help and for carrying out the chemometrics, to Sian Sloan-Dennison and Rachel Norman for supplying me with gold and silver nanoparticles and my biggest thanks goes to Fatima Ali for all your help and hard work with the chalcogen dye studies. I couldn't have done it without you!

Thank you to everyone within the Centre of Nanometrology for their helpful input and fun times over the past 4 years! In particular, I would like to thank Samantha and Tara, the last 6 months have being interesting, emotional but we have made it. I would also like to extend this thanks to Rachel, Kirsten and Stacey for being great friends too and to Megan, for allowing me to come and escape to your office for tea breaks!

Finally, I would like to say a special thanks to my wonderful family and friends for their support, encouragement and most importantly for just being there through the tough times. In particular Scott and Louise; I know I've had a few crazy moments but knowing you are always there to listen and talk to made it so much easier. The greatest thank you of all goes to my wonderful husband Euan and to my mum, dad and grampa as they have always believed in me. Without your love, support and encouragement I would never have made it this far!

Abstract

Hollow gold nanoshells (HGNs) demonstrate a tunable localised surface plasmon resonance (LSPR) from the visible to the near infrared (NIR). The NIR region of the electromagnetic spectrum is of particular interest as it provides an uncongested spectral window for optical analysis due to many molecules having reduced absorption and scattering backgrounds. In addition, the superior depth of light penetration and reduced interference which is observed in this region when compared to the visible region means that there is a great need to design SERS nanotags which can provide a unique vibrational fingerprint in this uncongested optical region.

The research described herein demonstrates three ways in which red-shifted nanotags can be engineered to provide effective SERS signals in the NIR region. Firstly, NIR active HGNs were synthesised and encapsulated with seven non-resonant commercial Raman reporters and shown to provide effective SERS when excited with a 1064 nm laser. The nanotags were then tested using a 1280 nm laser excitation however; they were unsuccessful at providing a SERS spectrum. Through a successful collaboration with Professor Michael Detty's group (University at Buffalo) newly synthesised Raman reporters where obtained. The chalcogenopyrylium dyes were resonant from 650 to 1000 nm and when combined with HGNs, demonstrated an unprecedented performance. Through the design of these nanotags, extreme red-shifted SERS was achieved with laser excitations from 1064 nm up to 1550 nm and detection limits in the picomolar to femtomolar range where obtained. Finally, this research demonstrates that when hollow gold nanotags are functionalised with a thermopolymer such as poly(N-isopropylacrylamide), the LSPR can be shifted into the NIR region and laser induced plasmonic heating of the nanoshells can be used to turn on and off the SERS enhancement.

Overall, the development of NIR active nanotags could provide the basis for future advancements in bio-chemical, medical and optical applications.

Abbreviations

Ab-Ag	antibody-antigen
AgNP	silver nanoparticles
a.u.	arbitrary units
AuNP	gold nanoparticles
AZPY	4,4-azopyridine
BPE	1, 2-bis(4-pyridyl)ethylene
CCD	charge coupled device
Chalcogen	chalcogenopyrylium dyes
Citrate	trisodium citrate dihydrate
CoNP	cobalt nanoparticles
CTAB	cetyl trimethylammonium bromide
DLS	dynamic light scattering
DMF	dimethylformamide
DNA	deoxyribonucleic acid
DP	dipyridyl
EDFA	erbium-doped fibre amplifier
FT-RTA	Fourier transform – real time analyser
HER2	human epidermal growth factor
HGNs	hollow gold nanoshells
IR	infrared

LCST	lower critical solution transition temperature
LOD	limit of detection
LSPR	localised surface plasmon resonance
MBA	4-mercaptobenzoic acid
MPY	4-mercaptopyridine
NaCitrate	trisodium citrate dihydrate
Nanotag	combination of nanoparticles + Raman reporter + an aggregating agent (if required)
ND:YAG	neodymium-doped yttrium aluminium garnet
NIPAM	N-isopropylacylamide
NIR	near infrared
OCT	optical coherence tomography
OD	optical density
PCs	principal components
PCA	principle component analysis
PDDA	poly(diallyldimethylammonium chloride)
PEG	polyethylene-glycol
PNIPAM	poly (N-isopropylacrylamide)
PNIPAM-HGN	poly(N-isopropylacrylamide) coated hollow gold nanoshells
PPY	4-(1H-pyrazol-4-yl)pyridine
PSPR	propagating surface plasmon resonance
PTA	photothermal ablation therapy

PYOT	5-(pyridine-4-yl)-1,3,4-oxadiazole-2-thiol
RRS	resonance Raman scattering
RS	Raman scattering
RT	room temperature
s.d.	standard deviation
SEM	scanning electron microscopy
SERRS	surface enhanced resonance Raman scattering
SERS	surface enhanced Raman scattering
SPR	surface plasmon resonance
UCST	upper critical solution transition temperature
UV-Vis	ultraviolet-visible spectrometry
w/v	weight per volume
%RSD	relative standard deviation

Contents

1. General Introduction

Nanoscience and nanotechnology are at the forefront of modern research, with nanoparticles being defined as particles with one or more dimensions less than 100 nm in size. Over the last few decades, there has been an exponential increase in the number of publications in this research area, particularly at the interface between biodiagnostics and nanotechnology. Furthermore, several different types of nanostructures with different metallic cores (such as gold,[1] silver,[2] copper[3] and platinum[4]) have been reported and they have been employed in a wide range of chemical and biological applications.[1, 5] Silver and gold nanoparticles are the most commonly used for optical applications,[6] with gold nanomaterials being predominantly used in the work discussed in this thesis.

1.1 Gold Nanoparticles

Gold is a chemically inert and relatively non-toxic element when compared to other heavy metals and is therefore very useful for bio-medical applications.[7] In addition, gold nanoparticles (AuNPs) make for excellent biological and chemical nanosensors as they possess unique chemical and physical properties.[8] The synthesis is straightward therefore the colloidal solutions are highly stable and reproducible[9] and the synthetic methods reported allow for excellent control over the size, shape and surface chemistry of the nanoparticles. They have distinct optical properties which can be exploited for surface enhanced optical techniques[10] and finally they provide a high surface to volume ratio with excellent bio-compatibility when functionalised with appropriate ligands.[11] Exploiting these unique properties allows researchers to develop novel sensing strategies with improved sensitivity, selectivity and stability.

1.1.1 Synthesis of Gold Nanoparticles

Colloidal gold has a long history in chemistry and has been prepared and used for staining glass and colouring ceramics since ancient times.[11, 12] One of the most famous examples is the Lycurgus Cup which was manufactured in the 4^{th}-5^{th} century B.C. and due to the presence of the gold nanoparticles (AuNPs); the cup appears red

in transmitted light but green in reflected light.[1] However, it wasn't until 1857 when Michael Faraday investigated the red colour of colloidal gold and observed that the properties of colloidal solutions differ from the bulk material that research into metallic nanoparticles really began.[13]

In 1951, Turkevitch[14] reported his synthetic procedure for the preparation of gold nanoparticles, which was later modified by Frens *et al*. in 1973.[15] To date, this is still the most popular method for the preparation of colloidal gold and it generally involves the reduction of hot chloroauric acid ($H[AuCl_4]$), with small amounts of sodium citrate solution. The colloidal gold will form because the citrate ions act as both a reducing agent and a stabilising agent, leaving a negative surface layer that repels the nanoparticles from each other making the solution monodispersed.[1] The Turkevitch method generally yields AuNPs of ~20 nm, while the modified Frens approach, where the AuNP size is controlled by varying the feed ratio of gold to sodium citrate, gives rise to 40 nm AuNPs. The main issue with this method is polydispersity, especially for particles larger than 40 nm. In 2012, Krpetić *et al*. developed a two-step synthesis for larger AuNPs where a relatively monodispersed colloidal solution of greater than 40 nm was obtained.[16] Gold seeds with an approximate size of 14 nm were synthesised using the citrate reduction method and then a further gold layer was deposited on the seeds in the presence of excess sodium citrate producing high quality AuNPs with an approximate size of 45 nm.

Over the past decade or so, there has been a large increase in the number of reports and reviews detailing different preparation methods for colloidal gold, with advances in the synthesis having led to high yielding and reproducible methods with spherical and non-spherical shapes (nanorods/cages).[13] AuNPs from 1 nm to more than 200 nm can now be synthesised and due to their unique properties such as size and shape, they exhibit different chemical, electrical and optical properties from the bulk materials.[8] For optical and many biological applications, gold nanoparticles are favoured substrates as the localised surface plasmon resonance (LSPR) can be tuned from the visible to the NIR region by controlling the synthetic parameters.[17] In addition, the most commonly used property of metallic nanoparticles is the LSPR

which is affected when the nanoparticles interact with light of a specific wavelength.[17]

1.1.2 Surface Plasmon Resonance

The unique and intrinsic optical properties often displayed by metallic nanomaterials, such as intense colour, arise due to the interaction between these particles and electromagnetic radiation.[8] When light of an appropriate wavelength interacts with nanoparticles, an oscillating cloud of electrons is induced on the nanoparticle surface and this phenomenon is known as surface plasmon resonance (SPR). Two types of SPR exist, propagating (PSPR) and localised SPR (LSPR). Propagating SPR occurs on planar surfaces of thin metallic films (<80 nm),[18] whereas localised SPR is observed in metallic nanoparticles and surfaces with nanostructure features, less than 100 nm. Both PSPR and LSPR are sensitive to changes to the dielectric environment surrounding the metallic structure.[17] Herein, only LSPR will be considered as the work discussed only concerns nanoparticles.

LSPR arises due to the collective oscillation of free conductive band electrons at the nanoparticle surface induced by interaction with an incoming electric field. The result of this interaction with electromagnetic radiation, is the displacement of the surface electrons and polarisation extending a considerable distance away from the surface.[6] The collective oscillation of these electrons can be characterised by the resonance band in the extinction spectrum of the nanoparticle. Furthermore, electron oscillations create a highly localised electric field which is greatest at the interface between the particle and the surrounding dielectric medium. This plasmonic field has been shown to enhance a wide number of electrical and vibrational optical properties including fluorescence, Rayleigh and Raman scattering.[18] In addition, the energy of electromagnetic radiation required to excite LSPR depends on a number of factors, including the particle size and shape, morphology of the nanostructure as well as the dielectric constant of the surrounding media.[8] The interaction of light with a spherical metallic nanoparticle is depicted in figure 1.1.

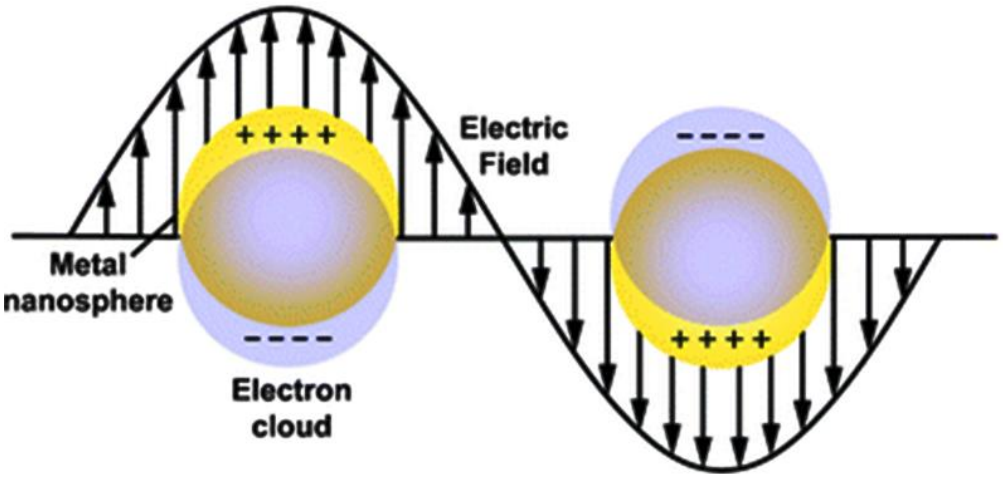

Figure 1.1 – Schematic illustrating localised SPR induced by an electromagnetic field interacting with a spherical nanoparticle.[17]

In 1908 the German physicist, Gustav Mie elucidated the origin of the LSPR phenomenon by solving Maxwell's equation for small spherical nanoparticles interacting with light.[19] He concluded that the plasmon band was due to dipole oscillations of the free electrons in the conduction band occupying the energy states directly above the Fermi energy level. In addition, Mie theory predicts the scattering and absorbance properties of solid metal nanoparticles.[20]

$$C_{ext} = \left[\frac{24\pi^2 R^3 \varepsilon_m^{3/2}}{\lambda}\right]\left[\frac{\varepsilon_2}{(\varepsilon_1+2\varepsilon_m)^2 + \varepsilon_2^2}\right] = C_{abs} + C_{sca} \qquad \text{Equation 1.1}$$

where C_{ext} is the extinction cross co-efficient, R is the radius of the nanospheres, λ is the wavelength of incident light, ε_m is the dielectric constant of the surrounding medium, and $\varepsilon_1 + i\varepsilon_2$ is the complex dielectric constant of the particle where ε_1 and ε_2 are the real and imaginary components respectively. The extinction co-efficient itself is made up of two components, C_{abs} is the absorption co-efficient, and C_{sca} is the scattering co-efficient.

From equation 1.1, a resonance peak occurs whenever the condition of $\varepsilon_1 = -2\varepsilon_m$ is satisfied. This is the SPR peak which accounts for the strong colour of metal nanoparticles. For example, using Mie theory the surface plasmon band for 15 nm

gold nanoparticles is 520 nm and for 35 nm silver nanoparticles the surface plasmon band is 400 nm. The surface plasmon band will shift depending on nanoparticle size, shape, the inter-particle distance and changes in the local environment for example the refractive index of the surrounding medium.[20] Hence, it is important to note that different solvents or capping agents used during the synthesis can cause the LSPR peak to shift. Moreover, aggregating nanoparticles causes a large change in the extinction co-efficient as bringing metal surfaces into contact with one another results in a significant change in the value of ε_m. Bringing two or more particles into close contact will cause the size to increase, a pronounced colour change to occur (from red to purple for gold nanoparticles) and a red-shift in the LSPR to be observed. This is due to plasmonic coupling between particles, thus when the inter-particle distance is shorter, a red shift to longer wavelengths is obtained.[20]

Equation 1.1 shows that the extinction co-efficient (C_{ext}) varies depending on the wavelength of incident light and the properties of the substrate material. The higher the extinction value, the more likely it is that individual nanoparticles can be optically detected. From equation 1.1, for C_{ext} to be large, the denominator ((ε_1 + $2\varepsilon_m)^2$ + ε_2^2)) needs to approach zero and this occurs when ε_2 is small ($\varepsilon_1 = -2\varepsilon_m$). For metals such as gold and silver, ε_1 and ε_2 are strongly wavelength dependent, with ε_2 increasing at longer wavelengths. For spherical gold nanoparticles with a size of ~10 nm, approximate values for ε_1 and ε_2 at 633 nm are 0.18 and 3.4 respectively, while at 785 nm, these are 0.15 and -4.8 respectively.[21]

Furthermore, the scattering co-efficient (C_{sca}) is also dependent upon the dielectric constant of the surrounding medium; increasing the value of ε_m leads to a decrease in the extinction, and a red shift in the LSPR being observed.[22] In addition, the nanoparticle size strongly influences the C_{ext} as the equation contains the component R^3 where R is the radius of the nanoparticle. A small change to the size or width of the nanoparticle will lead to a large change in C_{ext}. The extinction peak will become significantly broader upon increasing particle size,[20] with the width of the distribution also providing a good indication of the homogeneity of the nanoparticles.[23] Polydisperse samples will have broad extinction spectra.[1] For larger particles, the scattering co-efficient dominates due to the particles scattering light

more efficiently and strongly. Therefore, as the particle size decreases the absorption co-efficient (C_{abs}) begins to dominate.[22]

In general, Mie theory applies to nanoparticles that are quasi-spherical (particles with a more or less rounded profile and with facets on the surface), with a size less than 100 nm and where the nanoparticles have a relatively narrow plasmon excitation window.[20] However, when larger nanoparticles and/or non-spherical shapes are to be modelled, Mie theory on its own can no longer be applied. Other methods such as Gans formula,[24] discrete dipole approximation[25] and T-matrix formulation[26] have to be employed, but note they all use Mie theory as a basis for understanding.[20]

1.1.3 Exploiting Nanoparticle Size and Shape

While initial research focussed around spherical nanoparticles, recently the ability to directly control growth of the nanoparticles and specifically to control their size, shape, morphology and composition has been identified as an essential goal in nanoparticle research.[27] Several procedures for producing nanoparticles of defined shape and size have been published in the literature, i.e. hollow gold nanoshells,[28] nanocages,[29] nanorods,[30] nanocubes,[31] nanodumbbells,[32] nanostars,[33] and even nanocastles,[34] have been described plus many more.[27]

Controlling the size, shape and metal of nanoparticles allows for fine tuning of the optical properties in particular the LSPR, across a range of wavelengths which can be exploited to make them application specific. Figure 1.2 shows a range of colloidal nanoparticle solutions with their associated absorption wavelengths.

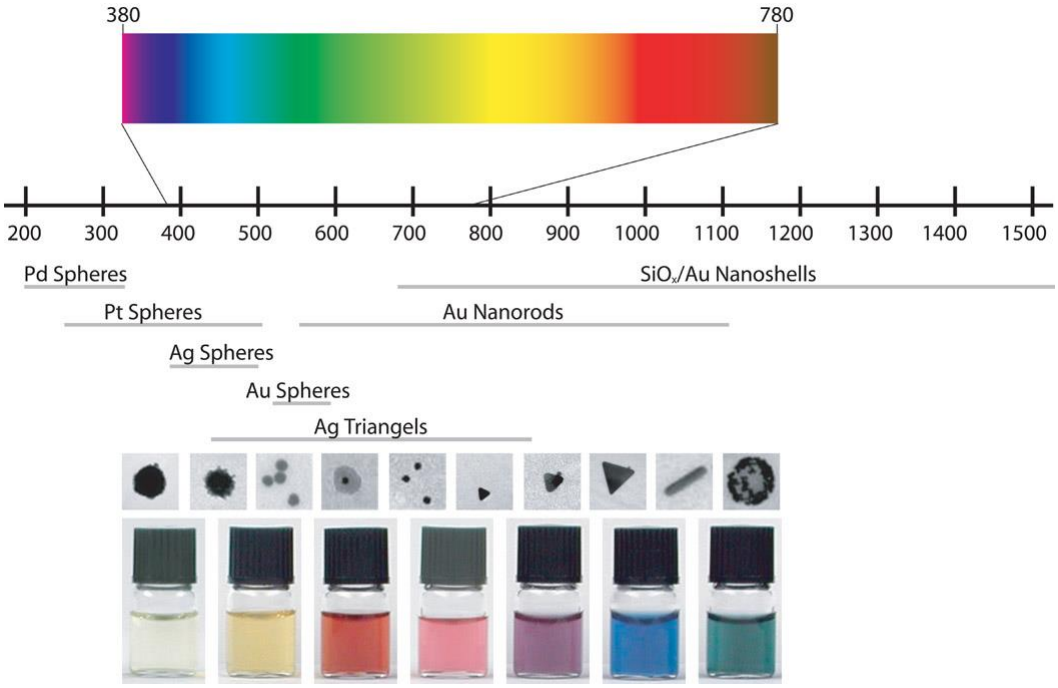

Figure 1.2 - Colloidal nanoparticles of different material, dimension, and shape covering a wide range of the electromagnetic spectrum. Pd: Palladium. Pt: Platinum. Ag: Silver. Au: Gold. SiO_x: Silicon oxide. From left to right the colloidal solutions are as follows: pale yellow/colourless solution is Ag spheres with an average particle size of 5 nm; yellow solution is Ag spheres with an average size of 20 nm; red solution is Au spheres with an average size of 30 nm; pink solution is Au spheres with an average size of 60 nm; purple solution is Au triangles with an average size of 25 nm; blue solution is Au triangles with an average size of 50 nm and green solution is Au nanoshells with an average size of 70 nm.[35-38]

Individual spherical nanoparticles only cover a small range of the visible spectrum, in the case of silver, from ~380 to 500 nm[39] and with spherical gold, from ~515 to 580 nm.[40] Aggregating the nanoparticles or alloying them with other noble metals, increases the range of wavelengths covered, as does changing the shape.[35] Gold nanorods and gold nanoshells can be tuned well into the NIR region by controlling the growth parameters during synthesis.[9, 20] By exploiting the unique properties of gold nanostructures, researchers have been able to achieve unprecedented control over the dimensions, morphology and optical properties of these nanoparticles.[41] Further, allowing these gold nanomaterials to be employed in a wide range of applications.[17]

Gold nanoparticles have been exploited in catalysis, electronics, biological, optical and medicinal applications.[42] Since AuNPs exhibit excellent light scattering properties, they can be used in biological imaging and surface enhanced Raman spectroscopy (SERS).[43] Their relatively small particle size corresponds to a large surface area which helps facilitate transport of particles into biological environments and as such provides exciting opportunities for drug and gene delivery.[44] The problem with small gold nanoparticles is that the spectral window for laser excitation is limited to the visible region and the depth of penetration in turbid media such as blood and tissue samples is limited. However, these problems can be overcome with the use of NIR (near infrared) active nanoparticles.[45]

Larger gold nanoparticles and nanostructures of non-spherical shape can be tuned to be optically active in the NIR region. In recent years, researchers have exploited the properties of these nanostructures by employing them in a range of bio-medical and optical applications specific to the NIR region, see figure 1.3. [46, 47] To date, gold nanoshells,[48-50] nanocages[51-53] and nanorods[54-56] appear to be the most utilised nanomaterials with applications in optical coherence tomography (OCT) imaging which uses light scattering to produce *in-vivo* images of tissue with resolution approaching a few micrometres.[57] They have also served as contrast agents for photoacoustic (PA)[58-62] and multimodal (PA/fluorescence) imaging.[63-65] Furthermore, they have been functionalised with cancer-specific antibodies and used as photothermal agents for the selective targeting and destruction of cancerous or diseased tissue.[66] In addition, due to their bio-compatibility they can serve as drug delivery vehicles for controlled and localised release in response to external stimuli such as NIR radiation or high-intensity focused ultrasound.[53]

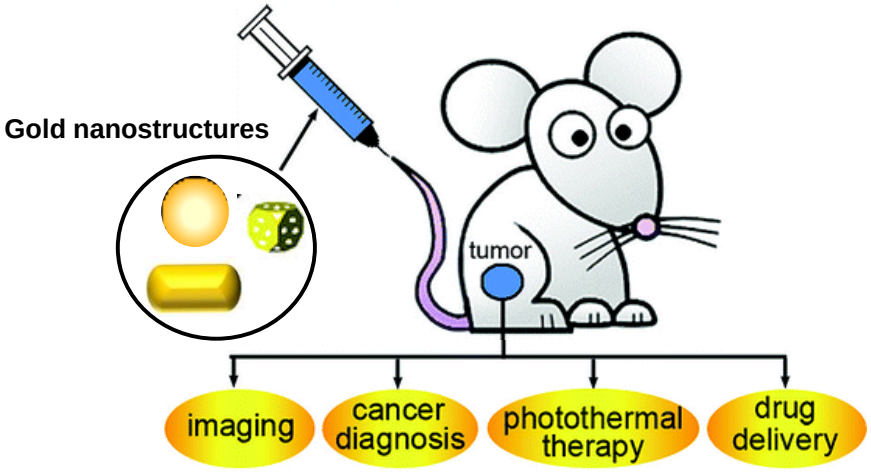

Figure 1.3 – Theranostic applications utilising gold nanostructure.[53]

The ability to tune the optical properties from the visible to the NIR region is widely considered to be the greatest advantage these nanostructures have over spherical nanoparticles.[20] As previously mentioned alloying gold nanoparticles with other noble metals or aggregating them can cause a change to the size, morphology and ultimately increase the wavelength range covered.[35] However, changing the shape of the nanoparticle is the dominant method researchers have adopted, in order to design NIR active nanostructures.[9] Gold nanocages were first synthesised by Xia *et al*. in 2005,[67] using a galvanic replacement reaction between silver (Ag) nanocubes and chloroauric acid ($HAuCl_{4)}$ in an aqueous solution. These unique gold nanostructures possess hollow interiors and ultrathin, porous walls with a size ranging from 10 to over 150 nm.[62] By controlling the molar ratio between Ag and $HAuCl_{4;}$ gold nanocages can be precisely tuned from the visible to the NIR region up to 1200 nm.[20]

Since the late 1990s, several methods for the growth of gold nanorods have been developed.[68-70] The most commonly used method however, is surfactant directed seed mediated synthesis, which was first described in 2001 by Jana *et al*.[71] For gold nanorods the LSPR band is split into two distinct modes, corresponding to a transverse (short axis) band and a longitudinal (long axis) band, with the resulting extinction spectrum being dependent on the aspect ratio of the particles.[20] Again by modifying the experimental parameters during the synthesis, nanorods of various lengths and sizes can be obtained and as such the longitudinal band can be tuned well into the NIR region (up to 1500 nm).[72] In general, increasing the length of the

nanorods leads to a red shift of the LSPR, while an increase in width results in a blue shift.[73]

By exploiting the characteristics (size, shape and tunable plasmon band) of these nanostructures, researchers have noticed that these unique nanoparticles make prime candidates for use in a wide range of applications from optical sensing[29, 74, 75] to bio-diagnostics.[49, 53, 76] In this research, relatively new class of nanostructures have been employed called "hollow gold nanoshells" (HGNs). Research interest into these nanoparticles has flourished over the last few years, due to their strong NIR absorption, small spherical structure and excellent optical properties.[49]

1.2 Hollow Gold Nanoshells

1.2.1 Synthesis of HGNs

In 2003, Sun *et al.*[77] synthesised new metal nanostructures with tunable sizes and excellent optical properties. The new nanomaterials were termed 'gold nanoshells with hollow cores' and were synthesised utilising a sacrificial galvanic replacement of silver with gold.[77] The synthesis utilises the difference in redox potential between metallic silver (sacrificial template) and gold salt in solution, figure 1.4. When the gold ions (Au^{3+}) come into contact with the silver atoms, there is electroless plating that causes the Au^{3+} ions to be reduced to gold atoms and the silver atoms are oxidised to Ag^{+} ions. A single gold atom is generated when 3 silver atoms are oxidised, resulting in the thickness of the Au nanoshell being $1/9^{th}$ of the lateral dimension of the initial silver template, thus leaving a hollow core.[77] The structure is no longer a solid sphere and as such the LSPR shifts from ~420 nm which is characteristic of silver nanospheres to ~680 nm. This synthetic process has been extended to hollow cubes which have also been shown to be SERS-active, however, not at the single particle level.[78]

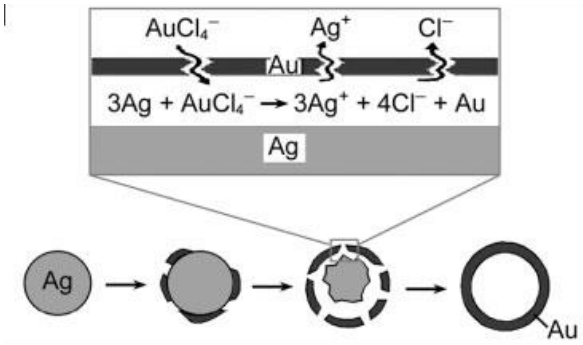

Figure 1.4 – Schematic illustration of the experimental procedure that generates gold nanoshells with hollow interiors by templating against silver nanoparticles. Redox potentials: $AuCl_4^-$/Au redox pair 0.99 V and Ag+/Ag redox pair 0.88 V.[77]

In 2005, Liang *et al*. reported an alternative synthetic process for making gold nanoshells with hollow cores, however, this time cobalt nanoparticles were used as the sacrificial template.[79] In this report, a range of HGNs were synthesised by controlling the size of the interior cavity and as such the LSPR of the HGNs were tuned through the visible region from 526 to 628 nm. This was the birth of hollow gold nanoshells as they are known today, and they can be used for single particle detection when HGNs with a particle size ≥30 nm are used (nanoshells ≥30 nm in size are generally uniform and stable).[80] This synthesis was later improved, by Schwartzberg *et al*. in 2006 to create high quality, nearly homogeneous nanoshells with a small size, spherical shape and a LSPR absorption range tuneable from the visible to the NIR region (from 550 to 820 nm).[28]

The HGN synthesis is based on the galvanic displacement of cobalt with gold, to produce homogeneous nanoshells. Hollow gold nanospheres consist of a spherical gold shell filled with embedding medium and are synthesised initially by forming cobalt nanoparticles (CoNPs) which act as the sacrificial template for the HGN synthesis. The CoNPs are synthesised under an inert atmosphere due to these particles being very sensitive to oxygen; by reducing Co^{2+} ions to Co^0 atoms in the presence of sodium borohydride and trisodium citrate, the reducing agent and capping agent respectively. The gold shells are then grown onto the CoNPs via a galvanic replacement reaction. Here, the Co atoms are oxidised back to Co^{2+} ions and the Au^{3+} ions are reduced to Au^0 atoms, depositing on the Co template. It is believed that the porous nature of the materials during the galvanic replacement, allows for

diffusion of the Co^{2+} ions outwards and away from the transient cobalt template and the Au^{3+} ions inwards and onto the transient cobalt template. After, exposure to air any resultant CoNPs are oxidised leaving a hollow core and complete gold shell, figure 1.5.[27, 28, 79]

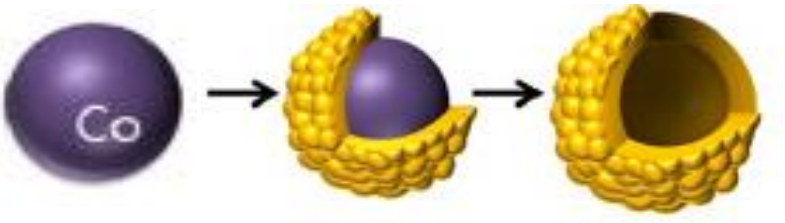

$$2CoCl + 2NaBH_4 + 9H_2O \longrightarrow Co_2B + 4NaCl + 12.5\ H_2 + 3B(OH)_2$$

$$4Co_2B + 3O_2 \longrightarrow 8Co + 2B_2O_3$$

$$3Co^0 + 2Au^{3+} \longrightarrow 3Co^{2+} + 2Au^0 \qquad (AuCl_4^-/Au: 0.935V \quad Co^{2+}/Co: -0.377V)$$

Figure 1.5 - Schematic of synthesis process in the basis of using cobalt nanoparticles as sacrificial templates that allow different shapes and sizes of HGNs to be produced following gold deposition.[81]

Schwartzberg *et al*. reported that the quality and overall size of the resultant HGNs depends highly on the quality of the starting CoNPs.[28] In addition, the LSPR of HGNs can be tuned from the visible to the NIR region (figure 1.6) by reducing the concentration of capping agent and gold salt during synthesis, as these parameters are responsible for controlling the inner diameter and shell thickness of the HGNs respectively.[28, 82] On the basis of theoretical calculations, Hao *et al*. reported that HGNs with large diameters and thin shells will ultimately have LSPR bands which are red-shifted.[41] Like standard gold nanoparticles, the LSPR bandwidth of HGNs depends on the uniformity of the shell's diameter and thickness. Poorer uniformity results in broader spectral distributions being observed.[28] In order to make high-quality HGNs, especially those with LSPRs in the NIR region, the synthesis must be carefully controlled, with exclusion of oxygen being the most vital factor.[28] Further discussion on the synthesis of HGNs can be found in section 2.4.1.

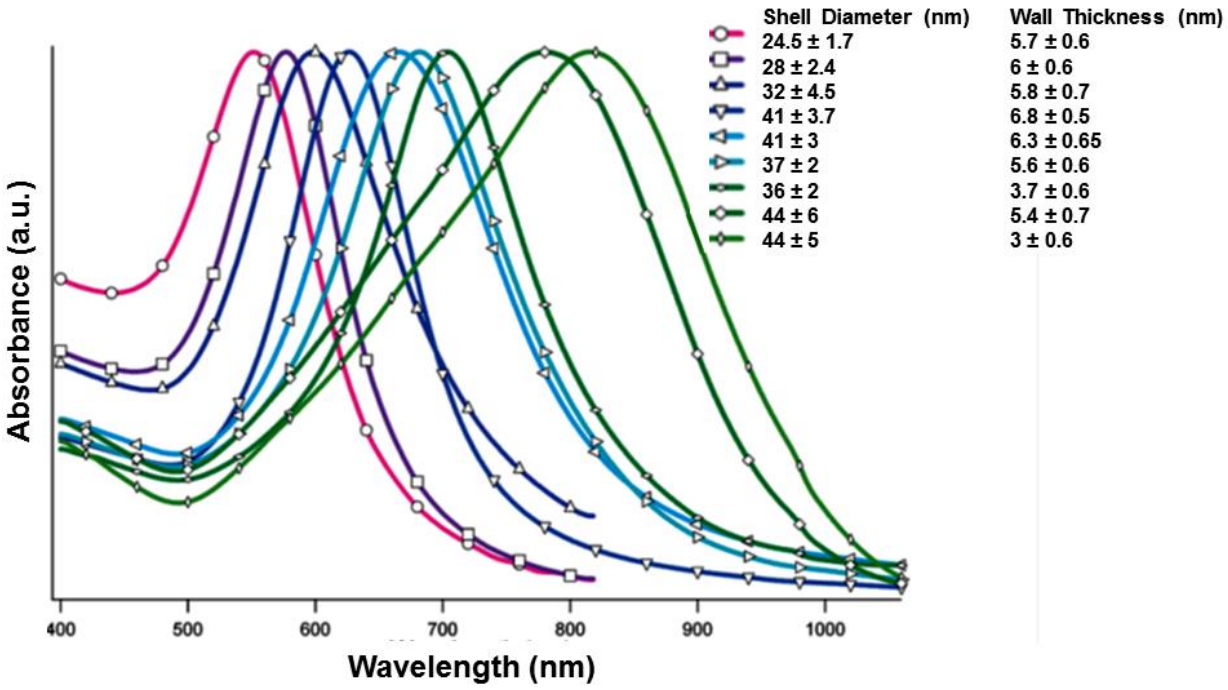

Figure 1.6 – Extinction spectra of nine HGN samples with varying diameters and wall thickness.[28]

1.2.2 Applications of HGNs

Due to their small size, spherical shape and their tunable plasmon absorption band, there is currently a wide interest in these nanostructures, especially in biological and chemical applications.

For photothermal ablation therapy (PTA), the ideal metal nanostructure should be able to absorb electromagnetic radiation effectively, have a strong and tunable LSPR in the NIR for better tissue penetration, be easy to deliver, have a low toxicity, and be convenient for bio-conjugation for actively targeting specific cancer cells.[49] HGNs are the perfect candidates for PTA due to them having these characteristics. In 2008 & 2009, Zhang *et al*. reported that HGNs had been successfully utilised in both, *in-vitro* and *in-vivo* PTA of carcinoma and melanoma cancer cells.[83,84]

Figure 1.7 demonstrates the basic idea behind PTA. The HGNs are actively targeted to cancer cells though antibody (Ab)-antigen (Ag) or ligand (eg. hormone-receptor interactions. Heat (represented by the symbol Δ) generated from light illumination (h*v*) of the HGNs is used for thermal imaging and/or destroying of the cancer cells.

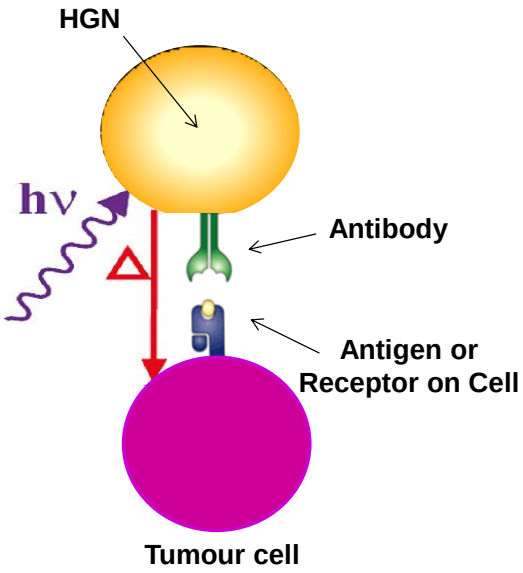

Figure 1.7 – Illustration of the basic principle of PTA. HGNs are first functionalised with specific targeting groups for the tumour cells and then heat generated by the conversion of the illumination light selectively targets and destroys the tumour cells.[49]

Due to their unique properties, HGNs are ideally suited for both *in-vitro* and *in-vivo* applications. Melancon showed for the first time, that by functionalising HGNs with a small molecular weight peptide (polyethylene glycol-SH), receptor-mediated active targeting of melanoma and efficient PTA (with photothermal coupling agents) *in-vivo* can be achieved.[83] In addition, Lu *et al*. reported that HGNs are at least 8 times more efficient than solid gold nanoparticles in PTA treatment due to their much stronger NIR absorption and more effective photothermal conversion.[84]

HGNs have also been successfully used for pH sensing,[85] SERS imaging of cancer markers in single cells,[81] on-chip immunoassay,[86] and as a DNA biosensor.[87] Due to their unique optical properties and small size (usually from 30 to 80 nm) they will be at the forefront of many new applications from bio-diagnostics to imaging and from cancer therapy to drug-delivery.

1.3 Surface Plasmon Enhanced Spectroscopies

When metallic particles are confined to the nanoscale, the optical scattering properties are enhanced due to the presence of LSPR. This leads to an attractive opportunity to combine metallic nanoparticles with classical spectroscopic techniques in order to develop more sensitive analytical measurements.

According to Mie theory, light scattering efficiency is greatly enhanced under certain resonance conditions. The excitation of surface plasmons creates highly localised intense electric fields (hot spots) close to the nanoparticle surface, which decay exponentially into the dielectric medium away from the surface.[6, 23] This means that noble metal nanoparticles are able to effectively focus resonantly coupled light.[76] As a result, there is an increase of all radiative properties, such as light absorption, fluorescence, Rayleigh scattering and Raman scattering. The strong scattering displayed by these nanoparticles is the main reason for increasing interest in utilising these materials for optical applications.[76]

1.3.1 UV-Visible and Fluorescence Spectroscopy

The interaction of light with matter is the fundamental optical process that underpins spectroscopies such as absorption, fluorescence and Raman spectroscopy, figure 1.8. The process of absorption occurs when a photon of light interacts with a molecule. The photon will be absorbed if the energy of the incident photon matches the energy difference between the band gap of an electronic transition within a molecule. Thus an electron will be excited from the ground state to an excited electronic state. Infrared (IR) spectroscopy and UV-visible spectroscopy are commonly employed absorption spectroscopies in analytical chemistry.[6]

Fluorescence spectroscopy arises when a molecule, known as a fluorophore, absorbs a photon of light and is promoted from the ground electronic state to a higher vibrational level of the excited electronic state. However, this higher energy state is unstable so vibrational relaxation occurs to the lowest excited state. Following this relaxation back to the ground state occurs which is accompanied by the emission of a

photon, this is known as fluorescence. The emitted photon is lower in energy; therefore it has a longer wavelength than the absorbed light.

In general, the concentration of the fluorophore is proportional to the intensity of the emitted light which enables quantification of analytes. However, structural information is minimal since spectra are not specific to individual molecules. In addition, due to fluorescence producing broad bands the multiplexing capabilities of this technique is limited because when multiple fluorophores are present their peaks tend to overlap. Despite these disadvantages, the use of fluorescence detection is still widespread as it is an extremely sensitive technique.[88-91]

1.3.2 Raman Scattering

Raman spectroscopy is an alternative optical detection technique which can overcome some of the disadvantages observed with fluorescence. Its main advantage is that it can generate a unique spectral fingerprint of the molecule being analysed; thus allowing structural identification and multiple analytes to be simultaneously detected.[6]

When light interacts with matter, the photons of light may be absorbed (as discussed in section 1.3.1) or scattered, or they may pass through without any interaction. Initial studies on the scattering of light focused on elastic scattering, in which scattered photons have the same energy as those of the incident light. Elastic scattering is better known as Rayleigh scattering, named after Lord Rayleigh who discovered the phenomenon.[92] However, approximately one in every $10^6 – 10^8$ of the scattered photons will have energy higher or lower than the incident light and this weak effect is described as inelastic scattering. This phenomenon was first proposed by Smekal in 1923 and was observed experimentally in 1928 by Raman and Krishnan; this process is referred to as Raman scattering.[93]

When light interacts with a molecule, polarisation of the electron cloud results in a short-lived virtual state being formed. In the case of Rayleigh scattering, the distortion of the electron cloud has no effect on the nucleus, with the light being scattered at the same frequency as the incident light. In the case of Raman scattering, nuclear motion is induced and energy is transferred from the incident photon to the

molecule (Stokes scattering) or from the molecule to the scattered photon (anti-Stokes scattering).[6] The diagram in figure 1.8 illustrates the energy transitions in each of the optical processes discussed; absorption, fluorescence and the different forms of Raman scattering.

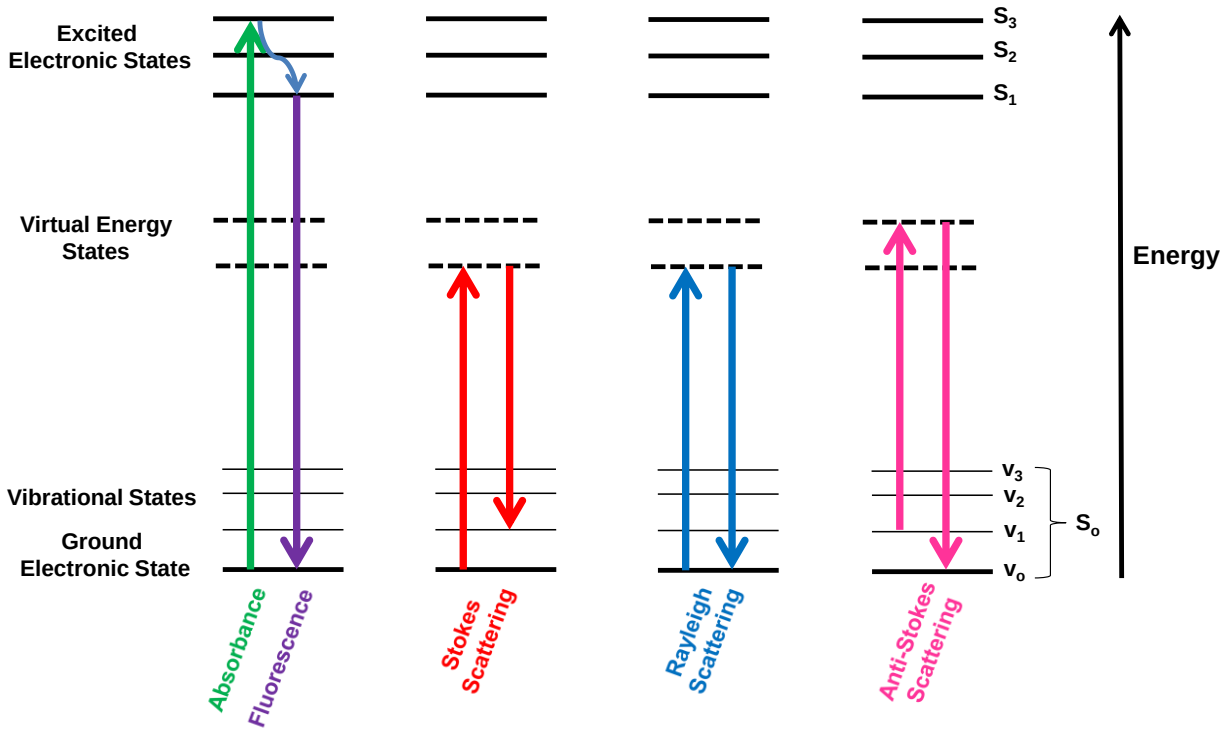

Figure 1.8 - Jablonski diagram depicting the various optical processes: absorption, fluorescence and the different forms of Raman scattering.

Stokes Raman scattering occurs when photons are scattered with less energy than the incident photons. This is a due to molecules absorbing energy from incident photons and being promoted from the ground vibrational state to an excited vibrational state that is higher in energy. At higher temperatures, some molecules will be present in the excited vibrational state and anti-Stokes scattering can occur, where the molecules will lose energy to the scattered photons on returning to the ground state. However, it should be noted that at room temperature most molecules will be present in the ground state. Therefore, the intensity of Stokes scattering is greater than that of anti-Stokes scattering and is employed more commonly in Raman spectroscopy for acquiring spectra.[6] The Boltzmann equation (equation 1.2) can be used to calculate the ratio of the intensities of Stokes and anti-Stokes scattering, where Nn is the number of molecules in the excited energy state En, Nm is the number of molecules

in the ground energy state Em, g is the degeneracy of the levels, En – Em is the difference in energy between states En and Em, k is the Boltzmann's constant (1.3807 x 10-23 JK-1) and T is temperature (K).

$$\frac{N_n}{N_m} = \frac{g_n}{g_m} \exp\left[-\frac{(E_n - E_m)}{kT}\right]$$ Equation 1.2

The shift in energy between the exciting laser beam and the scattered energy is known as Raman shift and it corresponds to molecular vibrations. The number of possible vibrations is related to how many atoms are present in the molecule. The frequency of the vibration is related to the bond strength and mass of the atoms. Hence, Raman spectra can provide information regarding the structure of the molecule under analysis.

Interest in Raman is extensive as it is a non-destructive technique, requires minimal sample preparation and analysis of samples can be carried out in water. In addition to this it gives molecularly specific spectra and with the discovery of SE(R)RS it has been shown to be extremely sensitive, fulfilling criteria for single molecule detection.[94]

The intensity of the scattering increases with the fourth power of the excitation frequency.[6] Therefore, at the UV end of the electromagnetic spectrum, the sensitivity is far greater due to the frequency increasing and the scattering becoming stronger. However, problems with sample absorption, fluorescence and decomposition can be encountered at these higher energies.[95, 96] It is possible to move into the infra-red part of the electromagnetic spectrum, with laser excitations above 785 nm. Many compounds do not fluoresce at these lower energies so the laser power can be increased for improved signal intensity.[6] In addition, if the laser power is increased the scattering is stronger, but it can lead to sample decomposition due to the increase in energy being applied.[95] Another problem encountered is, if an impurity is present in the sample, which fluoresces at the excitation wavelength it will produce a broad spectrum that will overlap and obscure the Raman peaks produced, even at very low concentrations.[97]

1.3.3 Resonance Raman Scattering

The sensitivity and selectivity of Raman scattering can be improved by tuning the frequency of the wavelength of interrogating light to the frequency of an electronic transition in a molecule. This gives rise to the technique known as resonance Raman scattering (RRS) and it can be used to obtain both electronic and vibrational information from a molecule. Signal enhancements in the region of 10^4 are typically reported, however there are reports in the literature with enhancements up to 10^{6}.[6]

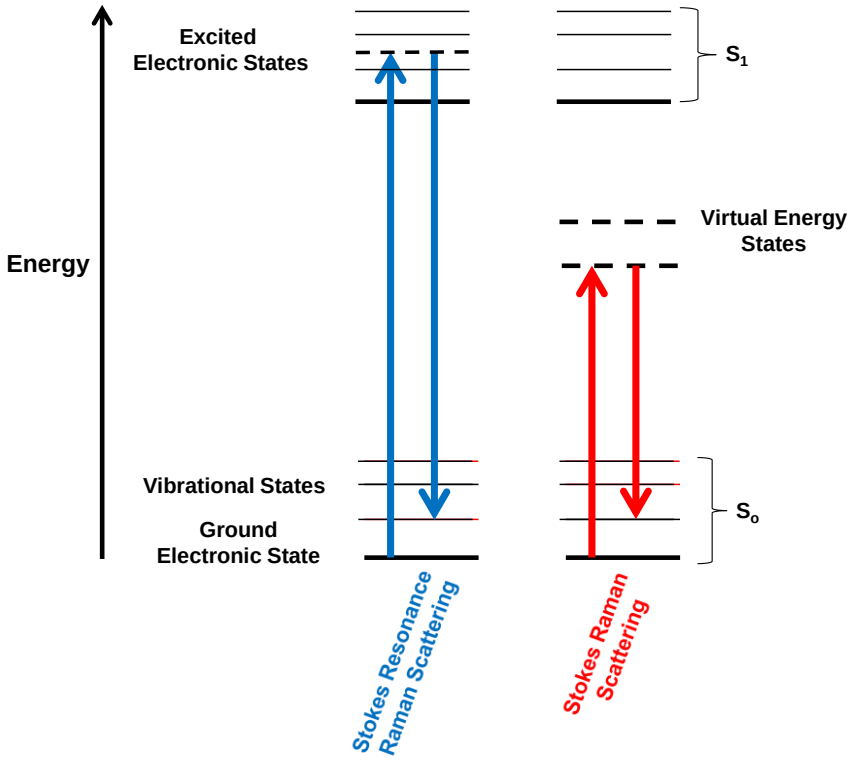

Figure 1.9 - Energy transitions of resonance Raman scattering.

The main difference between Raman and RRS is depicted in figure 1.9. In RRS absorption results in the excitation of a molecule to an excited vibronic state within the first electronic state, whereas in Raman scattering the molecule is excited to a virtual energy level. As a result, RRS allows for more intense spectra to be obtained and can therefore be used for positively identifying analytes in a complex matrix such as biological samples. There are limitations however, such as sample decomposition and unwanted fluorescent backgrounds due to the unavoidable absorption process that can occur alongside RRS.[6] These limitations can be

overcome using other Raman techniques known as surface enhanced Raman scattering (SERS) and surface enhanced resonance Raman scattering (SERRS)

1.3.4 Surface Enhanced Raman Scattering

SERS was first reported by Fleishman *et al.* in 1974,[98] when an enhancement in the Raman signal was observed from pyridine immobilised on a roughened silver electrode, in comparison to a smooth silver electrode. At the time, the increase in Raman signal was explained by an increase in surface area of the electrode, thus more pyridine molecules were able to adsorb, leading to an increase in the concentration of pyridine in the sampled area. However, this theory was soon disputed by two research groups, who proposed two separate hypotheses, as they determined that a signal increase of 10^6 could not be explained simply by an increase in surface area and that the effect must be due to increased scattering due to surface enhancement by the roughened silver electrode.[99, 100] Albrecht and Creighton proposed a charge transfer enhancement,[99] while Jeanmaire and Van Duyne suggested that the enhancement was from an electromagnetic effect.[100]

There is evidence supporting both of these theories and it is generally believed that both contribute to the SERS enhancement; however the electromagnetic effect is thought to be the dominant process. This arises when a molecule is adsorbed onto or in close proximity to a metal surface leading to an interaction between the surface plasmons and analyte molecule. In order for maximum enhancement to occur, the incident laser should be tuned in resonance with the surface plasmon. This will lead to the surface plasmons oscillating, which will increase the electromagnetic field surrounding the analyte and cause greater polarisation around the molecule. Furthermore, when the plasmons oscillate perpendicular to the surface a greater enhancement is observed. It should also be noted that the analyte does not need to be adsorbed onto the surface of the metal for an electromagnetic enhancement to occur.[6, 101]

The charge-transfer theory describes the analyte as being chemically bonded to the metal surface and excitation occurs by transferring the electrons from the metal to the molecule and back to the metal again. The formation of these bonds induces a

charge-transfer which increases the polarisability of the molecule and as such increases the scattering effect.[102, 103]

To date, there have been several different metals which have been used to provide surface enhancement including silver,[2] gold,[1] copper[3] and a series of other transition metals.[96] In addition, the most common form of SERS substrates are colloidal suspensions, electrodes, metal films and metal nanoparticles.[99] The surface enhancement observed upon an analyte being adsorbed onto a metal surface is dependent upon the amount of roughening of the surface and therefore, for colloidal solutions this depends upon the size of the nanoparticles, the metal chosen and the surface area.[104] An aggregating agent is often added to colloidal solutions in order to decrease the repulsion energy between nanoparticles allowing them to come together. Thus it increases the surface roughness, creates SERS hotspots and increases the electromagnetic field, which ultimately increases the SERS signal.[105]

Commonly, silver and gold nanoparticles are utilised in SERS as they are resonant in the visible region, with silver generally providing greater signal enhancements.[6, 96] This is due to the greater polarisability of silver, giving rise to larger surface plasmons. Moreover, gold possesses a smaller scattering to absorbance ratio and so the scattering obtained from silver is greater.[106] However, as already explained in this introduction, gold has many attributes such as the LSPR can be tuned well into the NIR region and as such is commonly used in SERS.

1.3.5 Surface Enhanced Resonance Raman Scattering

Surface enhanced resonance Raman scattering (SERRS) combines both RRS and SERS by incorporating surface enhancement and a resonant chromophore. This technique was first discovered by Stacy and Van Duyne in 1983,[107] with enhancements in the Raman signal up to 10^{14}.[6, 96]

In SERRS, a chromophore is adsorbed onto a roughened metal surface and the laser excitation chosen coincides with or lies close to, an electronic transition of the chromophore. In addition, the enhancement is maximised if the laser frequency also coincides with the resonant frequency of the surface plasmons on the metal surface. Thus the enhancement is due to both surface plasmon resonance and molecular

resonance.[6] This allows for greater enhancement factors to be obtained and as such vast improvements in sensitivity and selectivity.[108]

There are further advantages of using SERRS, such as fluorescence interference is quenched on the nanoparticle surface, therefore fluorescence backgrounds are minimised and sensitivity is improved.[96] This greater sensitivity allows reduced laser powers to be employed, which also leads to the risk of sample degradation being reduced.[6, 109] The multiplexing capabilities can be further improved by introducing dye labels with differing resonant frequencies. This allows for the detection of multiple analytes by choosing dyes that are in resonance at different laser wavelengths.[110] The greater sensitivity and multiplexing capabilities of SERRS are the main advantages this technique has over rivalling fluorescence detection methods.[109, 110]

1.3.6 SE(R)RS Applications employing HGNs

The penetration depth of photons in biological tissues is limited by the inherent absorption and scattering of the components which make up tissues such as blood and water.[28, 49] These processes are mainly limited due to the strong absorption of blood at short wavelengths and water at longer wavelengths.[82] These components however, have reduced absorption and scattering effects in the NIR region which provides a relatively transparent optical sensing window for bioanalysis.[28, 49] Therefore, to take advantage of this there is a great need to develop new materials and sensing probes which work at longer excitation wavelengths such as the design of NIR active SERS nanotags which will give a unique spectral fingerprint in this uncongested spectral window. However, designing SERS-active nanostructures with maximum reproducibility and intensity are some of the challenges in which researchers working in the field of bio-nanotechnology are currently facing. Furthermore, engineering a SERS substrate with a consistent size, shape, and tunable LSPR is also a significant problem. Therefore, the development of nanosensors which can provide optical detection across a range of wavelengths are greatly desired. The combination of HGNs and SE(R)RS could potentially provide a solution to these problems, thus research groups across the world have been looking into exploiting the optical properties of HGNs.[28, 49, 82, 111]

Laurence *et al*. compared the SERS response from solid spherical gold nanoparticles of uniform size, randomly aggregated poly-disperse silver nanoparticles, linked clusters of poly-dispersed silver nanoparticles and HGNs. It was found that HGNs had a lower Raman activity than randomly aggregated nanoparticles, however, they are more uniform than any other nanoparticle substrate.[112] Furthermore, Zhang *et al*. used HGNs as a SERS-based pH sensor and due to the consistency of particle size and shape, a 10-fold increase in SERS was observed over aggregated silver nanoparticles.[49] Schwartzberg *et al*. demonstrated the consistency and reproducibility of the optical response of HGNs in nanophotonics and sensing applications.[113] In addition, Chon *et al*. showed that HGNs can be used for highly reproducible immunoanalysis of cancer markers. Using SERS as the detection method they demonstrated limits of detection in the region of 1-10 ng/mL for rabbit immunoglobin.[86] Moreover, Lee *et al*. employed HGNs for SERS imaging of HER2 (human epidermal growth factor) cancer markers where they demonstrated greater homogeneous scattering properties than silver nanoparticles. They proposed that HGNs would make highly sensitive and homogeneous sensing probes for bio-chemical imaging.[81] Recently, Lee *et al*. reported HGNs can enhance the SERS signals of individual particles to a greater extent due to pinholes being present in the HGN shell which caused an increase in the electromagnetic field. This newly developed 'enhanced imaging' allowed for single molecule detection as well as HGNs to be employed in the detection of specific biological markers expressed in living breast cancer cells.[114]

Therefore, the detection capabilities of SE(R)RS in conjunction with the unique physical properties of HGNs such as small size, spherical shape and tunable plasmon band, looks like a plausible solution for combatting the current challenges faced by bio-nano researchers. To date, however, there are a limited number of reports of HGNs being used in SE(R)RS applications in the NIR region and thus the development of nanosensors for use in this uncongested spectral window is vital. Therefore, the basis of this research was to design SERS substrates which were highly stable, reproducible and could provide intense SERS signals beyond the visible region; ideally beyond 785 nm in order to provide the basis for future advancements in the NIR region.

1.4 Research Aims

The overall aim of this research was to create extreme red-shifted nano-sensors which could be detected by SERS. More specifically, to synthesise hollow gold nanoshells and encapsulate them with a range of commercial Raman reporters, NIR active Raman reporters and/or thermopolymers for SERS detection using extremely red-shifted laser excitations. The aims of this research can be separated into three main sections:

- Chapter 2 discusses the design of a NIR active SERS substrate. Particularly how the synthetic procedure of the HGNs was optimised in order to shift the plasmon band further into the red than normal gold nano-structures and in particular beyond 800 nm so they were NIR active. The nanomaterials were then fully characterised in order to investigate their optical properties and in particular their SERS capabilities with a range of commercially available Raman reporters using 1064 nm laser excitation.

- Chapter 3 investigates how hollow gold nanotags can be developed in order to achieve extremely red-shifted SERS. In these studies, chalcogenopyrylium Raman reporters have been added to HGNs and analysed using a range of NIR laser excitations (from 1064 to 1550 nm). Furthermore, investigation into how one of these dyes bonds and orientates on the HGN surface has also been carried out using theoretical calculations and space filled models.

- Chapter 4 investigates the synthesis, characterisation and optical properties of thermosensitive SERS nanotags. In this work HGNs were functionalised with the thermopolymer, poly(N-isopropylacrylamide) (PNIPAM) and the SERS response monitored using a 1064 nm laser initially and then a 785 nm laser. In the initial studies an external heating appliance was employed and then plasmonic heating from an incident 785 nm laser was used to heat the bulk solution in order to see the desired polymer effects. In addition, a range of PNIPAM coated HGNs and citrate capped HGNs were monitored simultaneously over time in order to determine the photothermal and SERS effects.

2. 1064 nm SERS of NIR Active Hollow Gold Nanotags

2.1 Introduction

Longer excitation wavelengths provide a better penetration ability in turbid media such as human tissues[49, 82] however, the scattering intensity depends on the 4th power of the excitation frequency, therefore Raman scattering at these wavelengths tend to be weak.[6] To take advantages of NIR laser excitations for sensing, an appropriate SERS substrate is required to enhance the weaker scattering at these wavelengths.

SERS tags are *in situ* probes that can provide sensitive and selective probes for optical analysis in biological materials. Engineering tags for use in the near infrared region is of particular interest since there is an uncongested spectral window for optical analysis due to the low background absorption and scattering from many molecules. However, designing SERS-active nanostructures with maximum reproducibility and enhancement is a current challenge in bio-nanotechnology. To date, aggregated noble metal nanoparticles, commonly silver and gold have been used as suspension based SERS substrates, as they are stable materials and have localised surface plasmon resonances that range from the visible to NIR region.[5-11] Aggregation of these nanoparticles induces the formation of clusters which in turn creates SERS 'hot spots.'[105] These are created where there are highly localised electromagnetic fields between a number of metal nanoparticles. When a molecule is trapped in this area or in close proximity to the nanoparticle surface, a large electromagnetic enhancement is experienced which results in an intense Raman signal, specific to the molecule of interest being observed.[115] However, controlling the enhancement from single aggregates of noble metal

nanoparticles in a reproducible manner can be difficult particularly in the NIR. Furthermore, engineering a nanostructure with a consistent size and shape and one that has a tuneable and strong plasmon resonance in the NIR region is still a challenge.

Several SERS substrates have been developed for use at an excitation wavelength of 1064 nm. These include gold nanoshells,[116] carbon nanotubes,[117] silver colloid[118] and gold nanorods.[30]. Unfortunately, these nanostructures are normally stabilised in harsher solvents and/or covered with harsher surfactants than trisodium citrate (commonly used for hollow gold nanoshells (HGNs)), making further functionalisation more problematic. Halas *et al.* developed gold coated silica nanoshells that are highly stable, resonant at 1064 nm and therefore have strong optical properties.[116] These nanoshells have been modified and employed in a wide range of applications including immunoassays[119] and photothermal ablation therapy.[120, 121] However, the size of these nanoshells are approximately 170 nm which is problematic for cellular penetration.[53]

Alternatively, HGNs which were first reported by Liang *et al.* have potential as a SERS substrate for use with 1064 nm laser excitation.[79] HGNs consist of spherical gold shells filled with an embedding medium and the synthesis involves a galvanic replacement reaction of cobalt with gold.[28] These nanostructures have strong SERS properties[1, 86, 122, 123] and have unique characteristics such as small size (usually from 50-80 nm), spherical shape and a strong tunable plasmon band from the visible to NIR region.[28] HGNs can be synthesised to be optically active in the NIR region by reducing the inner diameter and thickness of the shell simultaneously.

Xie *et al.* reported the synthesis of HGNs with LSPRs from 650 to 1320 nm and in the same paper compared the optical and photothermal properties of these nanomaterials.[82] It was found that only the HGNs with a LSPR of 650 nm gave a strong SERS signal; with the HGNs with a LSPR of 775 nm giving very weak SERS signals. Beyond this wavelength no optical response was obtained; therefore suggesting that red-shifted (LSPR >800 nm) HGNs are

inactive SERS substrates. The aim of this study was to optimise the synthetic procedure for HGNs in order to design hollow gold nanotags that were optically active in the NIR region.

2.2 Aims

There is a great need to design SERS nanotags which are reproducible, provide strong enhancements and in particular, optically active in the NIR region. This region of the electromagnetic spectrum is of particular interest as it provides an uncongested spectral window for optical analysis due to the low background absorption and scattering from many molecules, in particular bio-molecules.[124, 125] Hence, hollow gold nanotags have been developed to fulfill this requirement. The work presented here will show that red-shifted HGNs are in fact good SERS substrates at 1064 nm excitation when the shell thickness is adjusted. Seven reporters using either aromatic amine or thiol groups to attach to the surface were used to label the HGN's, thus developing 'hollow gold nanontags'. In order to obtain effective SERS signals at this excitation wavelength, both these components where required; NIR active HGNs and Raman reporter. Furthermore, the two Raman reporters which gave the largest enhancements and one standard reporter (all commercially available and commonly used with gold nano-substrates) were chosen for further analysis so that the binding and orientation of these reporters on the surface of the HGN could be determined.

2.3 Experimental

2.3.1 Synthesis of Nanoparticles

All glassware used in the synthesis of nanoparticles was first soaked in aqua regia (HNO_3 + 3HCl) for a minimum of 12 hours before being rinsed thoroughly in doubly-distilled deionised water (d.H_2O) prior to use.

2.3.1.1 Synthesis of HGNs with LSPRs from 600 to 800 nm

The HGN synthesis was carried out under inert conditions using a standard Schlenk line to prevent the cobalt nanoparticles from prematurely oxidising. The method

described was modified slightly from previous reports.[28, 82, 111] In a typical synthesis, cobalt chloride hexahydrate (100 µL, 0.4 M; Fisher Scientific, 99.99%) and trisodium citrate dihydrate (600 - 500 µL, 0.1 M; Sigma-Aldrich, >99%) were added into deionised water (100 mL) and degassed several times (10 min vacuum and 15 min argon). Sodium borohydride (1 mL, 0.1 M; Fisher Scientific, 99%) was injected into the solution and allowed to react for a further 20 minutes (under constant argon flow) until hydrogen evolution ceased, indicating complete hydrolysis of the reductant. The solution was degassed again (8 min vacuum and 10 min argon) before different concentrations ranging from 100 µM to 260 µM of chloroauric acid trihydrate (33 mL; Fisher Scientific, ACS reagent grade) was injected. This mixture was allowed to react for an additional 10 minutes under argon with vigorous stirring before being exposed to air, where an obvious colour change from brown to green was observed. Finally, trisodium citrate (500 µL, 0.1 M) was added to stabilise the hollow gold nanoshell solutions. Post synthesis, the HGN solution was concentrated through centrifugation (5500 x rpm) and the precipitate was re-dispersed in trisodium citrate solution (2 mM) to give final concentrations between 2-4 nM.

A Nanosight LM10 was used initially to obtain concentrations in particles per L and following this the molar concentrations were calculated.

2.3.1.2 Synthesis of NIR active HGNs

The HGN synthesis is described in section 2.3.1.1. Specifically for NIR active HGNs which are stable and produce strong SERS signals at 1064 nm laser excitations, the following modifications were made to the previous conditions:

- cobalt chloride hexahydrate (200 µL, 0.4 M; Fisher Scientific, 99%)
- trisodium citrate dihydrate (400 µL, 0.1 M; Sigma-Aldrich, >99%)
- deionised water (200 mL)
- sodium borohydride (1 mL, 0.2 M; Fisher Scientific, 99%)
- chloroauric acid trihydrate (33 mL, 124 µM; Fisher Scientific, ACS reagent grade)
- trisodium citrate dihydrate (1 mL, 0.1 M; Sigma-Aldrich, >99%) was added to stabilise the HGN solution

- centrifugation (4500 x rpm) with re-suspension in trisodium citrate dihydrate (2 mM) to yield final concentrations of 1-2 nM
- LSPR ≥800 nm and HGN solution had a pale green colour
- No stirring of solution during the synthesis of CoNPs however, vigorous stirring is employed after the addition of chloroauric acid

Again, a Nanosight LM10 was used initially to obtain concentrations in particles per L and following this the molar concentrations were calculated.

2.3.1.3 Gold Nanoparticles

Gold nanoparticles approximately 60 nm in size (500 µL; 3.4 nM) were provided by Sian Sloan-Dennison. The concentration was altered to match the NIR active HGNs before the SERS comparison was undertaken.

2.3.2 Preparation of Stock Solutions

Raman reporters - All powders (5-10 mg) were dissolved in 5 mL of ethanol to yield concentrations of 0.01 M. With the exception of 4,4-azopyridine which was dissolved in methanol. Subsequent dilutions were prepared in d.H_2O.

Potassium chloride – 44.7 mg of potassium chloride was dissolved in 20 mL d.H_2O.

2.3.3 Characterisation of hollow gold nanotags

All the Raman and SERS spectra presented in this thesis have been background corrected using a multi-point linear fit and a level and zero levelling mode in Grams AI software (version 7.0).

2.3.3.1 SERS Analysis

Before SERS measurements, the concentrations of the nanoparticle solutions were adjusted to the same level with the aid of a Nanosight LM10 via the procedure described in the instrument technical notes. Briefly, the original concentrated solutions were diluted with deionised water until 5 to 25 nanoparticles per CCD frame were obtained. The imaging videos were recorded for 60 seconds and analysed using the provided software (NTA 2.1). The required dilution

factor was then applied to the samples so that each nanoparticle solution had a concentration which matched that of the NIR HGNs.

Investigation into the SERS properties of the hollow gold nanotags were carried out by mixing 'as prepared' HGN solution (200 µL) with Raman reporter(s) solution (15 µL, 10 µM) and potassium chloride (150 µL, 30 mM; Sigma-Aldrich).

The Raman reporters added were 1, 2-bis(4-pyridyl)ethylene (BPE, Sigma-Aldrich >98%), 4,4-azopyridine (AZPY, Sigma-Aldrich), 4-mercaptopyridine (MPY, Sigma-Aldrich), 4,4-dipyridyl (DP, Sigma-Aldrich), 4-mercaptobenzoic acid (MBA, Sigma-Aldrich), 5-(pyridine-4-yl)-1,3,4-oxadiazole-2-thiol (PYOT, Sigma-Aldrich) and 4-(1H-pyrazol-4-yl)pyridine (PPY, Fluorochem). Analysis was carried out using a Real Time Analyzer FT-Raman spectrometer (Connecticut, USA). The laser excitation source was an Nd:YAG (neodymium-doped yttrium aluminium garnet) laser, with 1064 nm excitation. All the measurements had a 20 second acquisition time and a laser power operating at 420 mW. Each sample was prepared in triplicate and 5 scans of each replicate were recorded.

For the Raman reporter concentration studies, all reporters were tested over the concentration range 10 mM to 0.1 µM. All experimental and instrumental conditions were kept the same as previously stated, except the reporter concentration was altered.

For the displacement studies, the two reporters which were not in excess were added (15 µL; 10 µM for each reporter) to the HGN solution and mixed for 30 mins. The reporter which was to be 'in excess' was then added (15 µL; varied concentration) and left for a further 30 mins before adding KCl and analysing the sample. All other experimental and instrumental conditions were kept the same as previously stated.

2.3.3.2 Raman Analysis

Raman spectra for the three reporter molecules used in the bulk Raman vs 1064 nm SERS experiment were obtained using solid samples (~100 mg) of AZPY, BPE and MPY.

2.3.3.3 Extinction Spectroscopy

Extinction measurements were taken on one of two instruments depending on the wavelength range required. The first was a Varian Cary 3000 Bio UV-Visible spectrophotometer with a wavelength range from 200-900 nm and the second instrument used was a Perkin Elmer Lambda 35 UV-Visible spectrophotometer with a spectral range from 200-1100 nm.

For all 'HGN only and gold nanoparticle' measurements, 100 uL of 'as prepared' HGN solution was added to 550 uL of d.H_2O in a microcuvette and analysed.

For the aggregation studies, conditions comparable with the SERS experiments were employed. Initially a solution containing HGN solution (135 µL), Raman reporter (15 µL, 10 µM) and d.H_2O or KCl (150 µL; 30 mM) was prepared. 100 µL aliquot of this 'as prepared' solution was taken and added to 550 µL d.H_2O and analysed.

2.3.3.4 Dynamic Light Scattering

Dynamic light scattering (DLS) measurements were performed to determine the average particle size of the HGNs. For 'HGN only' solutions the analysis was carried out by adding 'as prepared' HGN solution (400 µL) to d.H_2O (400 µL) in a plastic cuvette and analysed using a Malvern Zetasizer nano ZS system.

For the aggregation studies a solution containing HGNs (135 µL), Raman reporter (15 µL, 10 µM) and d.H_2O or KCl (150 µL; 30 mM) was prepared and then 200 µL aliquot of this 'as prepared' solution was taken and added to 600 µL d.H_2O and analysis performed.

2.3.3.5 Zeta Potential

The Zeta potential provides information regarding the charge on the nanoparticle surface. These measurements were performed using the same instrument and samples were prepared in the same way as described in section 2.3.3.4. However, this time the dip cell was placed into the cuvette and analysis followed.

2.3.3.6 Scanning Electron Microscopy

SEM images were obtained using a FEI Sirion 200 ultra-high resolution Schottky field emission scanning electron microscope with FEI software. The SEM samples were prepared on polyelectrolyte functionalised silicon wafers as previously reported.[126, 122] Briefly, silicon wafer substrates (5 x 5 mm) were washed with methanol wipes and placed in an oxygen plasma cleaner for 90 seconds. Immediately after, they were treated with poly(diallyldimethylammonium chloride) (PDDA; used as obtained from Sigma Aldrich - 20 wt. % in H_2O) solution to create a positive charge on the wafer surface. PDDA solution (10 µL) was dissolved in sodium chloride (1 mL, 1 mM; Sigma Aldrich, 99%) and then this solution (15 µL) was added dropwise onto the wafer surface. The wafers were left for 20 minutes in a petri dish, before being washed off with water and dried under a stream of nitrogen. Each wafer was then treated with concentrated HGN solution (50 µL) and left for a further 10 minutes before being removed and rinsed with water and dried under nitrogen. This spotting and removal process of the HGN solution was repeated a further twice.

From the SEM image, both the particle size and shell thickness of the HGNs were confirmed using image-J software. Furthermore, the shell thickness was manually calculated using the average thickness of 100 HGN particles.

2.4 Results and Discussion

2.4.1 Properties and Characterisation of a range of HGNs

The HGN synthesis is based on the galvanic replacement of cobalt with gold, to produce homogeneous nanoshells. Initially, a cobalt nanoparticle is synthesised as a template for the growth of HGNs, and by utilising the difference in redox potential between cobalt and gold, it is possible to reduce gold ions while oxidising the cobalt nanoparticles. The localised surface plasmon resonance of HGNs is controlled by the size of the inner core and the thickness of the gold shell i.e. large inner cores and thin shells produce HGNs with red-shifted LSPRs, see figure 2.1.[28, 82]

It has been previously reported that if the concentration of cobalt chloride and sodium borohydride ($NaBH_4$), the sacrificial template and reducing agent respectively, are kept constant then the trisodium citrate capping agent is solely responsible for controlling the core particle size.[28] By reducing the amount of trisodium citrate present, there are fewer citrate ions available for stabilising the CoNPs. The small particles aggregate into larger ones resulting in the formation of large inner cores and ultimately causing the LSPRs of the HGNs to red-shift towards the NIR region.[82]

The thickness of the gold shell can also significantly affect the LSPR of the HGNs. High concentrations of gold (Au^{3+}) ions result in thick shells being formed which increases the plasmon oscillation energy resulting in an increase in SERS signal; however it pushes the LSPR towards the visible region as seen in figure 2.1.[82]

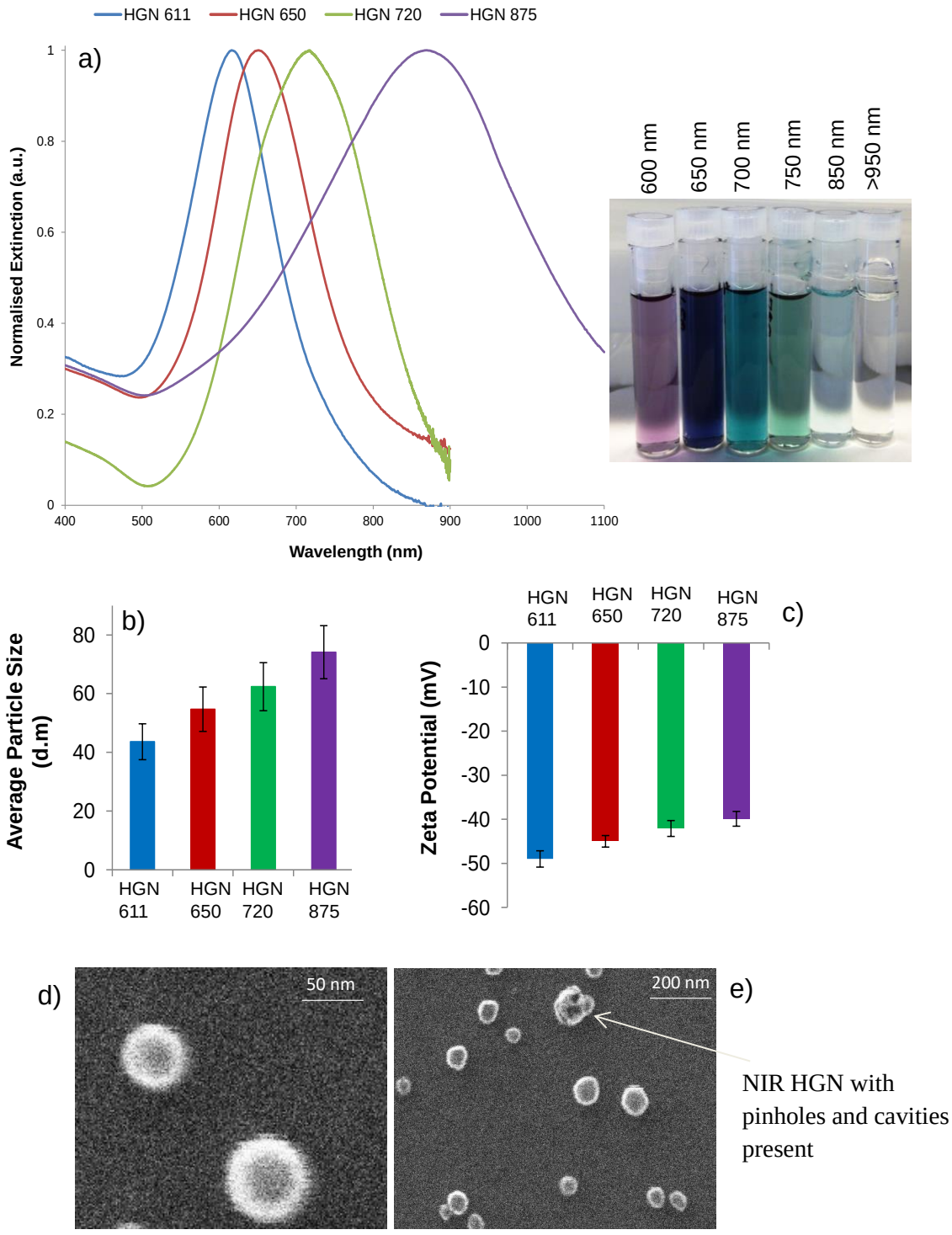

Figure 2.1 – Characterisation of HGNs with a range of LSPRs. Figure a) is the extinction spectra showing that the HGNs have tunable LSPRs from the visible to NIR region with the insert highlighting the colloidal colour change for HGNs with LSPRs from 600 to >950 nm. Figures b and c) are the average particle size and zeta potential, respectively for the range of HGNs tested. Figures d and e) are SEM images representing batches of HGNs with LSPRs at ~650 nm and ≥850 nm respectively.

Figure 2.1 illustrates that by simultaneously reducing the concentration of citrate and chloroauric acid, it is possible to synthesise a range of HGNs from the visible to NIR region. As the HGNs become red-shifted, their average particle size increases and the colour of the colloidal solution changes from purple (<600 nm) to blue (650 nm) to green (750 nm) and eventually to colourless when the LSPR is greater than 950 nm.

The zeta potential provides information regarding the charge on the nanoparticle surface and thus indicates the stability of colloidal suspensions.[127] As the HGNs possess a negatively charged citrate layer on the surface, the more negative the value the more stable the nanoparticles are said to be in solution. Therefore, based on figure 2.1c, the HGNs in the visible region are the most stable colloidal solutions and although this is true, the NIR active HGNs synthesised using the modified method are also considered stable as their value is greater than the proposed value of ±30 mV.[127]

In figure 2.1e, there are indications of pinholes and cavities in the SEM image. The pinholes and cavities visible in this HGN (LSPR at 893 nm) are due to the reduced citrate volume. When the aggregates become too large, the capping agent is present in inadequate quantities to control and stabilise the hollow centers, resulting in extremely large inner cores with holes as big as 25 nm being formed. This in turn has an effect on the thickness and uniformity of the gold shell, and as shown in the SEM, the shell will be non-uniform and incomplete. The surface cavities can range from 1-25 nm and are present in most red-shifted HGNs.[82] Furthermore, the holes and cavities are responsible for increasing the size of the inner core, thus red-shifting the LSPR of the HGNs. However, only a few HGNs in a batch are as extreme as the one highlighted in image 2.1e. It has been previously reported that small surface cavities of a few nanometers can generate an extra enhancement in the surface electric field. However cavities of similar size to the one observed in image 2.1e are too large and as a result do not contribute to the surface enhancement effect observed in SERS.[122, 128]

2.4.2 Characterisation of NIR active HGNs

Previous reports have stated that HGNs with LSPRs in the NIR region are inactive SERS substrates and therefore cannot produce SERS signals. However, in this work the synthetic procedure has been modified so that HGNs with LSPRs greater than 800 nm can produce SERS signals and in fact are good SERS substrates at 1064 nm excitation when the shell thickness is adjusted. An optimum concentration of 124 µM chloroauric acid was added and this produced a shell thickness of 8-9 nm, which was sufficient for the HGNs to be effective SERS substrates. Figure 2.2, shows the LSPR of the prepared HGNs to be 814 nm (black line), with the SEM insert clearly showing an image of these unaggregated hollow gold nanoshells. The plasmon resonance frequencies obtained do not match exactly the 1064 nm excitation frequency but it is has been previously reported that for effective SERS to be achieved, the excitation wavelength does not need to match the wavelength of the plasmon maximum.[129-131] Using image J, one hundred HGNs were manually calculated and the average particle diameter was calculated to be 74 ± 19 nm while the shell thickness was 8.5 ± 1 nm (figure 2.2 insert). The SEM image in figure 2.2 represents a zoomed in area of the full SEM image which can be seen in appendix I. In addition, a histogram detailing the frequency-size was obtained using the image-J software and it determines the average particle size to be 83 nm. It should be noted that for the manually calculated diameters the HGNs with the large cavities visibly present in their surface (like the one observed in figure 2.1e) were omitted from the analysis as they have no effect on the SERS whereas the histogram will have taken these into account. Thus, explaining why an increased average size was observed with the histogram data. Furthermore, the standard deviation observed in the histogram was 39.5 nm, indicating that the HGNs are of various sizes but this is further confirmed in the histogram and SEM images where an increase in the number of particles where observed with sizes <15 nm and >100 nm. For SERS studies, a Raman reporter concentration of 10 µM was used and it can be seen clearly from the extinction spectrum (figure 2.2), that when 10 µM BPE solution was added to the HGN solution (red line), a damping of the LSPR band was observed.

However the band maximum did not shift in wavelength, indicating that the reporter concentration was low enough that uncontrolled aggregation did not occur, but it was still sufficient to produce intense SERS (figure 2.3). When 30 mM potassium chloride, the aggregating agent used in SERS studies later, was added a 9 nm blue-shift in the maximum was observed, indicating that partial aggregation of the HGNs was occurring.[83]

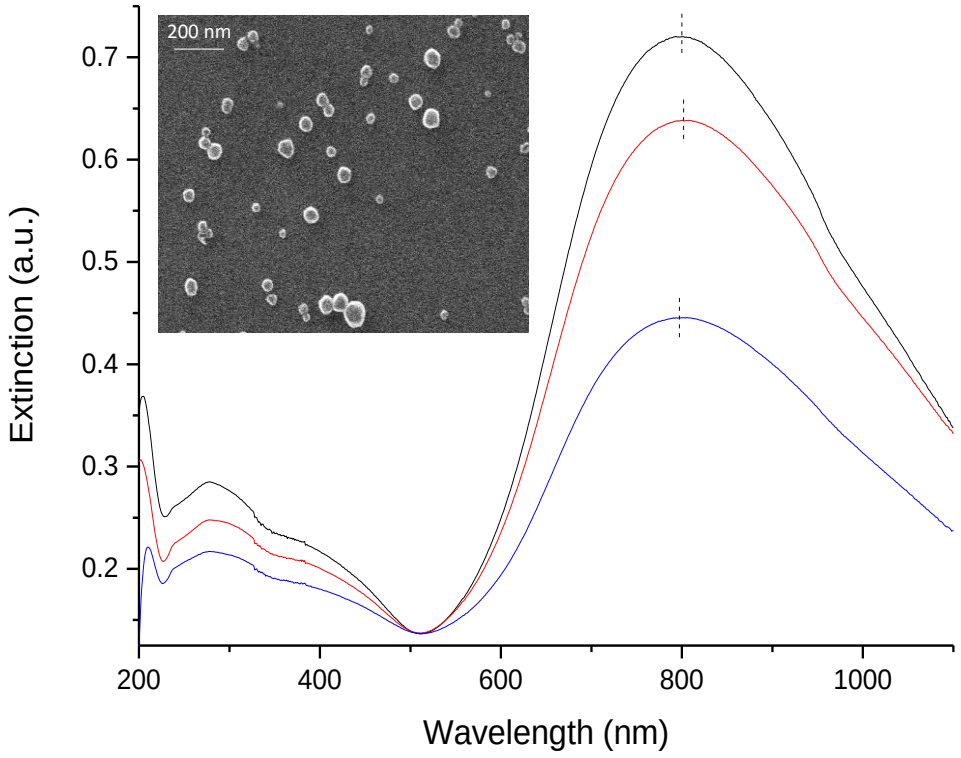

Figure 2.2 - Extinction spectra showing controlled aggregation caused when 10 µM BPE and 30 mM KCl salt were added to HGN solutions; black line highlights the hollow gold nanoshells only spectrum; red line is HGN 814 plus the reporter molecule BPE and the blue line is HGN 814 plus BPE and KCl salt. The blue dotted line shows that a small shift in the spectrum occurs with the new SPR recoded at 805 nm. Insert is a zoomed in area of an SEM image for HGNs with a LSPR of 814 nm; an average particle size of 74 ± 19 nm and shell thickness of 8.5 ± 1 nm. The full SEM image and frequency-size chart can be seen in appendix I.

2.4.3 SERS of hollow gold nanotags with a laser excitation of 1064 nm

In the near-infrared region of the electromagnetic spectrum the absorption and scattering of many bio-molecules is at a minimum.[132] Since SERS is dependent mainly on plasmon assisted enhancement rather than the fourth power of frequency,[6] SERS nanotags that are NIR active can provide sensitive probes with unique spectral fingerprints in this uncongested spectral window. Moreover, with the addition of a 1064 nm laser excitation there are further SERS benefits such as limited photobleaching, reduced background autofluorescence and greater penetration depth into biological tissues.[124, 125]

The HGNs were functionalised with 7 commercially available Raman reporters and aggregated with potassium chloride (KCl). Initially, the reporters were analysed to see which provided the most intense SERS and following this, three reporters were further characterised to give a better understanding of these '1064 nm SERS nanotags.' An investigation specific to the binding and orientation of these reporter molecules on the surface of the NIR active HGNs was conducted through displacement studies and a comparison study between bulk Raman and three of the SERS nanotags.

Figure 2.3 shows a concentration study over the range 10 mM to 0.1 μM (reporter concentration) which determined the optimum concentration of reporter to be used in the SERS studies. The black dashed line highlights the peak intensity of the blank sample (HGN only). Peaks will be observed in the SERS spectrum if the intensity values are above this line. At 10 μM concentration all the reporters have intensity values above the 'blank' line; hence all the dyes have their characteristic peak clearly visible in their SERS spectrum (see figure 2.4 for confirmation of characteristic peaks being visible). BPE and AZPY have a maximum intensity value at this concentration but lower concentrations of reporter could be used and SERS signals would still be obtained. However, for Raman scatterers such as MBA and MPY, this was the lowest observable concentration; hence for consistency and comparison between all the reporters, 10 μM was chosen as the optimum concentration. In addition to the strong SERS signals being produced at this concentration, it is important to note that 10 μM concentration of reporter does not aggregate the HGNs

uncontrollably (figure 2.2 - red line), therefore making it the obvious choice for the SERS studies.

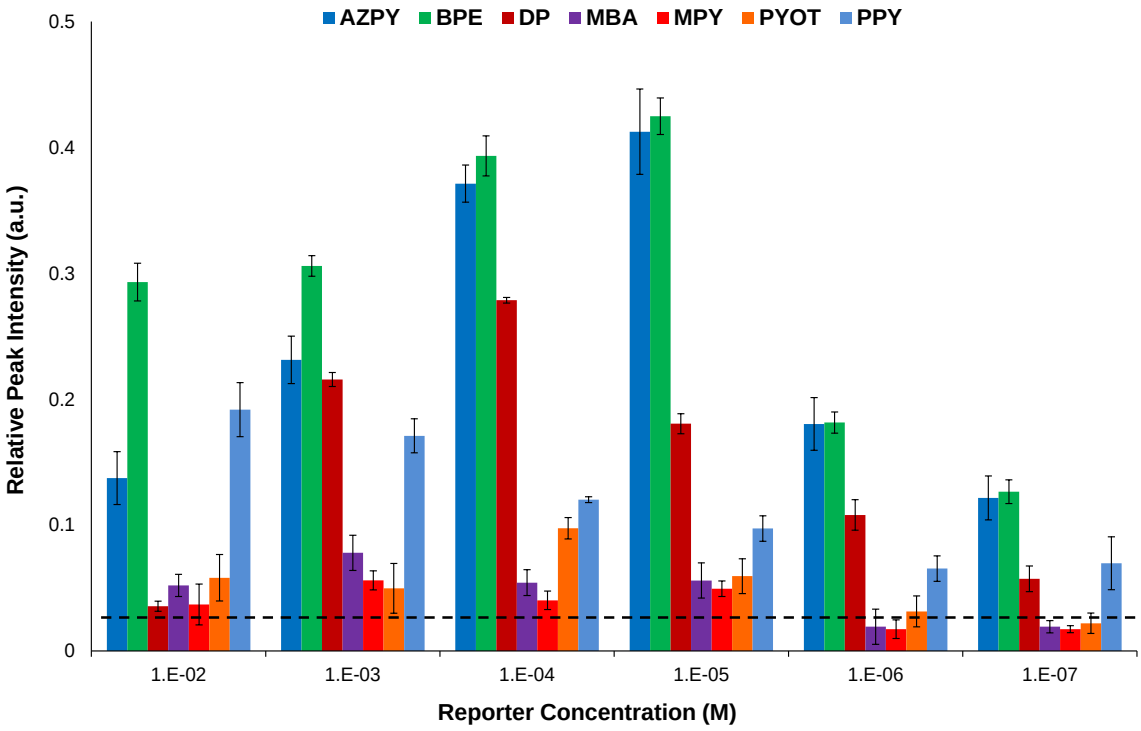

Figure 2.3 - SERS concentration study with NIR active HGNs for all the Raman reporters tested over the concentration range 10 mM to 0.1 µM (reporter concentration). A laser excitation of 1064 nm and an exposure time of 20 seconds were employed in this analysis. The black dashed line highlights the peak intensity of the blank sample (HGN only).

Figure 2.4, shows the SERS spectra obtained when each of the reporter molecules at a concentration of 10 µM were added to the red-shifted HGNs. All experimental parameters such as HGN concentration, sampling geometries and instrumental parameters including depth of focus, laser power and acquisition times where kept constant for all the hollow gold nanotags tested. Therefore, the reporters were compared based on their relative intensities. The black circle highlights a peak which could be used to identify each reporter. Depending on the reporter; adsorption onto the gold surface can occur via the lone pair electrons of the sulfur or nitrogen atoms or via the conjugated π-electron system.[133] Previous studies report that the MPY and MBA bind through the thiol group, whereas BPE, AZPY and DP bind via the

nitrogen (N) atom of the pyridyl ring. All are reported as binding with the main axis perpendicular to the surface.[133-137]

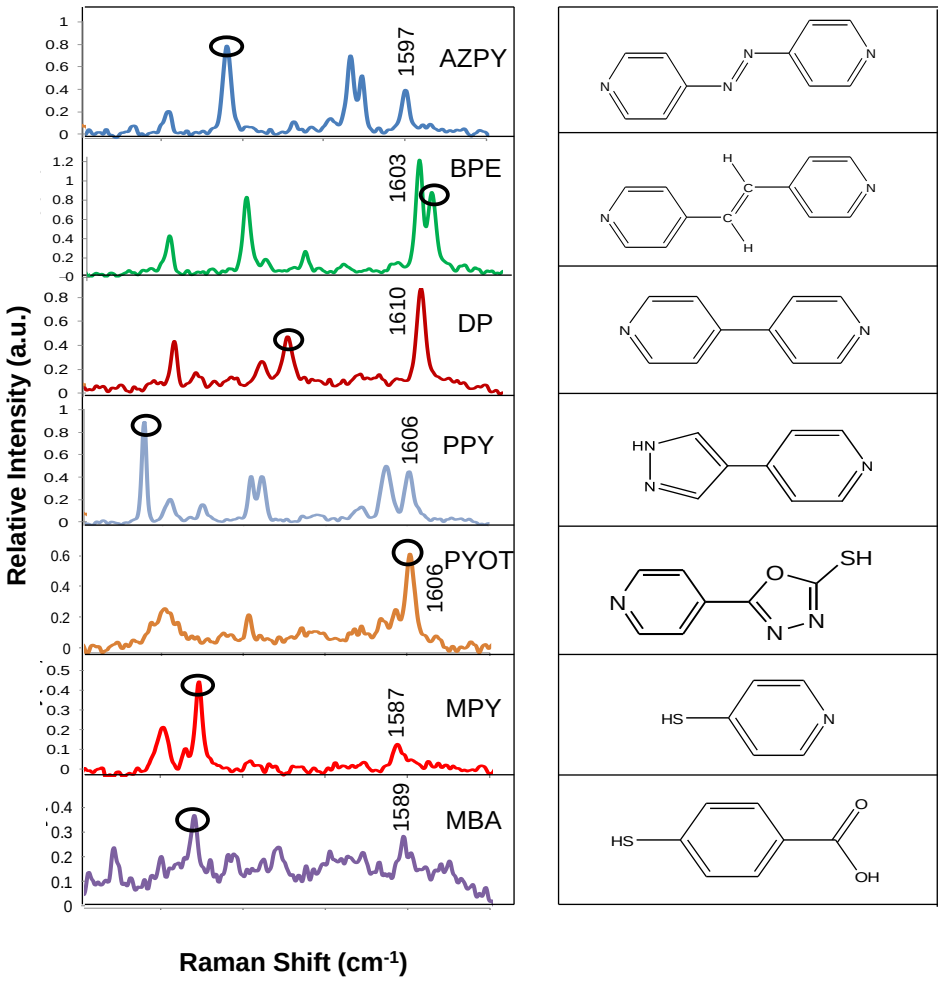

Figure 2.4 - SERS spectra and structures of all Raman reporters analysed with NIR active HGNs + KCl. The circle highlights the characteristic peak which could be used to identify each reporter molecule. A laser excitation of 1064 nm and an exposure time of 20 seconds were employed. All spectra have been background corrected. Figure has been reproduced by permission of the PCCP Owner Societies.[111]

It is expected that PPY will bond to the HGNs via the pyridyl ring N atom and PYOT through either the thiol group or the N atom (of the pyridyl ring) with the softer thiol most likely to bind more strongly. However if effective adsorption is occurring as would be expected, 10 µM solutions would lead to about monolayer coverage. This could produce reporter-reporter interactions which will stabilise a particular orientation of a reporter by creating a packed surface layer.

The reporter molecules were chosen to bind strongly by chemisorption and consequently when a reporter is adsorbed, there is an overlap between the molecular and metal orbitals resulting in a change in molecular structure and causing some bands to shift and relative intensities to change.[135] One of the peaks that should be enhanced upon adsorption to metal nanoparticles is the peak at ~1600 cm^{-1}. For reporters that are bound through the pyridyl group, this band arises due to the aromatic ring C-C/N stretching.[135-136] When the surface seeking group from the reporter molecule is in close proximity to the HGN surface and the reporter's adopt an approximately perpendicular orientation it often results in a significant enhancement of this peak being observed. Figure 2.4 shows that intense peaks were observed in the SERS spectra for AZPY, BPE, DP, PPY and PYOT suggesting that these molecules orientated in an upright position on the HGN surface and as such when the laser penetrated the samples a large electromagnetic enhancement was experienced, resulting in the molecules scattering very efficiently and producing strong SERS.

MPY and MBA give weaker SERS possibly because the layers are packed horizontally. However estimating relative SERS cross sections is very difficult and it may be that they are less polarisable due to the less extended π-systems. Based on these SERS results it can be concluded that the order of performance of these reporters (at 10 μM) as '1064 hollow gold nanotags' from best to worst was as follows: BPE > AZPY & PPY > DP > PYOT > MPY > MBA. It should be noted however, that although this is generally the order of performance, there have been data sets obtained were AZPY has produced comparable or stronger SERS signals than BPE and these results are verified in the displacement studies in section 2.4.4. BPE and AZPY have previously been reported to be strong Raman scatterers.[82, 135, 136, 138, 139] They possess conjugated structures with their highly delocalised π-electron systems and two chemically active nitrogen atoms which are ideal for binding to metal surfaces. These molecules can undergo electron transport, intramolecular photoinduced electron transport and energy transfer processes.[135, 136] Therefore, they form the building blocks of many supramolecular systems, have been employed for designing luminescent metal complexes and have been widely utilised as stable reporter molecules for evaluating SERS substrates.[82, 135 136, 139]

2.4.4 Understanding the binding and orientation of NIR active hollow gold nanotags using a 1064nm laser excitation

In order to maximise the spectroscopic information being obtained, displacement studies were undertaken in a simple multiplex system consisting of three Raman reporters; two strong and one weaker reporter (BPE, AZPY and MPY). This allowed the unique binding interactions occurring between these reporter molecules and the HGN surface to be investigated. In this study, the ratios of the reporter molecules were varied by changing the concentration only; for example MPY: AZPY: BPE = 2:1:1 (ratio) = 20:10:10 (concentration in μM). By varying the ratios of reporters it enabled the determination of which reporter(s) bound preferentially to the HGN surface and whether it was possible to completely displace a reporter while the others remained firmly attached. Therefore, giving further insight into the binding strength and SERS capabilities of these nanotags at 1064 nm laser excitation.

Figure 2.5 shows the varied multiplex ratios with red-shifted HGNs. The top graphs are the SERS spectra showing how the peak intensities of the reporters within the multiplex changed when one of the reporters was in excess over the other two. The arrows highlight the characteristic peaks which are important for distinguishing between the Raman reporters i.e. red is MPY with a characteristic peak at 1096 cm^{-1}, blue is AZPY with characteristic peak at 1162 cm^{-1} and green is BPE with characteristic peak at 1635 cm^{-1}. The bar charts give further clarification of the reporters within the multiplex system, with the change in peak heights being plotted. The black dashed line represents the background signal of the blank sample (HGN only). Above the dashed line the reporter's characteristic peaks are said to be visible in the SERS spectra but below this dashed line the peaks are not present in the multiplex system.

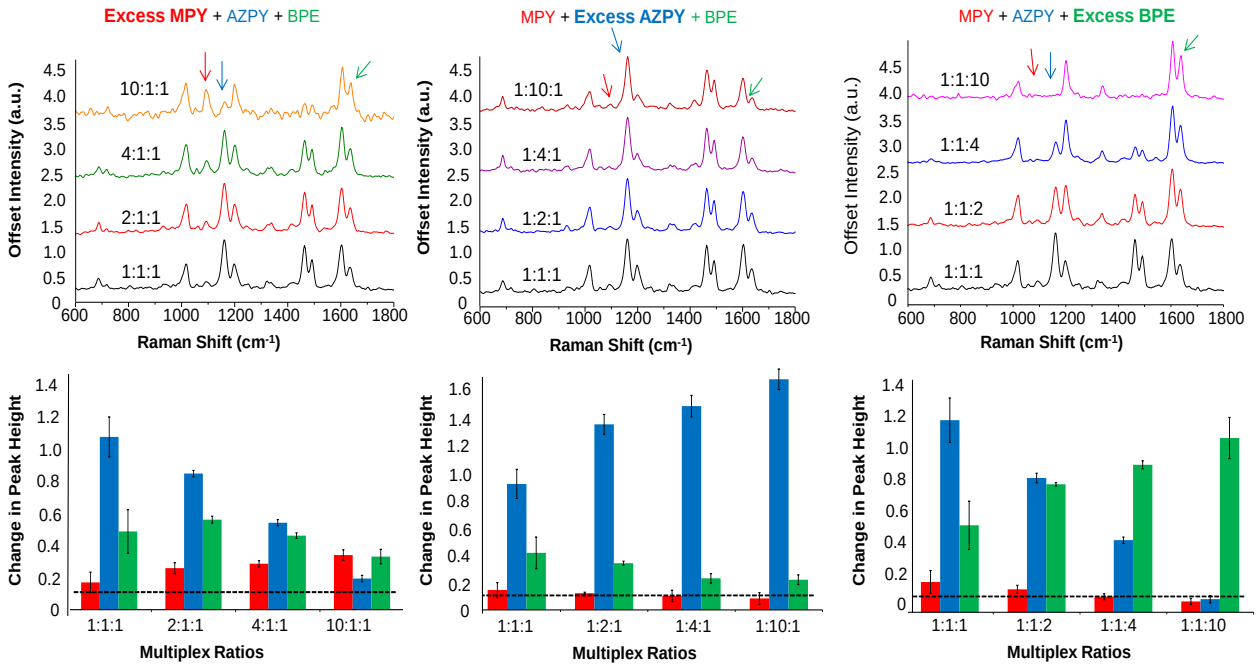

Figure 2.5 - Displacement studies with NIR active HGNs. The top graphs are the SERS spectra showing how the peak intensities of the reporters within the multiplex change when one of the reporters has an excess concentration over the other two. The ratios of the reporter molecules were varied by changing the concentration only; for example MPY: AZPY: BPE = 2:1:1 (ratio) = 20:10:10 (concentration in µM).The arrows highlight the characteristic peaks, and the associated colours are important for distinguishing between the Raman reporters i.e. red is MPY with characteristic peak at 1096 cm^{-1}, blue is AZPY with peak at 1162 cm^{-1} and green is BPE with peak at 1635 cm^{-1}. The bar charts give further clarification of the reporters within the multiplex system with the changes in peak height being plotted. Dashed line across bar charts highlights the intensity of the blank (HGN only). A laser excitation of 1064 nm and an exposure time of 20 seconds were employed in this analysis.

For the excess MPY data set, it can be seen that the three Raman reporters have their characteristic peaks in all the multiplex ratio spectra, even in the most extreme case where MPY was present at a concentration 10 times greater than that of the other two reporters. This suggests that MPY is weakly bound therefore less enhanced and as such unable to dominate the SERS spectrum or displace the other two reporters from the HGN surface. Although it is important to note (across all spectra) that for the two reporters not in excess there is a decrease in their signal intensities, indicating that displacement of these reporters from the HGN surface would occur if the concentration of the

reporter in excess was high enough. Furthermore, due to this decrease in SERS intensity it can be deduced that when MPY is in excess (by a concentration greater than 0.1 mM) AZPY would be displaced from the surface first followed by BPE. Implying that, in this multiplex system AZPY has the weakest binding interaction with the HGN surface followed by BPE and then MPY.

In the case of excess AZPY, BPE was present at the most extreme condition; however according to the bar chart MPY was displaced at a ratio of 1:10:1. Conversely, for MPY there appears to be a very weak peak present in SERS spectrum at this ratio, thus indicating that AZPY doesn't bind or scatter strongly enough that it can dominate over the other two reporters and successfully displace them from the HGN surface at these concentrations. However, at a higher concentration AZPY would be able to dominate and displace the other two reporters from the surface. It can be seen in the multiplex spectra that MPY has the weakest signal intensity and as such has the weakest binding interaction with the surface therefore MPY would be displaced first followed by BPE.

When BPE was added in excess to the multiplex system, the scattering from BPE was so strong that it could dominate and displace MPY first at a ratio of 1:1:4, and then AZPY at 1:1:10. These results further confirm that BPE and AZPY are strong Raman reporters as they can displace one or both reporters from the HGN surface and dominate the spectrum. Whereas MPY cannot unless the ratio (from MPY to AZPY/ BPE) was significantly increased, further confirming that MPY + HGNs was the weakest of the three hollow gold nanotags. Moreover, figure 2.6 highlights that spherical gold nanoparticles of a similar size (~60 d.nm) produce weaker SERS intensities with these three reporters than the hollow gold nanotags, with the AZPY reporter producing a slightly stronger signal than BPE. Gold nanoparticles in excess of 100 nm however, would produce comparable if not better SERS results with these reporters. Chapter 3 demonstrates that large gold nanoparticles also make excellent SERS substrates for enabling detection in the NIR region.

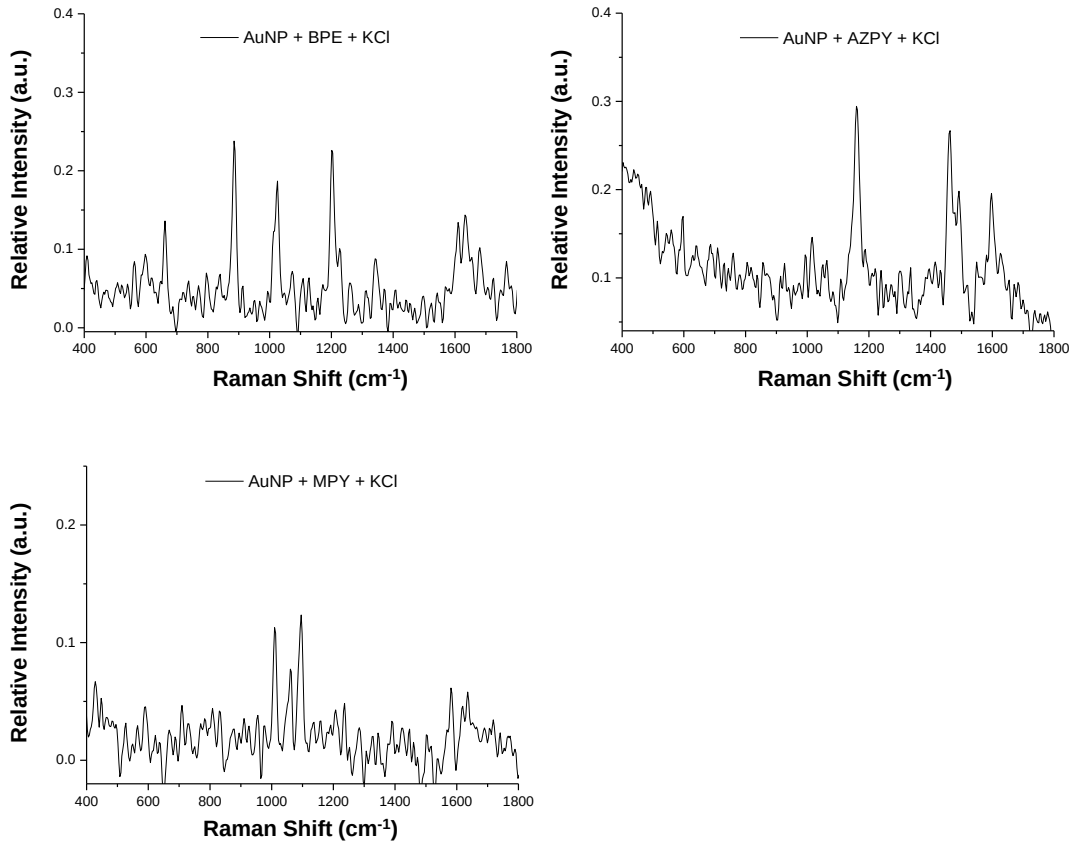

Figure 2.6 - SERS spectra for MPY, AZPY and BPE analysed with 60 nm spherical AuNPs + KCl. A laser excitation of 1064 nm and an exposure time of 20 seconds were employed. All spectra have been background corrected. Figure has been reproduced by permission of the PCCP Owner Societies.[111]

To the best of our knowledge the binding and orientation of these reporter molecules on the surface of a NIR active nano-substrate had yet to be investigated. Therefore a comparison study between bulk Raman and 1064 nm SERS was undertaken for HGNs (LSPR >800 nm) with AZPY, BPE and MPY, three reporters commonly used with gold nano-substrates for SERS analysis (figure 2.7).[139-141]. Zhuang *et al.* previously reported the binding and orientation of BPE and AZPY on silver foil at a laser excitation of 1064 nm.[135, 136] The peaks for MPY binding to silver foils was assigned by Hu *et al.*[133] Due to there being limited assignments and information on how these reporters bind to gold nano-substrates, Hu and Zhuang's assignments on silver were used to help understand and support how these reporters bind to the gold surface of HGNs. There are a few peak shifts and intensity differences to be noted between the silver and gold SERS data and these will be commented on throughout

the discussion as it helps in understanding how these reporters bind and orientate on the HGN surface. For all three reporters, the Raman spectra had to be obtained using solid samples as no spectra could be obtained from the 10 µM bulk solution, showing the greater sensitivity of SERS over Raman for solution based systems. A close examination of the peak shifts and intensities for each reporter molecule was undertaken, however only the main bands which are specific to the binding and orientation on the HGN surface will be discussed here, with their peak assignments being presented in tables 2.1 to 2.3. Extended peak assignment tables detailing all the peaks observed in the Raman and SERS spectra for each of the reporter molecules can be found in appendix II.

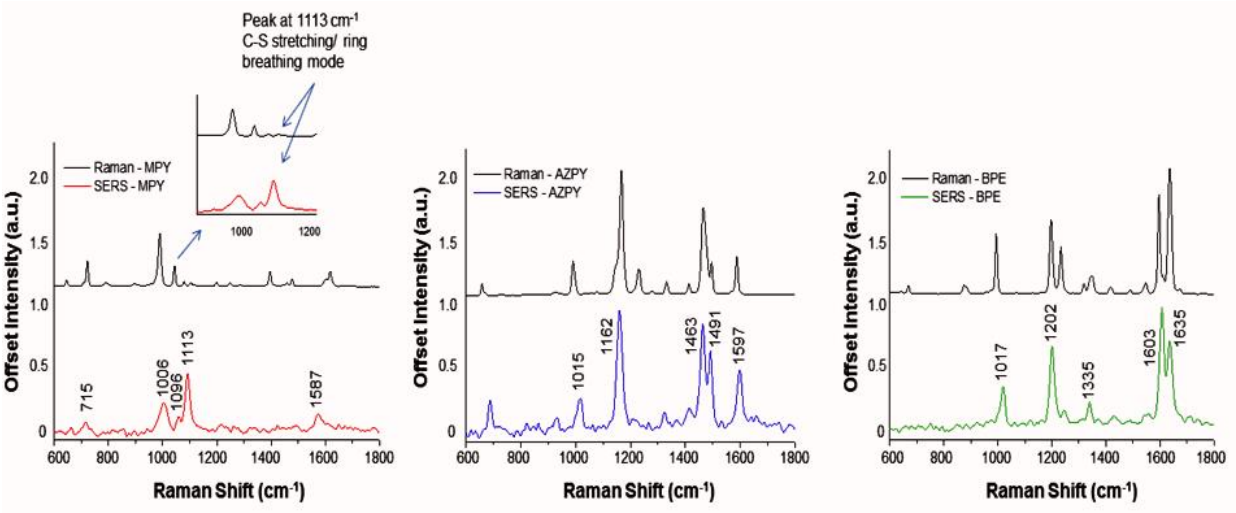

Figure 2.7 - Comparison of bulk Raman and SERS spectra for each of the Raman reporters. The black lines indicate the bulk Raman spectrum (solid sample). The coloured lines represent the HGN SERS spectrum for each of the reporter molecules at a concentration of 10 µM (MPY- red, AZPY, blue and BPE-green) and the insert in the MPY comparison spectra is an enlargement of the important characteristic peaks associated with this molecule. A laser excitation of 1064 nm and an exposure time of 20 seconds were employed in this analysis. All spectra have been background corrected and normalised to a cyclohexane standard. The Raman spectra were obtained using solid samples, as no spectra could be obtained for any of the reporter bulk solutions at a concentration of 10 µM. Figure has been reproduced by permission of the PCCP Owner Societies.[111]

Table 2.1 - Raman shifts (cm^{-1}) and peak assignments for AZPY (solid), HGN +AZPY + KCl (SERS-HGN) and Zhuang's silver foil + AZPY (SERS-Ag).[135, 137, 142] Table has been reproduced by permission of the PCCP Owner Societies.[111]

Raman	SERS-HGN	SERS-Ag	Assignments for AZPY
990	1015	1010	Ring breathing
1167	1162	1163	Ring breathing, ν(C–Nazo), δ(C–H)py
1465	1463	1466	ν(C–C)py, ν(C–N)py, δ(C–H)py
1493	1491	1497	ν(C–C)py, ν(N=N)
1587	1597	1597	ν(C–N)py, ν(C–H)py, ν(N=N)

ν = stretch, δ = bend, py = pyridyl ring.

For AZPY, the peak at 990 cm^{-1} in the Raman spectrum assigned as the symmetric ring breathing mode of pyridine and involving a significant displacement of the N atom of the pyridyl ring, undergoes a 15 cm^{-1} shift in the SERS spectrum. Furthermore, the peak at 1587 cm^{-1} also undergoes a shift of 10 cm^{-1} to appear at 1597 cm^{-1} in the AZPY SERS spectrum. This band is associated with ν(C–C), ν(C–N), ν(N=N). These modes involve a significant stretch of the pyridyl rings and displacement of the nitrogen along the major axis of the molecule indicating the main interaction with the HGN surface is via the lone pair on this nitrogen atom as is the case for silver.[135] Furthermore, since these ring breathing modes endured the largest displacements it suggests that significant chemisorption occurred.

When a reporter molecule adsorbs onto a metal substrate with a perpendicular orientation there should be a greater enhancement of the C-C/N stretch (~1600 cm^{-1}) over the symmetric ring breathing mode (~1000 cm^{-1}). For AZPY, these peaks occur at 1597 and 1015 cm^{-1} respectively and it can be seen that indeed the C-C/N stretch is stronger suggesting that AZPY binds with its main axis perpendicular to the HGN surface. In addition, intense azo and ring stretching peaks are observed at 1463 and 1491 cm^{-1}, further suggesting that a vertical orientation is adopted. In general, the HGN SERS spectrum for AZPY is in good agreement with that reported by Zhuang, however, there is one noticeable difference and that is the peak observed at 668 cm^{-1} in the HGN SERS spectrum is not visible in Zhaung's silver foil spectrum. Peaks

below 900 cm^{-1} are difficult to assign, however, this band could be enhanced due to the HGNs being resonant in the NIR.

Table 2.2 - Raman shifts (cm^{-1}) and peak assignments for BPE (solid), HGN + BPE + KCl (SERS-HGN) and Zhuang's silver foil + BPE (SERS-Ag).[136, 139, 143] Table has been reproduced by permission of the PCCP Owner Societies.[111]

Raman	**SERS-HGN**	**SERS-Ag**	**Assignments for BPE**
995	1017	1011	Ring breathing
1198	1202	1205	ν(C–C)py, δ(C–N)py, δ(C–H)py
1341	1335	1329	δ(C–H)py, δ(C=C)
1595	1603	1600	δ(C–N)py, δ(C–H)py,, ν(C–C)py
1635	1635	1635	ν(C=C)

ν = stretch, δ = bend, py = pyridyl ring.

For BPE the ring breathing mode and C-N stretching mode of the pyridyl ring behave similarly to the corresponding modes for AZPY suggesting chemisorption occurs once again due to the large displacements being observed. In the SERS spectrum these vibrations undergo a shift of 22 and 8 cm^{-1} respectively to occur at 1017 and 1603 cm^{-1} and as stated for the AZPY molecule, involve the movement of the N atom of the pyridyl ring. The unshifted band at 1635 cm^{-1} in the SERS spectrum is associated with the vinyl C=C stretching mode. If the BPE molecule interacted with the gold (shell) via the π-electrons, the conjugation between the aromatic ring and vinyl bond would be disrupted, resulting in a peak shift of the vinyl group. Thus, BPE also adsorbs onto the HGN surface via the N atom of the pyridyl ring and not the π-bonds.[136] Furthermore, there is no shift in the 1635 cm^{-1} peak only a decrease in intensity therefore there is no direct interaction between the vinyl group and HGN surface. Therefore this evidence all supports the view that BPE binds strongly to the HGN surface through the pyridyl nitrogen's lone pair. Moreover, intense peaks are observed at 1017 and 1603 cm^{-1} with the C-C/N stretch being significantly stronger than the ring breathing mode indicating that this reporter also binds to the HGN surface with a perpendicular orientation.

Table 2.3 – Raman shifts (cm^{-1}) and peak assignments for MPY (solid), HGN + MPY + KCl (SERS-HGN) and Hu's silver foil + MPY (SERS-Ag).[133] Table has been reproduced by permission of the PCCP Owner Societies.[111]

Raman	SERS-HGN	SERS-Ag	Assignments for MPY
721	715	707	ν(C–S), ring breathing
990	1006	1010	Ring breathing
1080	1096	1061	δ(C–H)py
1106	1113	1098	ν(C–S), ring breathing
1595	1587	1580	ν(C–C)py

ν = stretch, δ = bend, py = pyridyl ring.

For MPY, the peak at 721 cm^{-1} in the Raman spectrum associated with ring breathing and C-S stretching undergoes a shift to 715 cm^{-1} in the SERS spectrum upon adsorption to the HGN surface. Another band which shifts by 7 cm^{-1} and is significantly enhanced upon adsorption, is the ring-breathing/C–S stretching mode occurring at 1113 cm^{-1} in the SERS spectrum. The enhancement of this peak can be seen more clearly in the inserted picture (figure 2.7). The band at 1595 cm^{-1} corresponds to the C-C stretching mode and undergoes a shift to 1587 cm^{-1} in the SERS spectrum. Whereas, the C-H and ring breathing modes at 990 and 1080 cm^{-1} undergo shifts to 1006 and 1096 cm^{-1} in the SERS spectrum respectively.[133, 140] The peak shifts and intensity changes predominately involve ring breathing modes and C-S stretches therefore it is assumed that the MPY molecule will bind to the HGN surface via the sulfur atom. For MPY, the C-C stretch at 1587 cm^{-1} is slightly weaker than the symmetric ring breathing mode at 1006 cm^{-1}, suggesting that this molecule binds with the main axis parallel to the HGN surface. These results are contrary to Hu's as he reported an upright orientation with the C-C stretch appearing stronger (difficult to say for sure as there is no intensity scale). However, the difference in orientation could be due to the thiol binding more strongly to the silver surface than the gold shell of the HGNs or it could be a packing effect of the reporters on the surface. Hu *et al.* used a reporter concentration of 0.1 mM, a factor of 10 greater than in these studies. Both concentrations should give monolayer coverage and this should induce reporter-reporter interactions which will stabilise a particular orientation of a

reporter. However, with the higher concentration, it is likely that for effective packing to occur on the surface a vertical orientation will be forced.

These results are in good agreement with previous reports where BPE and AZPY bind to the nanoparticle surface via the N atom of the pyridyl ring, with a perpendicular or nearly perpendicular orientation being adopted. Whereas MPY binds through the thiol group and depending on the metal substrate and/or concentration of reporter, it may lie flat on the surface as indicted with HGNs or orientate with the main axis perpendicular to the surface as suggested by Hu's silver surface.[133] Moreover, it is expected that the majority of the Raman reporters tested will adsorb onto the HGN surface in an upright (perpendicular to the surface) orientation, allowing for uniform packing on the HGN surface.[133, 135, 136] This perpendicular orientation and the extended π-system present in these molecules ultimately allows for a greater polarisability change to be experienced when the laser interacts with the sample resulting in the Raman scattering increasing and therefore strong SERS signals being observed at the 1064 nm excitation wavelength. With the addition of biological targets these unique 1064 SERS nanotags could be used in the NIR region for biosensing and labelling of turbid media such as human tissue and blood.

2.5 Conclusions

1064 nm SERS detection of NIR active hollow gold nanotags has been demonstrated. An improved synthesis has resulted in the formation of HGNs with a LSPR beyond 800 nm which provide effective SERS when excited at 1064 nm. There are many advantages of using a 1064 nm laser and in combination with a good SERS substrate such as these red-shifted HGNs, it was possible to investigate the interactions occurring between the HGN surface and seven Raman reporters; which contained aromatic amine or thiol attachment groups. All were effective but BPE and AZPY provided the largest enhancement. At approximately monolayer coverage, these molecules pack on the HGN surface with a perpendicular or nearly upright orientation allowing for a greater polarisability to be experienced and as a result strong SERS being obtained at 1064 nm excitation. Furthermore, the comparison studies between

gold and silver led to the understanding that these HGNs are NIR resonant due to the significant enhancement of the vinyl C-C stretch at 1635 cm^{-1} in the HGN spectrum. This band appears very weak in Zhang's silver foil spectrum at 1064 nm excitation.[143] Therefore, adding weight to the argument that these HGNs are NIR active and effective candidates for use with a 1064 nm laser excitation.

2.6 Future Work

Red-shifted HGNs are small (<100 nm) and spherical in shape which means they have the potential to penetrate cellular membranes and tissue cells easily. They are less toxic to cells than silica coated and solid gold nanoparticles[144] and are stable in sodium citrate allowing for easier functionalisation of the outer shells. It would make for a very interesting investigation if these NIR active hollow gold nanotags were applied to biological applications. Initially they could be functionalised with a PEG (polyethylene-glycol) linker such as SH-PEG-COOH to increase their stability and with the COOH group present it provides an opportunity for further surface functionalisation with small bio-molecules such as proteins and peptides.

Due to the low absorption and scattering of bio-molecules in the NIR region, these nanotags could be an alternative SERS substrate for use in turbid media such as tissue or blood. An investigation into this could make for an essential advancement in this research area.

Furthermore, another interesting test would be to compare these NIR active hollow gold nanotags with HGNs (LSPRs at ~600 nm) for use in PTA therapy. The HGNs (at 600 nm) were reported to be at least 8 times more efficient than solid gold nanoparticles for PTA treatment due to their stronger red-shifted absorption and more effective photothermal conversion.[83, 84] Hence it would be interesting to determine how these new nanosensors would compare, with their LSPR being further red-shifted again.

A combination of the unique physical properties of the HGNs and the demonstration of the great SERS capabilities make hollow gold nanotags with LSPRs >800 nm potential candidates for future use in cellular and human tissue imaging, where 1064 nm lasers are already widely employed.

3. Extreme Red-Shifted SERS Nanotags

3.1 Introduction

To date, SERS nanotags have been utilised as extremely sensitive analytical probes for studying multiple biological targets.[145-147] Medical research has mainly focussed on designing nanotags for use with 785 nm laser excitations and very recently with 1064 nm laser excitations for PTA treatment.[48, 132, 148, 149] The optical absorbance of human tissue is minimal in the 600-800 nm window, but increases at longer wavelengths due to water absorption. Furthermore, the depth of penetration of NIR light increases at longer wavelengths due to decreased scattering, reaching a minimum near 1300 nm.[45] This superior penetration depth of light at 1300 nm compared to 800 nm has previously been reported,[150, 151] but due to the 4^{th} power law, Raman scattering would be much weaker and impossible to use at these longer excitation wavelengths. However, by trapping Raman reporter molecules close to the surface of roughened metal nanoparticles such as HGNs can cause signal enhancements to occur which would allow SERS signals to be obtained in the uncongested spectral window of the NIR region. Moreover, there are several advantages of using a longer excitation wavelength for optical analysis such as reduced sample degradation, limited photo-bleaching, reduced background autofluoresence and as previously mentioned greater penetration depth into turbid media such as biological tissues and blood.[45, 95, 124, 152]

SERS nanotags operating at 785 nm,[149, 153-155] 1064 nm[30, 116-118] and the eye-safe excitation at 1550 nm[156-159] have previously been reported. However, there had been no reports of a 1280 nm laser excitation being employed in SERS analysis. Recently, there have been reports which use 1280 nm laser

excitations for optical coherence tomography[150, 160, 161] and fluorescence microscopy.[162] However, there appear to be no SERS nanotags compatible with a 1280 nm excitation laser, or 'universal nanotags' which could be used with any NIR laser wavelength.

3.2 Aims

The previous chapter has explained that the NIR region is of significant biological and optical importance due to the absorption and scattering of many molecules being at a minimum. It was also demonstrated that in order to take advantage of this uncongested spectral window, SERS substrates which were optically active in the NIR region could be synthesised and when encapsulated with Raman reporters, SERS nanotags which produce strong SERS signals in this region were developed. However, this chapter will demonstrate that it is possible to design Raman reporters which are NIR active and encapsulate HGNs with LSPRs at ~700 nm and still produce intense SERS signals. In these studies, the SERS nanotags were tested across a range of laser excitations from 633 nm to 1550 nm.

In the initial studies 14 SERS nanotags were analysed using a 1280 nm laser excitation and particle dilution studies were conducted to obtain limits of detection (LOD). Following this principal component analysis (PCA) was conducted to see if the nanotags could be grouped according to their unique structures and vibrational fingerprints.

Moreover, the number of SERS nanotags was increased to 17 and analysis was performed using 1064 nm laser excitation and a comparison conducted between these newly synthesised dyes (by Matthew Bedics, student in Prof. Michaeal Dettys group from the University at Buffalo) and the commercially available reporters BPE and AZPY. Following this LOD studies were also carried out at this excitation wavelength and the results compared with the 1280 nm SERS nanotags.

In addition, a comparison study with large gold nanoparticles (obtained from BBI solutions) and HGNs were performed with 3 of the newly synthesised dyes at 1064 nm and 1280 nm laser excitations to determine how partial aggregation, size and

shape affected the SERS response. Moreover, a study was then conducted using a 1550 nm laser to determine the LODs for two of the newly synthesised nanotags and compared with the commercially available Cabot tags.

Finally, it was important to determine how these dyes orientate and bond to the HGN surface, so one dye was chosen (II-MB-114) and computational Raman studies were performed. These calculations were compared to experimental Raman and SE(R)RS results which were obtained across a range of laser wavelengths (514 to 1280 nm).

3.3 Experimental

3.3.1 Synthesis of HGNs

The HGN synthesis is described in section 2.3.1. Specifically for HGNs used in this work the following modifications were made to the previous conditions:

- trisodium citrate dihydrate (550 μL, 0.1 M; Sigma-Aldrich, >99%)
- chloroauric acid trihydrate (33 mL, 248 μM; Fisher Scientific, ACS reagent grade)
- centrifugation (5000 x rpm)
- final concentration of 2-3 nM
- LSPR at 700 ± 20 nm.

Again, a Nanosight LM10 was used initially to obtain concentrations in particles per L and following this the molar concentrations were calculated.

3.3.2 Gold and Silver Nanoparticles

Gold nanoparticles approximately 60 nm in size (1 mL; 3.4 nM) were provided by Sian Sloan-Dennison and the silver nanoparticles with an approximate size of 40 nm (1 mL; 9.3 nM) were provided by Rachel Norman. These nanoparticles were prepared ‘in-house.’

3.3.3 80 nm, 100 nm Gold Nanoparticles and Cabot tags

Prof. Neil Shand (DSTL) kindly provided all the large gold nanoparticles and Cabot tags used in the comparison studies with HGNs. The following nanoparticles had optical densities (OD) at 30 a.u. and concentrations were obtained using the Nanosight.

- ~80 nm gold nanoparticles (5 mL; 5.37 nM; BBI solutions)
- ~100 nm gold nanoparticles (5 mL; 3.73 nM; BBI solutions)
- Cabot tags which incorporate the reporter molecule BPE (5 mL; 3.37 nM)

3.3.4 Preparation of Stock Solutions

Raman reporters - All powders (6-10 mg) supplied from University at Buffalo, were dissolved in 2.5 mL dimethylformamide (DMF) to yield concentrations of 3-5 mM. Subsequent dilutions to 10 µM were prepared in 1:1 ratios of DMF to d.H_2O. Concentrations <10 µM, were prepared by diluting with d.H_2O only.

Potassium chloride was prepared as detailed in section 2.3.2.

3.3.5 Characterisation of 1280 nm SERS nanotags

Before SERS comparison measurements, the concentrations of the nanoparticle solutions were adjusted to the same level with the aid of a Nanosight LM10 via the procedure described in section 2.3.3.1.

3.3.5.1 SERS Analysis

The conditions employed in these studies were modified slightly from the previous chapter. Investigation into the SERS properties of the hollow gold nanotags were carried out by mixing 'as-prepared' HGN solution (270 µL; 2.9 nM) with Raman reporter solution (40 µL, 10 µM; synthesised by Prof. Michael Detty's group, University at Buffalo) and potassium chloride (300 µL, 30 mM; Sigma-Aldrich) or d.H_2O for the unaggregated studies. Initially, 14 dyes were analysed at this excitation wavelength and these are detailed in the 1280 nm SERS section 3.4.1 However, for the comparison study with 1064 nm SERS nanotags in section 3.4.2 a further 3 dyes were tested.

The SERS measurements were performed using a Snowy Range portable Raman spectrometer (Laramie, USA) incorporating a diode laser with an excitation at 1280 nm. All the measurements had a 7 second acquisition time (except the 114 dye which had to be reduced to 3 seconds) and a laser power of 100 mW. Each sample was prepared in triplicate and 5 scans of each replicate were recorded. All the Raman spectra were background corrected as described in section 2.3.3.

For the SERS particle dilution studies, the optimum conditions were initially used and deionised water was added to obtain subsequent concentrations, over the concentration range 1.9 nM to 6 pM. All other experimental conditions were kept the same as those stated previously. It should be noted however, that the reported concentrations are for non-aggregated systems based on the particle concentration of HGNs and as such the nanotag concentrations reported will be different due to aggregation occurring.

3.3.5.2 Limit of Detection

For all the particle dilution studies the limit of detection was calculated to be 3 times the standard deviation of the blank, divided by the gradient of the straight line. Error bars represent one standard deviation resulting from 3 replicate samples and 5 scans of each.

The standard deviation errors reported were calculated by multiplying the %RSD (relative standard deviation) by the LOD value.

%RSD was initially calculated by dividing the average standard deviation by the mean peak intensity and multiplying by 100.

3.3.5.3 Chemometrics

The chemometrics detailed in this section was carried out by Dr. Samuel Mabbott. Principal component analysis (PCA) was performed to assess the reproducibility and separation of individual features within the data set using Matlab software version R2012a (The MathWorks, Natick, MA, USA). PCA reduces the dimensionality of the SERS data, making it easier to identify any variations in the spectra.[163, 164] PCA

was carried out on 14 data sets, consisting of the spectra obtained from each individual dye experiment.

3.3.5.4 Extinction Spectroscopy

The same instrumental conditions as previously described in section 2.3.3.3 were employed.

For all measurements, 100 uL of nanoparticle solution was added to 550 uL of d.H_2O in a microcuvette and analysed.

3.3.6 Characterisation of 1064 nm SERS nanotags

Before SERS comparison measurements, the concentrations of the nanoparticle solutions were adjusted to the same level with the aid of a Nanosight LM10 via the procedure described in section 2.3.3.1.

3.3.6.1 SERS Analysis

Investigation into the properties of the 1064 SERS hollow gold nanotags were carried out by mixing 'as-prepared' HGN solution (270 µL; 2.8 nM) with Raman reporter solution (40 µL, 10 µM) and potassium chloride (300 µL; 30 mM). At this excitation wavelength 19 Raman reporters were analysed, two of which where the commercial reporters BPE and AZPY for comparison.

The SERS measurements were performed using a hand-held Snowy Range 'CBEx' Raman spectrometer (Laramie, USA) with a diode laser operating at 1064 nm excitation wavelength. All the measurements had a 0.05–0.1 second acquisition time and a laser power operating at 30 mW. Each sample was prepared in triplicate and 5 scans of each replicate were recorded. All the Raman spectra were background corrected as described in section 2.3.3.

For the SERS particle dilution studies, the optimum conditions were initially used and deionised water was added to obtain subsequent concentrations, over the concentration range of 2 nM to 0.1 pM. 0.05-7 second acquisition times were employed and the LODs were calculated as described in section 3.3.4.2. Note optimum conditions were obtained with 0.05-1 second acquisition times and then

subsequent dilutions in d.H_2O were analysed using a 7 second exposure time. It should be noted however, that the reported concentrations are for non-aggregated systems based on the particle concentration of HGNs and as such the nanotag concentrations reported will be different due to aggregation occurring.

For the Raman reporter concentration studies, 6 dyes were chosen and compared over the concentration range 0.1 mM to 10 nM. All experimental conditions were kept the same as previously stated, except the reporter concentration was altered.

For the comparison study between HGNs and BBI's large AuNPs, all the experimental conditions were the same as stated previously for the SERS investigation into 1064 nm hollow gold nanotags; except that the large Au solutions had to be diluted prior to analysis so their concentrations matched that of the HGNs.

3.3.6.2 Extinction Spectroscopy

The same instrumental conditions as previously described in section 2.3.3.3 were employed.

For all 'HGN only' measurements, 100 uL of 'as prepared' HGN solution was added to 550 uL of d.H_2O in a microcuvette and analysed.

The large gold nanoparticle solutions (80 and 100 nm from BBI Solutions) had to be diluted prior to analysis as the solutions were too concentrated; ODs ~30 a.u. Initially, 150 µL aliquot of the concentrated nanoparticle solutions were taken and added to 1500 µL of d.H_2O and vortexed.

For the aggregation studies, conditions comparable with the SERS experiments were employed. Initially a solution containing nanoparticle solution (270 µL), Raman reporter (40 µL, 10 µM) and d.H_2O or KCl (300 µL; 30 mM) was prepared. 100 µL aliquot of this 'as prepared' solution was taken and added to 550 µL d.H_2O and analysed.

3.3.6.3 DLS and Zeta Potential

The same instrumental conditions as previously described in sections 2.3.3.4 and 2.3.3.5 were employed.

For ‘HGN only’ solutions the analysis was carried out by adding ‘as prepared’ HGN solution (400 µL) to d.H_2O (400 µL) and analysed.

For the aggregation studies a solution containing nanoparticle solution (270 µL), Raman reporter (40 µL, 10 µM) and d.H_2O or KCl (300 µL; 30 mM) was prepared and then 200 µL aliquot of this ‘as prepared’ solution was taken and added to 600 µL d.H_2O and analysed.

3.3.7 Characterisation of 1550 nm SERS nanotags

3.3.7.1 SERS Analysis

In the initial comparison study between 100 nm AuNPs and HGNs, the HGNs were re-suspended in 5 mL of trisodium citrate to obtain a concentration of 6 nM. The 100 nm AuNPs were used ‘as supplied.’ Investigation into the properties of the 1550 SERS nanotags were carried out by mixing ‘as-prepared’ nanoparticle solution (270 µL) with Raman reporter solution (dye 184, 40 µL, 10 µM; synthesised by Prof. Michael Detty’s group, University at Buffalo) and potassium chloride (300 µL; 30 mM). The SERS measurements were performed using a FT-Raman Real Time Analyzer spectrometer (Connecticut, USA) incorporating an external EDFA (erbium-doped fibre amplifier) laser with an excitation at 1546 nm. All the measurements had a 10 second acquisition time and a laser power operating at 100 mW. Each sample was prepared in triplicate and 5 scans of each replicate were recorded. Furthermore, all the Raman spectra have been background corrected as described in section 2.3.3.

A SERS comparison was undertaken between commercially available Cabot tags and gold nanoparticles (~100 nm) encapsulated with dye II-MB-184 or II-MB-198. Before SERS analysis, the concentrations of the gold nanoparticle solutions were adjusted to match that of the Cabot tags (3.4 nM) with the aid of a Nanosight LM10 via the procedure described in section 2.3.3.1. The gold nanotags were prepared by adding 100 nm AuNPs (450 µL, BBI Solutions) plus Raman reporter solution (50 µL; 10 µM); while the Cabot tags were used ‘as supplied’ (500 µL). The SERS measurements were performed using the same instrumental conditions as described in the initial 1550 nm SERS studies.

For the SERS particle dilution studies, the chalcogen nanotags were prepared by mixing nanoparticle solution (100 nm AuNPs - 250 µL) with Raman reporter solution (dye 184 or 198 - 50 µL, 10 µM) and deionised water (250 µL). The Cabot nanotags were prepared by adding colloidal solution (250 µL) to deionised water (250 µL) and analysed over the concentration range of 1.7 nM to 80 pM, with the subsequent dilutions being made in deionised water. All other experimental conditions were kept the same as those previously stated, with the LODs being calculated as described in section 3.3.4.2. It should be noted however, that the reported concentrations for the chalcogen nanotags are for non-aggregated systems based on the particle concentration of AuNPs and as such the nanotag concentrations reported will be different due to aggregation occurring. Moreover, the concentrations reported for the Cabot tag is for the aggregated system and will be more accurate.

3.3.7.2 Extinction Spectroscopy, DLS and Zeta Potential

The same experimental conditions described in sections 3.3.6.2 and 3.3.6.3 where employed.

3.3.8 Determination of the orientation and bonding of dye 114 to HGNs

3.3.8.1 Raman Analysis

Silicon was used to optimise the signal collection as well as to provide an intensity reference for data normalisation, with respect to the peak at 520 (±2 cm^{-1}).

Raman spectra of dye II-MB-114 were acquired by placing ~5 mg of solid sample onto a microscope slide and analysing it.

Measurements were performed using two Renishaw *InVia* Raman microscope systems (Gloucestershire, UK), equipped with 50x objectives. Three excitation sources were employed; the first was an Ar+ (argon ion) laser with 514.5 nm excitation and an 1800 g/mm grating. In this analysis a 10 second acquisition time and 0.825 mW (10 %) laser power was used.

The second excitation source was a He-Ne (helium-neon) laser with 1800 gr/mm grating and 632.8 nm excitation, while the third used a diode laser with 785 nm

excitation and 1200 gr/mm grating. For these measurements, 25 second acquisition times were employed and laser powers operating at 0.525 mW (10 %; 633 nm) and 0.345 mW (0.1 %; 785 nm) were used.

3.3.8.2 SE(R)RS Analysis

Cyclohexane was used to optimise the signal collection as well as to provide an intensity reference for data normalisation, with respect to the peak at 801 (±2 cm^{-1}).

SERS investigations into dye II-MB-114 were carried out by adding 'as-prepared' HGN solution (135 µL) with Raman reporter solution (20 µL; 10 µM) and potassium chloride (150 µL; 30 mM). Note for the 1280 nm SERS analysis the volumes of each component were doubled.

For SERS at 633 and 785 nm the same instruments and operating parameters described in the Raman analysis section were used (3.3.6.1) with 10 second acquisition times. Samples were analysed through transparent bottom micro-titre plates by focussing the 5x objective into a well containing 300 µL of the nanotag solution.

The nanotags were also analysed using the 1064 nm FT-Raman spectrometer described in section 2.3.2.1 and the 1280 nm spectrometer described in section 3.3.4.1. Acquisition times of 3 and 5 seconds were employed at 1280 nm and 1064 nm respectively.

3.3.8.3 Computational Analysis

The theoretical calculations detailed in this section were carried out by Ivan Ramos-Sasselli. All the calculations were performed in Gaussian 09[165] with the Def2-TZVP[166, 167] basis set. The DFT functional B3LYP[168-171] was used for the structure optimisation, Raman activity calculations and torsion profile calculations for the rotation of ring 1 and ring 3. Raman calculations were carried out in four conformations. The first disposition (min) is extracted from the crystal structure and corresponds with the minimum in the Se rings torsions. The other three conformations were obtained by rotating ~180º ring 1, ring 2 and both. The

calculated Raman frequencies were corrected to fit the experimental mode at 1588 cm^{-1} *min* Raman prediction (correction factor: 0.968).

3.4 Results and Discussion

3.4.1 1280 nm SERS Nanotags

3.4.1.1 SERS analysis of nanotags

In this study, 1280 nm SERS nanotags have been designed by combining HGNs and Raman reporter molecules selected from a small library of chalcogeno(pyrylium/pyranyl) monomethine and trimethine dyes. These dyes were synthesised at Buffalo University and have phenyl, 2-thienyl, and 2-selenophenyl substituents at the 2- and 6-positions of the pyrylium/pyranyl rings, which allow them to bind strongly to the HGN surface with multiple attachment groups. The interchange of sulfur (S) and selenium (Se) atoms in the chalcogenopyrylium backbone, the use of monomethine and trimethine bridges, and the interchange of phenyl, 2-thienyl, and 2-selenophenyl substituents at the 2-,2'-, 6- and 6'-positions, not only allows the fine tuning of wavelengths of absorption from 653 to 826 nm [172, 173] but also gives each dye its unique Raman fingerprint.

The enhancement obtained from SERS is related to the frequency of the surface plasmon excited on the metal rather than the 4th power law.[158] Therefore, in general it is believed that in order to make SERS a viable method at 1280 nm, the SPR should have some resonance with the NIR excitation source. The HGNs used in this study have a LSPR at 720 nm as shown in the extinction spectrum in figure 3.1a with the extinction spectra showing that the LSPR does not shift upon functionalising HGNs with these dyes or with the addition of KCl, as shown in figure 3.1b. It is important to note that the plasmon resonance frequencies obtained do not match the excitation frequency at 1280 nm, however, it has been reported previously that for effective SERS to be achieved, the excitation wavelength does not need to match the wavelength of the plasmon maximum.[111, 115, 129, 130]

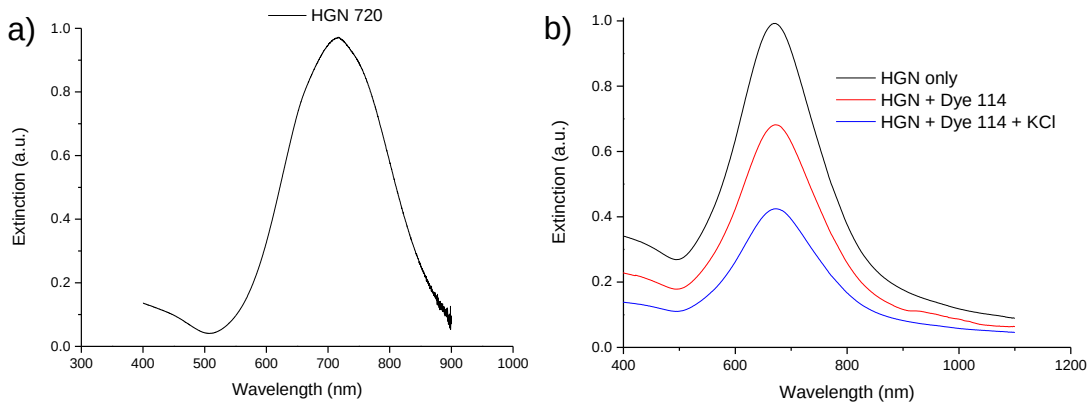

Figure 3.1 - a) Normalised extinction spectrum showing the LSPR of the HGNs at 720 nm. b) Extended extinction spectra showing that the LSPR does not shift upon aggregation. The black line is the HGN only spectrum; red line is HGN plus dye 114 (10 µM) and the blue line is HGN plus dye 114 and KCl salt (30 mM). Figure a) has been reproduced by permission of the Royal Society of Chemistry.[174]

The 1280 nm SERS nanotags, consist of three important components, the first being the SERS substrate. In addition to strong SERS properties,[1, 86, 122, 123] HGNs have unique characteristics (small size, spherical shape and tunable plasmon band) which make them effective candidates for these studies.[28] The SERS spectrum and structures for all these newly synthesised chalcogen dyes can be seen in figure 3.2. The first 8 are monomethine dyes while the last 6 have trimethine substituents. The trimethine dye 114**,** with two sulfur atoms in the thiopyrylium/thiopyranyl core and four 2-selenophenyl substituents at the 2,2',6,6'-positions were exceptionally bright in this library of reporters. In addition, extinction spectra highlighting the wavelength maximum for a selection of chalcogenopyrylium dyes are provided in appendix III.

Dye 070 λ_{max} = 653 nm

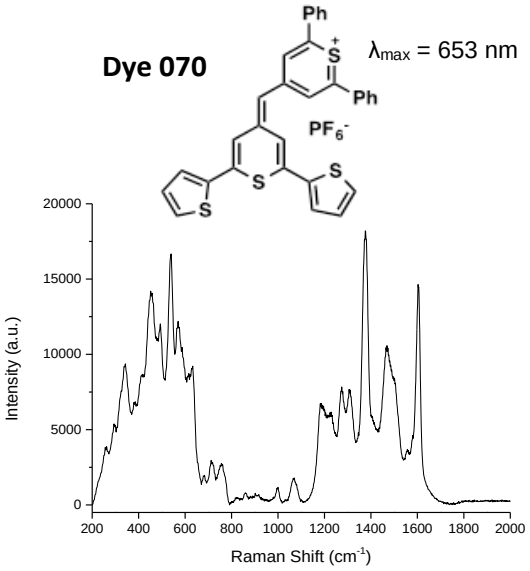

Dye 069 λ_{max} = 676 nm

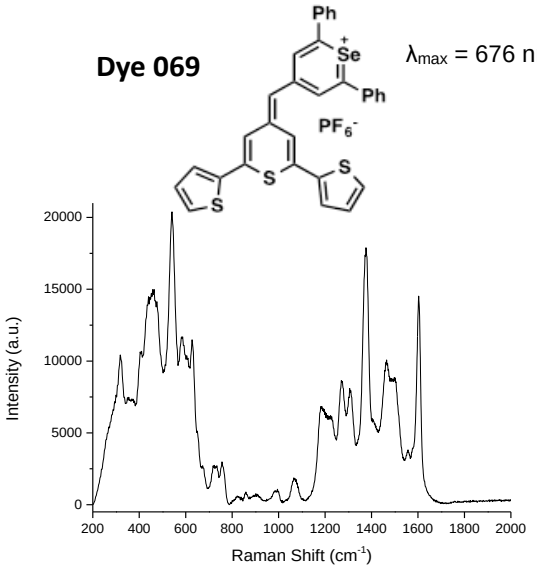

Dye 071 λ_{max} = 699 nm

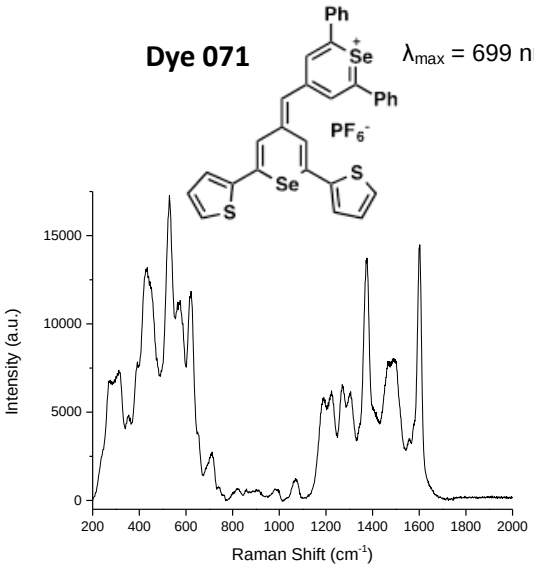

Dye 020 λ_{max} = 676 nm

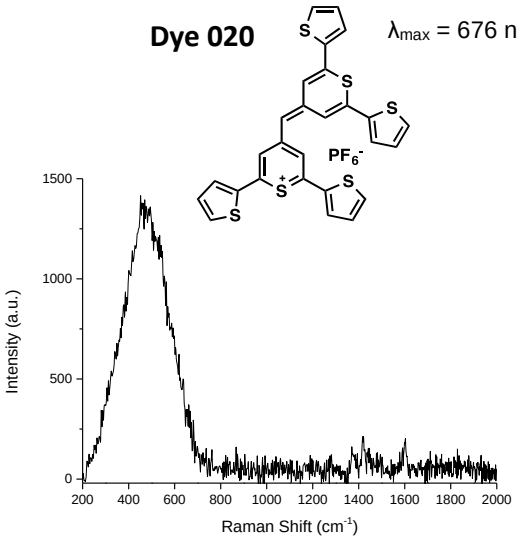

Dye 067 λ_{max} = 698 nm

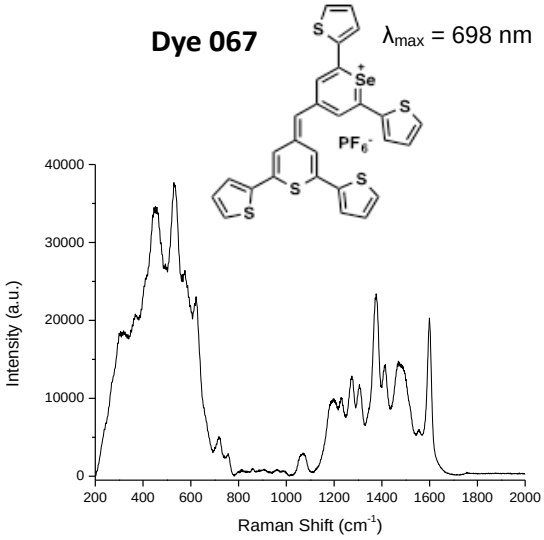

Dye 162 λ_{max} = 724 nm

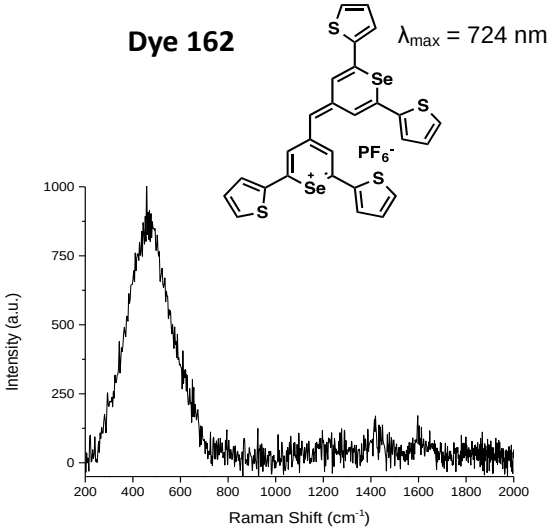

Dye 099 λ_{max} = 659 nm

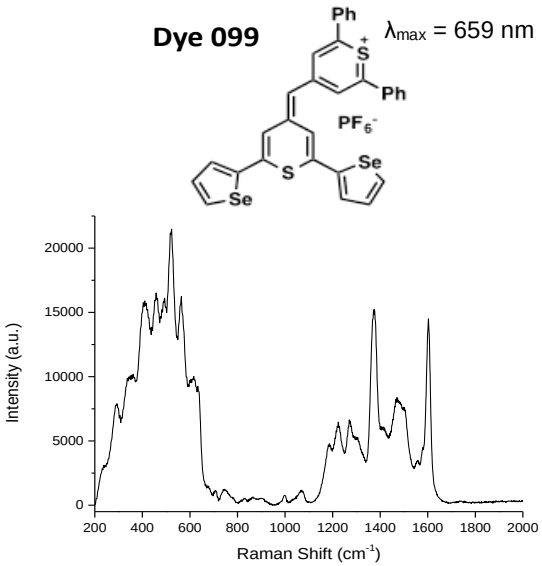

Dye 095 λ_{max} = 687 nm

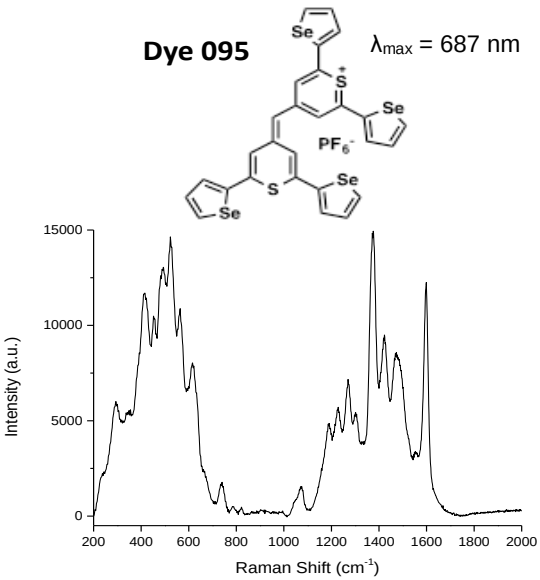

Dye 075 λ_{max} = 806 nm

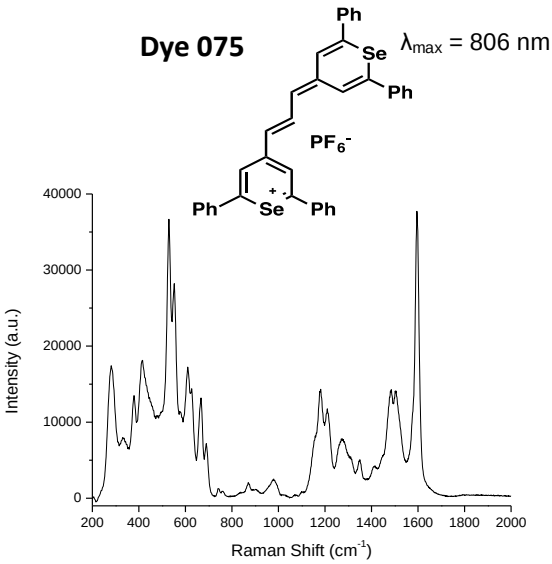

Dye 089 λ_{max} = 784 nm

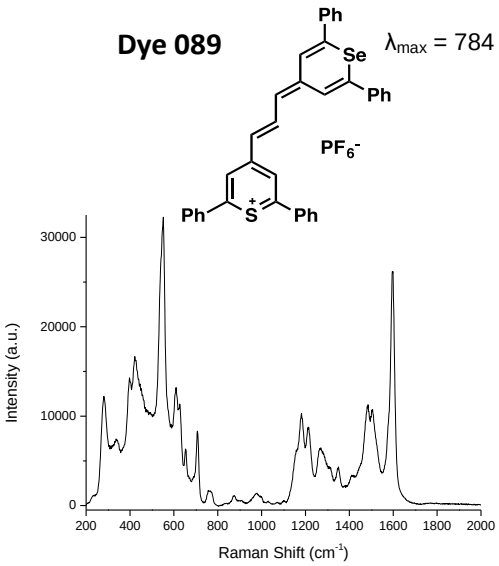

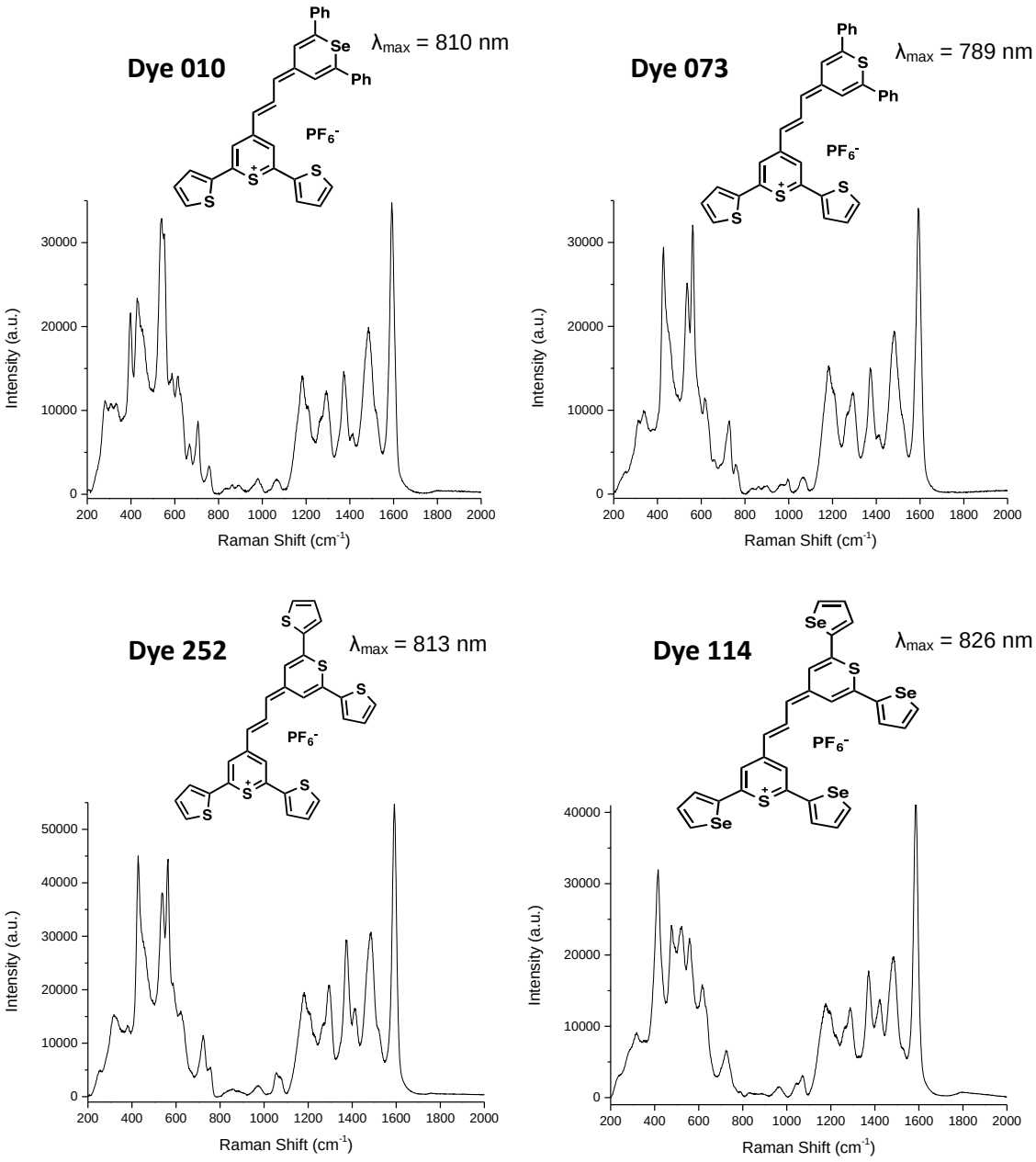

Figure 3.2 - SERS spectra with associated structures and absorption maximum values for all the dyes tested. The dyes with a concentration of 10 μM were analysed with HGNs and KCl. A laser excitation of 1280 nm and an exposure time of 7 seconds were employed in this analysis, with the exception of dye 114 where the acquisition time was reduced to 3 seconds. All spectra have been background corrected. Figure has been reproduced by permission of the Royal Society of Chemistry.[174]

Commonly, Ag and Au spherical nanoparticles with plasmon bands in the visible region are used as SERS substrates.[145] However, these 14 dyes on Ag and Au nanoparticles produced significantly weaker SERS signals than those observed with the HGNs (see figure 3.3) possibly due to their lack of red-shifted LSPR and/or slightly smaller size. Furthermore, it should be noted that the background signal observed from 200-800 cm^{-1} in all the 1280 nm SERS spectra was from the glass cuvettes.

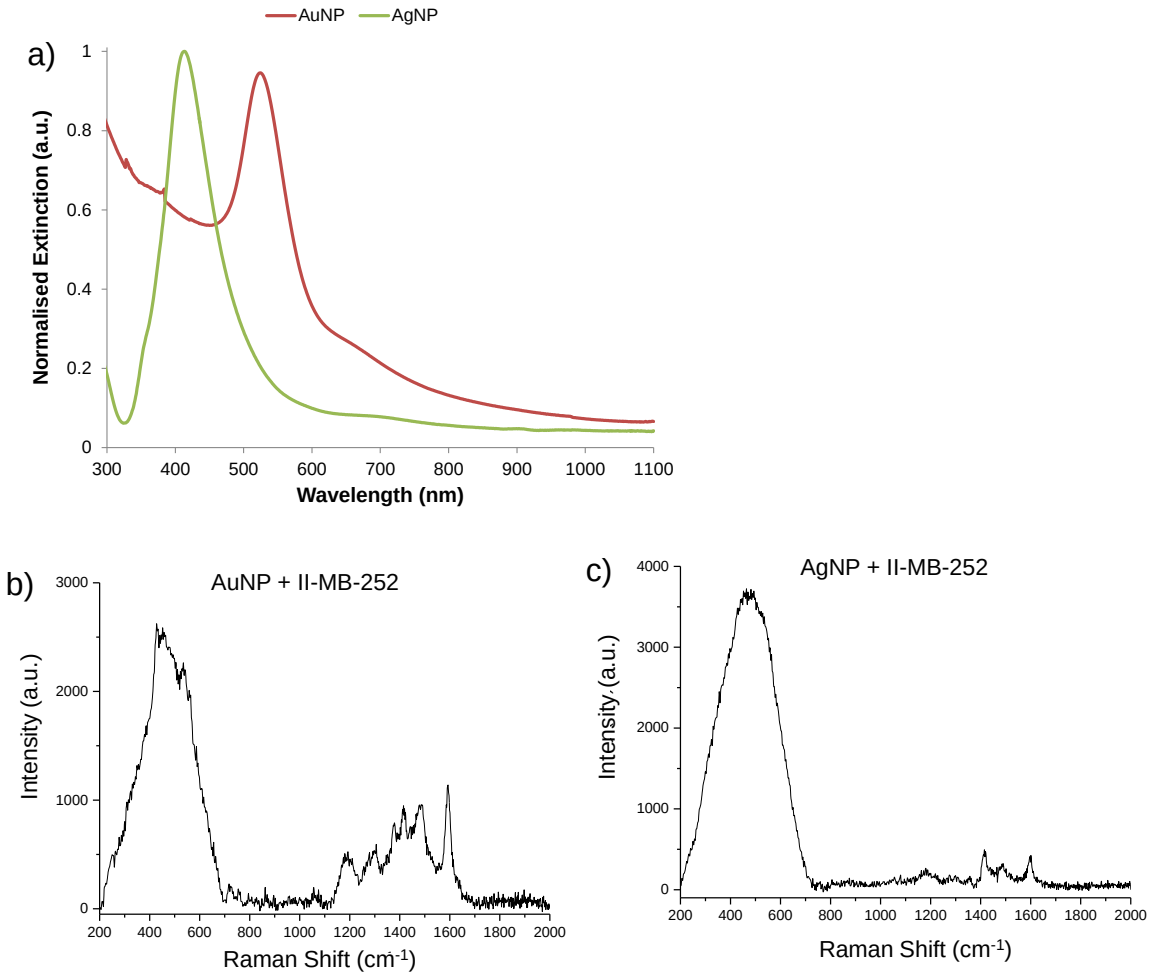

Figure 3.3 – a) Normalised extinction spectra showing the LSPR of the gold and silver nanoparticles to be at 525 nm and 410 nm respectively. SERS spectra for dye 252 with b) gold and c) silver nanoparticles of similar size and aggregated with KCl. A laser excitation of 1280 nm and an exposure time of 7 seconds were employed in this analysis. All spectra have been background corrected and normalised to a cyclohexane standard. Figure b and c) have been reproduced by permission of the Royal Society of Chemistry.[174]

The second necessary component for these SERS nanotags was the Raman reporter. Since the SERS effect decreases exponentially as a function of distance from the nanoparticle,[175] the Raman reporter must be near the gold surface. It can be seen that all these dyes incorporate S and Se atoms in the chalcogenopyrylium core with the 2-thienyl and 2-selenophenyl groups on select members of this library providing novel attachment groups to the gold surface. Earlier studies have shown that thiophenes[176] and selenophenes[177] are both capable of forming self-assembled monolayers on gold, with the selenolates showing a greater affinity for the gold surface than thiolates.[178, 179]

It can be seen in figure 3.2 that all these dyes are highly aromatic and produce vibrationally rich and intense SERS spectra with a laser excitation of 1280 nm. The trimethine dyes 075-114 produce more intense signals than their monomethine counterparts (dyes 070-095), with the selenophene-substituted reporters producing stronger SERS spectra than the thiophene-substituted dyes. The SERS spectra for dyes 070-252 were acquired with a 7 second acquisition time with the 1280 nm laser. The SERS spectrum of dye 114 with four 2-selenophenyl substituents was collected with only a 3 second acquisition time due to the signal intensity saturating the spectrometer. Both 252 and 114 are significantly red-shifted with light absorption maxima >800 nm, making them NIR active. Dye 252 with four 2-thienyl substituents gave a weaker SERS signal compared to dye 114 with four 2-selenophenyl substituents. This suggests that the selenophene group adheres more effectively to the gold surface than thiophene and supports previous reports where selenolates have shown a greater affinity for gold surfaces than thiolates.[178, 179]

The third component in the SERS nanotag is the aggregating agent, usually a simple inorganic salt such as KCl that screens the Coulombic repulsion energy between the nanoparticles, creating SERS hot-spots. When the reporter molecules are trapped in these areas a huge increase in the SERS signal is observed.[105] Although the aggregating agent was necessary for most of the dyes, it is important to note that with dyes 252 and 114, KCl was not required for intense signals to be observed see figure 3.4. This is possibly due to a strong interaction occurring between the reporter and HGN surface inducing

self-aggregation. This partial aggregation observed from these nanotags perhaps widens the scope for future SERS applications where aggregating agents are not required and the aggregation of the nanotags comes solely from a biological recognition event. Thus due to their strong scattering properties, these nanotags could potentially be used in studies where the SERS enhancement is switched on due to the controlled assembly between DNA-DNA, DNA-protein, peptide-protein or sugar-protein interactions [145, 146]

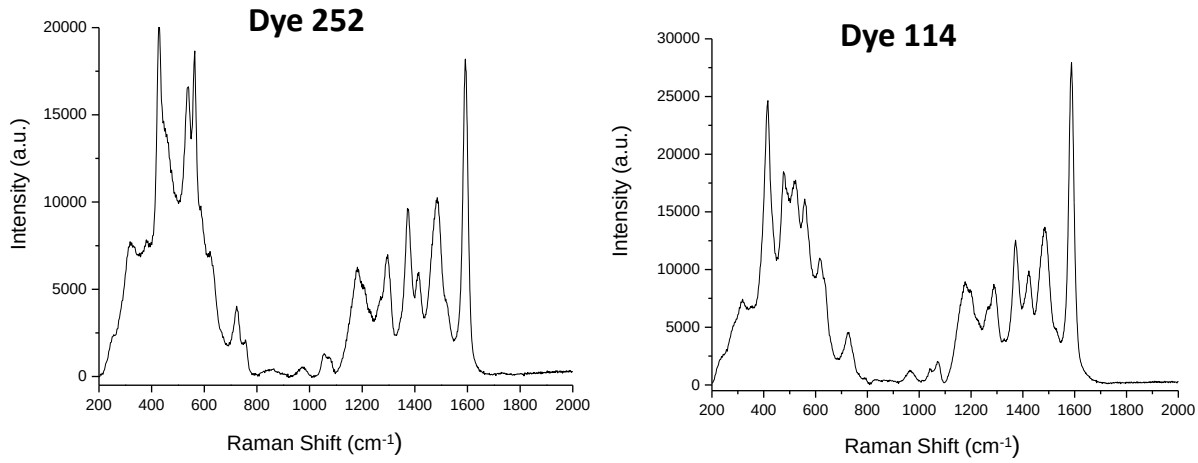

Figure 3.4 - Unaggregated SERS spectra of dyes 252 and 114 analysed with HGNs and deionised water. A laser excitation of 1280 nm and an exposure time of 7 seconds were employed in this analysis. All spectra have been background corrected. Figure has been reproduced by permission of the Royal Society of Chemistry.[174]

3.4.1.2 Limits of Detection

Due to the exceptional response obtained with these dyes and HGNs, particle dilution studies were conducted in order to calculate limit of detections at this extremely red-shifted laser wavelength. The LOD study was carried out by initially using the optimum conditions (those used in figure 3.2 to obtain SERS at 1280 nm) in which the particle concentration was 1.9 nM and then subsequent dilutions in water were made until no signal was observed. The peak at ~1590 cm^{-1}, which arises from heterocyclic aromatic ring stretching within the molecules[129] was used to calculate the LOD since it was the most intense peak in the spectra. Figure 3.5 shows that linear responses were obtained and therefore LODs could be calculated; see table 3.1 for a list of all the LOD values with associated standard deviation values. The LODs

were calculated to be 3 times the standard deviation of the blank (HGN only), divided by the gradient of the straight line. Trimethine dyes 075-114 all gave LODs of <10 pM with the 252 and 114 dyes producing the best results with exceptionally low values of 1.5 ± 0.1 pM. Dyes 095, 099 and 067 gave LODs of 3.4 to 5.4 pM, respectively, while monomethine dyes 070, 069 and 071 gave LODs of 22 to 33 pM. The 1280 nm SERS signals from reporters 020 and 162 were too weak to allow determination of LODs. It should be noted however, that the reported concentrations for the chalcogen nanotags throughout this chapter are for non-aggregated systems based on the particle concentration of HGNs or large AuNPs and as such the nanotag concentrations reported will be different due to aggregation occurring.

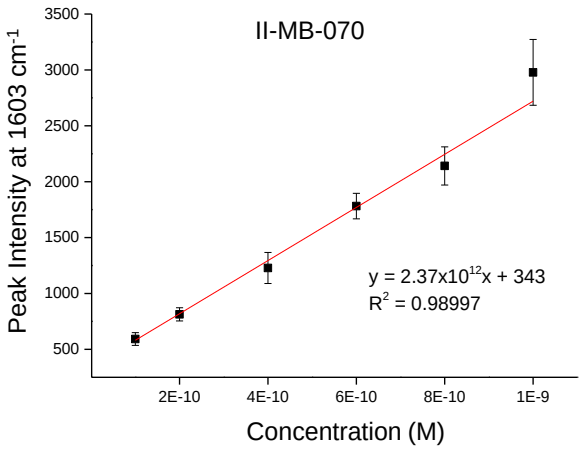

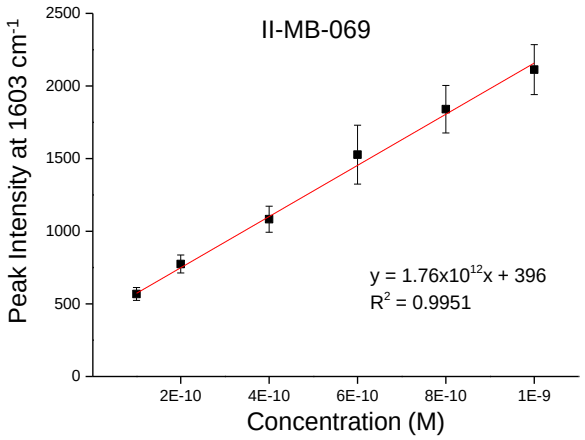

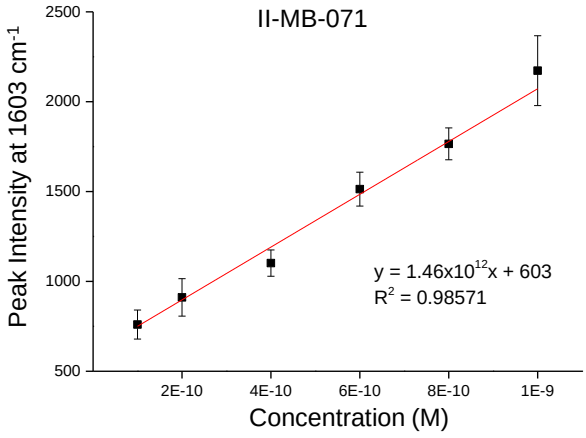

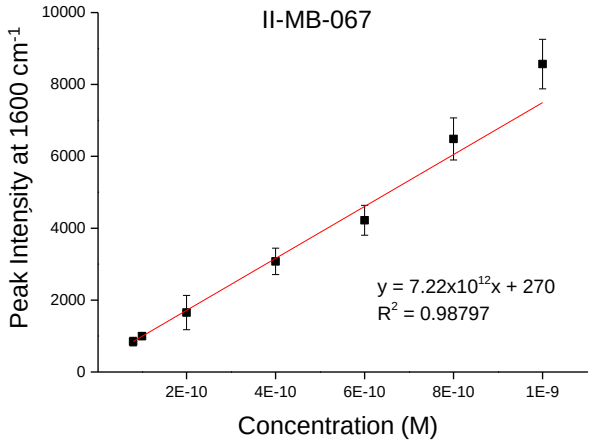

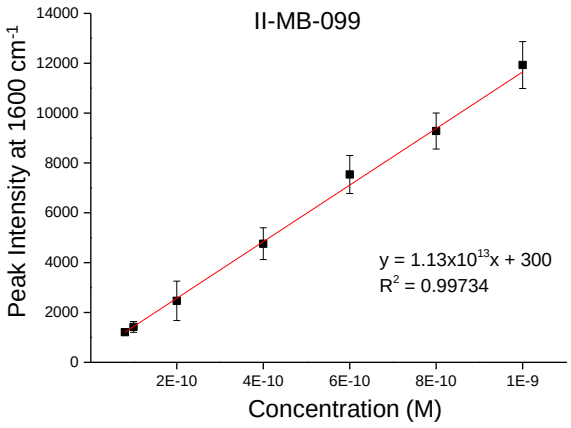
II-MB-099
Peak Intensity at 1600 cm-1
Concentration (M)
y = 1.13x10^13x + 300
R^2 = 0.99734

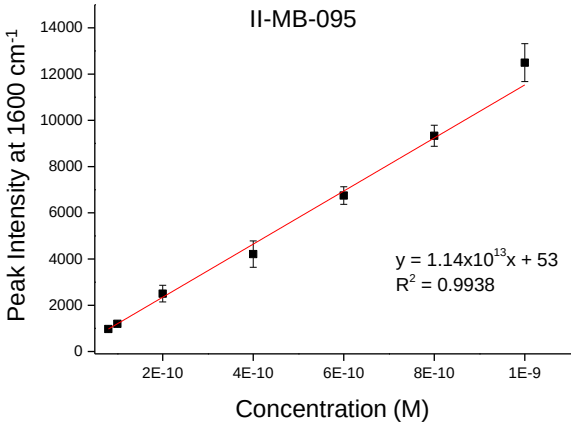
II-MB-095
Peak Intensity at 1600 cm-1
Concentration (M)
y = 1.14x10^13x + 53
R^2 = 0.9938

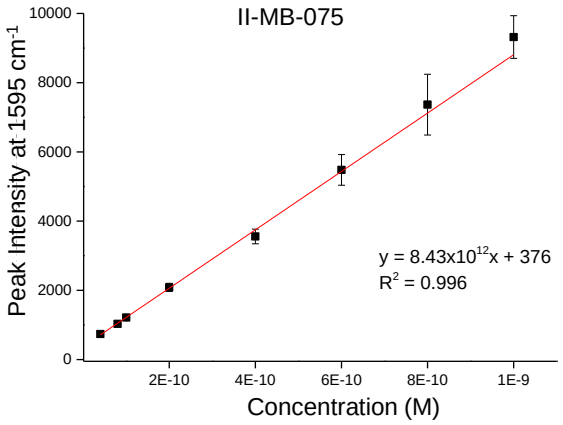
II-MB-075
Peak Intensity at 1595 cm-1
Concentration (M)
y = 8.43x10^12x + 376
R^2 = 0.996

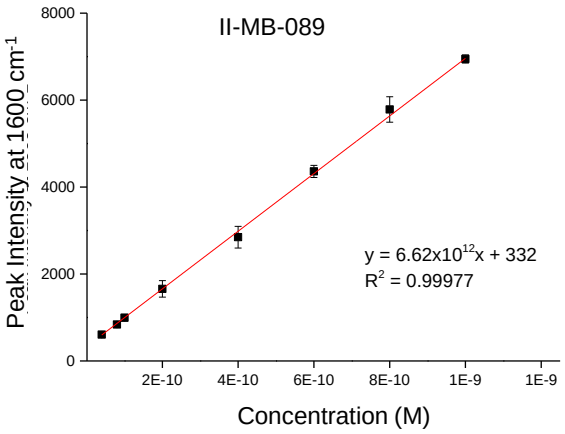
II-MB-089
Peak Intensity at 1600 cm-1
Concentration (M)
y = 6.62x10^12x + 332
R^2 = 0.99977

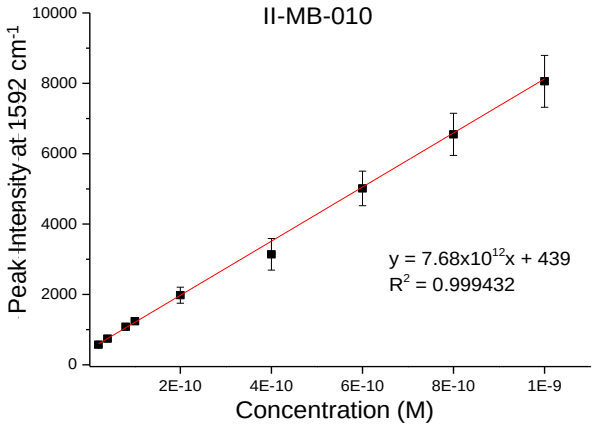
II-MB-010
Peak Intensity at 1592 cm-1
Concentration (M)
y = 7.68x10^12x + 439
R^2 = 0.999432

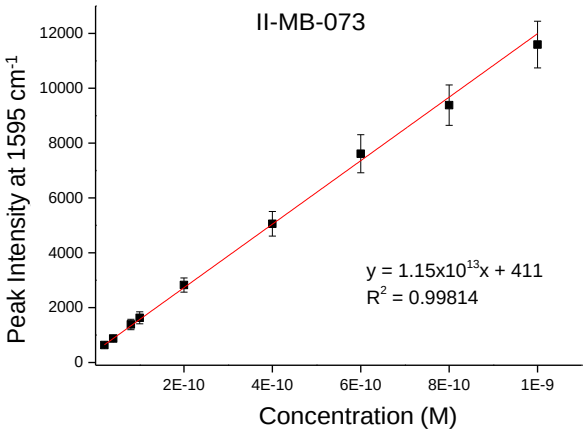
II-MB-073
Peak Intensity at 1595 cm-1
Concentration (M)
y = 1.15x10^13x + 411
R^2 = 0.99814

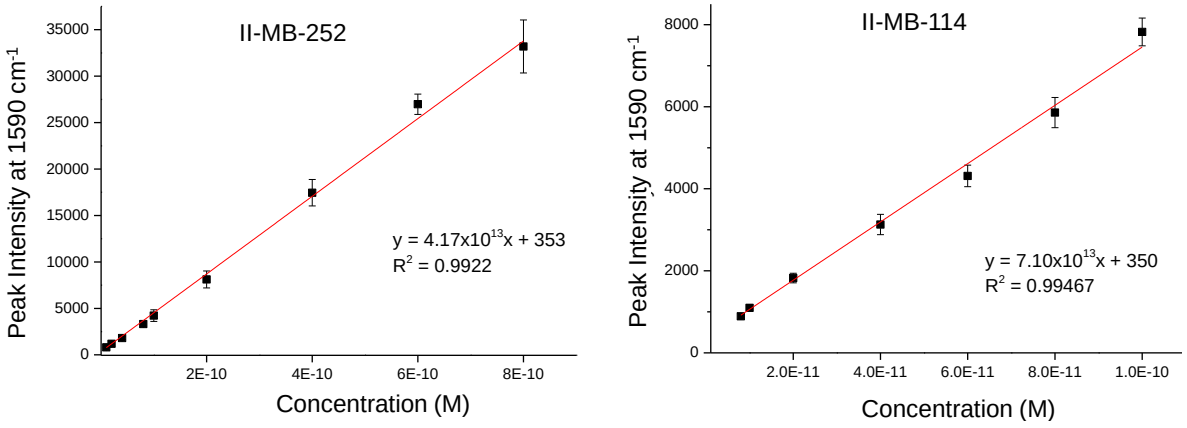

Figure 3.5 - SERS particle dilution studies for the batch of dyes with HGNs and KCl over the concentration range 1.9 nM to 6 pM. A laser excitation of 1280 nm and an exposure time of 7 seconds were employed in this analysis. Error bars represent one standard deviation resulting from 3 replicate samples and 5 scans of each. Figure has been reproduced by permission of the Royal Society of Chemistry.[174]

Table 3.1 - Values of the absorption maximum (λ_{max}), molar extinction co-efficient (ε) and calculated LOD values from the SERS experiment with associated standard deviation (s.d.) error for chalcogenopyrylium dyes 070-114. Table has been reproduced by permission of the Royal Society of Chemistry.[174]

Dye	**λ_{max}, nm (CH_2Cl_2)**	**ε, M^{-1} cm^{-1} (CH_2Cl_2)**	**LOD, pM[a]**	**Structure Type**
1 - **070**	653	1.3×10^5	21.8 ± 1.9	Monomethine dyes
2 - **069**	676	1.3×10^5	29.4 ± 2.7	
3 - **071**	699	1.5×10^5	32.8 ± 2.4	
4 - **020**	676	1.2×10^5	--	
5 - **067**	698	1.1×10^5	5.4 ± 0.6	
6 - **162**	724	1.3×10^5	--	
7 - **099**	659	1.4×10^5	4.6 ± 0.5	
8 - **095**	687	1.1×10^5	3.4 ± 0.2	
9 - **075**	806	2.5×10^5	9.1 ± 0.7	Trimethine dyes
10 - **089**	784	2.0×10^5	5.9 ± 0.3	
11 - **010**	810	2.5×10^5	1.8 ± 0.2	
12 - **073**	789	2.2×10^5	6.6 ± 0.6	
13 - **252**	813	2.8×10^5	1.5 ± 0.1	
14 - **114**	826	2.3×10^5	1.5 ± 0.1	

[a] SERS - LOD ± s.d.

To get a better understanding of how promising these newly synthesised nanotags were the non-resonant commercial dyes BPE and AZPY, which are commonly used with gold nano-substrates for SERS analysis[111, 139] were also tested with the HGNs at this laser wavelength (see figure 3.6). However, they failed to produce a SERS signal showing the superiority of these new nanotags.

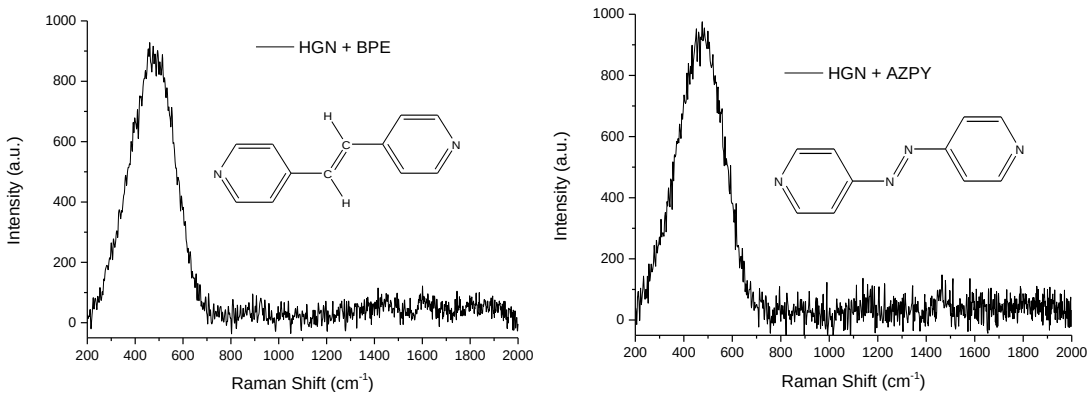

Figure 3.6 - SERS spectra and structures of commercial dyes BPE and AZPY with HGNs and KCl. A laser excitation of 1280 nm and an exposure time of 7 seconds were employed in this analysis. All spectra have been background corrected. Figure has been reproduced by permission of the Royal Society of Chemistry.[174]

3.4.1.3 Principal Component Analysis

Dyes 070-114 can be separated out and individually identified in a reproducible manner based on their unique structures and SERS spectra through multivariate analysis in the form of principal component analysis. PCA is employed to reduce the dimensionality of the spectroscopic data thus facilitating identification of variations in the SERS spectra.[30] It should be noted that Dr. Samuel Mabbott carried out all the PCA detailed in this section.

PCA was carried out on 14 data sets consisting of three replicate spectra obtained from each individual dye. The resulting principal component (PC) scores plot (figure 3.7) clearly illustrates three unique groupings. The red cluster contains the trimethine dyes 075-114; these reporter molecules produced the most intense SERS signals and all contain 3 sp^2 carbons in their trimethine bridge. The blue clustering highlights the monomethine dyes (070-

071,067,099,095), which are good Raman reporters and produce intense SERS spectra with HGNs and KCl while the green cluster contains the two dyes which produced a weak SERS response (dyes 020 and 162) when excited with the 1280 nm laser. The monomethine dyes only contain 1 sp^2 carbon in their monomethine bridge and this simple difference in molecular structure could be responsible for the variation in signal intensities observed between the trimethine and monomethine dyes. Moreover, this simple structural change can affect the distance, orientation and/or the polarisability of the reporter which ultimately affects the SERS response. Loadings plots showing the spectral variations responsible for the classification of the dyes and can be viewed in figure 3.8.

Additionally, it can be observed that within the three groupings, all 14 dyes can be individually identified by PCA and classified according to their unique structure and SERS spectra. Replicates for each dye are tightly clustered illustrating the excellent reproducibility of the SERS spectra. A further benefit for these 1280 nm SERS nanotags is their potential for use in future multiplexing systems, where multiple analytes need to be identified simultaneously, such as in chemical or medical detection assays.[146, 180]

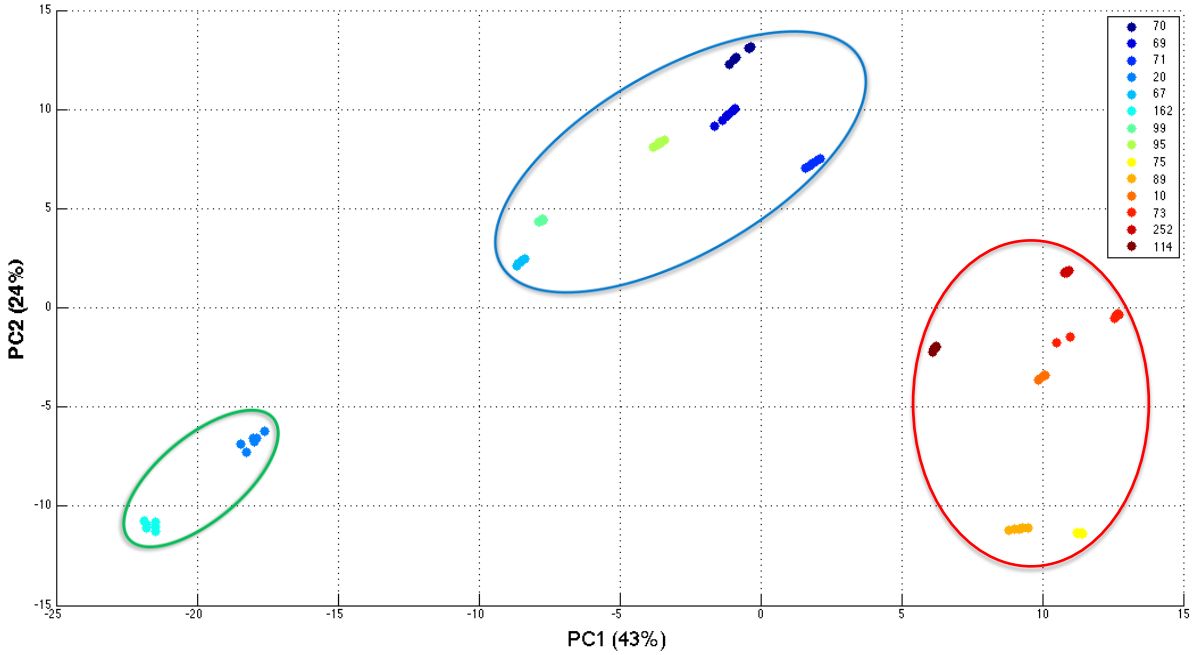

Figure 3.7 - PCA scores plot discriminating between each of the 14 chalcogenopyrylium dyes and grouping them according to their structures and SERS spectra. The red cluster contains the trimethine dyes 075-114 which produce the best SERS signals, blue cluster highlights the monomethine dyes (070-071,067,099,095) which work well as reporters for SERS and the green clustering contains the two dyes which produce only weak signals with HGNs (dyes 020 and 162). Figure has been reproduced by permission of the Royal Society of Chemistry.[174]

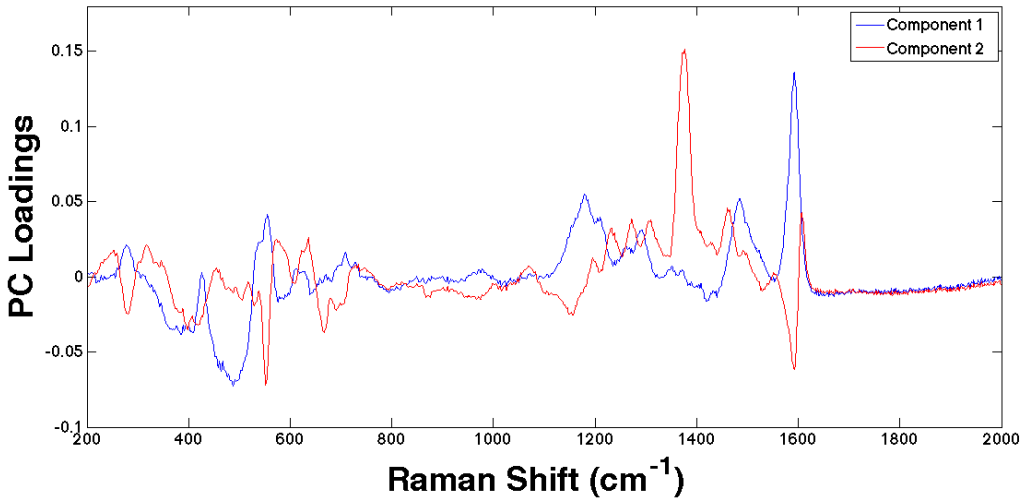

Figure 3.8 - PC Loadings plots showing the Raman peaks that are responsible for the classification of the dyes across components 1 and 2. Figure has been reproduced by permission of the Royal Society of Chemistry.[174]

3.4.2 1064 nm SERS Nanotags

3.4.2.1 SERS analysis of nanotags

The 1280 nm SERS investigations have shown that these newly synthesised dyes are exceptionally bright and when added to HGNs, they make great SERS nanotags. Furthermore, they demonstrate pM detection limits using a laser excitation which has never been employed in SERS before.

Moreover, these studies were conducted to build on this knowledge by initially adding dyes to the chalcogen library and then comparing the 17 dyes analysed with the commercially available reporters BPE and AZPY, which were shown in the previous chapter to produce effective SERS with NIR-HGNs when excited with a 1064 nm laser.

Furthermore as previously demonstrated in figure 3.3 (section 3.4.1.1), when these chalcogen dyes were added to AuNPs and AgNPs of a similar size (40-60 nm; prepared 'in-house') they produced much weaker SERS signals than when HGNs are used as the SERS substrate. Therefore the 1064 nm data which also confirms this has not been included in this chapter but can be seen in appendix IV.

The experimental conditions used for the 1280 nm SERS studies, were modified slightly from the conditions detailed in chapter 2. Therefore, before the 1064 nm SERS studies were conducted, it was important to determine that the optimum concentration of Raman reporter was been utilised, hence 4 chalcogen dyes and two commercial dyes were chosen for analysis. Figure 3.9 shows a concentration study over the range 0.1 mM to 10 nM (reporter concentration) which determined if the optimum concentration of reporter was being used. Only dyes 184 and 198 have observable peaks at the lowest concentration (10 nM) and this is because the lowest observable concentrations for the other reporters were above this value and so they weren't tested at 10 nM. It also appears that all dyes have maximum intensity values, thus optimum concentrations at 10 µM. Chapter 2 explained that for BPE and AZPY, this was due to approximately monolayer coverage which causes reporter-reporter interactions to force effective packing on the HGN surface. Furthermore, due to an examination of the SERS it was predicted that they adsorbed onto the HGN with a

perpendicular orientation. Due to the strong SERS signals observed for these newly synthesised dyes, see figure 3.11, it is expected that these dyes will also pack effectively on the HGN surface with a perpendicular or nearly perpendicular orientation. Although, how these dyes bond and orientate is discussed in more detail in section 3.4.3; where dye 114 was examined further with computational studies.

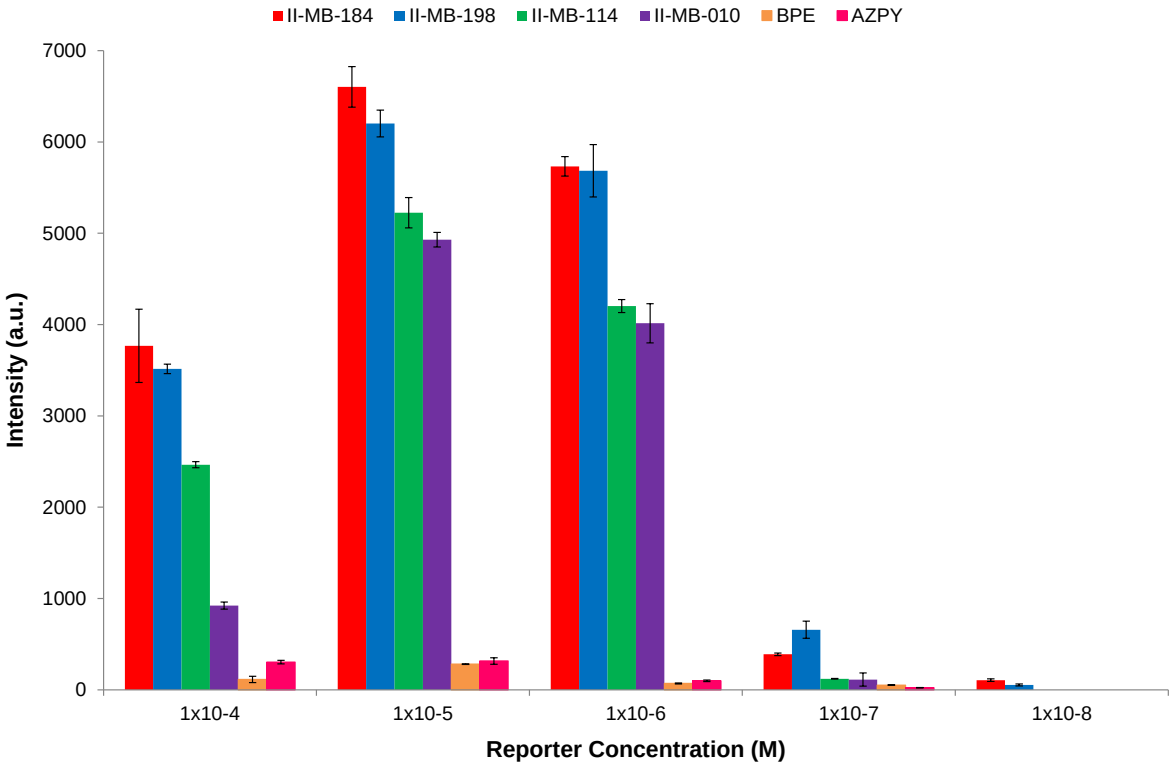

Figure 3.9 - SERS concentration study for Raman reporters tested over the concentration range 0.1 mM to 10 nM (reporter concentration) plus HGNs (LSPRs at 700 nm) and KCl. The Raman reporters tested where; chalcogen dyes 184, 198, 114 and 010 plus commercial reporters BPE and AZPY. A laser excitation of 1064 nm and exposure times of 0.05 – 0.1 seconds were employed in this analysis.

It is obvious from figure 3.9, that these newly synthesised dyes are far superior and brighter than the commercially available reporters. At the optimum concentration of 10 µM, there is approximately a 13 fold increase in the SERS signal for the chalcogen dye 184 when compared to BPE. Furthermore, it can be observed that dyes 184 and 198 are slightly stronger reporters than the 114 dye which in the 1280 nm SERS studies was the best reporter. With a laser excitation at 1064 nm however, these two dyes are very close to being on resonance with wavelength maxima at 959

nm (dye 184) and 986 nm (dye 198) and as such a contribution from both molecular resonance and surface enhancement is likely to have led to the increase in signal. In addition by adding another carbon-carbon double bond (C=C) into the backbone and designing pentamethine dyes; it further enhances the SERS signal, see figure 3.10. Moreover, this observation was briefly mentioned in section 3.4.1, when adding a sp^2 carbon into the backbone and changing from monomethine dyes to trimethine dyes enhanced the SERS signals. This structural modification allowed the dyes to be separated into distinct groupings by PCA too. Therefore, when designing effective Raman reporters it's not just essential to incorporate novel attachment groups such as Se and S rings but it is also important to understand how the core structure (structural backbone) will affect the SERS enhancement. As the number of sp^2 carbons is increased, it is likely that a greater displacement along the π-backbone will occur during the vibration, resulting in a greater polarisability and electromagnetic enhancement being experienced; further explaining why an increase was observed in the SERS signals. But note, there will be a point where adding to many sp^2 carbons to the backbone will cause over-aggregation and the nanoparticles to become unstable and precipitate out of solution.

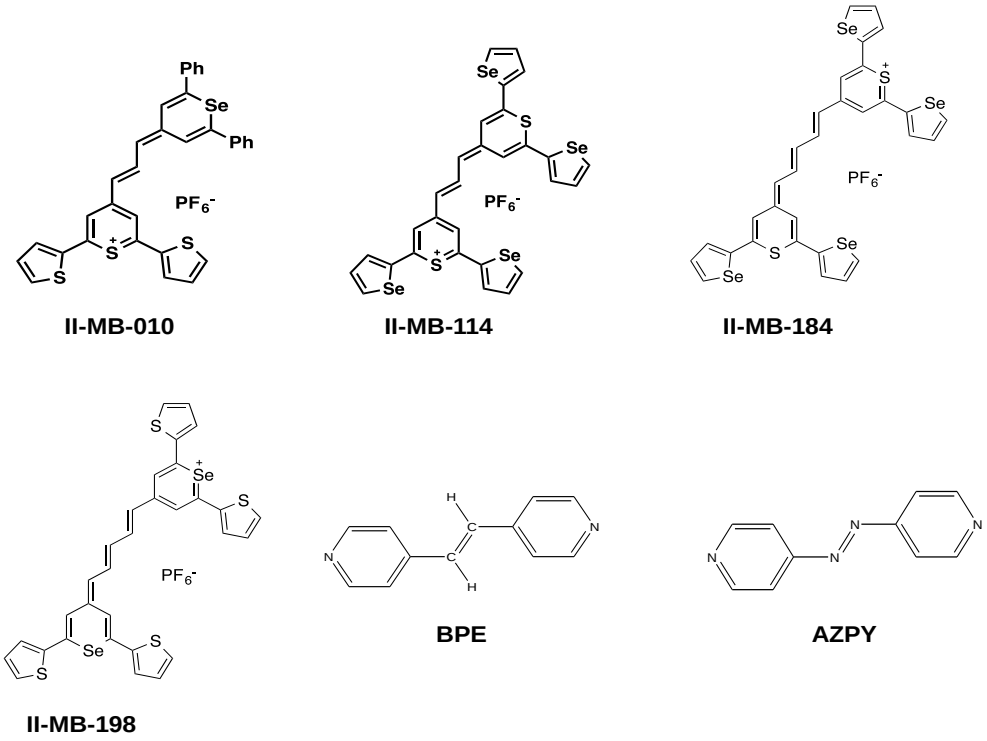

Figure 3.10 – Structures of reporter molecules chosen for the reporter concentration study.

The SERS spectra for all the chalcogen dyes (17) plus BPE and AZPY with a laser excitation of 1064 nm can be seen in figure 3.11. The structures of all the Raman reporters tested in this chapter can be seen in appendix V. The first 8 chalcogen dyes are monomethine substitutes, the next 6 are trimethine substituents and the last 3 where the newly tested dyes of which one is a trimethine dye and the last two are pentamethine dyes.

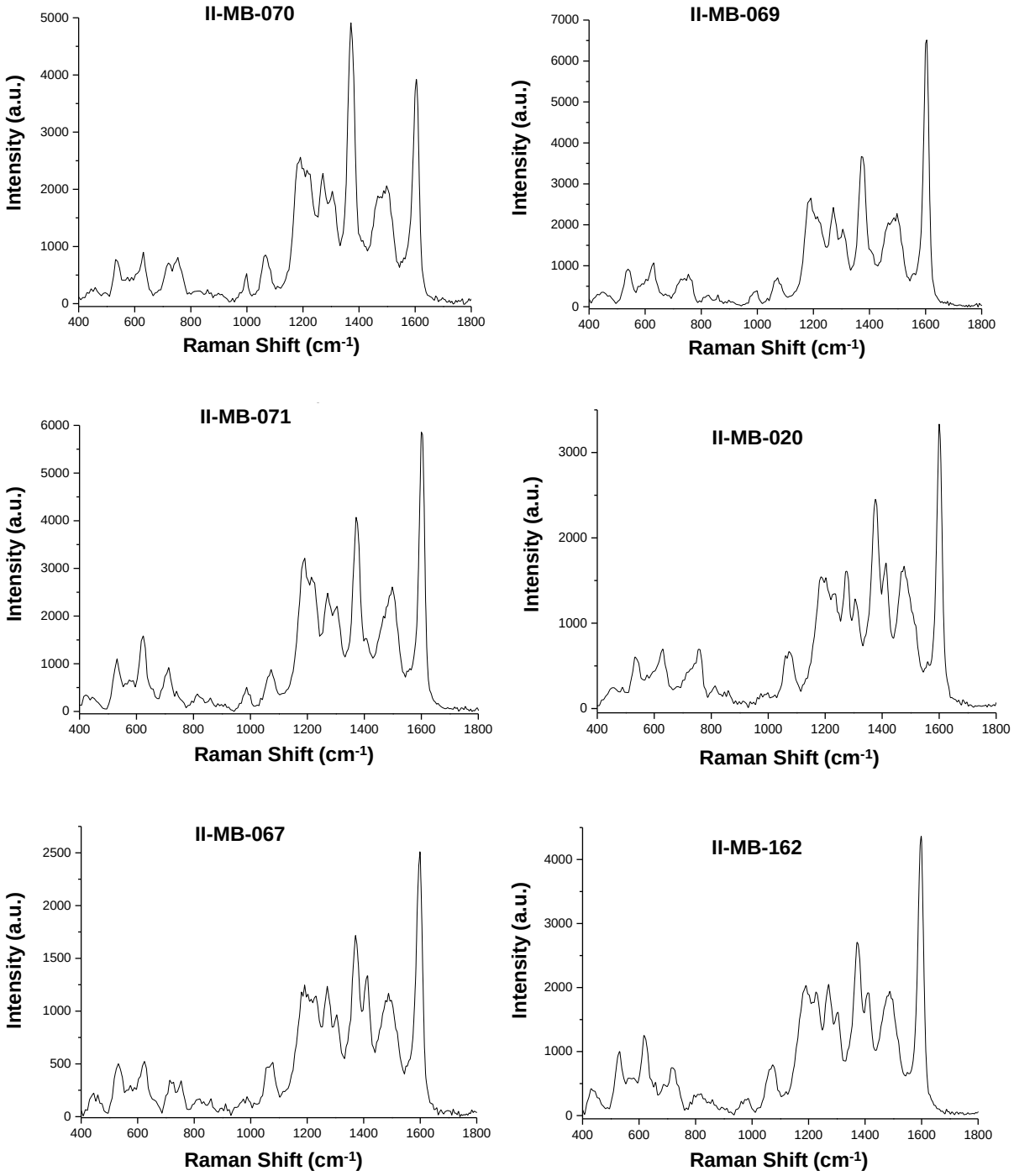

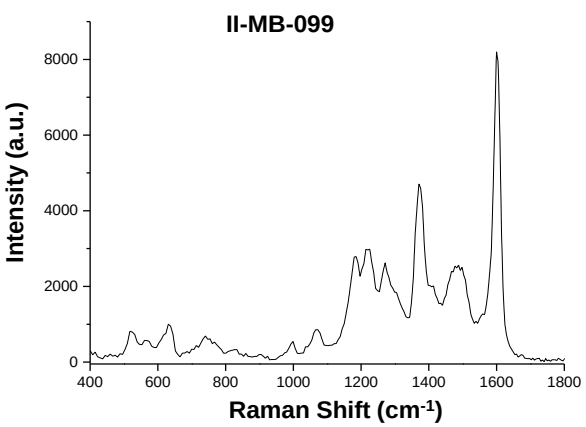
II-MB-099
Intensity (a.u.)
Raman Shift (cm-1)

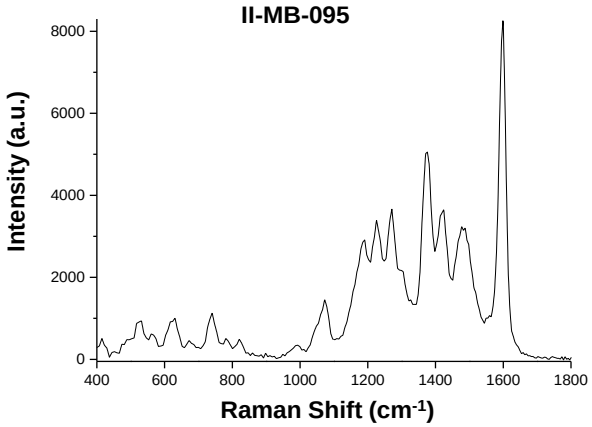
II-MB-095
Intensity (a.u.)
Raman Shift (cm-1)

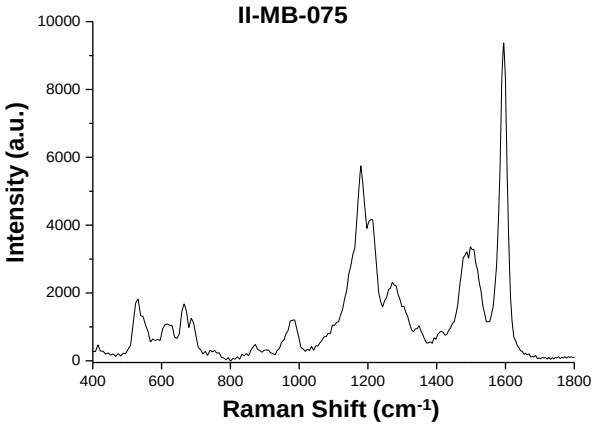
II-MB-075
Intensity (a.u.)
Raman Shift (cm-1)

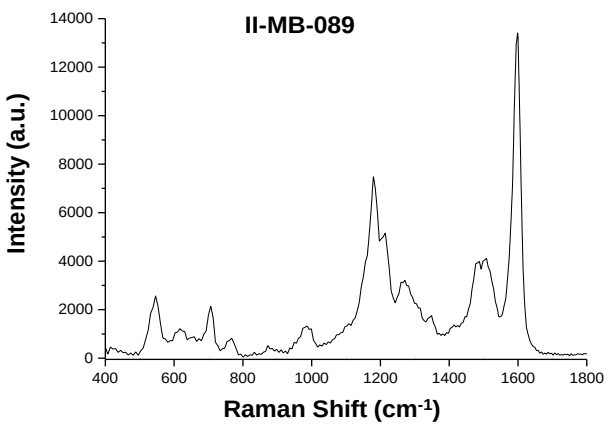
II-MB-089
Intensity (a.u.)
Raman Shift (cm-1)

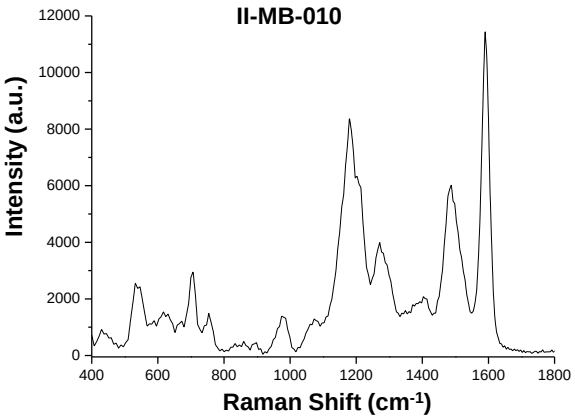
II-MB-010
Intensity (a.u.)
Raman Shift (cm-1)

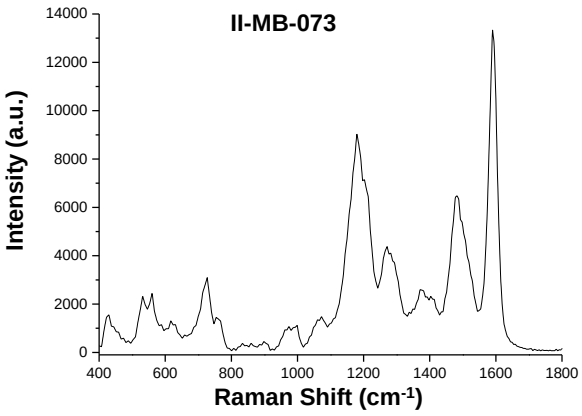
II-MB-073
Intensity (a.u.)
Raman Shift (cm-1)

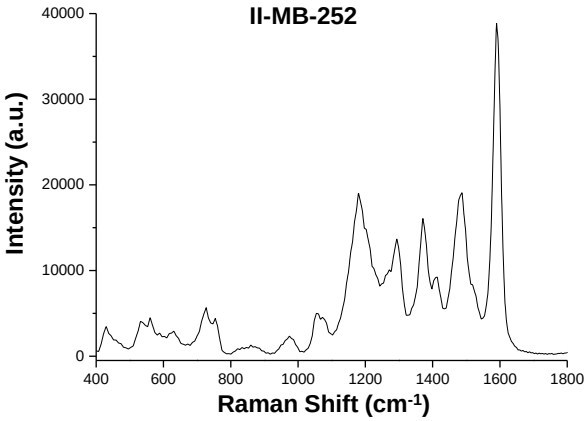
II-MB-252
Intensity (a.u.)
Raman Shift (cm-1)

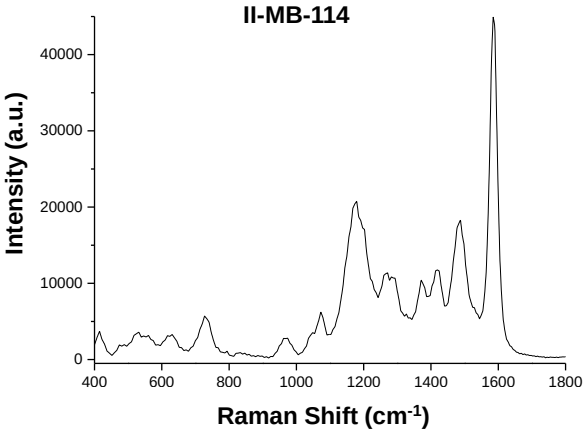
II-MB-114
Intensity (a.u.)
Raman Shift (cm-1)

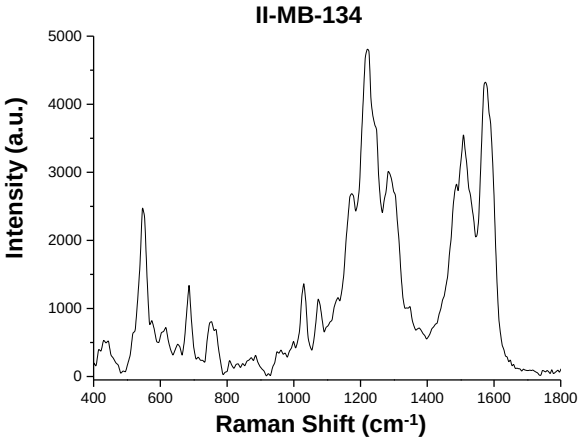
II-MB-134
Intensity (a.u.)
Raman Shift (cm-1)

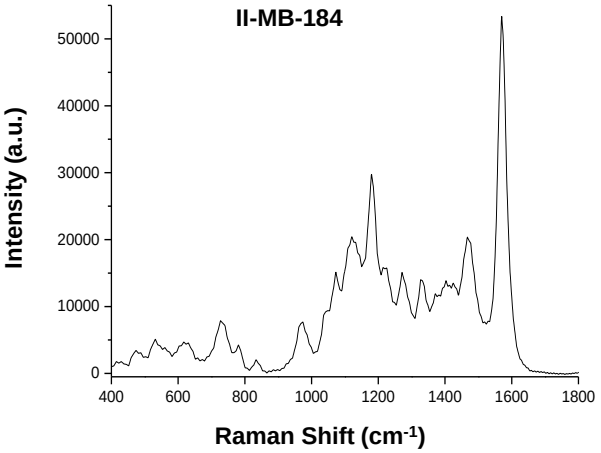
II-MB-184
Intensity (a.u.)
Raman Shift (cm-1)

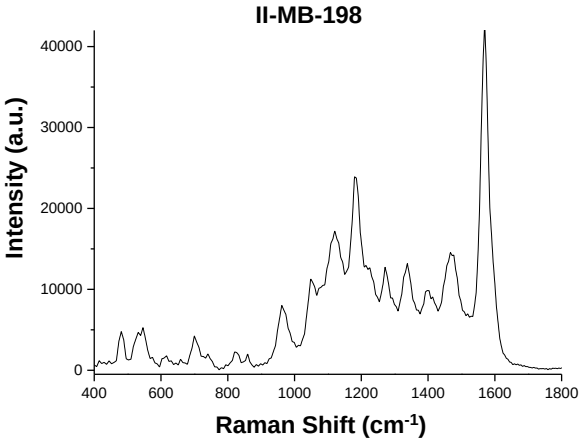
II-MB-198
Intensity (a.u.)
Raman Shift (cm-1)

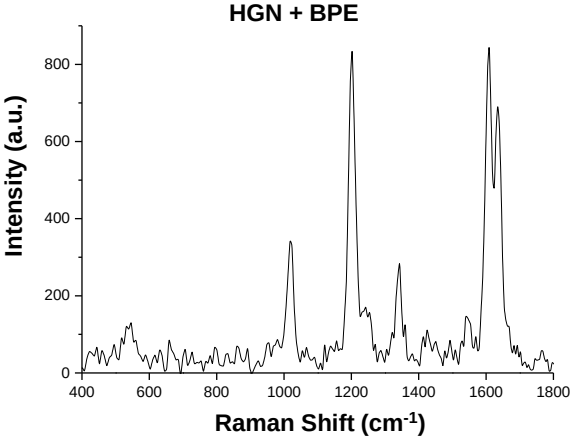
HGN + BPE
Intensity (a.u.)
Raman Shift (cm-1)

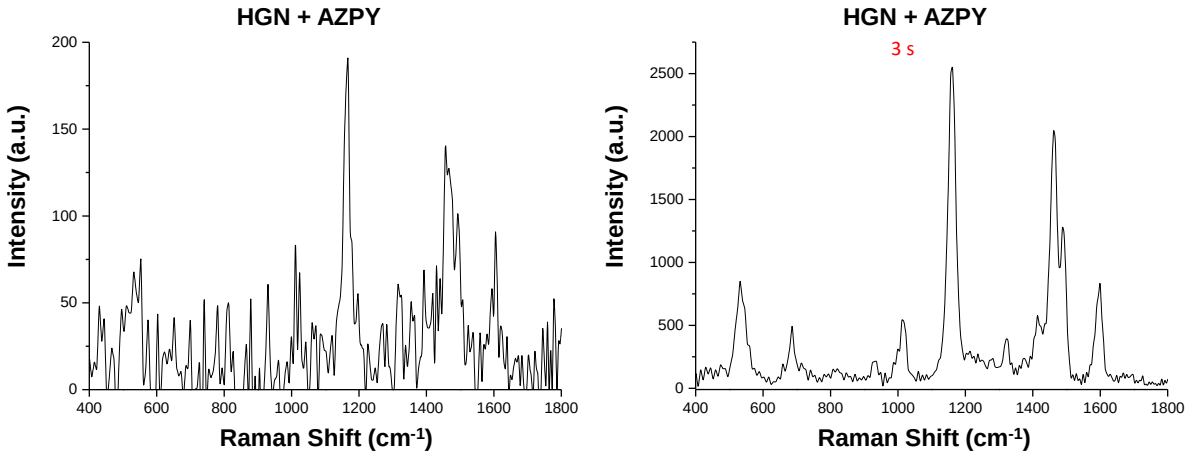

Figure 3.11 - SERS spectra for all Raman reporters tested. The dyes with a concentration of 10 µM were analysed with HGNs (SPR recorded at 710 nm) and KCl. A laser excitation of 1064 nm and an exposure time of 0.1 seconds were employed in this analysis, with the exception of dyes 184, 198 and AZPY where an acquisition time of 0.05-3 seconds were employed. All spectra have been background corrected.

These results further confirm that these newly developed SERS nanotags are superior to any commercially available reporter for using with NIR laser excitations. It can be seen that the pentamethine dyes 184 and 198 are the best Raman reporters followed by the trimethine substituents and then the monomethine substituents. It can also be seen that the 184 dye produces a more intense SERS spectrum than the 198 dye, further confirming that the selenolates have greater affinity to the gold surface of the HGNs than the thiolates.[178, 179] In general this result of the selenophenes producing stronger SERS spectra than the S substituents was observed when comparing all the reporter molecules. Furthermore, in order to have a complete understanding of these SERS nanotags it was important to undertake particle dilution studies in order to determine LODs at this laser excitation.

Therefore, all 17 chalcogen dyes plus BPE and AZPY were analysed over the concentration range 2 nM to 0.1 pM. Figure 3.12 shows that linear responses were obtained and therefore LODs could be calculated as before (section 3.3.5.2). Furthermore, table 3.2 lists all the LOD values with associated standard deviation values plus the LODs obtained with the 1280 nm laser excitation for comparison.

.

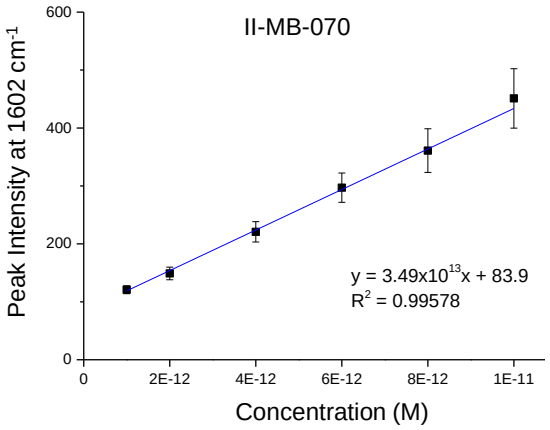
II-MB-070
Peak Intensity at 1602 cm-1
Concentration (M)
y = 3.49x10^13x + 83.9
R^2 = 0.99578
0
200
400
600
0
2E-12
4E-12
6E-12
8E-12
1E-11

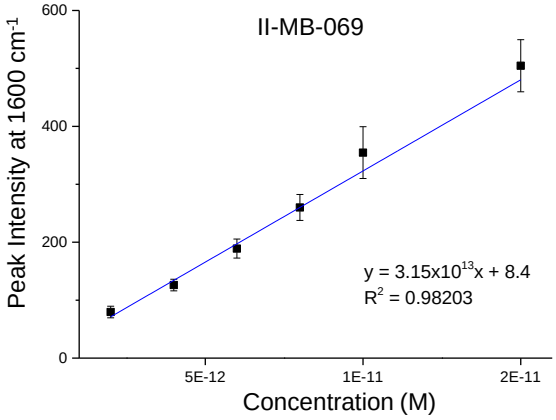
II-MB-069
Peak Intensity at 1600 cm-1
Concentration (M)
y = 3.15x10^13x + 8.4
R^2 = 0.98203
0
200
400
600
5E-12
1E-11
2E-11

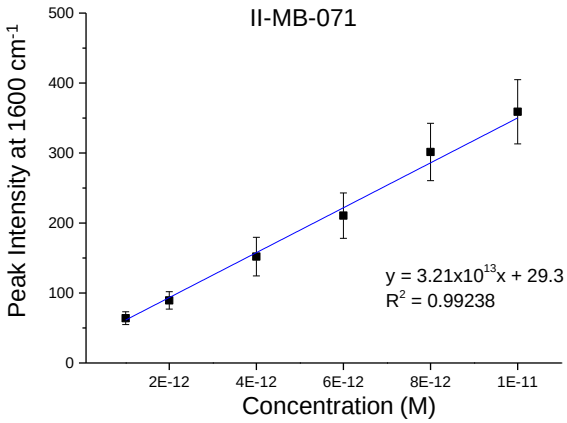
II-MB-071
Peak Intensity at 1600 cm-1
Concentration (M)
y = 3.21x10^13x + 29.3
R^2 = 0.99238
0
100
200
300
400
500
2E-12
4E-12
6E-12
8E-12
1E-11

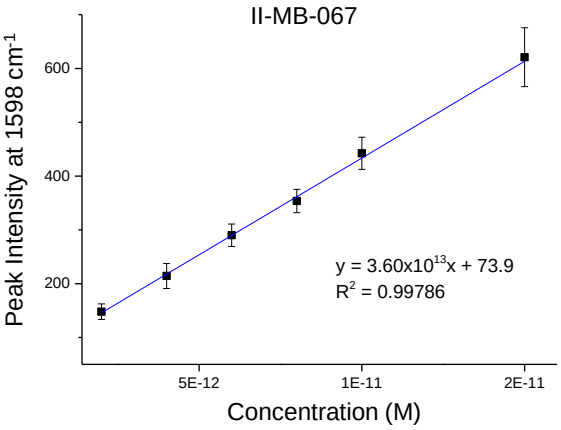
II-MB-067
Peak Intensity at 1598 cm-1
Concentration (M)
y = 3.60x10^13x + 73.9
R^2 = 0.99786
200
400
600
5E-12
1E-11
2E-11

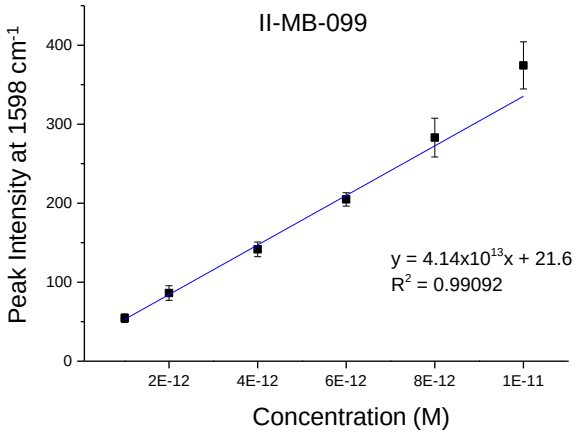
II-MB-099
Peak Intensity at 1598 cm-1
Concentration (M)
y = 4.14x10^13x + 21.6
R^2 = 0.99092
0
100
200
300
400
2E-12
4E-12
6E-12
8E-12
1E-11

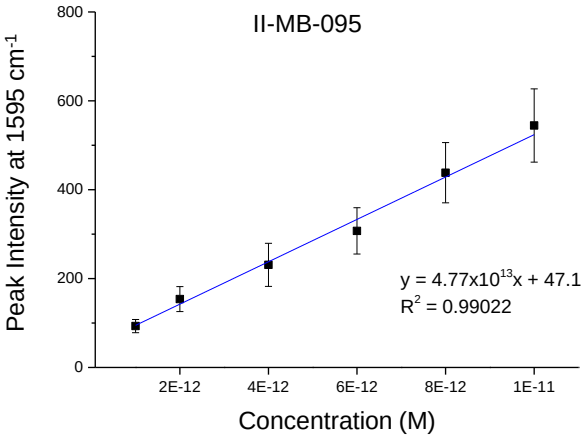
II-MB-095
Peak Intensity at 1595 cm-1
Concentration (M)
y = 4.77x10^13x + 47.1
R^2 = 0.99022
0
200
400
600
800
2E-12
4E-12
6E-12
8E-12
1E-11

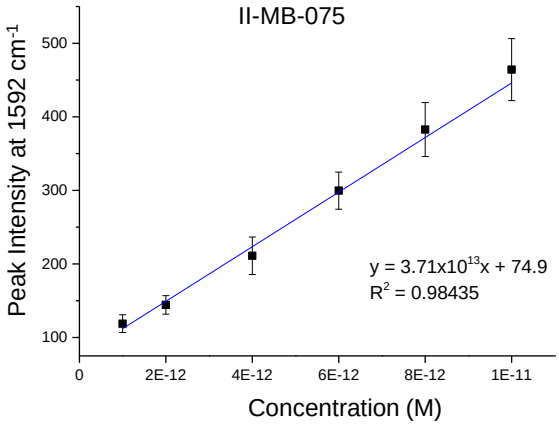
II-MB-075
Peak Intensity at 1592 cm-1
Concentration (M)
y = 3.71x10^13x + 74.9
R^2 = 0.98435

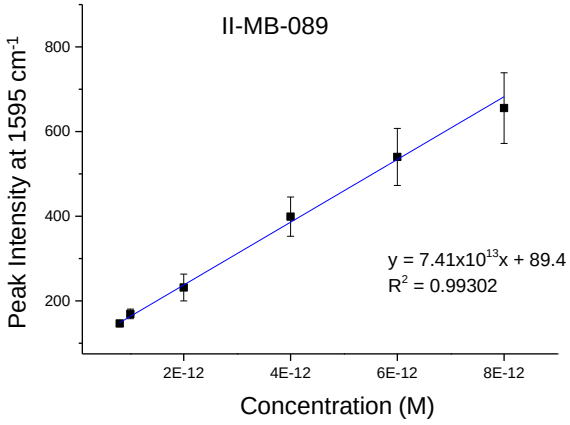
II-MB-089
Peak Intensity at 1595 cm-1
Concentration (M)
y = 7.41x10^13x + 89.4
R^2 = 0.99302

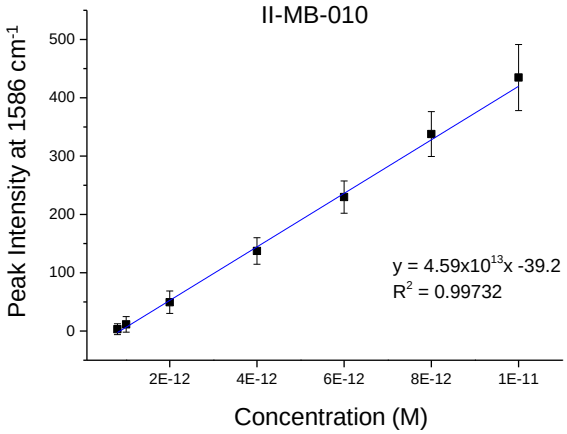
II-MB-010
Peak Intensity at 1586 cm-1
Concentration (M)
y = 4.59x10^13x -39.2
R^2 = 0.99732

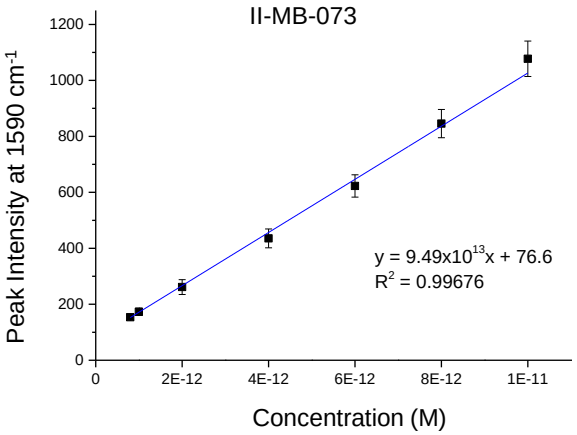
II-MB-073
Peak Intensity at 1590 cm-1
Concentration (M)
y = 9.49x10^13x + 76.6
R^2 = 0.99676

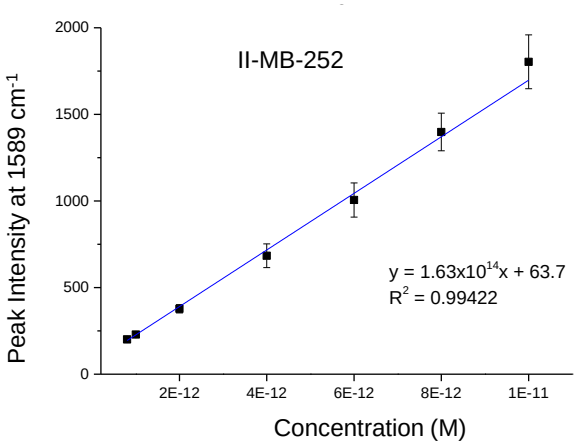
II-MB-252
Peak Intensity at 1589 cm-1
Concentration (M)
y = 1.63x10^14x + 63.7
R^2 = 0.99422

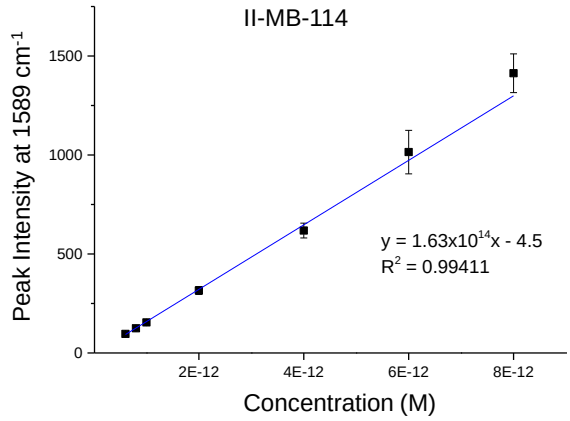
II-MB-114
Peak Intensity at 1589 cm-1
Concentration (M)
y = 1.63x10^14x - 4.5
R^2 = 0.99411

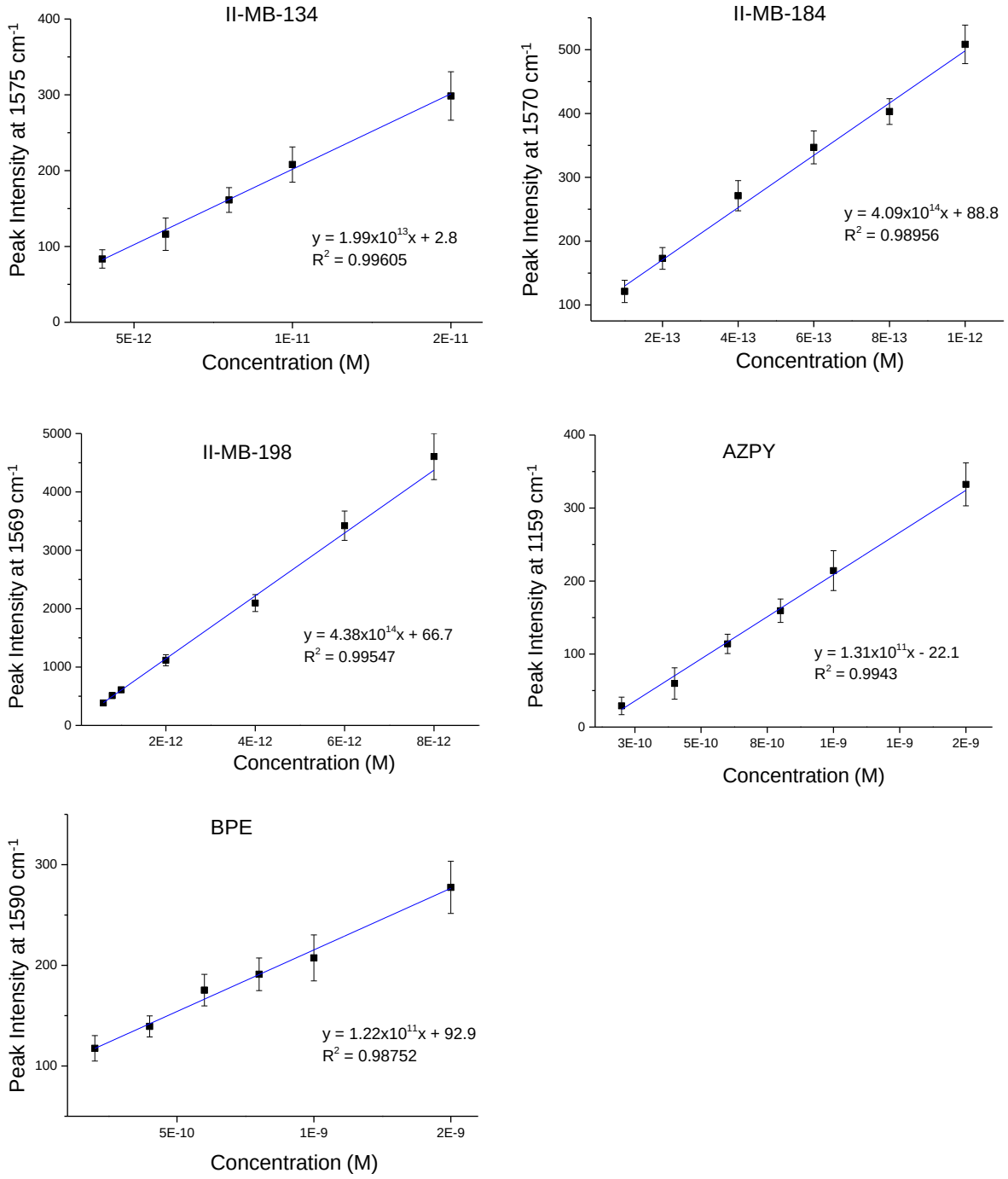

Figure 3.12 - SERS particle dilution studies for the batch of dyes with HGNs and KCl over the concentration range 2 nM to 0.1 pM. A laser excitation of 1064 nm and an exposure time of 7 seconds were employed in this analysis. Error bars represent one standard deviation resulting from 3 replicate samples and 5 scans of each.

Table 3.2 - Values of the absorption maximum (λ_{max}) and calculated LOD values from the SERS experiment with associated standard deviation (s.d.) error for 17 chalcogenopyrylium dyes plus BPE and AZPY using 1064 nm and 1280 nm laser excitations. In addition, extinction spectra for a selection of these chalcogenopyrylium dyes can be seen appendix III. *It should be noted that Fatima Ali (a placement student) helped to collect all the LOD data.*

Dye	**λ_{max} nm (CH_2Cl_2)**	**1064 nm LOD, pM[a]**	**1280 nm LOD, pM[a]**	**Structure Type**
1 – **070**	653	0.7 ± 0.07	21.8 ± 1.9	Monomethine dyes
2 – **069**	676	0.8 ± 0.08	29.4 ± 2.7	
3 – **071**	699	0.7 ± 0.10	32.8 ± 2.4	
4 – **020**	676	1.0 ± 0.12	-	
5 – **067**	698	0.6 ± 0.05	5.4 ± 0.6	
6 – **162**	724	1.1 ± 0.16	-	
7 – **099**	659	0.6 ± 0.05	4.6 ± 0.5	
8 – **095**	687	0.5 ± 0.08	3.4 ± 0.2	
9 – **075**	806	0.6 ± 0.05	9.1 ± 0.7	Trimethine dyes
10 – **089**	784	0.3 ± 0.03	5.9 ± 0.3	
11 – **010**	810	0.3 ± 0.02	1.8 ± 0.2	
12 – **073**	789	0.3 ± 0.02	6.6 ± 0.6	
13 – **252**	813	0.2 ± 0.02	1.5 ± 0.1	
14 - **114**	826	0.1 ± 0.01	1.5 ± 0.1	
15 - **134**	748	1.0 ± 0.12	9.2 ± 0.6	
16 – **184**	959	4.6 ± 0.34 fM*	0.9 ± 0.1	Pentamethine dyes
17 - **198**	986	4.8 ± 0.37 fM*	0.9 ± 0.1	
18 - **AZPY**	Non-resonant	0.15 ± 0.02 nM*	-	Commercial reporters
19 – **BPE**	Non-resonant	0.19 ± 0.02 nM*	-	

[a] SERS - LOD ± s.d; *highlight femtomolar and nanomolar concentrations.

For the 1064 nm LOD studies, the pentamethine dyes 184 and 198 produced the best results with extremely low values of 4.6 ± 0.34 fM and 4.8 ± 0.37 fM, respectively. Trimethine dyes 075-134 had LODs from 0.1 to 1.0 pM, while the monomethine dyes 070-095 had LODs from 0.5 to 1.1 pM. However, the commercially available reporters gave the highest LOD values at 0.15 and 0.19 nM for AZPY and BPE respectively. These are 3-4 orders of magnitude higher than the pentamethine

chalcogen dyes, demonstrating further the superiority of these newly developed SERS nanotags for use in the NIR region.

When comparing the LODs at 1280 and 1064 nm, it can be observed that the commercial dyes produced the poorest LOD values, but it is important to note that although they didn't produce a SERS signal at 1280 nm, they did manage to obtain LOD values in the nanomolar range when a 1064 nm laser excitation was employed. Of all the chalcogen dyes, the monomethine substituents still produced the weakest SERS response at 1064 nm, but the 020 and 162 dyes were significantly better reporters at this wavelength although they still produced the highest LOD values of all the chalcogen dyes tested. The trimethine dyes which showed great promise with the 1280 nm laser excitation, also produced exceptionally low LOD values at 1064 nm, with all the nanotags producing LODs values <1.0 pM.

In general it can be seen that by moving from a laser excitation of 1280 nm to 1064 nm, there was a decrease in the LOD values of at least one order of magnitude. This is probably due to the increased scattering effect that occurs at shorter wavelengths.[6] Furthermore when the 1064 nm laser was employed, dyes 184 and 198 were relatively close to being on resonance, therefore, it is plausible that a small amount of resonance Raman scattering is contributing to their signals and thus may give another reason why they produce the most enhanced SE(R)RS spectra.

Additionally, it can be observed from table 3.2 and figure 3.14, that when the pentamethine dyes were analysed using a 1280 nm laser excitation they were exceptionally bright at this laser wavelength too. The particle dilution studies produced LOD values of 0.9 ± 0.1 pM, which was 1.5 times lower than the 114 and 252 dyes that previously produced the lowest LODs at 1280 nm laser excitation. The 1280 nm LOD plots for dyes 184, 198 and 134, can be observed in figure 3.13 but note as these studies were conducted after the initial 1280 nm SERS studies, the concentration range was from 2 nM to 4 pM.

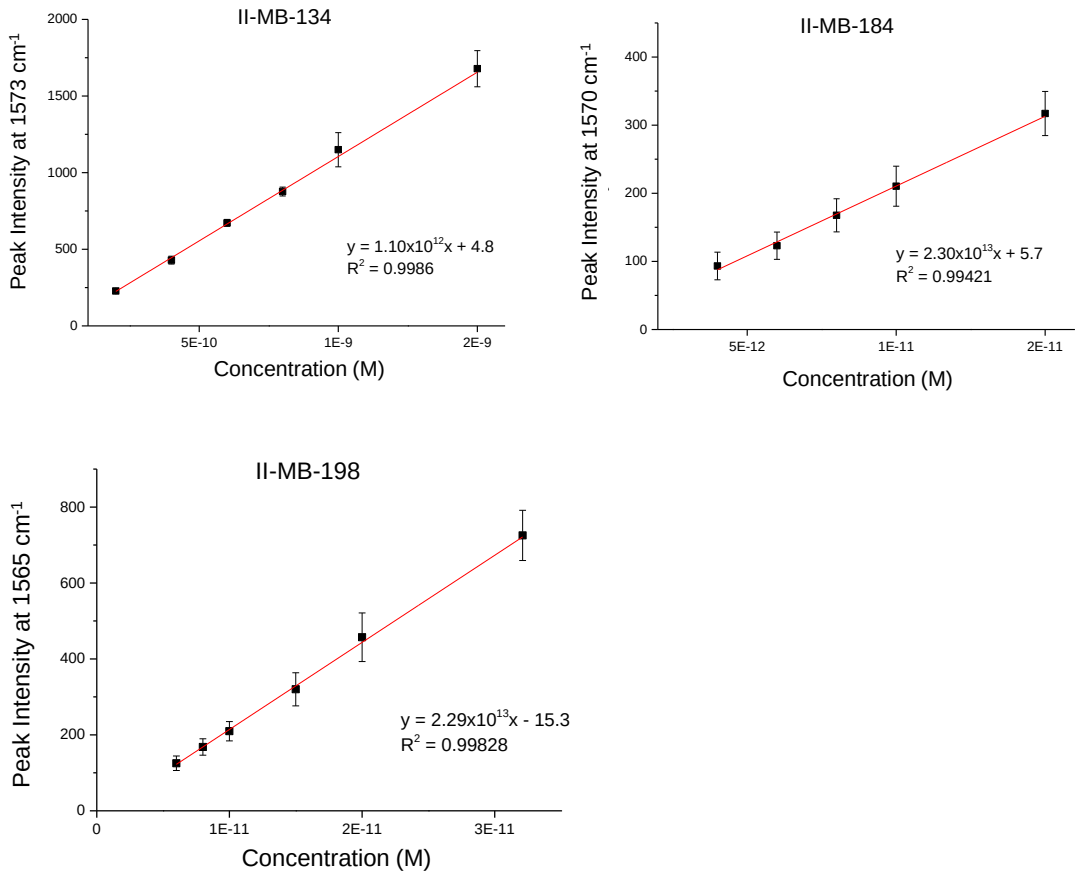

Figure 3.13 - SERS particle dilution studies for dyes 134, 184 and 198 with HGNs and KCl over the concentration range 2 nM to 4 pM. A laser excitation of 1280 nm and an exposure time of 7 seconds were employed in this analysis. Error bars represent one standard deviation resulting from 3 replicate samples and 5 scans of each.

3.4.2.2 Comparing SERS substrates for use with the Chalcogen dyes at 1064 and 1280 nm laser excitations

Cabot tags consist of AuNPs (~100 nm in size) encapsulated with the non-resonant reporter BPE and silica. Previously they have been reported to produce strong SERS signals with a 1550 nm laser excitation.[158] Therefore, it was important to understand if large AuNPs (80 or 100 nm in size; supplied by BBI solutions) plus chalcogen dyes could produce a SERS signal in the NIR region and thus compare their performance as SERS substrates to the HGNs using 1064 nm and/or 1280 nm laser excitations. Earlier results incorporated AuNPs of a comparable size to the HGNs and these were found to produce weaker SERS signals than the HGNs at both laser excitations of 1064 and 1280 nm. The importance of this study, however, lies with

the AuNPs being larger and therefore they will have a greater surface area for attracting and binding the Raman reporters onto. Their increased size should also cause the nanoparticles to scatter more efficiently, hence it was important to conduct these studies in order to determine the extent this increase in size has on the SERS response.

Figures 3.14 and 3.15 show the SERS spectra obtained when the three gold substrates were encapsulated with three different reporter molecules, dyes 114, 010 and 184 and excited at 1064 nm and 1280 nm respectively. In the spectra it appears that the HGNs produce the largest SERS enhancement, however, it is important to note that this was in fact not the case as the acquisition time for the 100 nm AuNPs had to be reduced due to the signal saturating the spectrometer when the same conditions as those previously attempted with the HGNs where employed.

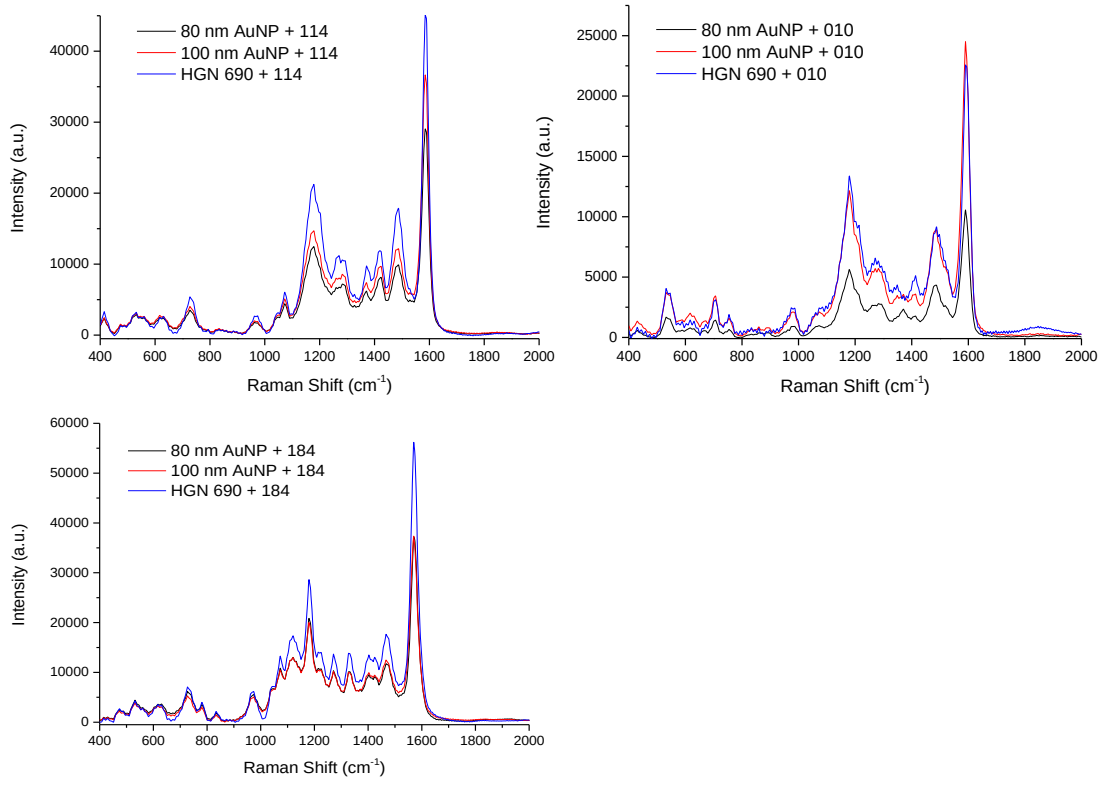

Figure 3.14 - 1064 nm SERS spectra comparing HGNs and large gold nanoparticles (80 and 100 nm) with dyes 114, 010 and 184 and aggregated with KCl. A laser excitation of 1064 nm and an exposure time of 0.1 seconds were employed in this analysis. The acquisition time for the 100 nm Au was reduced to 0.05 seconds as it saturated the spectrometer for dyes 114 and 184 using the conditions stated. All spectra have been background corrected.

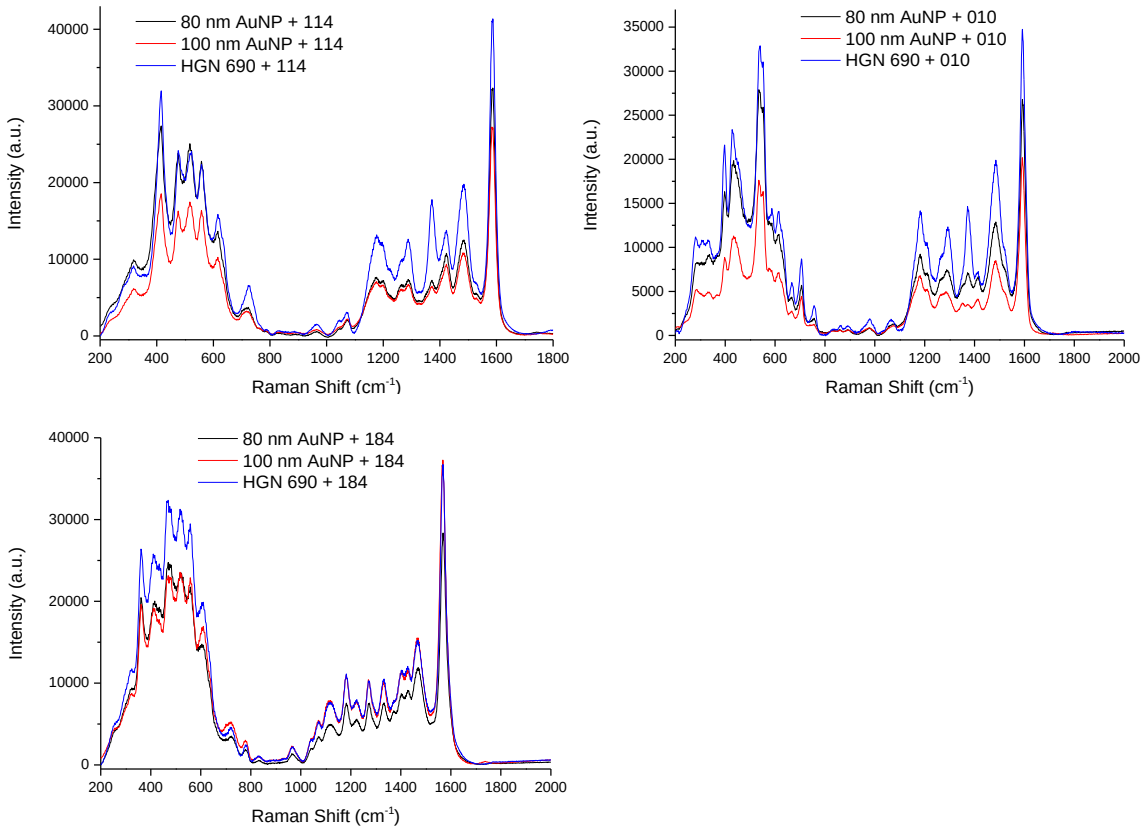

Figure 3.15 - 1280 nm SERS spectra comparing HGNs with large gold nanoparticles (80 and 100 nm) for dyes 114, 010 and 184 and aggregated with KCl. A laser excitation of 1280 nm and an exposure time of 3 seconds were employed in this analysis. The acquisition time for the 100 nm Au was reduced to 0.5 and 1 second as it saturated the spectrometer for dyes 184 and 114 respectively using the conditions stated. All spectra have been background corrected.

Taking into account the reduced exposure time of the 100 nm AuNPs, it was observed from both the 1064 and 1280 nm results that the 100 nm AuNPs produced the largest SERS response followed by the HGNs and then the 80 nm AuNPs. This suggests that the size of the gold nanoparticles does have an effect on the SERS enhancement, with the larger surface area allowing for more reporter molecules to bind to the nanoparticle surface and thus increase the SERS response. In addition, it is a well-known phenomenon in SERS that small aggregates will produce greater SERS enhancements due to creation of SERS 'hot-spots than single nanoparticles. Khan *et al*. reported that the 'SERS-active order for aggregates was as followed: aggregates of 10-20 nanoparticles > aggregates of 4-9 particles > trimers > dimers > single particles.[105, 181] Therefore, to fully understand why an increase in SERS signal

was observed for the 100 nm AuNP over the HGNs, it was important to undertake particle characterisation experiments such as extinction spectroscopy, DLS and zeta potential measurements. The results of this study can be seen in figure 3.16.

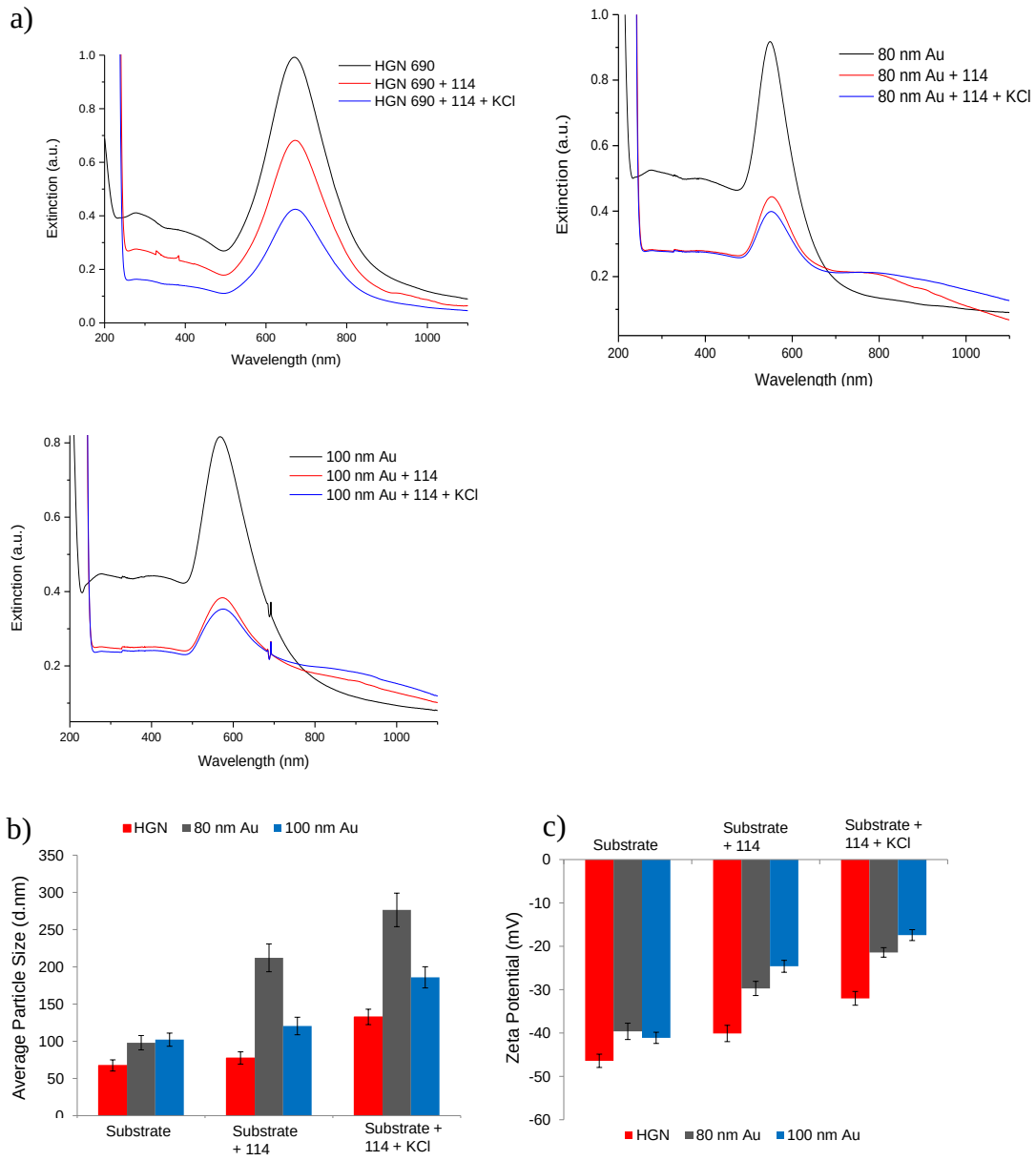

Figure 3.16 – a) Extinction, b) DLS and c) zeta potential data for determining how the substrates react to controlled aggregation, caused when 10 µM dye 114 and 30 mM KCl salt were added to nanoparticle solutions. In the extinction spectra black line highlights the nanoparticle only spectrum; red line is nanoparticles plus the reporter molecule 114 and the blue line is nanoparticles plus dye 114 and KCl salt. For the DLS and zeta potential measurements; the red bar indicates HGNs, grey bar is the 80 nm AuNPs and the blue represents the 100 nm AuNPs.

As previously shown the HGNs aggregate under these experimental conditions, with a slight damping of the absorption maximum at 690 nm but there was no shift or broadening of the peak to indicate that the nanoparticles were being over-aggregated. The stability of the HGNs was also demonstrated through the DLS and zeta potential measurements, with a slight increase in the size of the nanoparticles indicating aggregation with the likelihood of dimers being formed. In addition, there was a slight decrease in the zeta potential values, however, even when KCl was added, the HGNs had a zeta potential value greater than -30 mV indicating the colloidal solution was stable.[127]

Both the 80 and 100 nm AuNPs displayed a red-shift in their LSPRs from 520 nm indicative of standard gold nanoparticles to 548 and 569 nm respectively. When a shift in the LSPR is observed it is indicative of a change in size, shape and/or aggregation.[182] As the nanoparticles were larger in size than the standard AuNPs it was expected that they would have a red-shift in their LSPR, and it should be noted that the larger the nanoparticles are the more red-shifted the LSPRs will be, as observed in the extinction spectra with the 100 nm AuNPs being further into the visible region than the 80 nm AuNPs.

Furthermore, it can be observed for both substrates that when the Raman reporter was added there was a large damping of the extinction maxima with a slight shift of ~7 nm, but more importantly a secondary peak was starting to form at ~950 nm. This was further observed after the addition of salt and thus indicates that these samples are aggregating. There was also an increase in the particle sizes, especially for the 80 nm AuNPs, where a value greater than 250 nm was obtained after the addition of reporter and salt, thus indicating that these nanoparticles are forming aggregates with trimers being the smallest size of aggregate likely to be formed. This aggregation effect was also observed in the zeta potential measurements with values decreasing from -39.4 to -21.4 mV indicating that after the addition of KCl the 80 nm colloidal solution was becoming unstable and over-aggregating, this was likely to be due to the range of aggregates forming in suspension.

Similar results were observed for the 100 nm AuNPs with the zeta potential measurements indicating that this was the most unstable colloidal solution with

values decreasing from -41.1 to -17.4 mV after the addition of dye 114 and KCl. However, the DLS data contradicts this with it showing that the average particle size of the nanoparticles, increased by ~70 nm as would be expected with controlled aggregation due to the formation of small aggregates such as dimers. The size increase and development of aggregates is likely to be responsible for the increase in SERS response observed in figures 3.14 and 3.15. However, the variability in size and shape of aggregates forming could be responsible for the decrease in zeta potential values observed in figure 3.16c.[181]

Therefore, it is likely that the increase in SERS signals observed for the 100 nm AuNPs over the HGNs was due to an increase in SERS enhancement made possible with the larger size allowing for a greater number of reporter molecules to bind.

3.4.3 1550 nm SERS Nanotags

The 1064 nm investigations have further shown that these chalcogen dyes are far superior Raman reporters than the commercially available ones BPE and AZPY which are commonly used in NIR SERS studies. It was also shown that large AuNPs are capable of providing effective SERS at both 1064 and 1280 nm laser excitations, when the chalcogen dyes and KCl were added to the colloidal solutions. Therefore the range of SERS substrates for using with these extreme red-shifted laser excitations has widened and thus, isn't solely limited to HGNs.

When DSTL made available a 1550 nm FT-Raman spectrometer, it was important to carry out preliminary studies in order to determine if these substrates when encapsulated with a chalcogen dye, were capable of producing a SERS spectrum at the eye-safe laser excitation of 1550 nm.[158] In this study, the chalcogen dye 184 was chosen as the reporter molecule of choice as it previously provided the best SERS response with both 1064 and 1280 nm laser excitations. Also, only the 100 nm AuNPs were chosen to compare with the HGNs as these were shown to be better than the 80 nm AuNPs in the previous section. It should be noted, however, that when the previous conditions were attempted a SERS spectrum at 1550 nm was not obtained. This was due to the reduced brightness and concentration of the colloidal solutions. In addition, when the HGN concentration was altered to match that of the

100 nm AuNPs, a SERS spectrum was still not produced. In order to obtain a 1550 nm SERS spectrum, the HGN concentration had to be increased to 6 nM and the 100 nm AuNPs had to be used as supplied by BBI solutions (3.73 nM and OD at 30 a.u.), the results can be seen in figure 3.17.

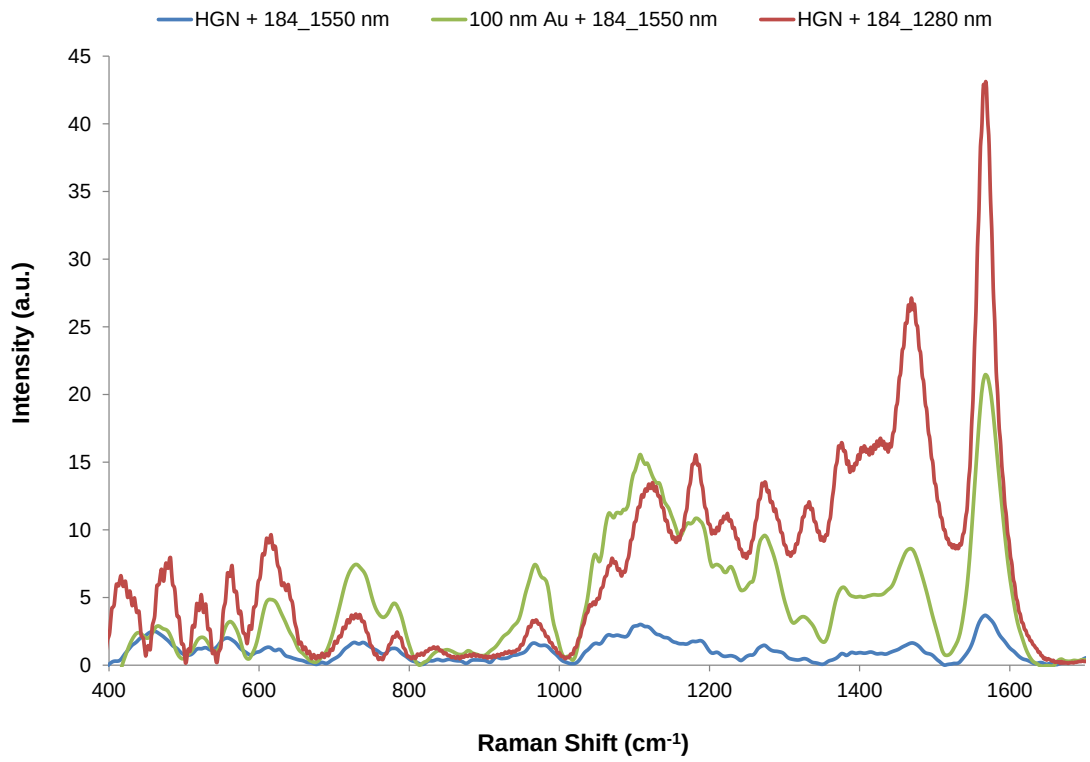

Figure 3.17 - SERS spectra for dye 184 with two SERS substrates plus KCl using a laser excitation at 1550 nm. The blue line represents dye 184 plus HGNs, the green line represents dye 184 plus 100 nm AuNPs and the red line is the 1280 nm SERS spectrum for dye 184 plus HGNs as a comparison. It should be noted that the y-axis has been scaled to enable this comparison. A laser excitation of 1550 nm and an exposure time of 10 seconds were employed in this analysis. All spectra have been background corrected.

The 1280 nm SERS spectrum for dye 184 and HGNs has been incorporated into figure 3.17 for comparison. The most notable observation is that the 100 nm AuNPs produced a far more intense spectrum than the HGNs and as previously mentioned in section 3.4.4.2, this is likely to be due to the increased size of the AuNPs allowing more reporters to bind effectively the their surface. The 1550 nm peaks are not as well resolved as the 1280 nm spectrum; however there are some noticeable spectral differences such as slight peak shifts and band enhancements. These will be

discussed in the next section (3.4.5) where the binding and orientation of dye 114 is examined in great detail across a range of laser wavelengths.

It is important to note, that after about 15 minutes of completing these experiments the nanotags started to precipitate out of solution with the colloidal solutions turning colourless. This was indicative that the nanoparticles had over-aggregated and it was likely to be due to the increase in concentration of the nanoparticle solution, not being able to withstand aggregation by addition of salt. Therefore, before further studies could be conducted this problem had to be overcome.

Previously in the 1280 nm SERS studies, it was shown that dyes 114 and 252 cause the HGNs to self-aggregate and this was also found to be true for dyes 198 and 184. All these dyes were able to produce intense SERS spectra without the addition of salt using both 1064 and 1280 nm laser excitations (for both HGN and 100 nm AuNP colloidal solutions). It should be noted that the signals were further enhanced when the particle concentration of the colloidal solutions were increased. This self-aggregation caused by the chalcogen dye was sufficient to increase the SERS response and solve the problem of over-aggregation, with the colloidal solutions remaining stable for several weeks.

As previously mentioned, Cabot tags which consist of 100 nm AuNPs encapsulated with silica and the Raman reporter BPE, have previously been reported to produce strong SERS signals with a 1550 nm laser excitation.[158] Therefore, it made for a very interesting investigation to compare these Cabot tags with the newly developed 'chalcogen' tags using the eye-safe laser excitation of 1550 nm. In these studies, the chalcogen dyes 184 and 198, where chosen as the reporter molecules of choice as they provided femtomolar and picomolar detection limits with HGNs at 1064 and 1280 nm excitations respectively and the 184 dye showed very promising results in the preliminary 1550 nm SERS study. Furthermore, only the 100 nm AuNPs were used in this experiment due to the 4-fold increase in SERS intensity over the HGNs in the preliminary study. Both the 100 nm AuNPs and Cabot tags had ODs at 30 a.u. however for further studies to be conducted such as limit of detection investigations the exact concentrations had to be determined and corrected using the Nanosight and this was conducted before any of the SERS experiments were carried out. The results

from the initial SERS comparison study between Cabot tags and 100 nm AuNPs encapsulated with dyes 184 and 198 can be observed in figure 3.18. In these studies no inorganic salt was used to induce aggregation; it was solely due to the reporter concentration being 10 µM. Thus having approximately monolayer coverage was sufficient to force effective packing of the reporter on the nanoparticle surface and encourage a strong interaction with the AuNPs which ultimately resulted in strong SERS signals being observed.

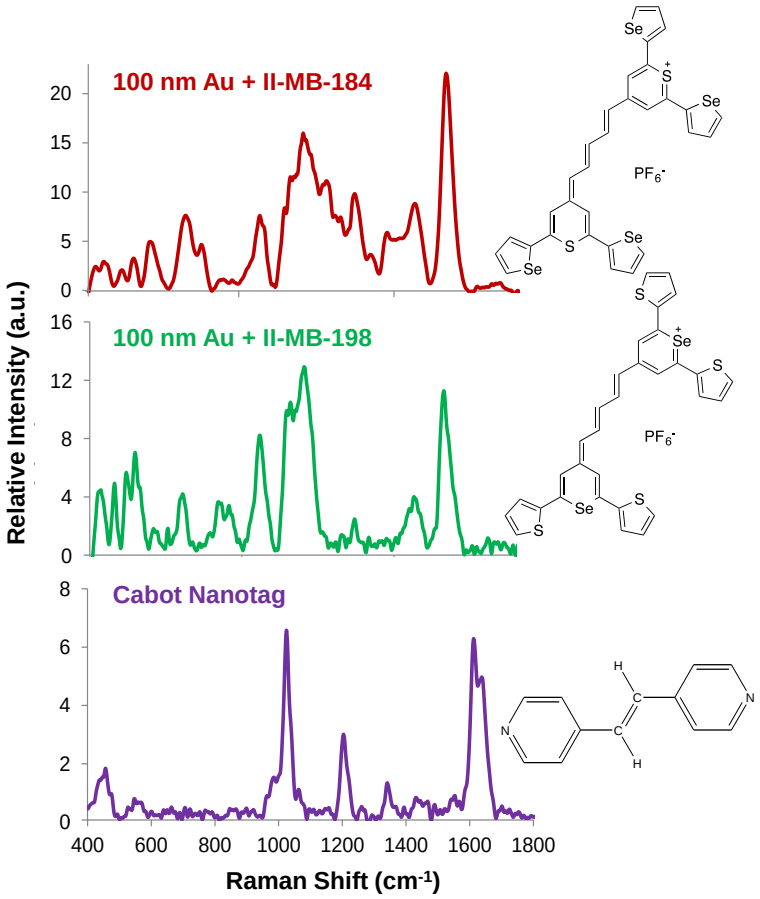

Figure 3.18 – SERS comparison study between Cabot tags and 100 nm AuNPs encapsulated with dyes 184 and 198 (10 µM) using a laser excitation at 1550 nm. A laser excitation of 1550 nm and an exposure time of 10 seconds were employed in this analysis. All spectra have been background corrected. Figure has been reproduced by permission of the Royal Society of Chemistry.

It can be observed in figure 3.18 that all three ‘nanotags’ produce intense SERS spectra with the 1550 nm laser excitation. The ‘184 chalcogen tags’ however

produced the most intense SERS response followed by the '198 chalcogen tags' and then the Cabot tags. When comparing the most intense peak at ~1600 cm^{-1} the 184 chalcogen tags had an increase of ~3 times that of the Cabot tags while the 198 chalcogen tags were twice as intense. Building on this study, it was important to determine the limit of detections for these nanotags through particle dilution studies and the results can be seen in figure 3.19. It should be noted however, that the reported concentrations for the chalcogen nanotags are for non-aggregated systems based on the particle concentration of AuNPs and as such the nanotag concentrations reported will be different due to aggregation occurring. Moreover, the concentrations reported for the Cabot tag is for the aggregated system and will be more accurate.

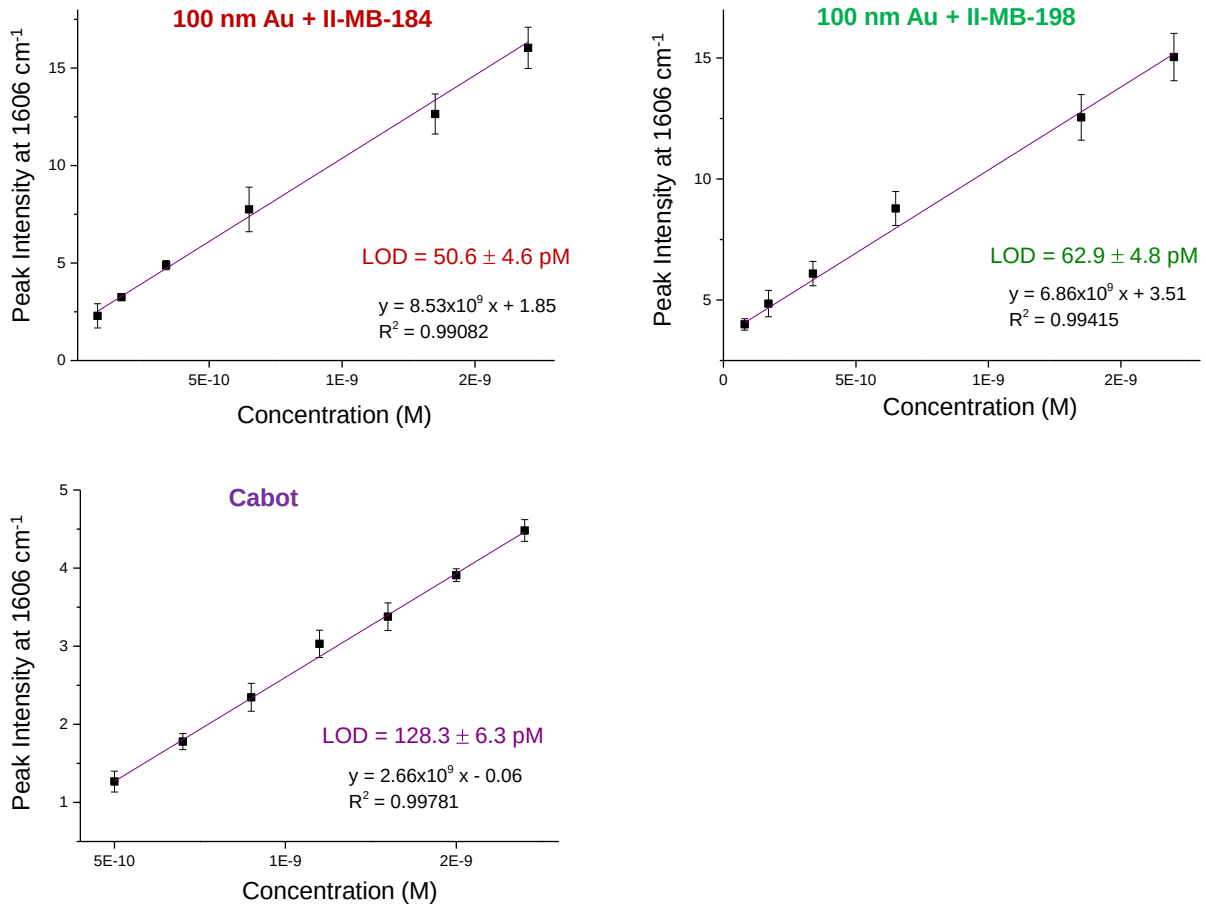

Figure 3.19 - SERS particle dilution studies for dyes 184, 198 with 100 nm AuNPs and Cabot tags over the concentration range 1.7 nM to 0.08 nM. A laser excitation of 1550 nm and an exposure time of 10 seconds were employed in this analysis. Error bars represent one standard deviation resulting from 3 replicate samples and 5 scans of each. Figure has been reproduced by permission of the Royal Society of Chemistry.

For the 1550 nm LOD studies, the pentamethine dyes 184 and 198 produced the best results with extremely low values of 50.6 ± 4.6 pM and 62.9 ± 4.8 pM, respectively. The commercially available Cabot tags gave the highest LOD value at 128.3 ± 6.3 pM. This value was approximately 2-2.5 times greater than the pentamethine chalcogen dyes, demonstrating further the superiority of these newly developed SERS nanotags for use in the NIR region. As previously mentioned, obtaining SERS signals in the NIR region is extremely difficult but obtaining SERS signals with pM detection limits at 1550 nm was an unexpected and yet extraordinary result at this wavelength, especially without the need for an aggregating agent.

Again, for a full comparison and better understanding of these nanotags the colloidal solutions were characterised by extinction spectroscopy, DLS and zeta potential measurements and the results can be observed in figure 3.20.

The Cabot tags were shown to have a very broad extinction spectrum with a maximum observed at 598 nm. The tail however, observed with these tags appears to increase again beyond 800 nm and continues to increase up to 1100 nm which was the upper limit for the wavelength range of the instrument employed. The very broad spectrum which is observed for the Cabot tags suggests that these nanotags are of a range of shapes and sizes.[182] This is further confirmed with the average particle size being 309.7 nm, however, it should be noted that these nanotags are very stable in solution with a zeta potential value of -40.2 mV. The extra stability is likely to come from the silica layer being present. The Cabot tags are commercially available and highly stable colloidal solutions; however, as observed in the extinction spectra and DLS data, these nanoparticles are of a range of sizes and shapes. It is very likely that a range of cluster sizes are present in the solution from dimers and trimers to small aggregates and possibly even large clusters which would explain the variability in these results but also explain why they are able to produce strong SERS signals with a 1550 nm laser excitation.

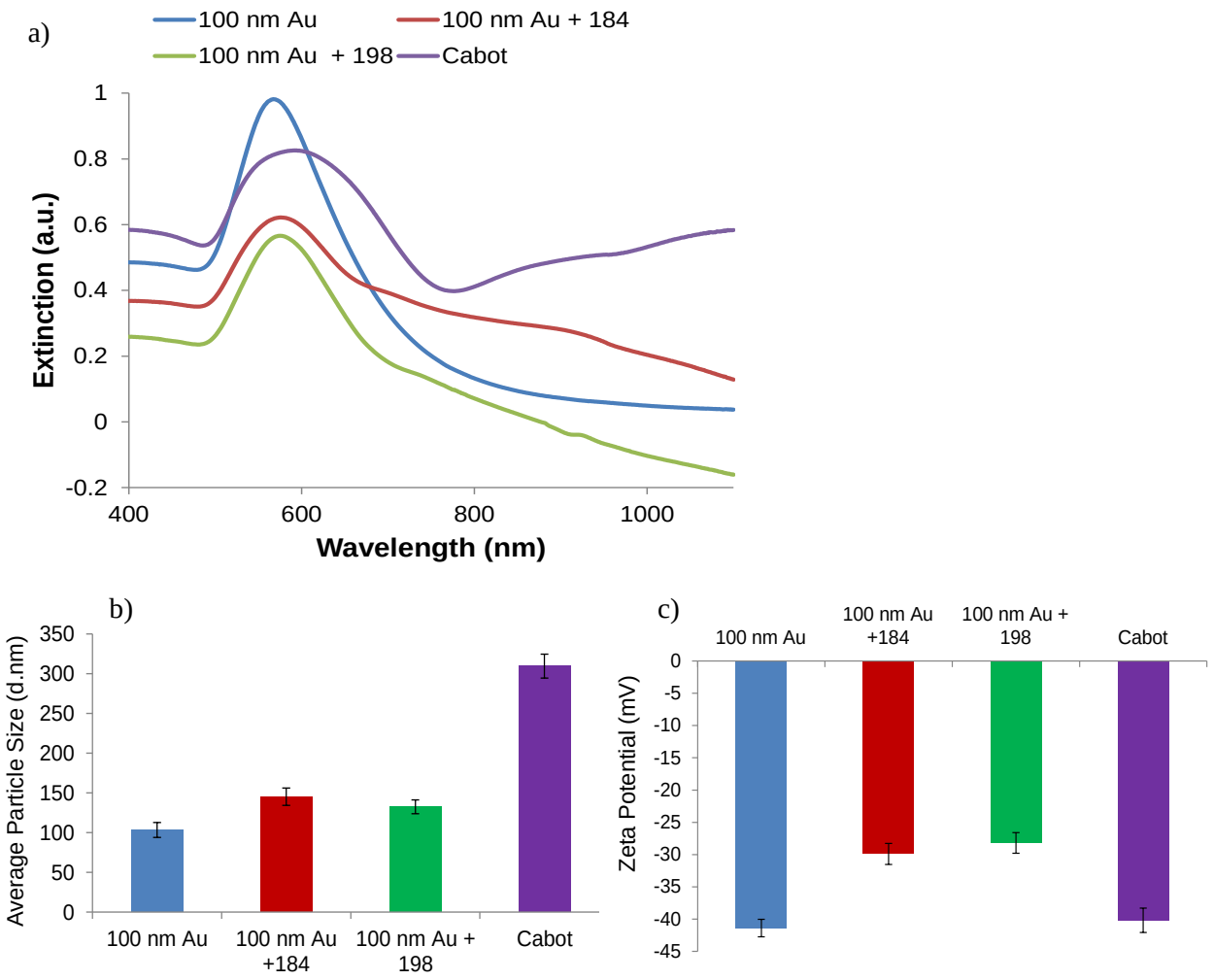

Figure 3.20 –Characterisation of nanotags with figures a) displaying the extinction spectra, b) and c) are the average particle size and zeta potential, respectively for the range of nanotags tested. Dyes 184 and 198 had a concentration of 10 µM.

The results obtained for the 100 nm AuNPs were very similar to those previously observed in section 3.4.2.2. Where encapsulating 100 nm AuNPs with a chalcogen dye causes not only significant damping in the absorption maxima at 569 nm, with a slight red-shift of ~7 nm but also a very broad tail well into the NIR region was observed. Indicating aggregation is occurring as would be expected due to the self-aggregation induced by these dyes on the 100 nm AuNPs. Furthermore, there is a slight increase in the particle size but not a massive increase as previously shown when the nanotags over-aggregate. The two colloidal solutions are said to be stable after the addition of the reporter molecules with values in the region of -30 mV.[127] Therefore by removing the aggregating agent and increasing the concentration and

brightness of the nanoparticles it had a very beneficial outcome for the nanotags, in terms of the overall colloidal stability and their ability to produce strong SERS signals at the 1550 nm laser excitation.

Moreover, these nanotags have yet again proven to be better than any commercially available ones and thus could provide the necessary components for future advancements in biomedical and optical applications.

3.4.4 Determination of the orientation and bonding of dye 114 to HGNs

Previous work in this chapter has shown the great optical benefits of these newly synthesised chalcogen dyes. In particular their superior SERS signals and detection limits over commercially available reporters and nanotags. However, what would make this research very valuable in terms of designing future nanotags is to understand how these reporter molecules bond and orientate on the surface of gold nanoparticles. In this study, hollow gold nanoshells were used as the SERS substrate, with dye 114 being used as the Raman reporter and the spectra assigned by comparing the SERS spectra obtained with resonance Raman spectra and theoretical Raman calculations. The SE(R)RS spectra were obtained across a range of wavelengths from 633 nm to 1280 nm, while the resonance Raman spectra were obtained across the excitation wavelengths 514 to 785 nm. The Raman spectra at the higher wavelengths of 1064 and 1280 nm couldn't be obtained due to the experimental set-ups for these instruments requiring a large sample volume (~100 mg).

Two distinct types of SE(R)RS spectra were obtained. The first due to the excitation being close to resonance, both the near infrared electronic transition in the dye (max 826 nm) and the plasmon resonance maximum of the HGNs (690 nm), SERRS spectra were obtained and the spectra was similar to the resonance Raman spectrum. The second with 1064 and 1280 nm excitations, with little or no molecular resonance contribution gave rise to SERS spectra and new bands were observed in these spectra. To fully understand how this molecule bonds and orientates on the HGN surface, it is essential to first look at the structure and electronic structure of the

Raman reporter and the HGNs which make up these SERS nanotags. Then go onto look at the bands which arise in the resonance Raman spectra before comparing them with the SERS spectra obtained. It should be noted that Ivan Ramos-Sasselli conducted all the theoretical calculations detailed in this section.

3.4.4.1 Molecular Structure and Electronic Structure

The molecular structure for dye 114 can be seen in figure 3.21 and with the 4 rings orientated as shown it essentially means the molecule is flat with some out of plane twisting. The green lines represent the angles and these indicate the degree of the twist. Se ring 1 shows the largest out of plane rotation with an angle of 7.37 degrees. Furthermore, due to the orientation of the rings and in particular rings Se2 and Se3, there is 2.5-7 % disorder in the structure. The calculation of the barriers to rotation of the rings shows that this disorder is very small at ~4 kcal (see figure 3.21b) and consequently when this dye is in solution or attached to the HGN surface the orientation of the rings will depend on other forces such as those created by bonding and packing.

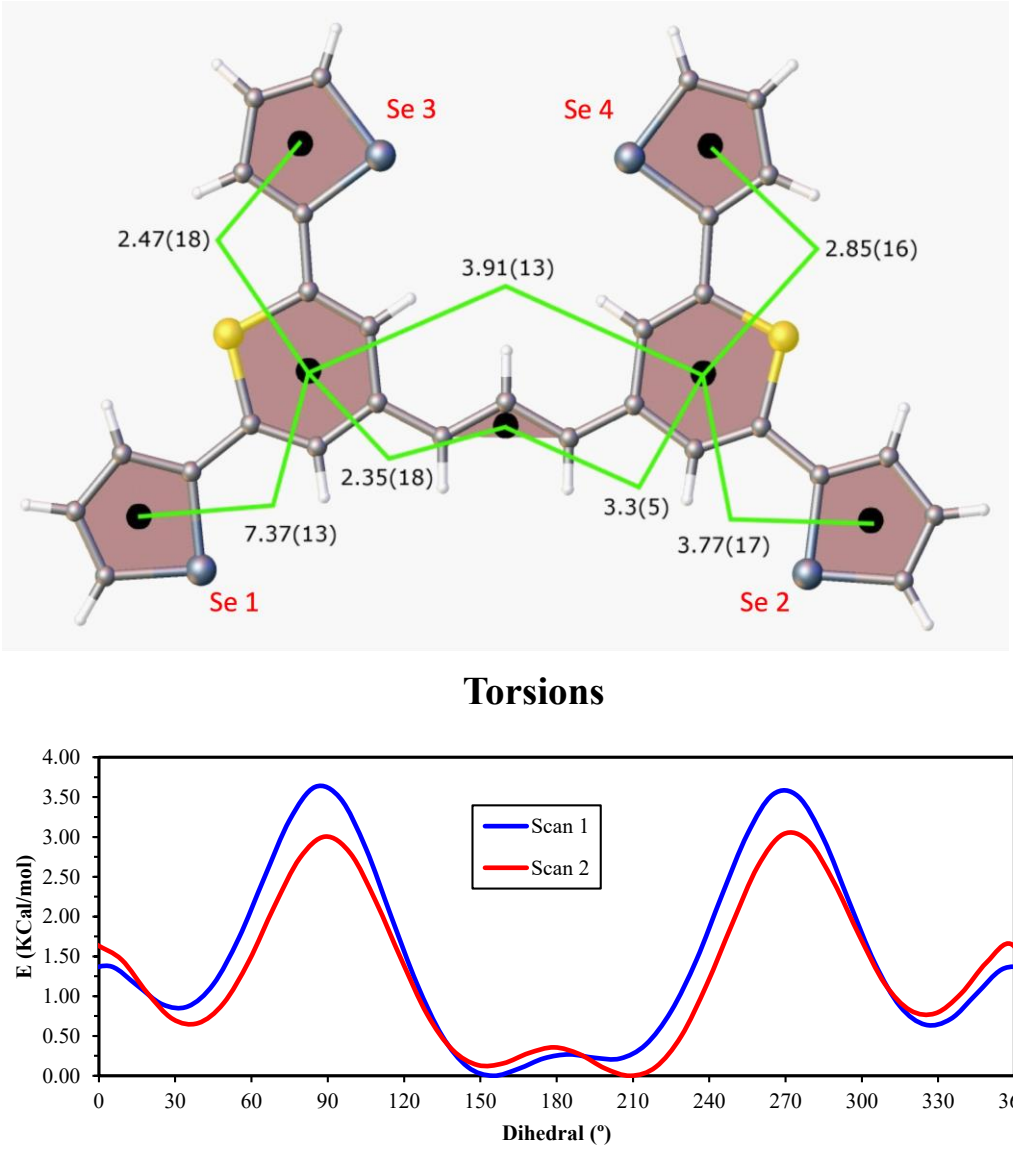

Figure 3.21 – a) Molecular structure of dye 114 with ring numbers and showing the torsion angles. b) Torsion angles demonstrating the barriers to rotation of the rings is ~4 kcal. Scan 1 = Se - C - C – S; scan 2 = Se - C - C –S.

Figure 3.22 shows the electronic structure of dye 114 with an absorption maximum at 826 nm. This band arises due to a π to π^* transition with the electron density mostly on the thiopyrylium core (figure 3.22b). The additional peaks observed in the electronic spectrum are likely to be due to vibronic structure. The HGNs used in this study where from the same batch as those utilised in the comparison study between HGNs and BBI's large AuNPs. Therefore, the extinction spectrum for this dye and the effect of salt addition can be seen in figure 3.16. Briefly, the HGNs had an extinction maximum at 690 nm, with a tail into the NIR. Partial aggregation was

observed with a damping of the extinction maximum but there was no broadening or shifting of the peak maximum. Extinction spectra for several other chalcogenopyrylium dyes can be seen in appendix III.

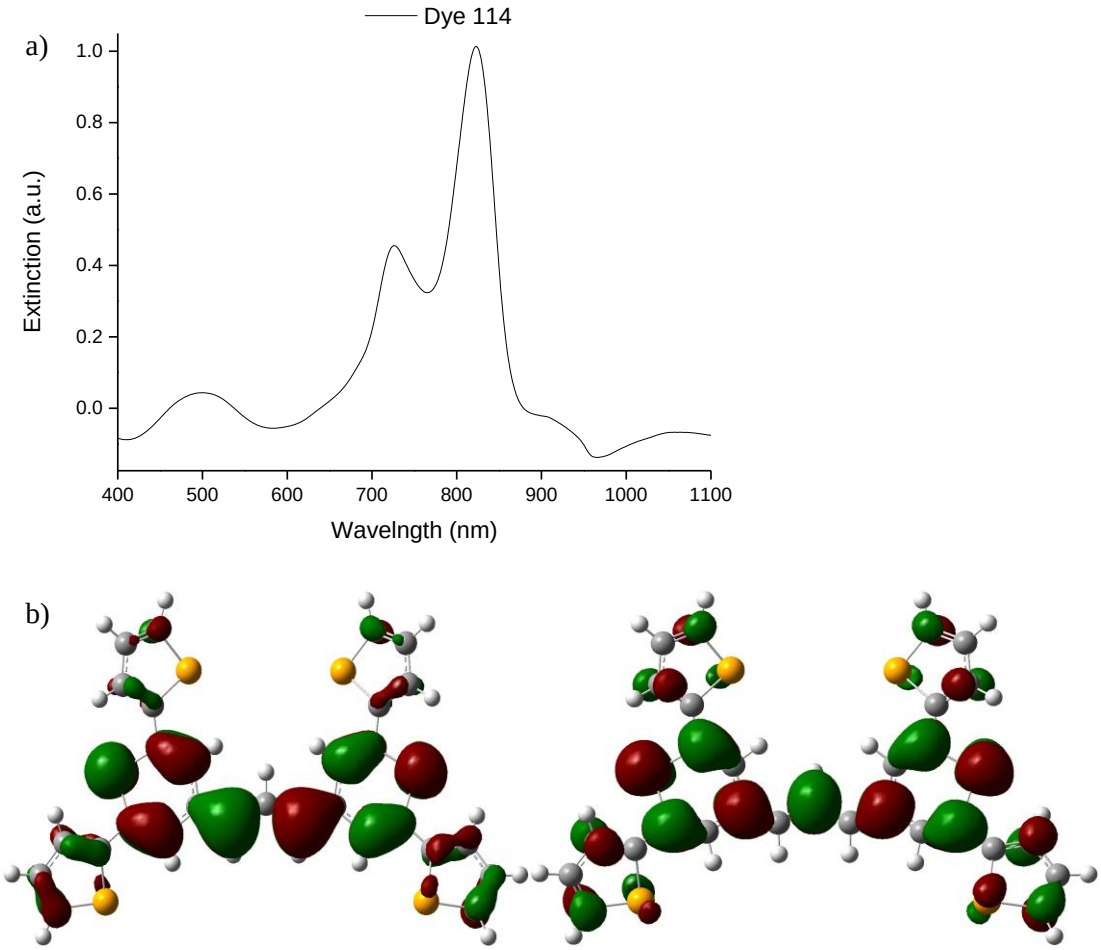

Figure 3.22 - a) Extinction spectrum for dye 114 obtained at a concentration of 10 µM (solvent used for baseline correction was 1:1 ratio of DMF to d.H_20). b) Electron density of the π (left) and π^* (right) orbitals which gave rise the 826 nm band observed in figure a).

3.4.4.2 Resonance Raman Scattering

Raman scattering was recorded using 514, 633 and 785 nm laser excitations and the spectra obtained were all resonant (figure 3.23). There was evidence of selective enhancement, with no dependence of intensity on the 4^{th} power of the frequency as the 785 nm excitation produced the most intense spectrum. This was further confirmed when the data was normalised to the cyclohexane standard and the peak at ~1590 cm^{-1} was twice as intense in the 785 nm spectrum than in the 633 nm

spectrum; as would be expected for resonance or pre-resonance when the electronic transition has an absorption maximum at 826 nm.

The 514 nm spectrum is significantly weaker and gives a different enhancement pattern. This is because at this wavelength the dye is resonant due to another transition which can be observed at ~500 nm in the extinction spectrum of the dye, figure 3.22a. Typically SERS from Au substrates using 514 nm excitation is weak;[6] hence the 514 nm resonance spectrum has only been considered as it affects the 633 and 785 nm spectra. The band at 1425 cm^{-1} appears as a doublet in the 633 nm spectrum and is relatively more enhanced than in the 785 nm spectrum. The band at 1422 cm^{-1} is strongly enhanced in the 514 nm spectrum with the theoretical Raman spectrum predicting two bands and a shoulder in this region (for clarity see figure 3.28). Since the spectra taken with 785 nm and 514 nm excitations give peaks at slightly different frequencies, it is plausible that the doublet observed in the 633 nm spectrum is due to pre-resonance enhancement of two closely spaced bands, each of which are enhanced due to different transitions.

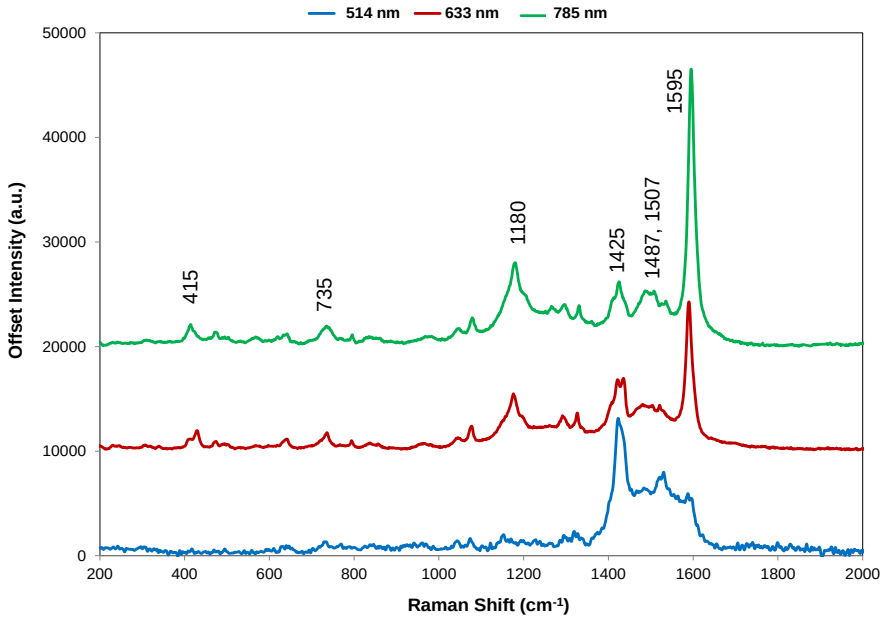

Figure 3.23 - Resonance Raman spectra at three excitation wavelengths. The 514 nm spectrum is multiplied by a factor of 10 for clarity. In this analysis, the 514 nm spectrum was acquired with a 10 second acquisition time while the 633 and 785 nm spectra were acquired with an exposure time of 25 seconds. . The 785-nm Raman bands which are discussed throughout have been labeled accordingly. All spectra have been background corrected.

3.4.4.3 Assignment of the Raman spectra

In the theoretical Raman spectrum the highest energy and most intense peak observed at 1588 cm^{-1} was originally calculated to appear at 1640 cm^{-1}. Therefore a correction factor was applied to the calculation to fit these two peaks. Correction factors are commonly applied to gas phase calculations which are based on Raman scattering from isolated molecules and they enable a better match with experimental samples, such as crystals or solutions which give rise to resonance Raman or SE(R)RS. A comparison between the 785 nm experimental Raman spectrum and the corrected calculation can be seen in figure 3.24 with the main displacements of the bands observed in the resonance and SERS spectra being given in table 3.3.

In both the theoretical and experimental spectra (obtained with 785 nm excitation), three intense bands were observed at 1595 (1588), 1425 (1416) and 1180 (1155) cm^{-1} (the theoretical values are in brackets). The most intense band at 1595 cm^{-1} arises due to vibrations in the sulfur rings and these displacements can be seen in figure 3.24, where the extreme positions have been highlighted with blue arrows for clarification. The major displacements which give rise to this peak are due to quadrant ring stretches in the sulfur ring and stretching along the backbone of the molecule. Neglecting symmetry, intense resonance is expected where there is significant electron density and the vibrational displacements take the ground electronic state geometry into the excited state geometry so that there is electronic overlap at all positions of the displacement.[6, 183] This is what happens here, hence this vibration is intense. The bands which occur at 1425 and 1180 cm^{-1} are associated with vibrations along the major axis in particular displacements in the bridge and sulfur rings extending out to the Se rings. The 1425 cm^{-1} mode has particular displacements associated with Se rings 1 and 2, whereas the 1180 cm^{-1} mode has displacements in Se rings 3 and 4. In the experimental spectrum however, there is evidence of structure causing broadening of the bands particularly with the 1180 cm^{-1} mode, but it should be noted this was not observed with the 1595 cm^{-1} band where most of the displacements were on the pyrillium core. To a large extent the theoretical calculation pairs the Se rings together, but the environment in the crystal is not entirely the same for each ring and this and the disorder may account for the

additional structure in the practical spectra of the 1425 and 1180 cm^{-1} modes. The effect of ring orientation is examined in section 3.4.4.4.

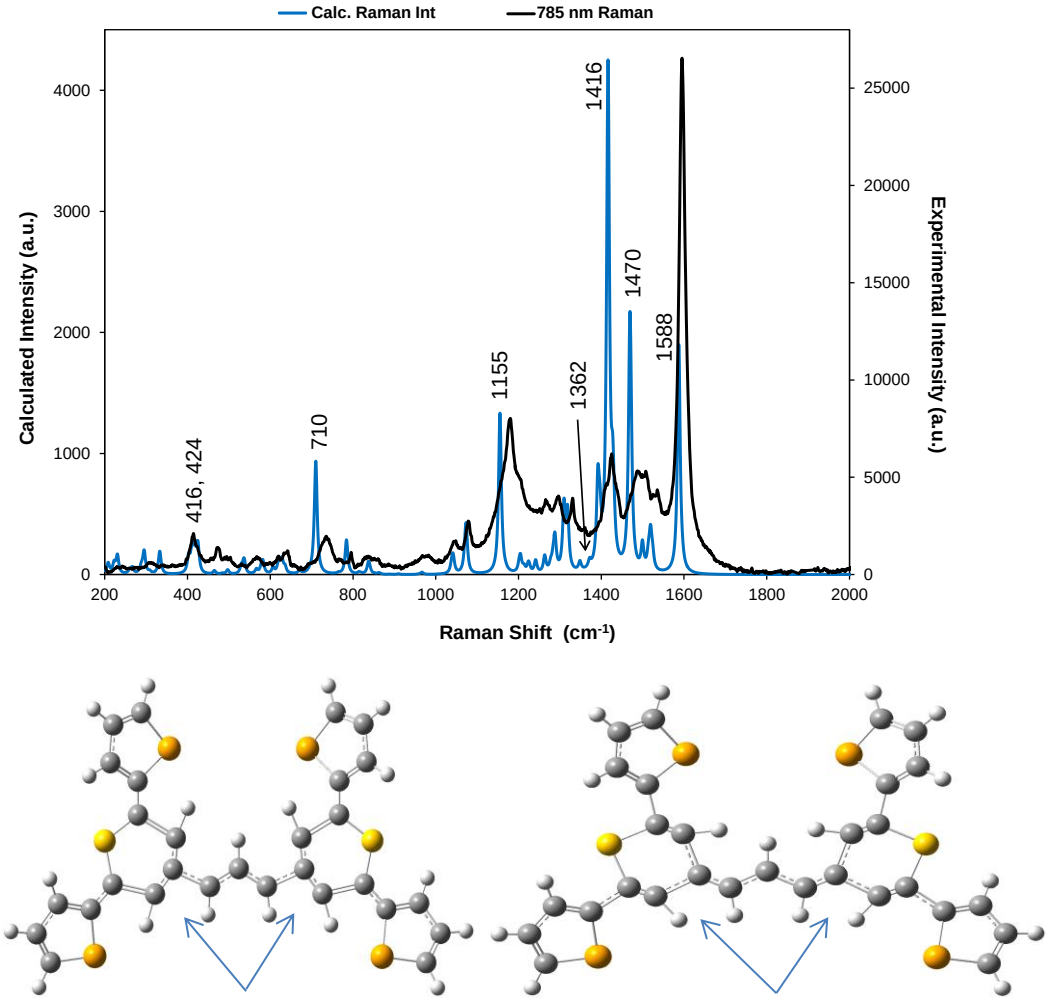

Figure 3.24 - Comparison of the 785 nm resonance spectrum with the corrected theoretical spectrum and displacement diagrams for the 1588 cm^{-1} vibration. The blue arrows point to where the largest displacements are occurring. In this analysis, the 785 nm experimental Raman spectrum was acquired with a 25 second acquisition time while the theoretical spectrum was calculated using Gaussian 09 software. The 785 nm Raman spectrum has been background corrected. The predicted Raman bands which are discussed throughout are labeled accordingly but for all band positions and assignments see Table 3.3.

The intense peak observed at 1470 cm^{-1} in the theoretical spectrum which arises due to some bridge displacement and movement in the S and Se rings appears weak in resonance. The displacements when examined in the Gaussian 09 software showed that the bridge displacements were less intense than the 1595 cm^{-1} vibrations and

they didn't occur along the major axis. Therefore, it is unlikely that the photons take the ground state to the excited state efficiently and as such is weak in resonance. However there will be a polarisation change with displacement which will be SERS active.

Table 3.3 - Assignment of main bands in the resonance and SERS spectra using the corrected calculation.

Comp Raman	**Expt Raman 785 nm**	**SERS FT-1064 nm**	**SERS 1280 nm**	**Assignments for Dye 114**
416; 424 (doublet)	415 (br) 428;410 (sh)-633 nm	415	416	416 – Out of plane rocking movement on bridge with extension to Se rings 3 & 4 424 - Stretch of S rings (C-S), (C=C), (C-H) with rocking movement on bridge (C=C), (C-H)
464; 486 (sh) (w)	472	479	478	Stretch of S rings (C-S), (C=C), (C-H) and all four Se rings (C-Se), (C=C), (C-H) (486– Se rings 1 & 2)
497; 536 (w)	500 (633 nm - w)	527	523	Elongation of all four Se rings (C-Se), (C=C), (C-H) with bending of S rings (C-S), (C=C), (C-H) – out of plane (497 – Se rings 3 & 4)
581	568	565	559	Rocking movement on bridge (C=C), (C-H) - out of plane
607 (w)	619	620	616	Extended vibration in core (C=C), (C-H) with elongation in S rings (C-S), (C=C), (C-H)
628	642	636	638 (sh)	Rocking movement on Se rings 1 & 3 (C-Se), (C=C), (C-H)
710	735	732	728	S ring breathing mode (C-S), (C=C), (C-H); extended to Se rings (C-Se), (C=C), (C-H)
969 (w)	965 (633 nm - w)	971	965	Se rings (C-H), (C=C)
1041	1044	1044	1044	Se rings 3 & 4 (C-Se), (C=C), (C-H)

1073	1078	1073	1071	(C-H) bending in Se rings with rocking movement throughout bridge, core (C=C), (C-H) and Se rings (C=C)
1155; 1204	1180 (br)	1179 (br) 1223 (sh)	1177 (br) 1200 (sh)	Core (C=C), (C-H) with extension through bridge (C=C) into Se rings (C-Se), (C=C), (C-H)
1263; 1288	1246 1297	1287	1265 (sh) 1288	Bridge (C=C) to Se rings 2 & 4 with less movement in Se 1 (C-Se), (C=C), (C-H)
1362 (w)	1360 (w)	1370	1372	Core (C=C), (C-H) with extension through bridge (C=C) into Se rings 3 & 4 (C-Se), (C-H)
1416	1425; 1417 (sh)	1425	1423	Se ring (C-Se), (C=C), (C-H) to S ring movement (C-S), (C=C), (C-H) (mainly Se 1 & 2) and core (C=C)
1470;	1487	1489	1485	Core (C=C), (C-H) and S rings (C-S), (C=C), (C-H) with extension to Se rings (C-Se), (C=C), (C-H)
1500; 1518	1507; 1535	1530 (sh)	1526 (w)	Core (C=C), (C-H) and Se rings (C-Se), (C=C), (C-H) (1518 – Se rings 3 & 4; 1500 – Se rings 1 & 2)
1588	1595	1588	1587	Core (C=C), (C-H) and S rings (C-S), (C=C), (C-H)

sh=shoulder; br=broad; w=weak

For an easy comparison the low frequency bands will be discussed based on figure 3.25, where the x and y-axis have been scaled in order to observe the spectra more clearly. However, it must be borne in mind that in reality the 785 nm Raman spectrum is twice as intense as the 633 nm. The peaks which occur at 1078 and 1044 cm^{-1} arise from displacements in the Se rings with some vibrations along the pyrillium backbone, see figure 3.25. The band at 735 cm^{-1} occurs due to breathing in sulfur ring and the broad band observed at 415 cm^{-1} (416 and 424 cm^{-1} in the theoretical) arises due to displacements in the pyrillium core with an extension out to the Se rings and some out of plane movement. There are a number of Se ring vibrations in the 500-600 cm^{-1} region and the 960-975 cm^{-1} region which appear to shift in frequency with different excitation frequencies probably because these weak bands have many atoms displaced and some will be enhanced by different electronic transitions.

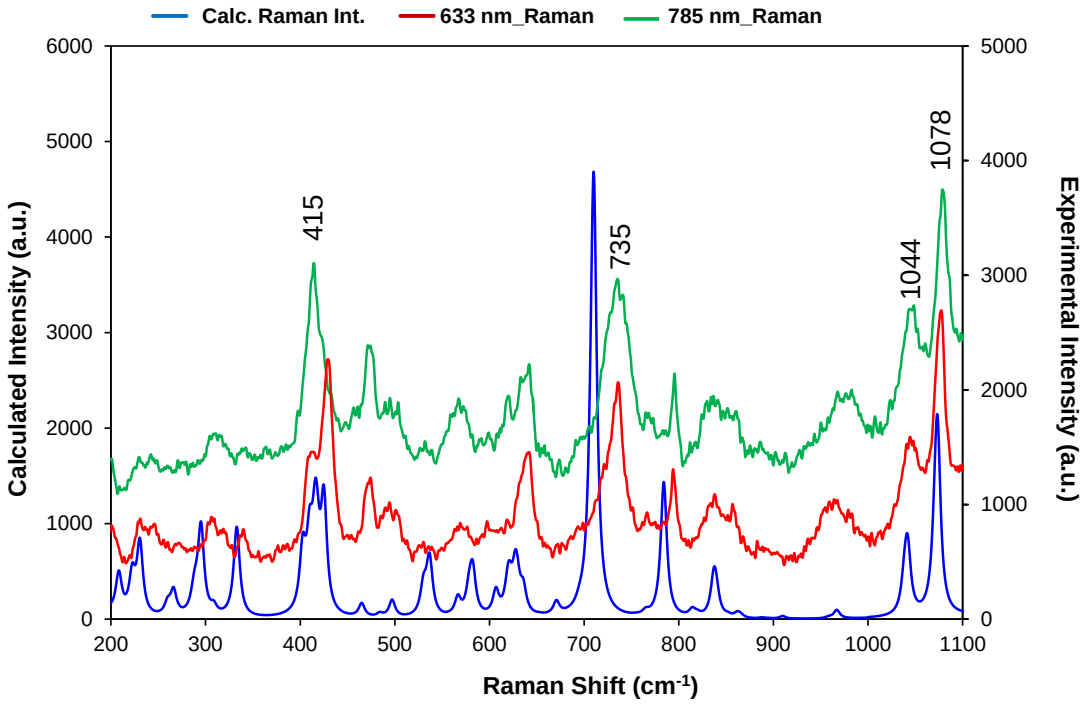

Figure 3.25 - Resonance Raman spectra in the low frequency region using 633 nm and 785 nm excitation compared to the corrected calculation. The x and y axis have been scaled for comparison, with the y-axis also being offset to make this comparison easier. In this analysis, the 633 and 785 nm experimental spectra were acquired with a 25 second acquisition time while the theoretical spectrum was calculated using Gaussian 09 software. The 633 and 785 nm Raman spectra have been background corrected and the 785 nm Raman bands which are discussed throughout have been labeled accordingly.

3.4.4.4 SERS

As previously mentioned, two different types of SERS spectra were obtained. The 633 and 785 nm SERS spectra had molecular resonance and surface enhancement contributions and appeared to be very similar to the Raman spectra obtained (figure 3.26). Whereas the 1064 and 1280 nm spectra had no contributions from molecular resonance, only surface enhancements giving rise to a number of new bands (figure 3.27). In this section, the 633 and 785 nm comparison will be conducted first, before then going onto discuss the new bands and shifts which were observed in the 1064 and 1280 nm SERS spectra.

The 785 nm excitation produced the most intense SERRS spectra as would be expected due to it being close to both molecular resonance and the plasmon

maximum. A plot of frequency against intensity expressed as a ratio of sample signal to cyclohexane signal is given as an inset in figure 3.26. The magnitude of relative enhancements should be treated with caution due to the spectra being obtained using colloidal solution of HGNs where some self-absorption of the scattered radiation may have occurred and also due to different instruments with different depths of focus being employed. Furthermore, the extinction so the contribution of scattering and absorption is wavelength dependent, with the scattering component increasing towards the infrared. This along with self-absorption of the scattered radiation helps to explain why the 633 nm spectrum is the weakest and the 1280 nm spectrum is as intense as that at 1064 nm.

It can be observed in figure 3.26 that the 633 and 785 nm SERRS spectra obtained are remarkably similar to the resonance Raman spectrum; however on close examination there are spectral differences. Such as the broad band at ~1500 cm^{-1} in resonance is more structured in SERS and the structure round the 1180 cm^{-1} band is different particularly with 633 nm excitation and a number of low frequency bands are more intense in SERRS. Furthermore, there are some spectral differences which arise between the two SERRS spectra. For example, the structure around the broad bands at ~1500 and 1180 cm^{-1} is different as is their relative intensities. Moreover, there are differences in the relative intensities and number of bands which occur in the 1480 cm^{-1} region and the relative intensities of the modes at 415 and 428 cm^{-1}.

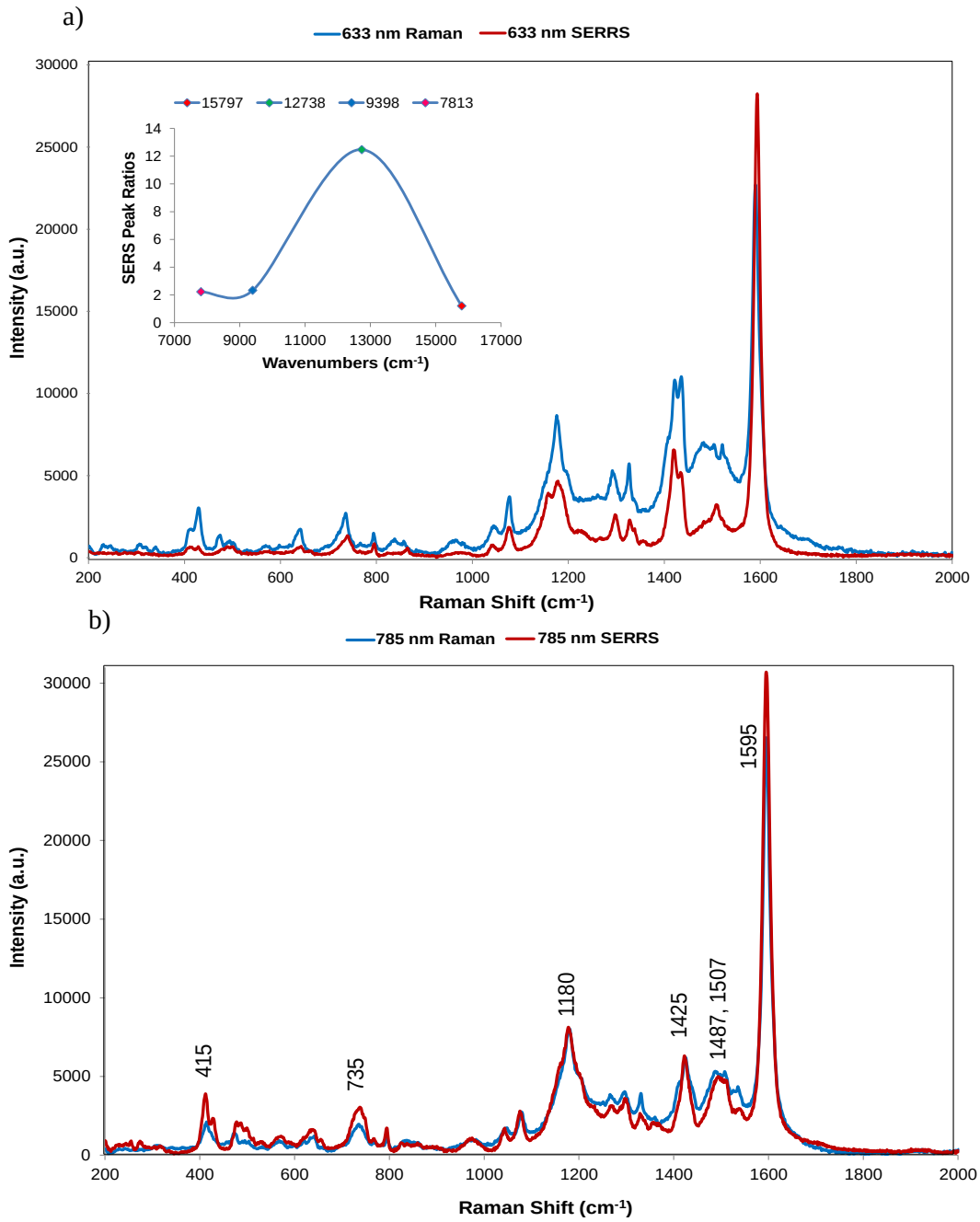

Figure 3.26 - SERRS obtained with 633 nm (a) and 785 nm (b) excitations compared to the resonance Raman spectra. The spectral intensities are set to show the differences. The actual intensities of the resonance spectra are indicated in figure 3.23 and the inset shows the relative intensities of the SERS/SERRS spectra compared to the cyclohexane standards plotted with the excitation wavelengths converted to wavenumber to obtain linear energy scale i.e. 1280 nm =7813cm^{-1}and 633 nm =15797cm^{-1}. The 633 and 785 nm Raman spectra were acquired with a 25 second acquisition time while the SERRS spectra were acquired using a 10 second exposure time. All spectra have been background corrected and the 785-nm Raman bands which are discussed throughout have been labeled accordingly.

As previously stated in chapter 2, using 10 μM of dye should be sufficient to give monolayer coverage of the HGN surface and this concentration is orders of magnitude lower than the resonance detection limit so the spectra must arise due to surface enhancement. The bands which appear intense in the SERRS spectra occur due to displacements along the major axis of the core pyrillium system and into the S rings giving maximum polarisability. The direction and the magnitude of the polarisation change along the backbone of the molecule is expected to be large, due to the long π-system which provides an easily polarisable electron cloud along the major axis. Surface enhancement arises from a change in polarisation perpendicular to the surface plane of the HGN's, therefore for these bands to be intense in SE(R)RS, the long axis of the pyrylium core must be close to being perpendicular to the surface. The changes in the spectra around 1500 cm^{-1}, at 1180 cm^{-1} and at 1425 cm^{-1} suggest that the Se rings may be orientated on the surface of the HGNs differently from the crystal but this is clearer in the SERS spectra.

The 1064 and 1280 nm spectra which were obtained at excitations away from molecular resonance show quite different results (figure 3.27). At these excitation wavelengths, the intensity is related to polarisation changes due to vibrational displacements in a direction vertical to the surface with much less, if any, coupling to the electronic transitions. Resonance Raman theory would predict a drop of in intensity away from the resonance maximum which is Loretzian in shape, however SERRS has been detected well away from the molecular resonance and plasmon resonance maxima[130, 184, 62] so the differences between the two may be largely due to some residual resonance contribution in the 1064 nm spectrum and the increased scattering efficiency with 1280 nm excitation.

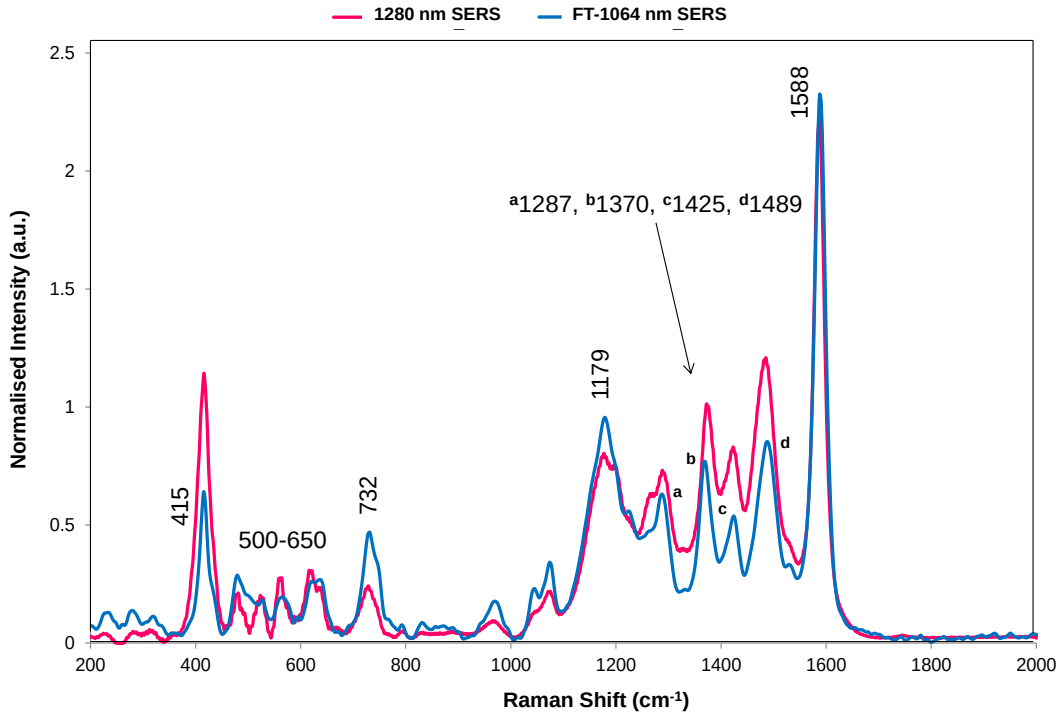

Figure 3.27 – Normalised SERS obtained with 1064 and 1280 nm excitation. The 1064 nm Raman bands which are discussed throughout are labeled accordingly. Acquisition times of 3 and 5 seconds were employed at 1280 nm and 1064 nm respectively. All spectra have been background corrected and normalised to a cyclohexane standard.

When comparing the 633, 785 nm resonance and SERRS spectra with the higher wavelength spectra at 1064 and 1280 nm, new bands are observed in the high frequency region with the low frequency region containing fewer but more intense bands. Furthermore some bands are selectively enhanced over others. New bands are observed in the high frequency region at 1489, 1370 and 1287 cm^{-1} and there is a significant rise in the intensity of the shoulder associated with the 1179 cm^{-1} (positions based on 1064 nm SERS spectrum). These modes have significant displacements on the Se rings suggesting that some rings may be oriented to give a polarisation change with a significant component vertical to the surface plane. The low barrier to rotation of the Se rings makes ring re-orientation very likely for when the dye adsorbs onto the HGN surface.

Therefore, theoretical calculations were conducted with Se rings 1 and 3 rotated to determine if this had an effect on the Raman spectrum. The spectral changes caused by rotating rings 1 and 3 can be seen in figure 3.28. Rotating ring 1 had little effect

on the spectrum with the result being very similar to the original geometry shown in figure 3.24. However, by rotating ring 3 and/or both there were explicit differences in the spectra which will be discussed throughout this section. The selection rules for Raman scattering and SERS are different,[6] therefore the assignments detailed in this section have been made after studying the displacements of each vibration and looking for changes which would give rise to SERS enhancement.

The band at 1588 cm^{-1} shifts up to four wavenumbers from the original geometry when two rings are rotated. The peak at 1489 cm^{-1} arises from selective enhancement of one of the modes contributing to the broad band or doublet observed in the resonance and SERRS spectra. This peak is also assigned to the strong Raman band predicted at 1470 cm^{-1} which is split when both rings are rotated but not by enough to be observed in the SERS spectrum. The main displacements in this band occur along the backbone of the pyrillium core with semi-circular stretches on the S rings and some extension to the Se rings. Given the likely surface geometry this will provide SERS enhancement.

The new bands observed at 1370 and 1287 cm^{-1} are difficult to assign due to SERS selection rules being quite different from Raman selection rules. The SERS spectra unlike the predicted Raman spectrum will be affected by the adsorption process whereby the dye interacts with the HGN surface and thus gives rise to selective enhancement. The predicted spectrum was calculated based on an isolated molecule and in general it can be observed that the 'corrected' theoretical bands are either fitted as shown with the 1588 cm^{-1} peak or they appear at a lower frequency in the experimental Raman and SERS spectra. Therefore on the basis of frequency, the most likely assignment for the 1370 cm^{-1} band is the weak mode predicted at 1362 cm^{-1}. This band arises due to displacements on the pyrillium core, extending through the bridge to the double bonds opposite the selenium's in the rings. However, by rotating Se rings 1 and 3, the Raman intensity is greatly reduced and the vibrations within these rings cease, leaving the major displacements on the core and along the bridge to the other two rings. It is likely that the displacements on the core cancel to produce a small polarisation change and hence a weak Raman spectrum. The effect of the dye bonding to the HGN surface could alter this and thus, the direction of the

displacements would be such as to cause a significant polarisation perpendicular to the surface. In addition, there are a number of bands between 1200 and 1300 cm^{-1} which have displacements along the pyrillium core extending into the Se rings. The peak observed at 1286 cm^{-1} is one of these, and it is likely that the surface will affect this vibration in a similar way and thus produce a new band with similar characteristics to the 1362 cm^{-1} mode.

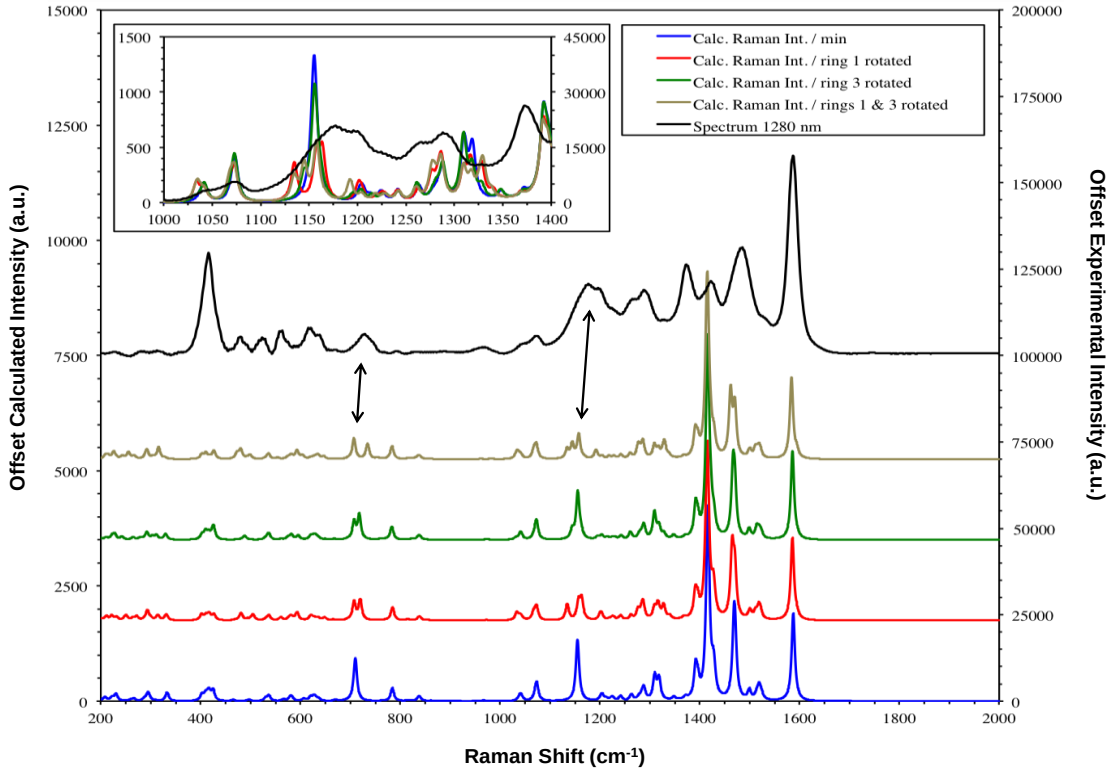

Figure 3.28 - SERS spectrum taken with 1280 nm excitation and compared to the theoretical calculation with the Se1 or Se3 ring or both rings rotated. The double headed arrows highlight the significant bands at 1179/1177 and 732/728 cm^{-1}. In this analysis, the 1280 nm SERS spectrum was acquired with a 3 second acquisition time while the theoretical spectra were calculated using Gaussian 09 software. The 1280 nm SERS spectrum has been background corrected.

The relative intensities cannot be used when comparing the computational Raman spectra to the experimental SERS spectra due to the difference in selection rules. However, useful information regarding the orientation of Se rings can be obtained by examining the peaks at 1179/1177 cm^{-1} and at 732/728 cm^{-1} in the 1064 and 1280 nm spectra respectively. The calculation predicts different results depending on which

ring is rotated and whether one or two rings are rotated. For the peak at 1179/1177 cm^{-1} it can be observed that when two rings are rotated the calculated spectra predicts 3 bands will be observed in the range where 2 peaks and a shoulder are present in the experimental 1280 nm spectrum. Figure 3.29 (top) shows that these bands arise due to displacements on the Se rings and bonds joining the ring to the core with the contribution from each ring being different in the three components.

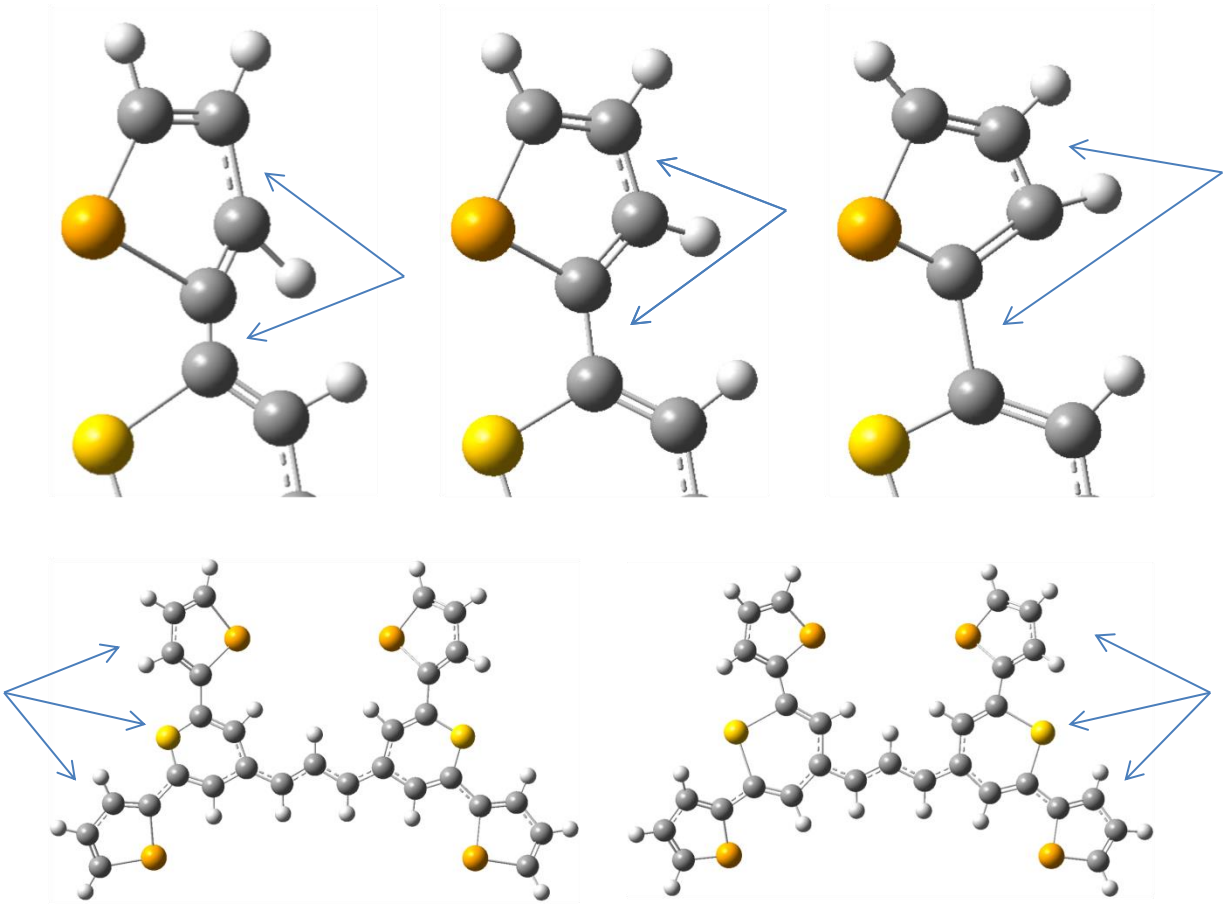

Figure 3.29 - Vibrational displacements for the vibration at 1179 cm^{-1} (top) and for the vibration at 732 cm^{-1} (bottom). The blue arrows point to where the largest displacements are occurring. For the 732 cm^{-1} vibration, the arrows have being placed at either side of the diagram to show which atoms are involved but it should be noted that during the displacement both S rings and the 4 Se rings are involved.

The peak observed at 732/728 cm^{-1} is the symmetric stretch of the S rings with some Se-C bond movement (figure 3.29, bottom). By rotating the rings away from the more symmetrical crystal arrangement a closely spaced doublet is created when one

ring is rotated and two more separated peaks when two rings are rotated. Only one band is predicted when either Se1 or Se3 is rotated but the SERS band is broad and better fitted to when both rings are rotated. This vibration is equivalent to the totally symmetric stretch commonly observed with phenyl molecules, except in this case there is a S atom present in the ring. Therefore, in the crystal arrangement both rings vibrate in phase but when one or two rings are rotated they will vibrate out of phase to give two distinct modes with their frequency depending on the ring angle. The position of the other rings are more difficult to predict since many options are possible but the fact that there is definite structure to the spectra rather than broad bands caused by many overlapping peaks in the regions sensitive to ring orientation suggests that they are oriented in a specific way rather than being randomly oriented.

In the SERS spectra there are fewer bands present in the 500-600 cm^{-1} region than observed in the resonance spectra; however, the bands which are present are significantly enhanced and they arise due to significant Se ring displacements. Predicting exactly where vibrations occur in this low frequency region is very difficult as the vibrations will be sensitive to any change in environment of the ligand so the effect of the surface and ring orientations may affect the band frequency. There are a large number of modes predicted in this region but many divide into two classes; ones have Se ring displacements with some pyrillium core displacements and the others are mainly pyrillium ring displacements. Although both types usually have out of plane displacements. It appears that the SERS enhancement occurs from modes with significant Se ring and/or core displacements. The intense band at 415 cm^{-1} in the experimental spectrum fits better with the band predicted at 424 cm^{-1} which has pyrillium displacements and Se ring displacements between the Se and the opposite C=C bond as well as some out of plane movement. Therefore, this band should give significant change in polarisability along the long axis of the molecule. The band predicted at 416 cm^{-1} is largely an out of plane vibration for much of the molecule.

A space filled model of the molecule with rings Se1 and Se3 rotated can be seen in figure 3.30. The low barrier to rotation of the Se rings means that the exact angle of the rings to the surface will be determined by surface bonding and packing forces. It

has been previously reported that S and Se atoms have a strong affinity for gold surfaces[174, 176-179] therefore, they are expected to bond to the gold atoms on the HGN surface. Furthermore, S and Se atoms are soft bases and since the gold atoms on the surface can relax their position easily this would further enhance their chance of bonding. However, the angles of the rings cannot be set so that the S and Se atoms can point directly at the surface to form simple linear bonds. The Se rings are therefore hindered from bonding to the surface by the ring angle and the S is somewhat protected from the surface by the Se rings.

The forces holding gold atoms on a plane surface are weak and it may be that a gold atom is displaced form the surface to bond between the Se atoms. Thus, the interaction is likely to be complex involving Au displacements and metal to ligand π-bonding. Moreover, there is no clear evidence of complex formation through frequency shifts and no clear charge transfer. There are however, some differences in frequency for some modes between SERS and resonance but these are quite small and could be explained by the re-orientation of the Se rings or by errors due to the use of different instruments. Hence there is little evidence of strong Se or S surface bonding but clear evidence of surface interaction from the large polarisability changes which give rise to the selective enhancement. All the experimental spectra show the 1588 cm^{-1} band as the most intense so based on this and other supporting data, it is suggested that the orientation of the backbone to the surface is near perpendicular with two rings rotated. The polarisation of the mode at 1179 cm^{-1} looks almost parallel to the surface in some models, however the space filled diagrams show that the rings are at an angle, therefore a significant vector perpendicular to the surface will be obtained.

The data presented in this section has shown the different enhancement mechanisms required to give rise to both SERS and SERRS spectra. The polarisable π-system involved in the electronic transition, couples well with the surface field gradient to give strong SERRS from vibrations which also give rise to the resonance enhancement by taking the ground electronic state into the excited electronic state. However, well away from this transition, the SERS spectra produced by the surface field gradient induced by the plasmon help define the Se ring orientations more

effectively. Therefore based on all the data examined, it can be concluded that the 114 dye orientates with its major axis at an angle of ~80 degrees to the HGN surface, with two Se rings pointing towards the gold surface allowing them to bond in a complex manner to the HGNs.

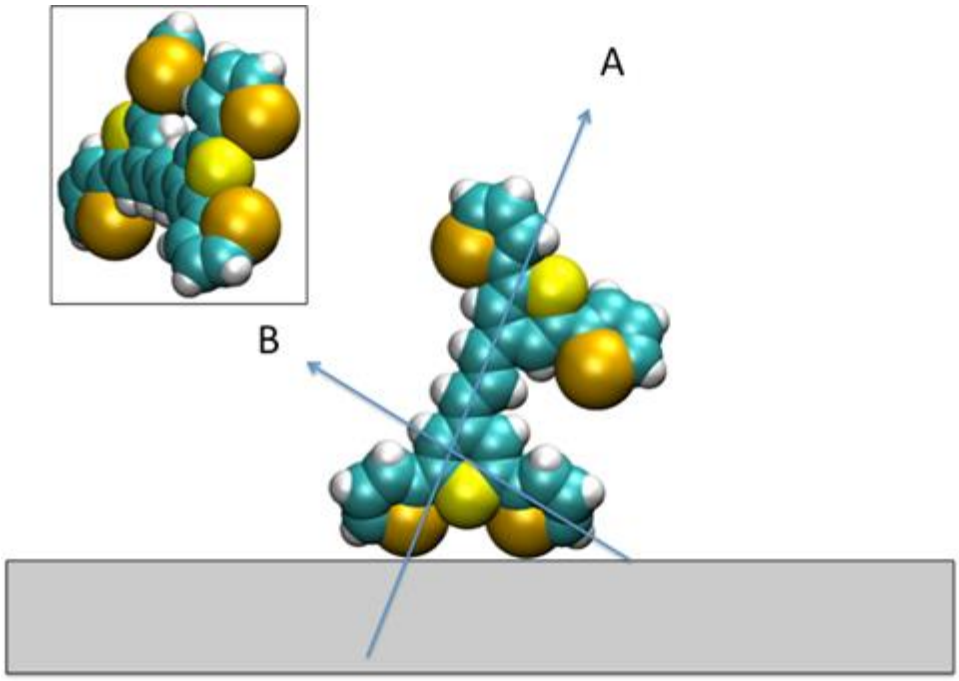

Figure 3.30 - Space filled model of the dye on the surface showing the two selenophene rings rotated and the position of the thiopyrylium S atom. Arrow A indicates the long axis of the thiopyrylium core and arrow B the direction of the bridge from one selenophene ring to the core. The inset shows the molecule rotated to show the relative positions of the Se and S atoms facing the surface.

3.5 Conclusions

In conclusion, a set of new extreme red shifted SERS nanotags have been designed to demonstrate unprecedented performance in the NIR region. The combination of HGNs or AuNPs in excess of 100 nm, a library of chalcogenopyrylium dye reporter molecules and laser excitations ranging from 1064 to 1550 nm have shown superior results when compared to commercially available reporters and nanotags. The chalcogen nanotags have shown LODs ranging from picomolar to femtomolar, which are extremely low detection limits for these laser wavelengths. Furthermore, the dye molecules have

multiple novel attachment groups through the thiophenes and selenophenes allowing them to bond strongly to the gold surface of the HGNs and produce intense SERS signals. In the last section of this chapter it was actually shown that the 114 dye in particular, orientates with its major axis almost perpendicular to the surface, with two of the Se rings pointing downwards at the gold surface allowing them to bond in a complex manner to the HGNs.

Additionally, it was observed through the PCA studies that the dyes could be individually identified in a reproducible manner and classified according to their unique structure and SERS spectra. Therefore a further benefit for these SERS nanotags is their potential for use in future multiplexing systems, where multiple analytes need to be identified simultaneously, such as in bio-medical detection assays.[146, 180]

3.6 Future Work

These SERS nanotags have been shown to produce strong SERS signals with exceptionally low detection limits across a range of NIR laser excitations. Throughout this chapter the design of these nanotags has been extensively studied, through changes to the substrate and aggregation effects but more importantly by testing a range of reporter molecules with different attachment groups. In addition by examining how they bond and orientate on the surface of a gold substrate, has led to a better understanding of what works well at these wavelengths and allows for future nanotags to be designed effectively. However, one experiment which would help in understanding these dyes further is if the limits of adding carbon-carbon double bonds into the backbone of the dyes were tested. Knowing how many sp^2 carbons can be added to the pyrillium core before it causes the nanoparticles to over-aggregate and precipitate out of solution is essential in understanding the limits of these dyes.

The design of these nanotags has been demonstrated but to date, no one has conducted any research on the biological application of these nanosensors. Therefore, what would make this research very valuable and beneficial is if the utility and applicability of these nanotags were demonstrated in biological analysis.

There are many ways in which these nanotags could be employed in a biological system; however the first step would be to test the nanotags in cellular studies to determine if SERS signals can be obtained but also to investigate their toxicity to the cell. Then more complex studies could be conducted such as depth of penetration studies in turbid media; where the nanotags could be embedded at different depths in tissue samples and detected using a NIR laser incorporated into a transmission Raman set-up. Furthermore, targeted SERS studies in tissues could be conducted; where the nanotags are functionalised with an antibody for example and used to target a specific receptor on a cell surface. Or they could be incorporated in a multiplexing assay for chemical or bio-medical detection.

These unique SERS nanotags produce strong SERS signals in the uncongested window of the NIR region and therefore could widen the scope for future advances in bio-medical and optical applications.

4. SERS Switching 'on and off' via heating of PNIPAM coated HGNs

4.1 Introduction

To date aggregated noble metal nanoparticles, commonly silver and gold are used as suspension based SERS substrates as they are stable materials and have LSPRs in the visible region.[6, 145] However, by changing the size, shape, surface chemistry and/or aggregating these plasmonic nanoparticles it is possible to shift the LSPR several hundred nanometers into the NIR region.[185] Aggregation can be achieved by the addition of a simple inorganic salt (as shown in chapter 2) or by a biological recognition event such as a DNA-protein interaction; usually resulting in an increase in the Raman signal.[145] In recent years, not only has there been extensive research into trying to control the SERS enhancement from single aggregates of metal nanoparticles but there has also been a large effort into functionalisation with protective coatings such as polymers,[186, 187] sugars[188] and silica[189] in order to increase their stability and compatibility with biomarkers. Functionalisation allows plasmonic nanoparticles to be employed in a range of applications from DNA detection to photothermal ablation therapy.[54, 146, 190, 191]

Recently, there has been a lot of interest into functionalising nanoparticles with three-dimensional (3D) water-swollen polymers, known as 'hydrogels,' due to their excellent bio-compatibility.[192] These unique nanomaterials are able to to trap water and biological fluids; their porous microstructure allows permeability; whilst the 3D structure offers mechanical support[193] allowing them to be employed in a variety of applications such as biosensors, cell scaffolds, implantable devices, microfluidic systems, separation systems, synthetic extracellular matrix and tissue engineering.[194-200]

Several hydrogels exhibit stimuli-responsiveness where they will undergo reversible conformational changes in response to environmental factors such as temperature,[201] pH,[202] light,[203] ionic strength[204] and/or magnetic/electric fields.[194, 205, 206] This means that when an external stimulus such as heat is applied to the system, the polymer will undergo large structural changes such as swelling and collapsing.[207] The theory of structural changes to the polymer due to external stimuli was first discovered by Dusek in 1968. It wasn't for another 10 years, however that this hypothesis was demonstrated experimentally by Tanaka *et al*.[208-210]

Temperature is possibly the most studied of the external stimuli as it's easy to control and applicable in many biological systems. Thermoresponsive polymers, usually in aqueous solutions will undergo phase transitions and solubility changes when a certain temperature is crossed. The polymers which become soluble upon heating have an upper critical solution transition temperature (UCST), whereas those which become insoluble with heating possess a lower critical solution transition temperature (LCST).[211] Figure 4.1 shows the phase diagrams for a thermopolymer solution with LCST and UCST, a) and b) respectively. At the phase transition shown in figure 4.1a, polymer chains which are soluble in water below the LCST will precipitate as the temperature is increased above the LCST.

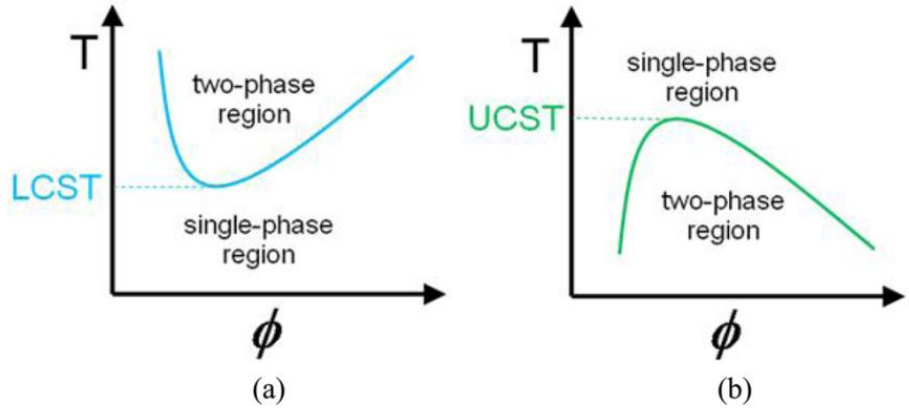

Figure 4.1 - Temperature vs. polymer volume fraction, Ø, for polymer solution with (a) LCST and (b) UCST.[212]

Generally hydrogels and thermoresponsive polymers don't dissolve and precipitate out of solution due to the strong covalent bonds within their network structure; however, changes in their swelling will occur above and below their critical solution temperature. To date, thermopolymers which exhibit a LCST are most commonly studied because below this transition temperature, the thermopolymer is in a swollen, hydrophilic state, where the polymer chains undertake a random coil formation and the water-polymer interactions are thermodynamically favoured. However heating above the LCST, causes the thermopolymer to collapse to a globular, hydrophobic state due to the water-polymer interactions becoming thermodynamically unfavourable and the polymer-polymer and water-water interactions dominating.

It should be noted, that the phase transitions and solubility changes are reversible so when the heat is removed and the thermopolymer solutions are cooled below the LCST, the hydrogels will swell and the polymer chains will once again become randomly coiled, see figure 4.2.

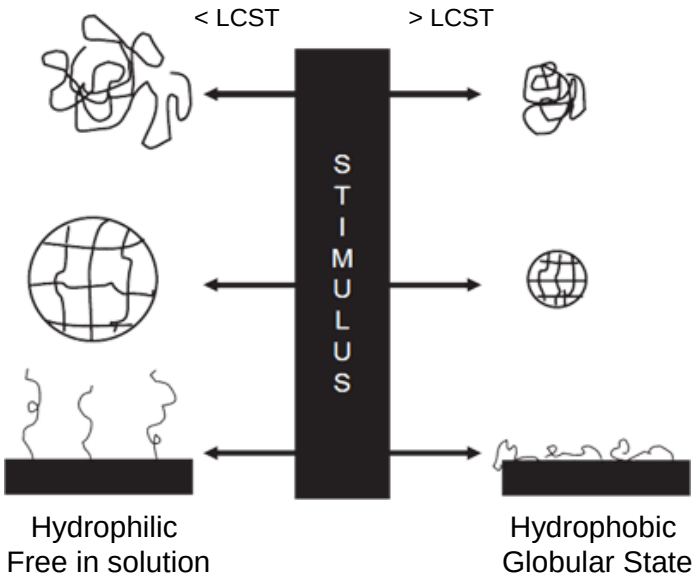

Figure 4.2 – Effect of heating and cooling stimuli-responsive polymers past their LCST. Classes of stimuli-responsive polymers based on physical forms; (a) linear free chains in solution, (b) covalently cross-linked reversible and physical gels and (c) chain adsorbed or surface-grafted forms.[213]

The LCST of thermopolymers is determined by the balance of polymer-polymer interactions and polymer-water interactions. Therefore, it is possible to tune the LCST by using co-polymerisation to shift the critical temperature making the thermopolymer application specific. The addition of hydrophilic; polar groups will cause the LCST to increase whereas the addition of hydrophobic; non-polar groups will ultimately cause the LCST of the co-polymer to decrease.

There have been several thermoresponsive polymers reported such as xyloglucan,[214-216] poloxamers,[217, 218] methylcellulose,[219-221] hydroxybutyl chitosan[222-224] and elastin-like polypeptides[225-228] but the one which has been of most interest and will be discussed in this work is poly(N-isopropylacrylamide) (PNIPAM, see figure 4.3).[193]

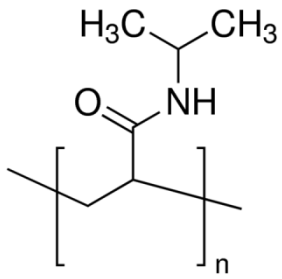

Figure 4.3 – Structure of PNIPAM.

PNIPAM exhibits a low LCST at ~32 ^{o}C making it ideal for biological applications.[129, 185, 229-231] Below this critical temperature, PNIPAM is hydrophilic and soluble in aqueous solution however by increasing the LCST above 32 ^{o}C, the polymer becomes hydrophobic and insoluble due to the fluctuation of hydrophobic interactions and hydrogen bonding.[230] Furthermore at a molecular level, the polymer chains undergo a conformational change from a swollen disordered coil, which is free in solution, to a collapsed ordered globule.[229] Therefore, when plasmonic nanoparticles are functionalised with stimuli-responsive polymers, any changes made to the system, such as conformational changes to the polymer will systematically affect the stability, solubility and optical properties of the nanoparticles.[229] Moreover, there are many benefits of adding a PNIPAM coating to core-nanoshells such as the porous protective shell enhances the long term stability of the colloidal

solution and prevents electromagnetic coupling between the nanoparticles, therefore increasing the reproducibility and signal intensities.[231]

To date, there have been several papers published which detail the importance and design of PNIPAM functionalised nanoparticles. Both silver and gold thermosensitive systems have been proposed for applications in catalysis,[232, 233] pH sensing,[185, 234, 235] and drug delivery.[236, 237] Additionally, there have been reports which use SERS as a detection method for monitoring the reversible conformational changes of the PNIPAM polymer. Liu *et al.* developed a pH/temperature dual stimuli-responsive system that allowed SERS signals to become greatly enhanced when two stimuli were exerted simultaneously.[235] Upon reducing the pH from 7.0 to 3.0 and increasing the temperature of the silver-hybrid microgels above 32 ^{o}C; the collapse of the polymer allowed the nanoparticles to adhere closely to one another which induced strong plasmonic coupling and electromagnetic enhancement and therefore gave rise to the increased SERS response. Furthermore, Liz-Marzán *et al.* showed that SERS signals can also be increased by using PNIPAM-microgels to trap small analytes close to the surface of solid metal nanoparticles.[231, 238] All these studies have used noble metal nanoparticles and since HGNs have previously been reported to withstand heat and photothermal effects better than solid nanoparticles,[83, 84] it was an appealing study to see how they would compare in a thermoresponsive set-up. Therefore in this work, a stimuli-responsive SERS system that uses PNIPAM coated hollow gold nanoshells was developed.

4.2 Aims

Thermoresponsive SERS nanotags are required for biological applications such as drug delivery and bio-sensing and as previously mentioned in chapters 2 and 3 there is a great desire for these nanotags to give effective SERS in the NIR region. In previous reports, the microgels have solely consisted of solid metal nanoparticles such as silver-magnetite or gold nanoparticles, where the spectral window for laser excitation is limited to the visible region. Another issue with these previously reported microgels is that the heating effect had to be applied prior to SERS measurement due to the nanoparticles LSPRs not being resonant with the laser

excitations; thus ‘plasmonic heating’ could not be induced by an incident laser. Therefore, the combination of hollow gold nanoshells which have tunable LSPRs, coated with PNIPAM which has a low LCST at ~32 ^{o}C and encapsulated with a Raman reporter (BPE or MPY) seems like a promising SERS nanotag for combatting these issues.

In the initial 1064 nm studies, PNIPAM coated HGNs (PNIPAM-HGNs) with a range of LSPRs were synthesised and encapsulated with a Raman reporter (BPE or MPY). These thermosensitive nanotags were then analysed to determine if a SERS response could be obtained when a hotplate stirrer was used to heat the solutions.

For the 785 nm studies, the PNIPAM-HGNs where synthesised to have an LSPR that coincided with the laser excitation source. Laser induced plasmonic heating was therefore used to increase the temperature of the bulk solutions past the LCST of PNIPAM, in order to observe the desired SERS effects. Furthermore, studies into the stability, reproducibility, and controlling the degree of signal enhancement were also carried out for these thermosensitive SERS nanotags.

4.3 Experimental

Initially to determine the optimum volume of PNIPAM to be added, 5 x 25 mL aliquots of the ‘as prepared’ HGN solution were obtained and to each one a different volume from 20-100 µL of PNIPAM-amine terminated (0.5% (w/v); Sigma-Aldrich) polymer was added. These solutions were left gently vortexing for one hour, before, being centrifuged and analysed by extinction spectroscopy, DLS and zeta potential as described in sections 2.3.3.3, 2.3.3.4 and 2.3.3.5.

4.3.1 Synthesis of PNIPAM coated HGNs with LSPRs at 690, 785 and 860 nm ±20 nm.

The method described was modified from the procedure reported by Singh *et al.*[239] The HGN synthesis is described in section 2.3.1.1. Specifically for PNIPAM coated HGNs, the following modifications were made to the previous conditions:

- trisodium citrate dihydrate (550 µL, 0.1 M; Sigma-Aldrich, >99%)

- chloroauric acid trihydrate (33 mL, 260 µM (PNIPAM 690) to 235 µM (PNIPAM-860); Fisher Scientific, ACS reagent grade)
- trisodium citrate dihydrate (500 µL, 0.1 M; Sigma-Aldrich, >99%) was added to stabilise the HGN solution and left to stir for 1 hour
- PNIPAM-NH_2 (300 µL, 0.5% (w/v); Sigma-Aldrich) was then added to the HGN solution and left to stir gently for a further 1 hour
- centrifugation (5000 x rpm) with re-suspension in d.H_2O to yield final concentrations of 4-5 nM
- LSPRs at 690, 785 and 860 ± 20 nm

Specifically, for the PNIPAM-HGNs employed in the 1064 nm SERS studies the final concentrations were 4.53 nM (PNIPAM-673) and 4.27 nM (PNIPAM-786) and for the PNIPAM-HGNs employed in the 785 nm photothermal and SERS studies the concentrations were 4.91 nM (PNIPAM-690), 4.78 nM (PNIPAM-785) and 4.94 nM (PNIPAM-860).

A Nanosight LM10 was used initially to obtain concentrations in particles per L and following this the molar concentrations were calculated.

4.3.2 Synthesis of citrate capped HGNs resonant at 785 nm

The HGN synthesis is described in section 2.3.1. Specifically for HGNs with LSPRs at 785 nm the following modifications were made...

- trisodium citrate dihydrate (550 µL, 0.1 M; Sigma-Aldrich, >99%))
- chloroauric acid trihydrate (33 mL, 130 µM; Fisher Scientific, ACS reagent grade)
- centrifugation (5000 x rpm)
- final concentration of 4.86 nM.

4.3.3 Characterisation of PNIPAM coated HGNs and citrate capped HGNs

Before SERS and photothermal measurements, the concentrations of the hollow gold nanoparticle solutions were adjusted to the same level with the aid of a Nanosight

LM10 via the procedure described in the instrument technical notes. Briefly, the original concentrated solutions were diluted with d.H_2O until 5 to 30 nanoparticles per CCD frame were obtained. The imaging videos were recorded for 90 seconds and analysed using the provided software (NTA 2.1). The required dilution factor was then applied to the samples so that each nanoparticle solution had a concentration of 4 nM ($2.4x10^{15}$ particles per L) for the 1064 nm studies and 4.7 nM ($2.8x10^{15}$ particles per L) for the 785 nm studies.

4.3.3.1 SERS Analysis at 1064 nm

Investigation into the SERS properties of the thermosensitive nanotags was carried out by mixing 'as prepared' HGN solution (270 µL) with Raman reporter solution (30 µL, 0.1 mM).

The Raman reporters added were BPE (Sigma-Aldrich >98%) and MPY (Sigma-Aldrich) and the stock solutions were prepared as detailed in section 2.3.2. The SERS measurements were performed using the same instrumental conditions as described in section 2.3.3.1; however the acquisition time was reduced to 5 seconds.

The samples were externally heated using a hot plate stirrer. Each cuvette was placed in a beaker of boiling d.H_2O and left to equilibrate for 20 minutes at 60 ^oC, before being removed and analysed. The solution was then left for a further 30 minutes to equilibrate at room temperature and analysis carried out once more. This process was repeated for 3 cycles of heating and cooling. The samples were monitored over the temperature range 23-60-23 ^oC. These conditions were sufficient to heat above and below the LCST of PNIPAM and the SERS effects observed.

4.3.3.2 Photothermal and SERS Analysis at 785 nm

The photothermal and SERS measurements were carried out by mixing 'as prepared' HGN solution (2025 µL) with the Raman reporter solution (225 µL, 0.1 mM of BPE, Sigma-Aldrich >98 %).The instrumental design was based on an in-house set-up

previously described by Xie *et al*.[82] Briefly, a 785 nm fibre coupled laser (B&W Tek Inc. Newark, USA) was used as the 'incident laser' for inducing plasmonic heating. The laser, with a power of 346.5 mW (at the sample) was focused into a plastic cuvette using a standard f=100 mm UV fused silica plano-convex lens (1" diameter). A thermocouple from a heating mantle was inserted into the solution perpendicular to the path of the incident laser light, ~1.5 cm above the focus point. A portable 785 nm spectrometer (Deltanu Reporter R spectrometer, Laramie, USA) with a 'point and shoot' attachment was incorporated into the set-up to obtain the SERS spectra. This diode laser had a power of 100 mW (at the sample) and was held at an angle of 90 degrees and 1 cm above the incident laser beam to minimise the interference between the two lasers. The cuvette contained 2.25 mL of the HGN suspension and a magnetic stirrer to ensure uniform heating of the sample. Additionally, a plastic stopper sealed with parafilm was used to cover the top of the cuvette in order to minimise heat loss to the environment. Initially the samples were left to stabilise for 3 minutes at room temperature with stirring, before the laser block was removed and the solution illuminated. The samples were illuminated for ~30 minutes; until the solution had equilibrated at its maximum temperature. The laser block was then applied and the solutions allowed to cool back down to room temperature and again the samples where left until the temperature had stabilised indicating the solution had equilibrated. This process was repeated over two cycles of heating and cooling. The SERS spectra and temperature readings were taken every 5 minutes. For the SERS measurements an exposure time of 5 seconds was employed and 5 scans at each time interval were recorded. All spectra have been background corrected as described in section 2.3.3 and the peak intensity values shown in the bar charts are from the C-C stretch of BPE at 1603 cm^{-1}. Error bars represent the standard deviation resulting from 5 scans at each time interval. It should be noted, that all experimental parameters such as HGN concentration (number of nanoparticles per L), sampling geometries and instrumental parameters including depth of focus, laser power and acquisition times were kept constant for all the hollow gold nanoparticle solutions analysed.

4.3.3.3 Extinction Spectroscopy

The same instrumental conditions as previously described in section 2.3.3.3 were employed.

For monitoring the stability of the resonant PNIPAM and citrate HGNs over two cycles of heating and cooling; 300 µL of concentrated HGN solution was added to 800 µL of d.H_2O and changes in extinction at 785 nm were monitored over the temperature range 20-90-20 ^oC. Note a rate of 3.5 ^oC per minute was applied with 5 minute holds at each stage of the cycle being incorporated to allow the solution to equilibrate (at each stage) in order to replicate the SERS experiments.

For monitoring the LSPR during each stage of the SERS experiments; 50 µL of the as prepared 'HGN + BPE solution' was added to 450 µL of d.H_2O and analysed.

4.3.3.4 DLS and Zeta Potential

The same instrumental conditions as previously described in sections 2.3.3.4 and 2.3.3.5 were employed.

For monitoring the average particle size and zeta potential during each stage of the SERS experiments; 50 µL of the as prepared 'HGN + BPE solution' was added to 450 µL of d.H_2O and analysed.

4.3.3.5 Scanning Electron Microscopy

SEM images were acquired using the same procedure as that described in section 2.3.3.6.

4.4 Results and Discussion

4.4.1 1064 nm – Thermosensitive SERS Nanotags

In this work, a thermoresponsive system that incorporates PNIPAM coated hollow gold nanoshells and a Raman reporter was developed for SERS detection at 1064 nm laser excitation. These studies were conducted to determine if this combination would be successful in producing a SERS response with a NIR laser excitation and if so, would the SERS signals increase and decrease with respect to the temperature change and ultimately could the signals be monitored over several cycles of heating and cooling.

4.4.1.1 Characterisation of PNIPAM coated HGNs

Singh *et al.* have previously shown that gold nanoparticles can be coated with commercially available PNIPAM polymers, to yield highly stable and reproducible nanogels.[239] In doing so they avoid the NIPAM (N-isopropylacylamide) polymerisation step which can cause the nanoparticles to become highly unstable and precipitate out of solution due to the extreme temperatures, harsh solvent conditions and/or cross-linking with bulky substituents. Another benefit of this synthetic procedure was that the PNIPAM employed had a structural modification, with an amine-substituent being added to one end of the polymer (figure 4.4) so that the polymer would have a greater affinity for the gold surface and thus increase the chance of chemisorption onto the nanoparticle surface.[239] Herein, the method described by Singh was modified to yield PNIPAM-coated HGNs with a range of LSPRs.

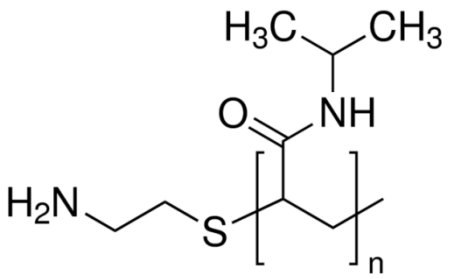

Figure 4.4 – Structure of amine terminated PNIPAM.

Before the SERS experiments could be conducted it was important to determine the optimum conditions for synthesising PNIPAM-HGN colloidal solutions which would yield stable and homogeneous hydrogels. Therefore, 5 x 25 mL aliquots of the 'as prepared' HGN solution were obtained and to each one a different volume of PNIPAM (20-100 µL; 0.5% (w/v)) polymer was added and left gently vortexing for one hour before being analysed by extinction spectroscopy, DLS and zeta potential, see figure 4.5.

It can be seen in figure 4.5a that the LSPR of the synthesised PNIPAM coated HGNs were 755 ± 5 nm. In these initial studies the experimental conditions used were complementary to the HGNs discussed in section 3.3.1 (LSPR ~700 nm) and as such it can be seen that by adding a PNIPAM shell to the HGNs a shift of ~50 nm was observed. These results are consistent with previous studies where adding polymer shells to HGNs can cause the LSPRs to red-shift by ~100 nm and as such produce NIR active SERS nanotags when a reporter molecule is incorporated into the system.[186]

Furthermore, it can be observed from figure 4.5a that adding 100 µL of PNIPAM (0.5% (w/v)) to the HGN solution; produced the most intense extinction spectrum however it also generated inhomogeneous nanoparticles with what appears to be a second peak being developed at ~900 nm. Two peaks in an extinction spectrum is indicative that the nanoparticles synthesised are of a range of sizes and/ or shapes and are therefore not homogeneous. This second peak is also seen in the extinction spectra for all the other conditions but it appears to be most dominant when either 40 µL or 100 µL of PNIPAM was added. It appears that when 40 µL of PNIPAM was added to the HGNs; the most unsuccessful hydrogels were synthesised with a very broad spectrum and no definitive extinction maximum being observed. Figures b and c also confirm that by adding 40 µL of PNIPAM; the poorest colloidal solution was prepared with the largest particle size and the lowest zeta potential values being obtained. Therefore, indicating that these particles were not homogeneous and that this volume of PNIPAM-HGN solution is not ideal for these studies.

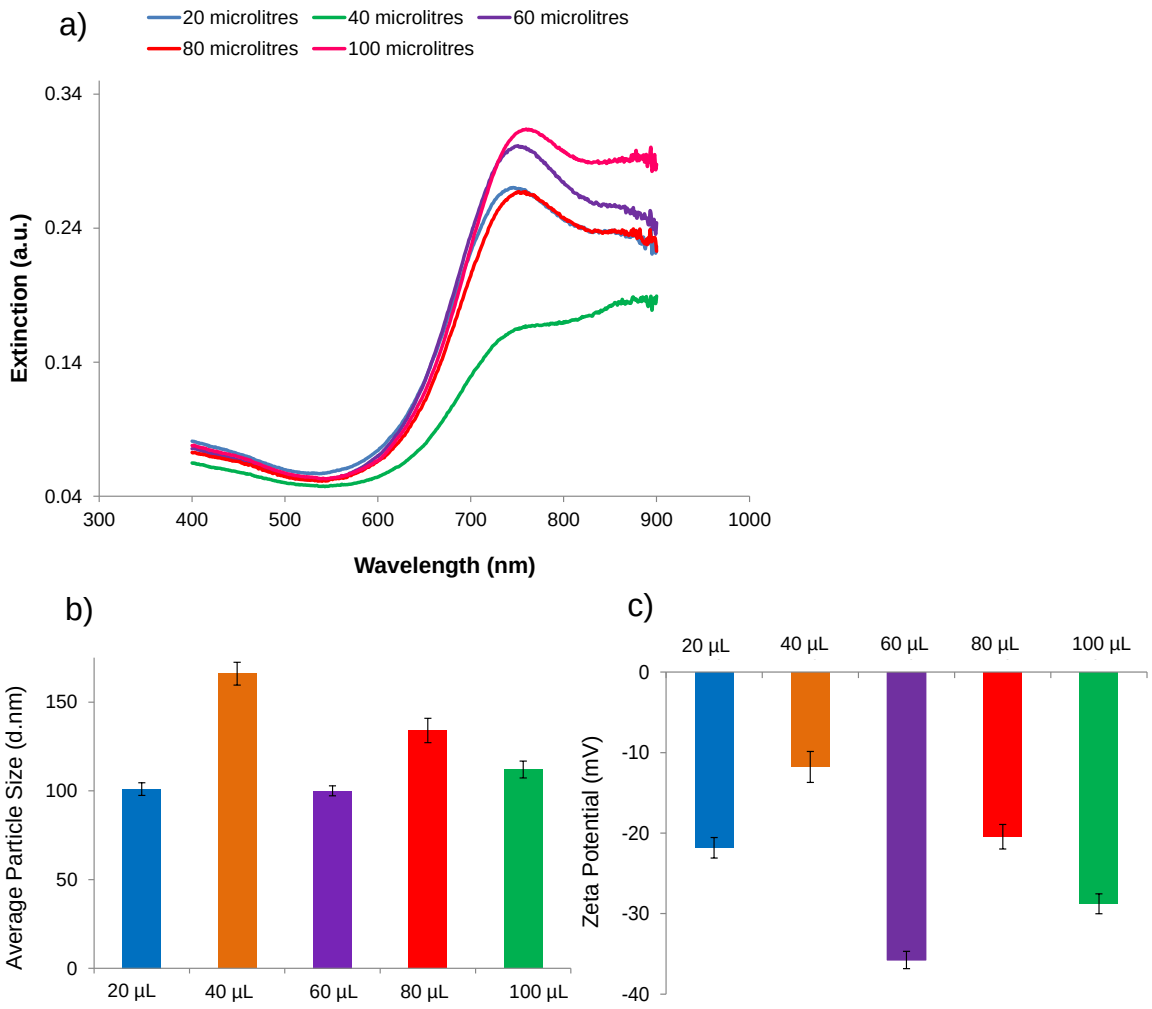

Figure 4.5 – a) Extinction, b) DLS and c) zeta potential data for determining the optimum volume of 0.5 % (w/v) PNIPAM to be added to the HGNs to yield stable and homogeneous thermosensitive hollow gold nanoshells.

By taking into account all the data, it was deduced that the optimum volume of PNIPAM to be added was 60 µL. These conditions produced the most stable colloidal solution with it being the only sample to obtain a zeta potential value greater than -30 mV; the recommended value for colloidal solutions to be classed as stable.[127] It also produced an average particle size of ~100 nm which seems to be consistent with two of the other conditions tested and it had the narrowest extinction spectra based on full-width half maximum estimations (the estimations were made to the left as the full peak was out with the wavelength range).

These results have shown that PNIPAM coated HGNs can be synthesised and the colloidal solutions are relatively stable and homogeneous. Furthermore based on these results, PNIPAM-HGNs with a range of LSPRs were synthesised by simultaneously reducing the concentrations of the capping agent and gold shell (as discussed in chapter 2) before coating with the PNIPAM polymer. These PNIPAM-HGNs were then encapsulated with a Raman reporter to determine if these thermosensitive nanotags could produce SERS signals.

4.4.1.2 SERS of PNIPAM coated HGNs with a 1064 nm laser excitation

Figure 4.6 shows the options of how it was believed these thermosensitive nanotags would respond upon heating and cooling past the LCST. Initially the PNIPAM-HGN solutions would be at room temperature (a) and thus the temperature would be below the critical temperature for PNIPAM. The polymer would be in a swollen, hydrophilic state with disordered coils fully extended and the reporter molecule would be at a distance 'far' from the HGN surface. Therefore, there would be no or very little SERS response observed due to SERS being a distance dependant technique.[6]

Upon heating past the LSCT ((b) in this case with an external appliance such as a hot plate stirrer), the polymer chains would collapse to a hydrophobic globular state and it was expected that the reporter molecule would adhere close to the HGN surface and an increase in the SERS signal would be observed. However, upon cooling the solution and the polymer undertaken a swollen, hydrophilic state once more; it was unknown whether the reporter molecules would remain trapped due to a strong interaction occurring between the reporter molecules and the HGN surface and as such a strong SERS signal would still be observed (c); or whether the reporter molecules would be removed from the surface, with little or no SERS signals being observed and thus the thermosensitive nanotags would once again take the configuration shown in figure 4.6a.

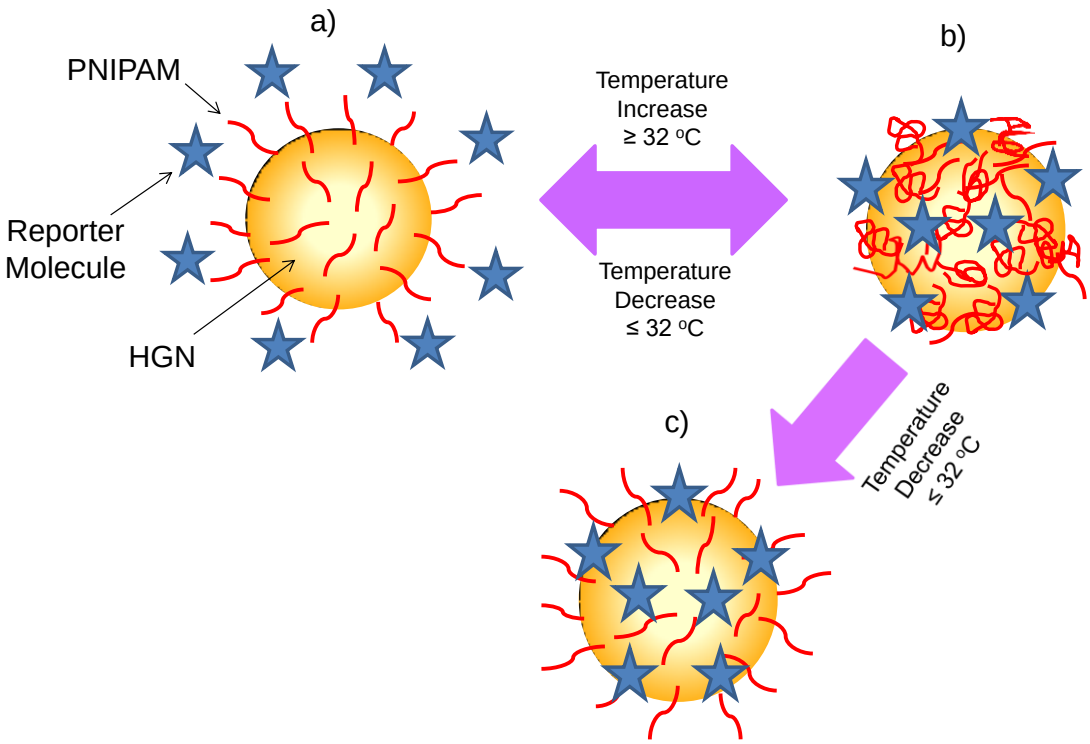

Figure 4.6 – Effect on the SERS signals upon heating and cooling the thermosensitive nanotags past the LCST of PNIPAM at ~32 °C. a) Temperature < LCST , polymer is swollen and reporter molecule is released, b) temperature > LCST, polymer is collapsed (globular) and reporter molecule is attached to HGN surface and c) temperature is < LCST, polymer is swollen but reporter molecule is trapped.

For these studies, PNIPAM-HGNs with a range of LSPRs were analysed. Furthermore, they were encapsulated with either BPE (strong reporter) or MPY (weaker reporter), to determine if the strength of the interaction occurring between the reporter and HGN surface would affect whether the reporter molecules would remain trapped or be released. Figure 4.7 shows the SERS response with a laser excitation at 1064 nm for BPE encapsulated PNIPAM-HGNs resonant at 673 nm. It can be seen in figure 4.7 that when the thermopolymer solution which was initially at room temperature (< LCST) was analysed, there was very little SERS response observed as was predicted by figure 4.6a, due to the polymer being swollen and BPE being far away from the HGN surface. However, the small amount of signal present could be due to BPE having a high affinity for the gold surface of the HGNs and as such this small molecule may have diffused through the porous polymer shell to reach the gold surface.[231]

Upon heating past the LSCT and the polymer collapsing, it can be seen that there was approximately a 6 fold increase in the SERS signal as the reporter molecules came into contact with the HGN surface, as was predicted would happen in figure 4.6b. Interestingly though upon cooling and the polymer swelling, the SERS signal didn't even decrease by half. This indicated that although some of the reporter molecules were being removed a large proportion of the reporter molecules remained trapped. This is possibly due to the strong interaction occurring between BPE and the gold surface of the HGNs. Moreover, these results were observed for a further 2 cycles of heating and cooling and therefore it can be stated that these thermosensitive nanotags undertake the configuration demonstrated in figure 4.6c.

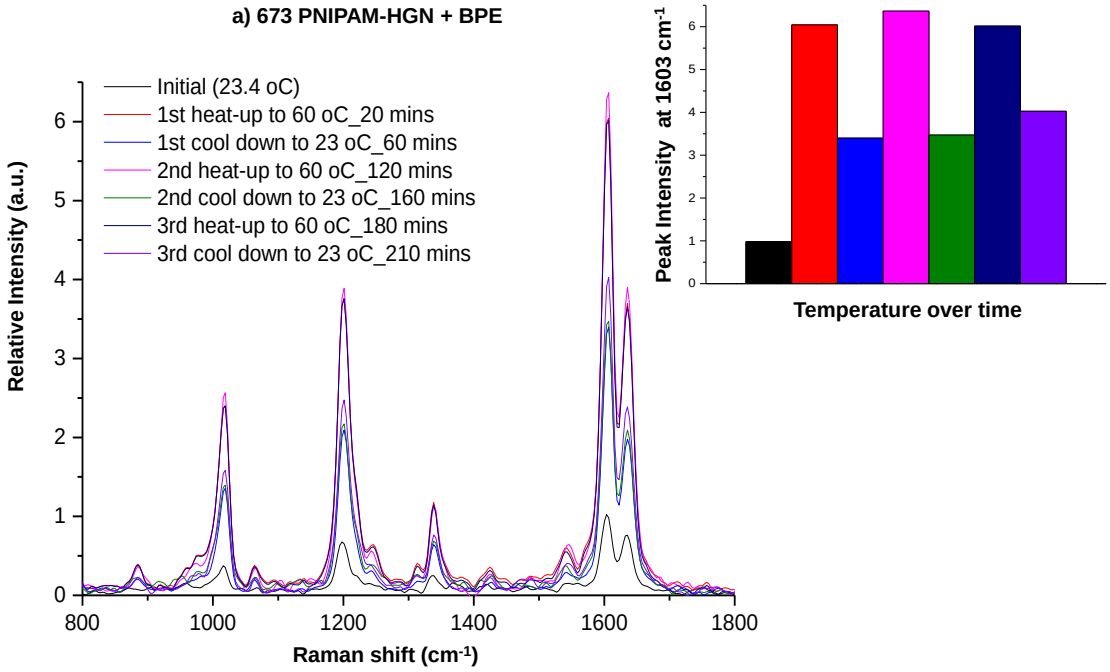

Figure 4.7 - SERS spectra with bar chart inserts showing the change in SERS signal for PNIPAM coated HGNs + BPE (0.1 mM) resonant at 673 nm over three cycles of heating and cooling past the LCST of 32 ^{o}C. A hot plate stirrer was used to heat the samples in this analysis. All the measurements had a 5 second acquisition time and a laser power operating at 420 mW. Each sample was prepared in triplicate and 5 scans of each replicate were recorded. All spectra have been background corrected and the peak intensity values shown in the bar chart are from the C-C stretch of BPE at 1603 cm^{-1}.

This experiment was also repeated for PNIPAM-HGNs with LSPRs at 786 nm and it can be seen in figure 4.8 that simply by red-shifting the LSPR it has a significant effect on the SERS results. The LSPR of the HGNs were altered by simultaneously reducing the capping agent and shell thickness during the synthesis as previously shown in section 2.4.1. It should be noted however, that when HGNs are red-shifted, there is an increase in their inner core but more importantly for SERS there is a decrease in their shell thickness which means there is a reduction in their plasmon oscillation energy and ultimately a decrease in their SERS response.[111]

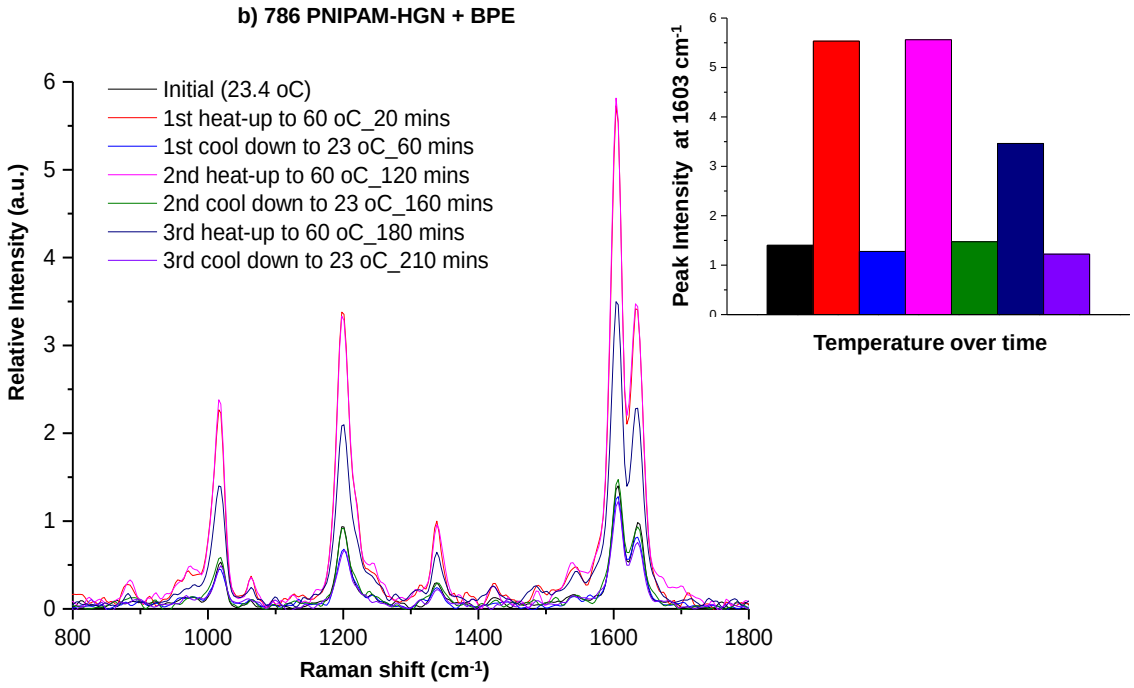

Figure 4.8 - SERS spectra with bar chart inserts showing the change in SERS signal for PNIPAM coated HGNs + BPE (0.1 mM) resonant at 786 nm over three cycles of heating and cooling past the LCST of 32 ^{o}C. A hot plate stirrer was used to heat the samples in this analysis. All the measurements had a 5 second acquisition time and a laser power operating at 420 mW. Each sample was prepared in triplicate and 5 scans of each replicate were recorded. All spectra have been background corrected and the peak intensity values shown in the bar chart are from the C-C stretch of BPE at 1603 cm^{-1}.

For the first heating cycle of 786 PNIPAM-HGN + BPE, the results obtained were very similar to those seen in figure 4.7 for 673 PNIPAM-HGN + BPE. This time

there was a signal increase of approximately 5 times that of the initial signal as the polymer collapsed and BPE adhered to the HGN surface. However this time upon cooling and the polymer swelling, the SERS signal decreased to match that of the initial SERS response, thus indicating that BPE was released from the HGN surface (figure 4.6a). It is plausible upon cooling, below 32 ^{o}C, the strong and favourable water-polymer interactions dominated as a result of the PNIPAM chains swelling and therefore, pushed BPE away from the surface of the HGN. These results are likely to be due to weaker interactions occurring between the reporter molecule and the thinner gold shell of the HGN as a result of the LSPR shift. This is a plausible explanation for determining why BPE would be released under these circumstances as opposed to before when the reporter molecules were trapped.

As previously mentioned, this experiment was also repeated for MPY encapsulated PNIPAM-HGNs to determine if weaker Raman reporters can be employed and SERS results still obtained. In addition it was also important to determine, if a weaker Raman reporter will remain trapped or whether it would be released from the HGN surface. Furthermore the effect of trapping and releasing the reporter was investigated to determine if it was solely dependent on the LSPR of the thermosensitive nanotags. Figure 4.9, shows the SERS results obtained for PNIPAM coated HGNs + MPY (0.1 mM) with LSPRs at 673 (figure 4.9a) and 786 nm (figure 4.9b) over three cycles of heating and cooling past the LCST of 32 ^{o}C.

It can be seen in both figures 4.9a and b, that MPY encapsulated PNIPAM-HGNs produce much weaker SERS signals than those previously seen with BPE nanotags (supporting previous work in chapter 2). Both these figures show similar trends to those previously seen with BPE + PNIPAM-HGNs. Figures 4.9a and b, show that upon heating there is an increase in the SERS signals, however figure 4.9a shows that as the bulk solution is cooled and the polymer becomes swollen, there is a decrease in the SERS signal indicating that some of the reporter molecules are removed but a large proportion of them remain trapped. Whereas, when the LSPR of the PNIPAM-HGNs was red-shifted to 786 nm it was observed in figure 4.9b that upon cooling the signal was once again as low as the initial SERS response. Thus indicating the reporters are removed from the surface, with this phenomenon being

explained by the fact that these PNIPAM-HGNs have thinner gold shells and as such causes a weaker interaction to occur between the reporter molecules and gold surface of the HGNs.

Furthermore, in these studies due to an external heating appliance (hot plate stirrer) being used to heat the bulk solutions; the nanotags may be experiencing harsher conditions than shown in the next section were a laser was employed to increase the temperature above the LCST. In section 4.4.2.1, it was observed that most of the reporter molecules were being removed from the surface with a small proportion remaining trapped, regardless of the LSPR of the HGNs. Hence, it is plausible that these harsher heating conditions have also had an effect on the nanotags such as weakening the bonds/interactions occurring within the hydrogels.

These experiments have shown that the combination of PNIPAM, HGNs and Raman reporter can be employed for SERS detection at 1064 nm. But more importantly, these thermosensitive nanotags can withstand temperatures of up to 60 ^{o}C for a minimal of three heating and cooling cycles. Furthermore, these studies have been informative in that the trapping and releasing effect of these thermosensitive nanotags was dependant on the LSPR of the HGNs and the heating environment and not on the reporter molecule chosen.

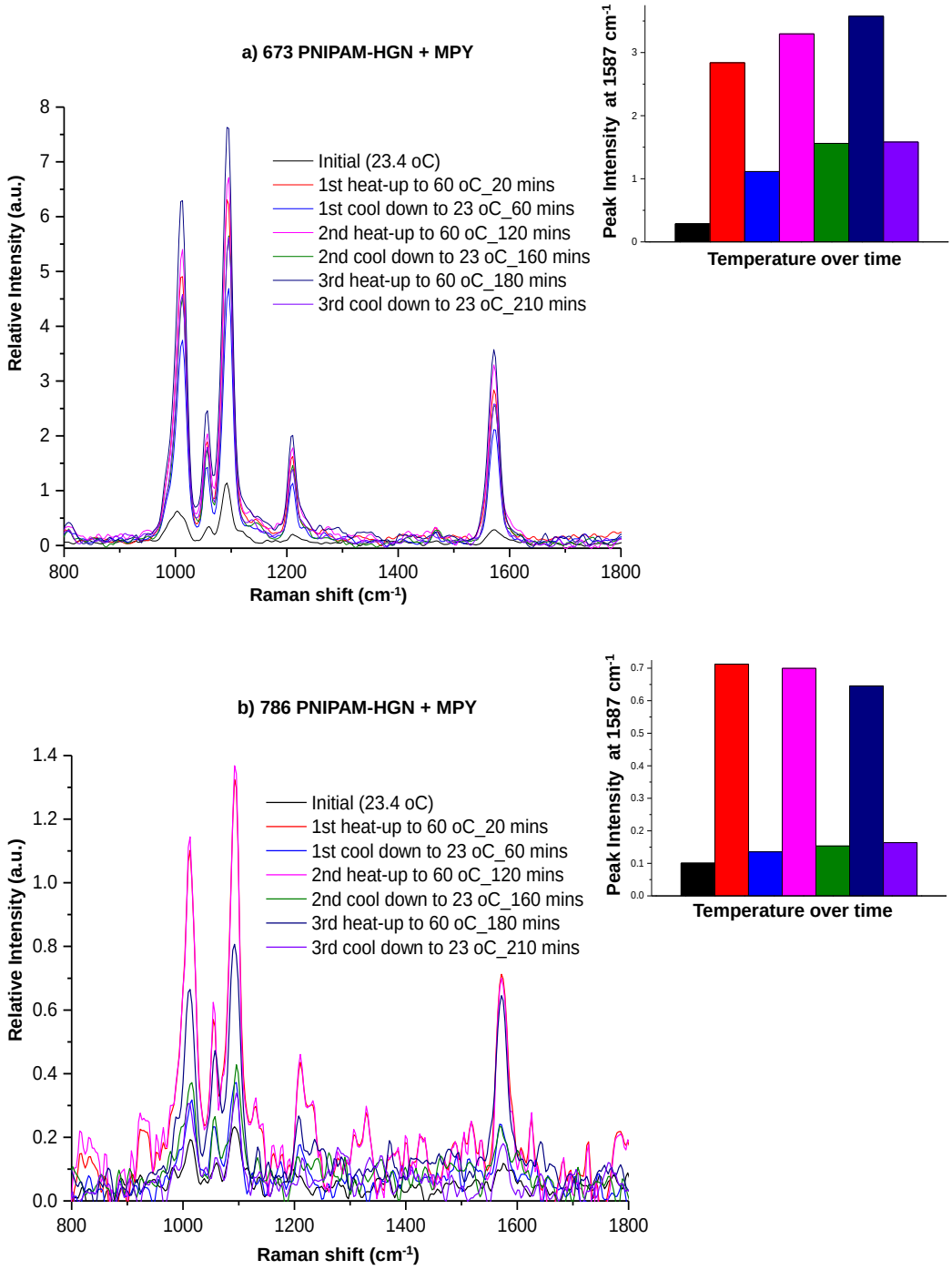

Figure 4.9 - SERS spectra with bar chart inserts showing the change in SERS signal for PNIPAM coated HGNs + MPY (0.1 mM) with LSPRs at 673 (a) and 786 nm (b) over three cycles of heating and cooling past the LCST of 32 ^{o}C. All the measurements had a 5 second acquisition time and a laser power operating at 420 mW. Each sample was prepared in triplicate and 5 scans of each replicate were recorded. All spectra have been background corrected and the peak intensity values shown in the bar chart are from the C-C stretch of BPE at 1603 cm^{-1}.

4.4.2 785 nm – Thermosensitive SERS Nanotags

4.4.2.1 SERS of PNIPAM coated HGNs with a 785 nm laser excitation

In this section, a thermosensitive SERS nanotag with a HGN core that is resonant at 785 nm, coinciding exactly with the laser excitation employed has been designed (figure 4.10). Therefore, in this work there was no need for an external heating appliance as a resonant laser was used to induce localised heating of the plasmon which in turn raised the temperature of the bulk solution past the critical temperature (32^{o}C), allowing the SERS and photothermal response of the PNIPAM coated HGNs to be simultaneously monitored over time. The photothermal effect is the process whereby a material converts incident photons into heat and the instrumental set-up for photothermal studies of HGNs was previously described by Xie *et al*.[49] However for these studies some modifications have been made to the set-up with a 785 nm laser being used to carry out localised heating of the HGNs and a secondary 785 nm Deltanu Reporter R spectrometer being used to obtain the SERS. Furthermore, to collect the SERS data the 785 nm spectrometer was placed at an angle of 90 degrees and 1.5 cm above the incident laser beam (solely used for heating the nanotags' solution) to ensure minimum interference between the lasers. In addition, larger sample volumes, a magnetic stirrer and a plastic stopper sealed with parafilm were incorporated into the set-up to ensure uniform heating of the bulk solutions with minimum heat loss.

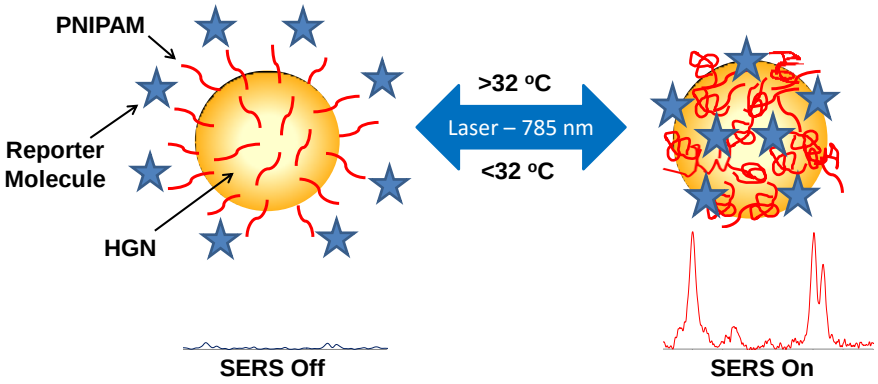

Figure 4.10 - SERS switching using plasmonic induced heating of PNIPAM coated hollow gold nanoshells; where the HGN core was resonant with the 785 nm laser excitation. Schematic illustrating how the SERS signals are affected upon heating and cooling the thermosensitive nanotags passed 32 °C (LCST of PNIPAM) with the photothermal response of the HGNs being induced solely by the 785 nm laser. Figure has been reproduced by permission of the Royal Society of Chemistry.[240]

Figure 4.11 clearly shows that it was possible to simultaneously monitor the SERS and photothermal effect over two cycles of heating and cooling. Additionally, by using a laser resonant with the LSPR of the HGNs it was possible to excite the plasmon and heat the local environment, which caused the polymer chains to collapse from swollen disordered coils to a collapsed ordered globule (as illustrated in figure 4.10).[229] Thus allowing the reporter molecule, in this case BPE to come close to the HGN surface and ultimately enhance the SERS signals observed. Upon cooling the solution below 32 °C, the SERS signals deceased as BPE was removed from the surface due to the polymer chains expanding and once again becoming hydrophilic and free in solution. Moreover in figure 4.11, by monitoring the C-C stretch at 1603 cm^{-1} for BPE,[111] it can be seen that by heating and cooling the solution past the critical temperature of 32 °C, highlighted by the dashed line, there was a steady rise and fall in SERS signal as the polymer collapses and swells respectively. Thus, allowing the reporter molecule to come close to the HGN surface and be removed again. In figure 4.11, it can be seen that it takes ~10 minutes for the incident 785 nm laser to heat the bulk solution above the LCST and ultimately for a 5 fold increase in SERS signal to be observed. However the solution was continually heated until equilibrium (further 15 minutes) was established at ~40 °C, thus ensuring the polymer had completely collapsed and BPE was close to the HGN

surface. This was confirmed with a 13 fold increase in the SERS response. Upon cooling to room temperature the polymer becomes swollen, removing BPE from the surface and as a result the signal intensity to decrease. This process of SERS switching on and off was observed reversibly over the two cycles of heating and cooling with at least a 5 fold change in the SERS signal.

Furthermore, this experiment was repeated with citrate-capped HGNs (as a control) hence there was no PNIPAM polymer present. It can be seen in figure 4.12 that there was no trend in the SERS response, suggesting that these unmodified nanoparticles were not dependent on the heating and cooling effect. Therefore, it must be solely due to the presence of the thermopolymer in the PNIPAM-HGN sample that enabled the conformational changes over time to be monitored by SERS.

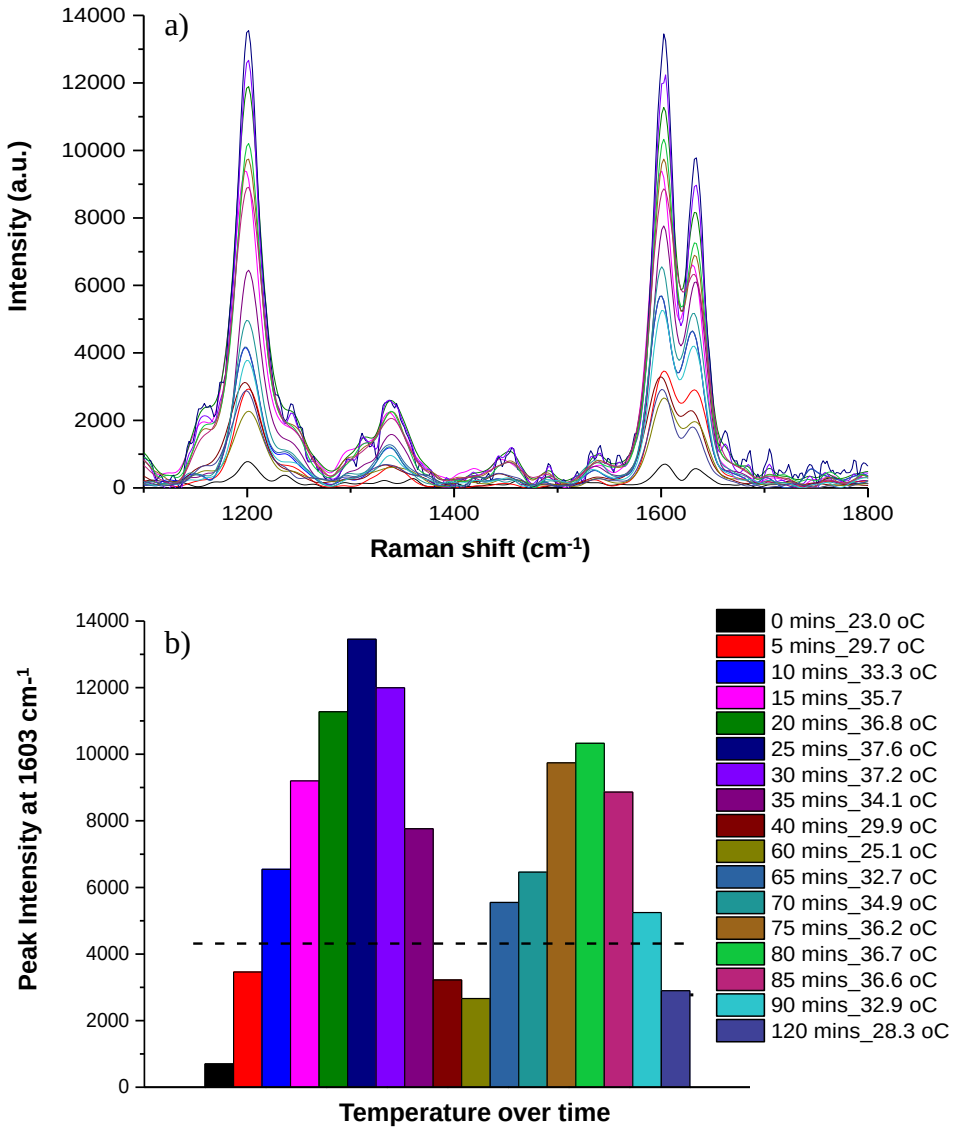

Figure 4.11 - SERS spectra (a) and bar chart (b) showing the change in SERS signal of PNIPAM coated HGNs + BPE (0.1 mM) resonant at 785 nm over two cycles of heating and cooling past the LCST of 32 ^{o}C. The SERS spectra and temperature readings were taken every 5 minutes. An accumulation time of 5 seconds was employed and 5 scans at each time interval were recorded. All spectra have been background corrected and the peak intensity values shown in the bar chart are from the C-C stretch of BPE at 1603 cm^{-1}. Bar chart containing error bars can be seen in appendix VI. The temperature was monitored over the range 23 ^{o}C to 40 ^{o}C, with the largest temperature increase being 14.6 ^{o}C. Figure has been reproduced by permission of the Royal Society of Chemistry.[240]

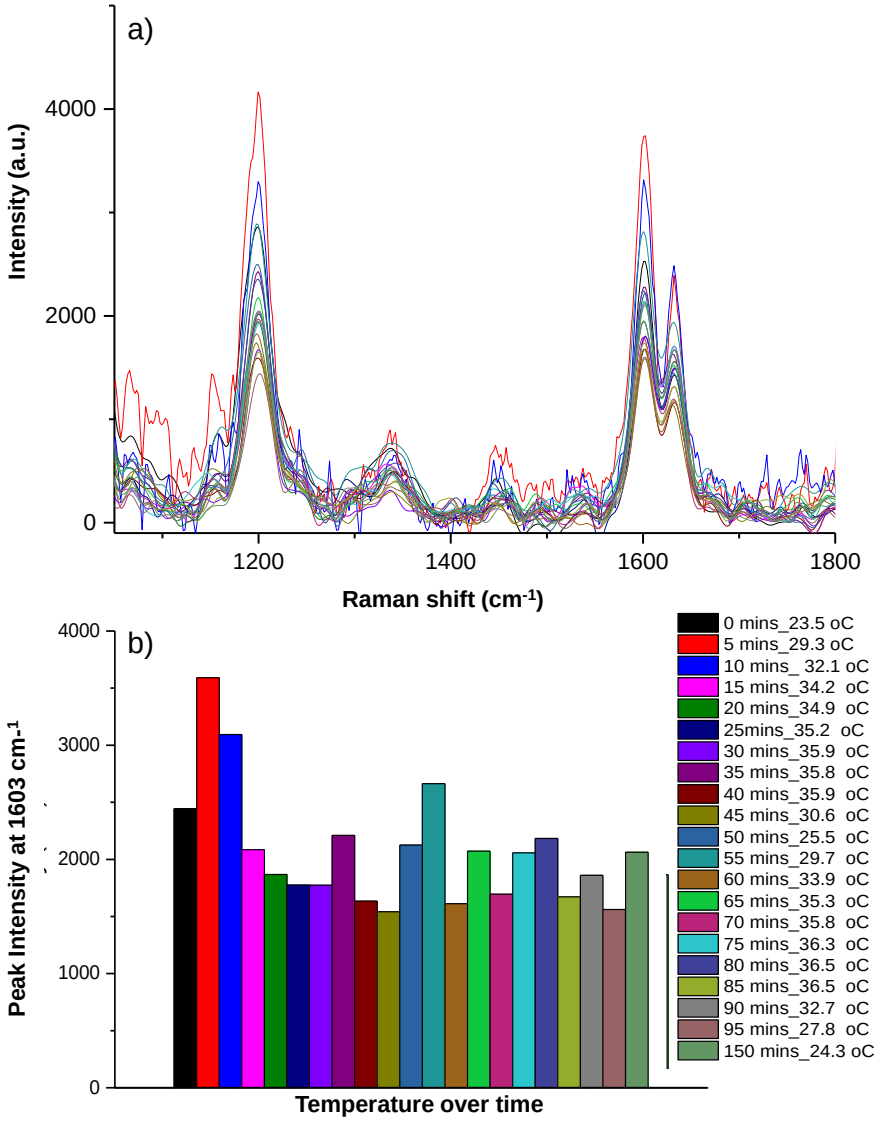

Figure 4.12 - SERS spectrum (a) and bar chart (b) showing the change in SERS signal of citrate capped HGNs + BPE (0.1 mM) resonant at 785 nm over two cycles of heating and cooling past the LCST of 32 ^{o}C. The SERS spectra and temperature readings were taken every 5 minutes. A laser excitation of 785 nm was used to induce plasmonic heating of the HGNs and a secondary portable Deltanu 785 nm spectrometer was used to collect the SERS data. An accumulation time of 5 seconds was employed and 5 scans at each time interval were recorded. All spectra have been background corrected and the peak intensity values shown in the bar charts are from the C-C stretch of BPE at 1603 cm^{-1}. Bar chart containing error bars can be seen in appendix VI. Error bars represent one standard deviation resulting from 5 scans at each time interval. The heating and cooling cycles were over the temperature ranges 23.5 ^{o}C to 36.5 ^{o}C, with the largest temperature increase being 13 ^{o}C. Figure has been reproduced by permission of the Royal Society of Chemistry.[240]

The degree of enhancement can be controlled by plasmonic tuning of the HGN properties. To confirm this, two further batches of PNIPAM-HGNs were synthesised with LSPRs at 690 and 860 nm, figures 4.13 and 4.14 respectively. Figures 4.13a and 4.14a show the SERS spectra obtained when these two bulk solutions were heated and cooled past the LCST, with their change in SERS response observed more clearly in the corresponding bar charts, figures 4.13b and 4.14b.

A similar trend in signal intensities were obtained for both samples as those previously seen in figure 4.11 (785 PNIPAM-HGN). Briefly, there was a steady increase in the signal intensity upon heating, due to the PNIPAM chains collapsing into a globular state and BPE coming close to the HGN surface and then a decrease in the SERS signal as the solution was cooled below 32 ^{o}C, with the polymer chains expanding and BPE being removed from the surface of the HGNs. For all the samples analysed using this method, it can be observed that not all the reporter molecules are removed from the surface but there was at least a 4-fold decrease in signal intensity during the cooling step; indicating that most of the reporter molecules are being removed from the surface due to the polymer swelling.

When comparing the results from the range of PNIPAM-HGNs analysed, it is important to note that the PNIPAM coated HGNs resonant with the laser excitation showed the largest SERS enhancement and photothermal effect; followed by the red-shifted batch (LSPR at 860 nm) and then the standard batch (LSPR at 690 nm) with temperature increases of 14.6, 13.2 and 12.1 ^{o}C respectively. This data can also be observed in figure 4.15, which shows solely the photothermal effect of a range of HGNs tested plus silver and gold nanoparticles as a comparison. It has previously been reported that resonant HGNs and HGNs that have NIR active LSPRs are more photothermally efficient so they are able to convert absorbed photons into heat more efficiently; exciting the nanoparticles to a greater degree which ultimately in these studies increased the SERS intensity and heated the bulk solution to a greater extent.[82] Therefore, by exploiting the plasmonic properties of HGNs it was possible to control the degree of enhancement from these thermosensitive SERS nanotags.

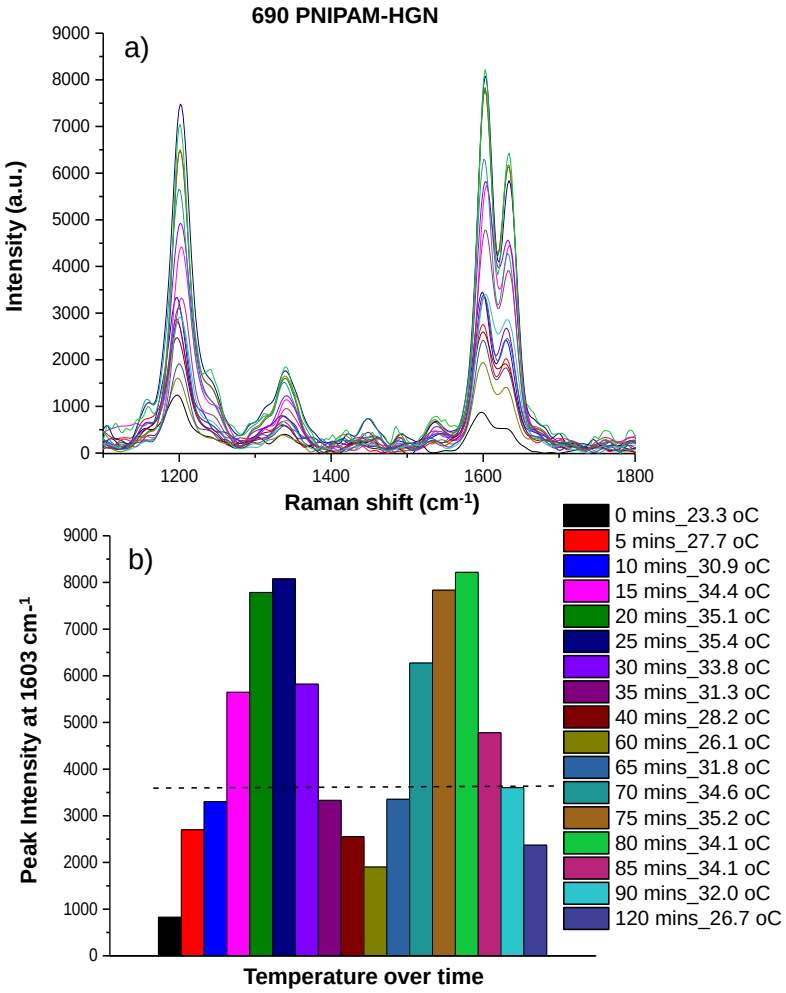

Figure 4.13 - SERS spectra showing the change in SERS response for PNIPAM coated HGNs + BPE (0.1 mM) resonant at 690 nm, over two cycles of heating and cooling past the LCST of 32 ^{o}C. The 690-PNIPAM nanotags had a temperature increase of 12.1 ^{o}C, an average particle size of 114.8 ± 18.3 nm and zeta potential value of -30.9 ± 7.05 mV. The SERS spectra and temperature readings were taken every 5 minutes. A laser excitation of 785 nm was used to induce plasmonic heating of the HGNs and a secondary portable Deltanu 785 nm spectrometer was used to collect the SERS data. An accumulation time of 5 seconds was employed and 5 scans at each time interval were recorded. All spectra have been background corrected and the peak intensity values shown in the bar charts are from the C-C stretch of BPE at 1603 cm^{-1}. Figure has been reproduced by permission of the Royal Society of Chemistry.[240]

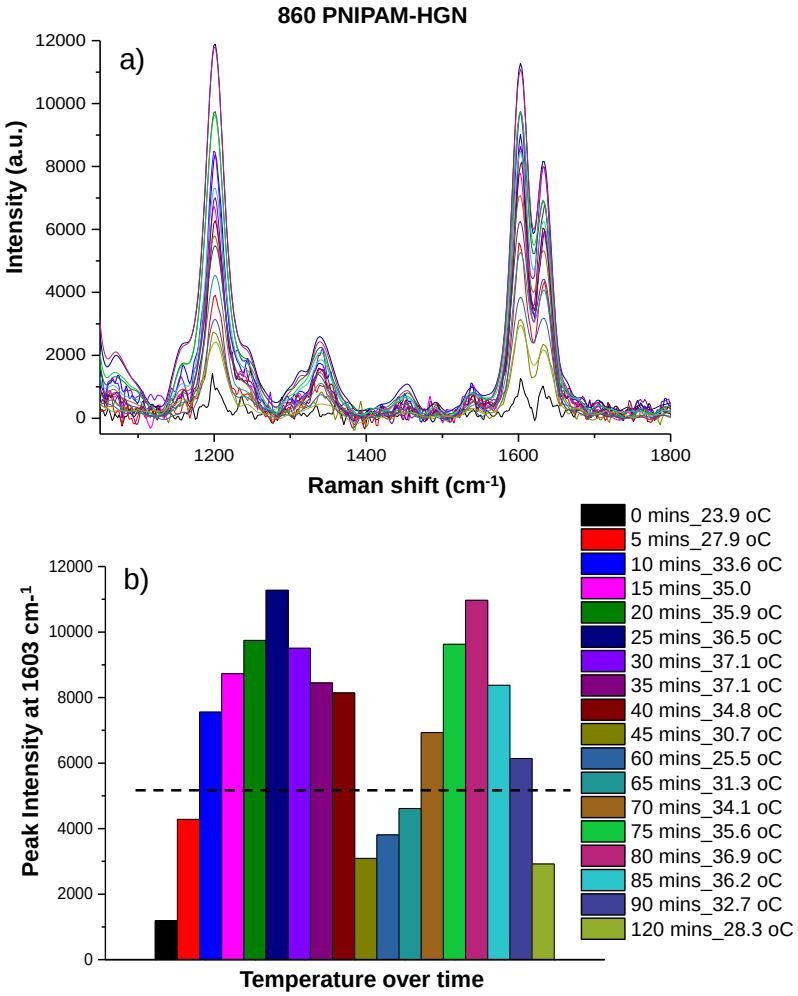

Figure 4.14 - SERS spectra showing the change in SERS response for PNIPAM coated HGNs + BPE (0.1 mM) resonant at 860 nm, over two cycles of heating and cooling past the LCST of 32 ^{o}C. The 860-PNIPAM nanotags had temperature increases of 13.2 ^{o}C, an average particle size of 156.3 ± 24.1 nm and a zeta potential value of -28.4 ± 6.82 mV; The SERS spectra and temperature readings were taken every 5 minutes. A laser excitation of 785 nm was used to induce plasmonic heating of the HGNs and a secondary portable Deltanu 785 nm spectrometer was used to collect the SERS data. An accumulation time of 5 seconds was employed and 5 scans at each time interval were recorded. All spectra have been background corrected and the peak intensity values shown in the bar charts are from the C-C stretch of BPE at 1603 cm^{-1}. Figure has been reproduced by permission of the Royal Society of Chemistry.[240]

Figure 4.15 shows that the resonant and NIR active PNIPAM-HGNs undergo the greatest temperature changes and photothermal increase, with the PNIPAM shell protecting the HGNs from any sample degradation induced by the laser. While, the citrate reduced silver and gold nanoparticles demonstrate the weakest photothermal effects with temperature changes of 4 and 5 ^{o}C respectively. The photothermal effect is highly dependent on the absorption properties of the materials under study and therefore the absorption value for HGNs dominates the overall extinction value. Thus, they are able to generate more heat than the solid silver and gold nanoparticles under the same conditions. This data is in agreement with previously reported work by Xie *et al*.[82]

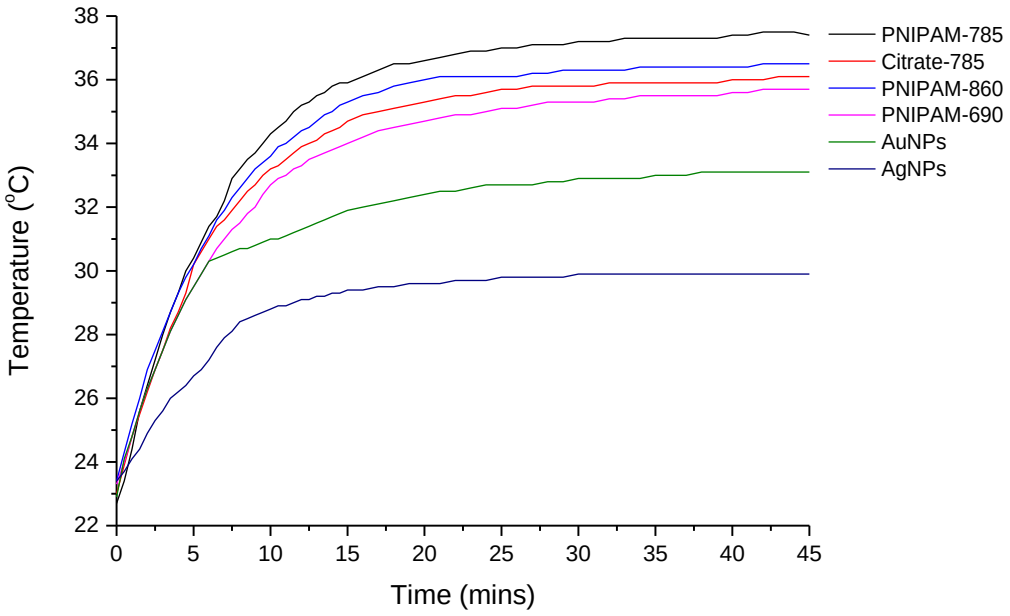

Figure 4.15 - Photothermal studies for a range of nanoparticles.

4.4.2.2 Characterisation of resonant PNIPAM coated HGNs and citrate capped HGNs

The effect on the LSPR, stability and reproducibility were investigated via extinction spectroscopy for the resonant HGNs only; where citrate-HGNs were compared to PNIPAM-HGNs, see figures 4.16 and 4.17.

During the SERS experiments before and after each cycle of the heating and cooling process, 100 uL aliquots of solution were taken and analysed; the extinction spectra,

particle sizing and zeta potential values were recorded for both batches of resonant HGNs and these can be seen in figure 4.16. The two batches of HGNs show a LSPR at 785 nm with a SEM insert clearly showing an image of these unaggregated hollow gold nanoshells. From image J it was possible to calculate that the average particle diameter (before the SERS experiments) for the PNIPAM coated HGNs was 128 ± 20 nm, while the citrate capped HGNs had an average particle size of 67 ± 10 nm. The sizes predicted by the DLS were very similar therefore it was used to obtain the sizes and zeta potential values during the SERS experiments in order to get a better understanding of how stable these nanotags were. It can be observed for the PNIPAM-HGNs that there was minimal change to the extinction spectra and average particle size with a slight decrease in the zeta potential value. Furthermore, after 2 cycles of heating and cooling the zeta potential value remained above -30 mV indicating that it's a stable colloidal solution.[127] Whereas, for the citrate-capped HGNs there was a slight increase in the average particle size with minimal decrease in the extinction spectra and zeta potential values after the first heating and cooling cycle indicating that some aggregation may be occurring but generally the nanotags were stable. However by the end of the second cycle the extinction maximum could no longer be observed due to significant broadening of the spectrum. Furthermore the average particle size had doubled and the zeta potential value was below -10 mV, indicating that these nanotags had significantly aggregated and were no longer stable colloidal solutions.

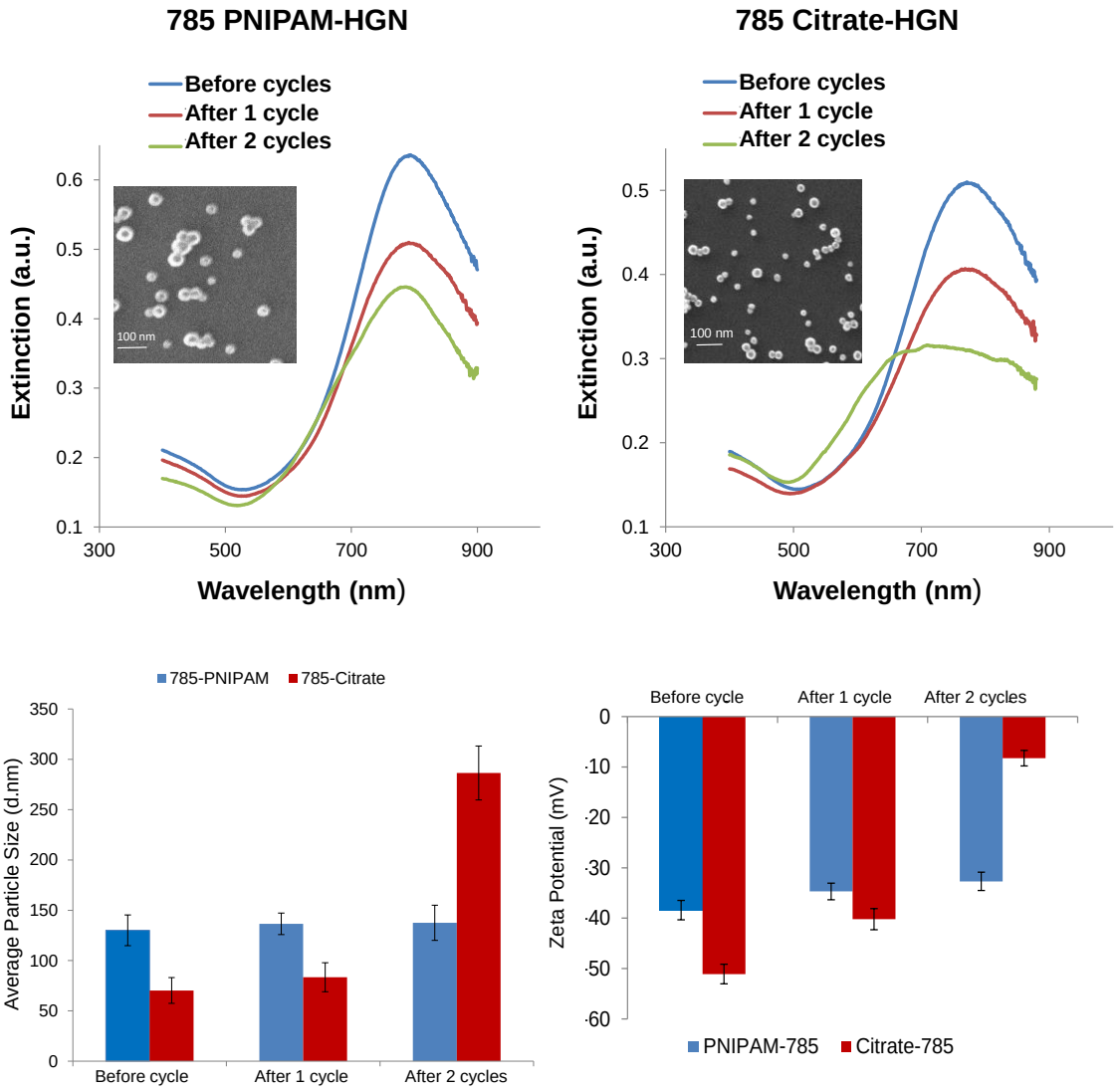

Figure 4.16 - Characterisation measurements taken during the SERS experiments for PNIPAM- HGNs and citrate-HGNs. Top figures are extinction spectra taken during SERS experiments, showing how the LSPR and stability changes over two cycles of heating and cooling past the LCST of 32 ^{o}C for PNIPAM coated HGNs and citrate capped HGNs resonant at 785 nm. Blue line highlights the extinction spectra for the bulk solutions before any heating and cooling occurs, red line is after 1 cycle of the heating and cooling process and the green line is after 2 cycles. Inserts are SEM images showing the HGN solutions before the heating and cooling process, with an average size of 128 nm and 67 nm for the PNIPAM-HGNs and citrate-HGNs respectively. Bottom figures highlight the average particle size and zeta potential values also recorded at each cycle of the SERS experiments, blue columns highlight the 785-PNIPAM HGN and the red ones indicate the 785-Citrate HGN. Figure has been reproduced by permission of the Royal Society of Chemistry.[240]

Furthermore to understand how stable these nanotags were during the heating and cooling process, they were monitored over time via extinction spectroscopy with changes in extinction at 785 nm being monitored over the temperature range 20-90-20 ^{o}C, see figure 4.17. The PNIPAM and citrate HGN solutions were heated to 90 ^{o}C, to replicate the temperatures that were likely to be experienced by the nanoshells during the SERS experiments.

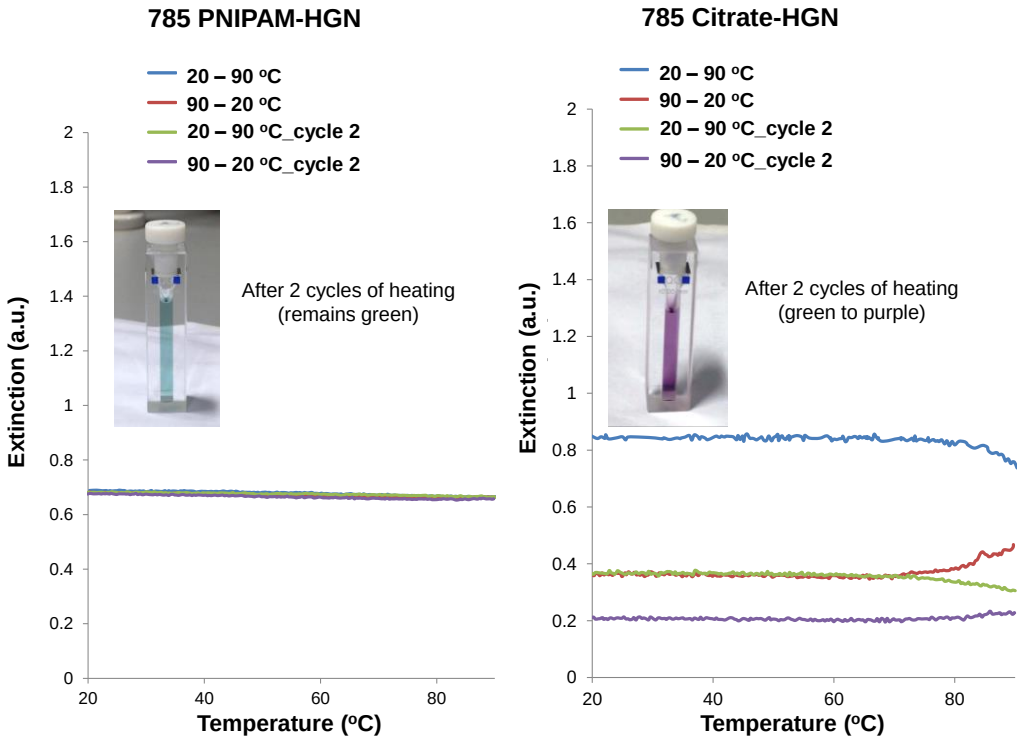

Figure 4.17 – Monitoring of wavelength maximum showing how the stability is affected for PNIPAM coated HGNs and citrate capped HGNs when the SPR maximum (785 nm) is monitored over two cycles of heating and cooling from 20 -90-20 ^{o}C. Blue and red lines highlight the first heating and cooling cycle respectively, while the green and purple lines indicate the second cycle. Note colour change for citrate-capped HGNs from green to purple showing sample degradation and over-aggregation. Figure has been reproduced by permission of the Royal Society of Chemistry.[240]

It can be observed that for PNIPAM-HGNs resonant at 785 nm, there was no change to the extinction maximum thus further confirming that these thermosensitive nanotags remain stable over two cycles of heating and cooling. Whereas for the citrate capped HGNs it can be seen that there was a decrease in the extinction maximum value indicating that they become unstable after the first heating cycle and

by the end of the second cycle there was evidence of over-aggregation and sample degradation. These claims are further confirmed by the colour change which is observed of the colloidal solution, from green (as shown with PNIPAM-HGNs) to purple.

Furthermore, from figures 4.16 and 4.17 it is evident that the PNIPAM-HGNs have minimum change to their extinction, a 33% damping but no broadening or shifting in the wavelength maximum suggesting that they do not aggregate.[23] Therefore the SERS changes must be coming from the reporter distance from the HGN surface as controlled by heating and cooling of the polymer. Whereas for the citrate-HGNs there was evidence to support sample degradation and over aggregation of the nanoshells due to significant damping and broadening of the extinction spectra. In addition, a distinct colour change was observed for the citrate-HGNs from green to purple also suggesting over aggregation. These results demonstrate the benefits of adding a PNIPAM protective coating to the HGNs through improvements to colloidal stability, reproducibility and signal intensities.[231]

4.5 Conclusions

In conclusion, thermosensitive SERS nanotags were developed and successfully detected using NIR laser excitations. The 1064 nm SERS experiments showed that the reporter molecules can be either trapped or removed from the HGN surface depending on the LSPR of the HGNs and the heating environment.

Furthermore the 785 nm experiments, demonstrated the first SERS switch using plasmonic induced heating of PNIPAM coated hollow gold nanoshells. Specifically, by designing these thermosensitive SERS nanotags the degree of enhancement was controlled by tuning the plasmonic properties of the HGNs ultimately allowing for the SERS and photothermal response of these nanotags to be monitored simultaneously over time. Moreover, it was shown that by exciting the plasmon via a resonant laser the local environment was heated, causing the polymer to collapse and the reporter molecule to come close to the HGN surface which ultimately increased the SERS response. However, upon

cooling and resultant polymer swelling, this process was reversible. These thermosensitive SERS nanotags have been shown to be stable, reproducible and they don't aggregate, and more significantly they produce strong SERS signals. Therefore they show potential for future use in a wide range of applications.

4.6 Future Work

These thermosensitive nanotags have been shown to be stable and produce strong SERS signals with BPE and MPY. Therefore, it would be of great interest to incorporate a 'chalcogen dye from chapter 3' into this set-up and determine if the SERS signals could be further enhanced and whether these reporter molecules would remain trapped or be released. It would be interesting to add a reporter molecule such as II-MB-114 or II-MB-184, which self-aggregate and are slightly larger in size than BPE or MPY to further understand whether the PNIPAM shell would still prevent aggregation and to determine if these molecules could diffuse through the porous shell to reach the HGN surface and produce a SERS signal at the beginning of the experiment or not.

To date, there have been a few papers which detail the importance of co-polymerisation to shift the LCST and make the thermopolymer application specific.[241, 242] A second polymer could be added to these thermosensitive nanotags to further increase stability, reproducibility and temperature ranges. Hence make the nanotags specific for applications in biomedical or optical research. Furthermore, a drug molecule or PTA linker could be incorporated into the set-up and these thermosensitive nanotags used for drug delivery or SERS sensing.

5. Research Conclusions

This work has demonstrated the design of NIR nanotags and thermosensitive nanotags for SERS detection. Specifically, it has been demonstrated that in order to achieve red-shifted SERS three approaches can be utilised. The first involved engineering a SERS substrate which was optically active in the NIR region and the second was the design of dye molecules which were NIR active. The third approach involved functionalising the hollow gold nanotags with the thermopolymer PNIPAM, which caused a red-shift in the LSPR and enabled SERS detection in the NIR region.

In chapter 2, 1064 nm SERS detection of NIR active hollow gold nanotags was demonstrated. By improving the synthetic procedure to yield NIR active HGNs and encapsulating these HGNs with 7 commercial Raman reporters, it allowed for effective SERS signals to be obtained at 1064 nm excitation. This work also demonstrated that red-shifted HGNs are in fact good SERS substrates and when the Raman reporters, BPE or AZPY were employed the largest SERS enhancement was observed. Furthermore, a reporter concentration of 10 μM was sufficient to give approximately monolayer coverage, forcing the reporter molecules to pack effectively with a perpendicular or nearly upright orientation on the HGN surface, thus giving strong SERS and providing effective 1064 nm SERS nanotags.

Chapter 3 went on to show the design of extreme red shifted SERS nanotags which demonstrate an unprecedented performance in the NIR region. These newly developed nanotags showed superior SERS results to the commercially available reporters and Cabot tags, across all the laser exctiation wavelengths tested. Furthermore, they demonstrated picomolar detection limits when analysed at 1280 nm and 1550 nm and femtomolar detection limits when excited at 1064 nm. These results were extraordinary, in particular the 1280 nm SERS studies as this was the first report of SERS ever being achieved at this wavelength. Furthermore, in order to design future nanotags it was

important to understand how the ligands were likely to bond and orientate on the surface of the HGNs. A computational and experimental comparison was conducted to determine that the 114 dye orientates with its major axis at an angle of ~80 degrees to the HGN surface, with two of the Se rings pointing at the surface allowing them to bond in a complex manner to the HGNs.

In the final results chapter, (chapter 4), thermosensitive SERS nanotags were developed and successfully detected using both 785 nm and 1064 nm laser excitations. It was shown that when the HGNs where functionalised with the PNIPAM polymer, a shift in the LSPR was observed and this resulted in NIR thermosensitive SERS nanotags being developed. Furthermore, the 1064 nm SERS studies demonstrated that weak and strong Raman reporters can be employed in this set-up and depending on the LSPR of the HGNs and/or the heating environment, the reporter molecules were ether trapped or removed from the HGN surface, ultimately having an effect on the SERS enhancement. Moreover the 785 nm studies, demonstrated the first report of SERS switching 'on and off' using laser induced plasmonic heating of PNIPAM coated HGNs. The degree of Raman enhancement for these thermosensitive SERS nanotags was controlled by plasmonic tuning of the HGN properties.

In summary, the design of these unique SERS nanotags which produce strong SERS signals in the uncongested spectral window of the NIR region. Could provide the basis for future advancements in bio-medical and optical applications, with a particular focus on NIR applications such PTA therapy or optical coherence tomography.

6. References

1. M. C. Daniel and D. Astruc, *Chemical Reviews*, 2004, **104**, 293-346.

2. M. Rycenga, C. M. Cobley, J. Zeng, W. Li, C. H. Moran, Q. Zhang, D. Qin and Y. Xia, *Chemical Reviews*, 2011, **111**, 3669-3712.

3. N. A. Dhas, C. P. Raj and A. Gedanken, *Chemistry of Materials*, 1998, **10**, 1446-1452.

4. Z. Peng and H. Yang, *Nano Today*, 2009, **4**, 143-164.

5. M. Rycenga, Z. Wang, E. Gordon, C. M. Cobley, A. G. Schwartz, C. S. Lo and Y. Xia, *Angewandte Chemie International Edition*, 2009, **48**, 9924-9927.

6. W. E. Smith, G. Dent and J. Wiley, *Modern Raman Spectroscopy: A Practical Approach*, Wiley Online Library, 2005.

7. A. M. Alkilany and C. J. Murphy, *Journal of Nanoparticle Research*, 2010, **12**, 2313-2333.

8. K. Saha, S. S. Agasti, C. Kim, X. Li and V. M. Rotello, *Chemical Reviews*, 2012, **112**, 2739-2779.

9. M. Grzelczak, J. Pérez-Juste, P. Mulvaney and L. M. Liz-Marzán, *Chemical Society Reviews*, 2008, **37**, 1783-1791.

10. I. A. Larmour and D. Graham, *Analyst*, 2011, **136**, 3831-3853.

11. D. A. Giljohann, D. S. Seferos, W. L. Daniel, M. D. Massich, P. C. Patel and C. A. Mirkin, *Angewandte Chemie International Edition*, 2010, **49**, 3280-3294.

12. P. Sciau, *Nanoparticles in Ancient Materials: The Metallic Lustre Decorations of Medieval Ceramics*, INTECH Open Access Publisher, 2012.

13. L. M. Liz-Marzán, *Langmuir*, 2006, **22**, 32-41.

14. J. S. Turkevitch, P. C. Hillier, *Discussions of the Faraday Society*, 1951, **11**, 55-75.

15. G. Frens, *Nature Physical Science*, 1973, **241**, 20-22.

16. Ž. Krpetić, L. Guerrini, I. A. Larmour, J. Reglinski, K. Faulds and D. Graham, *Small*, 2012, **8**, 707-714.

17. C. M. Cobley, J. Chen, E. C. Cho, L. V. Wang and Y. Xia, *Chemical Society Reviews*, 2011, **40**, 44-56.

18. J. Homola, S. S. Yee and G. Gauglitz, *Sensors and Actuators B: Chemical*, 1999, **54**, 3-15.

19. G. Mie, *Annalen der Physik*, 1908, **330**, 377-445.

20. M. Hu, J. Chen, Z. Y. Li, L. Au, G. V. Hartland, X. Li, M. Marquez and Y. Xia, *Chemical Society Reviews*, 2006, **35**, 1084-1094.

21. P. B. Johnson and R.W. Christy, *Physical Review B*, 1972, **6**, 4370-4379.

22. L. M. Liz-Marzán, M. Giersig and P. Mulvaney, *Langmuir*, 1996, **12**, 4329-4335.

23. K. A. Willets and R. P. Van Duyne, *Annual Review of Physical Chemistry*, 2007, **58**, 267-297.

24. C. L. Nehl, J. H. Hafner, *Journal of Materials Chemistry*, 2008, **18**, 2415-2418.

25. P. K. Jain and K. S. Lee, I. H. El-Sayed and M. A. El-Sayed, *The Journal of Physical Chemistry B*, 2006, **110**, 7238-7248.

26. P. Waterman, *Proceedings of the IEEE*, 1965, **53**, 805-812.

27. S. Preciado-Flores, D. Wang, D. A. Wheeler, R. Newhouse, J. K. Hensel, A. Schwartzberg, L. Wang, J. Zhu, M. Barboza-Flores and J. Z. Zhang, *Journal of Materials Chemistry*, 2011, **21**, 2344-2350.

28. A. M. Schwartzberg, T. Y. Olson, C. E. Talley and J. Z. Zhang, *The Journal of Physical Chemistry B*, 2006, **110**, 19935-19944.

29. S. E. Skrabalak, J. Chen, Y. Sun, X. Lu, L. Au, C. M. Cobley and Y. Xia, *Accounts of Chemical Research*, 2008, **41**, 1587-1595.

30. B. Nikoobakht and M. A. El-Sayed, *Chemistry of Materials*, 2003, **15**, 1957-1962.

31. C. J. Huang, Y. H. Wang, P. H. Chiu, M. C. Shih and T. H. Meen, *Materials Letters*, 2006, **60**, 1896-1900.

32. C. J. Huang, P. H. Chiu, Y. H. Wang, W. R. Chen, T. H. Meen and C. F. Yang, *Nanotechnology*, 2006, **17**, 5355-5362.

33. E. Nalbant Esenturk and A. Hight Walker, *Journal of Raman Spectroscopy*, 2009, **40**, 86-91.

34. X. Wang, J. Song and Z. L. Wang, *Chemical Physics Letters*, 2006, **424**, 86-90.

35. K. Schröder and A. Csáki, *Plasmonic tuning of optical fibers for biosensing*, *http://spie.org/x48694.xml*, Accessed 16th May 2015.

36. A. Csáki, F. Jahn, I. Latka, T. Henkel, D. Malsch, T. Schneider, K. Schröder, K. Schuster, A. Schwuchow and R. Spittel, *Small*, 2010, **6**, 2584-2589.

37. K. Schröder, A. Csáki, A. Schwuchow, I. Latka, K. Strehlau, T. Henkel, D. Malsch, K. Schuster, K. Weber and R. Möller, *SPIE Conference Optics + Optoelectronics*, June 2011.

38. P. Chow, *Gold Nanoparticles: Properties, Characterization and Fabrication*, Nova Science Publishers, 2010.

39. S. J. Oldenburg, *Silver Nanoparticles: Properties and Applications; http://www.sigmaaldrich.com/materials-science/nanomaterials/silver-nanoparticles.html*, Accessed 16th May 2015.

40. S. Link and M. A. El-Sayed, *The Journal of Physical Chemistry B*, 1999, **103**, 4212-4217.

41. E. Hao, S. Li, R. C. Bailey, S. Zou, G. C. Schatz and J. T. Hupp, *The Journal of Physical Chemistry B*, 2004, **108**, 1224-1229.

42. J. Zhou, J. Ralston, R. Sedev and D. A. Beattie, *Journal of Colloid and Interface Science*, 2009, **331**, 251-262.

43. A. M. Schwartzberg, C. D. Grant, A. Wolcott, C. E. Talley, T. R. Huser, R. Bogomolni and J. Z. Zhang, *The Journal of Physical Chemistry B*, 2004, **108**, 19191-19197.

44. E. Boisselier and D. Astruc, *Chemical Society Reviews*, 2009, **38**, 1759-1782.

45. R. R. Anderson and J. A. Parrish, *Journal of Investigative Dermatology*, 1981, **77**, 13-19.

46. N. J. Durr, T. Larson, D. K. Smith, B. A. Korgel, K. Sokolov and A. Ben-Yakar, *Nano Letters*, 2007, **7**, 941-945.

47. M. Eghtedari, A. V. Liopo, J. A. Copland, A. A. Oraevsky and M. Motamedi, *Nano Letters*, 2008, **9**, 287-291.

48. J. You, G. Zhang and C. Li, *ACS Nano*, 2010, **4**, 1033-1041.

49. J. Z. Zhang, *The Journal of Physical Chemistry Letters*, 2010, **1**, 686-695.

50. J. You, R. Zhang, G. Zhang, M. Zhong, Y. Liu, C. S. Van Pelt, D. Liang, W. Wei, A. K. Sood and C. Li, *Journal of Controlled Release*, 2012, **158**, 319-328.

51. J. Chen, D. Wang, J. Xi, L. Au, A. Siekkinen, A. Warsen, Z. Y. Li, H. Zhang, Y. Xia and X. Li, *Nano Letters*, 2007, **7**, 1318-1322.

52. J. Chen, C. Glaus, R. Laforest, Q. Zhang, M. Yang, M. Gidding, M. J. Welch and Y. Xia, *Small*, 2010, **6**, 811-817.

53. Y. Xia, W. Li, C. M. Cobley, J. Chen, X. Xia, Q. Zhang, M. Yang, E. C. Cho and P. K. Brown, *Accounts of Chemical Research*, 2011, **44**, 914-924.

54. X. Huang, I. H. El-Sayed, W. Qian and M. A. El-Sayed, *Journal of the American Chemical Society*, 2006, **128**, 2115-2120.

55. W. S. Kuo, C. N. Chang, Y. T. Chang, M. H. Yang, Y. H. Chien, S. J. Chen and C. S. Yeh, *Angewandte Chemie*, 2010, **122**, 2771-2775.

56. E. B. Dickerson, E. C. Dreaden, X. Huang, I. H. El-Sayed, H. Chu, S. Pushpanketh, J. F. McDonald and M. A. El-Sayed, *Cancer Letters*, 2008, **269**, 57-66.

57. J. Chen, F. Saeki, J. Benjamin, H. Cang, M. J. Cobb, Z. Y. Li, L. Au, H. Zhang, M. B. Kimmey and X. Li, *Nano Letters*, 2005, **5**, 473-477.

58. W. Lu, Q. Huang, G. Ku, X. Wen, M. Zhou, D. Guzatov, P. Brecht, R. Su, A. Oraevsky and L. V. Wang, *Biomaterials*, 2010, **31**, 2617-2626.

59. W. Lu, M. P. Melancon, C. Xiong, Q. Huang, A. Elliott, S. Song, R. Zhang, L. G. Flores, J. G. Gelovani and L. V. Wang, *Cancer Research*, 2011, **71**, 6116-6121.

60. X. Yang, S. E. Skrabalak, Z. Y. Li, Y. Xia and L. V. Wang, *Nano Letters*, 2007, **7**, 3798-3802.

61. A. Agarwal, S. Huang, M. O'Donnell, K. Day, M. Day, N. Kotov and S. Ashkenazi, *Journal of Applied Physics*, 2007, **102**, 064701.

62. J. Chen, F. Saeki, B. J. Wiley, H. Cang, M. J. Cobb, Z. Y. Li, L. Au, H. Zhang, M. B. Kimmey and X. Li, *Nano Letters*, 2005, **5**, 473-477.

63. J. Pérez-Juste, I. Pastoriza-Santos, L. M. Liz-Marzán and P. Mulvaney, *Coordination Chemistry Reviews*, 2005, **249**, 1870-1901.

64. H. Ding, K. T. Yong, I. Roy, H. E. Pudavar, W. C. Law, E. J. Bergey and P. N. Prasad, *The Journal of Physical Chemistry C*, 2007, **111**, 12552-12557.

65. J. Kim, Y. Piao and T. Hyeon, *Chemical Society Reviews*, 2009, **38**, 372-390.

66. E. Katz and I. Willner, *Angewandte Chemie International Edition*, 2004, **43**, 6042-6108.

67. J. Chen, B. Wiley, Z. Y. Li, D. Campbell, F. Saeki, H. Cang, L. Au, J. Lee, X. Li and Y. Xia, *Advanced Materials*, 2005, **17**, 2255-2261.

68. F. Kim, J. H. Song and P. Yang, *Journal of the American Chemical Society*, 2002, **124**, 14316-14317.

69. S. S. Chang, C. W. Shih, C. D. Chen, W. C. Lai and C. R. C. Wang, *Langmuir*, 1999, **15**, 701-709.

70. C. R. Martin, *Science*, 1994, **266**, 1961-1966.

71. N. R. Jana, L. Gearheart and C. J. Murphy, *The Journal of Physical Chemistry B*, 2001, **105**, 4065-4067.

72. C. Yu, L. Varghese and J. Irudayaraj, *Langmuir*, 2007, **23**, 9114-9119.

73. K. S. Lee and M. A. El-Sayed, *The Journal of Physical Chemistry B*, 2005, **109**, 20331-20338.

74. C. D. Chen, S. F. Cheng, L. K. Chau and C. C. Wang, *Biosensors and Bioelectronics*, 2007, **22**, 926-932.

75. G. Raschke, S. Brogl, A. Susha, A. Rogach, T. Klar, J. Feldmann, B. Fieres, N. Petkov, T. Bein and A. Nichtl, *Nano Letters*, 2004, **4**, 1853-1857.

76. X. Huang, S. Neretina and M. A. El-Sayed, *Advanced Materials*, 2009, **21**, 4880-4910.

77. Y. Sun, B. Mayers and Y. Xia, *Advanced Materials*, 2003, **15**, 641-646.

78. J. M. McLellan, Z. Y. Li, A. R. Siekkinen and Y. Xia, *Nano Letters*, 2007, **7**, 1013-1017.

79. H. P. Liang, L. J. Wan, C. L. Bai and L. Jiang, *The Journal of Physical Chemistry B*, 2005, **109**, 7795-7800.

80. H. Xie, I. A. Larmour, W. E. Smith, K. Faulds and D. Graham, *The Journal of Physical Chemistry C*, 2012, **116**, 14, 8338-8342.

81. S. Lee, H. Chon, M. Lee, J. Choo, S. Y. Shin, Y. H. Lee, S. W. Son and C. H. Oh, *Biosensors and Bioelectronics*, 2009, **24**, 2260-2263.

82. H. Xie, I. A. Larmour, Y. C. Chen, A. W. Wark, V. Tileli, D. W. McComb, K. Faulds and D. Graham, *Nanoscale*, 2013, **5**, 765-771.

83. M. P. Melancon, W. Lu, Z. Yang, R. Zhang, Z. Cheng, A. M. Elliot, J. Stafford, T. Olson, J. Z. Zhang and C. Li, *Molecular Cancer Therapeutics*, 2008, **7**, 1730-1739.

84. W. Lu, C. Xiong, G. Zhang, Q. Huang, R. Zhang, J. Z. Zhang and C. Li, *Clinical Cancer Research*, 2009, **15**, 876-886.

85. G. R. Souza, C. S. Levin, A. Hajitou, R. Pasqualini, W. Arap and J. H. Miller, *Analytical Chemistry*, 2006, **78**, 6232-6237.

86. H. Chon, C. Lim, S. M. Ha, Y. Ahn, E. K. Lee, S. I. Chang, G. H. Seong and J. Choo, *Analytical Chemistry*, 2010, **82**, 5290-5295.

87. S. Liu, J. Liu, X. Han, Y. Cui and W. Wang, *Biosensors and Bioelectronics*, 2010, **25**, 1640-1645.

88. K. Dowling, M. Dayel, M. Lever, P. French, J. Hares and A. Dymoke-Bradshaw, *Optics Letters*, 1998, **23**, 810-812.

89. L. Kaufman, F. Deconinck, D. Price, P. Guesry, C. Wilson, B. Hruska, S. Swann, D. Camp, A. Voegele and R. Friesen, *Investigative Radiology*, 1976, **11**, 210-215.

90. E. J. Irvine, A. Hernandez-Santana K. Faulds and D. Graham, *Analyst*, 2011, **136**, 2925-2930.

91. K. Gracie, W. E. Smith, P. Yip, J. Sutter, D. Birch, D. Graham and K. Faulds, *Analyst*, 2014, **139**, 3735-3743.

92. J. Strutt, *Philosophical Magazine*, 1871, **41**, 107-120.

93. C. V. Raman and K. S. Krishnan, *Nature*, 1928, **121**, 501-502.

94. B. Vlckova, I. Pavel, M. Sladkova, K. Siskova and M. Slouf, *Journal of Molecular Structure*, 2007, **834**, 42-47.

95. M. Culha, B. Cullum, N. Lavrik and C. K. Klutse, *Journal of Nanotechnology*, 2012, **2012**, 1-15.

96. G. McNay, D. Eustace, W. E. Smith, K. Faulds and D. Graham, *Applied Spectroscopy*, 2011, **65**, 825-837.

97. M. J. Pelletier, *Analytical Applications of Raman Spectroscopy*, Wiley-Blackwell, 1999.

98. K. Kneipp, M. Moskovits and H. Kneipp, *Surface-Enhanced Raman Scattering: Physics and Applications*, Springer Verlag, 2006.

99. M. G. Albrecht and J. A. Creighton, *Journal of the American Chemical Society*, 1977, **99**, 5215-5217.

100. D. L. Jeanmaire and R. P. Van Duyne, *Journal of Electroanalytical Chemistry and Interfacial Electrochemistry*, 1977, **84**, 1-20.

101. K. Kneipp, H. Kneipp, I. Itzkan, R. R. Dasari and M. S. Feld, *Chemical Reviews*, 1999, **99**, 2957-2976.

102. B. Persson, *Chemical Physics Letters*, 1981, **82**, 561-565.

103. L. Brus, *Accounts of Chemical Research*, 2008, **41**, 1742-1749.

104. I. Shadi, B. Chowdhry, M. Snowden and R. Withnall, *Spectrochimica Acta Part A: Molecular and Biomolecular Spectroscopy*, 2003, **59**, 2213-2220.

105. I. A. Larmour, K. Faulds and D. Graham, *The Journal of Physical Chemistry C*, 2010, **114** 13429-13254.

106. R. J. Stokes, A. Macaskill, P. J. Lundahl, W. E. Smith, K. Faulds and D. Graham, *Small*, 2007, **3**, 1593-1601.

107. A. Stacy and R. Van Duyne, *Chemical Physics Letters*, 1983, **102**, 365-370.

108. D. Graham, W. E. Smith, A. M. Linacre, C. H. Munro, N. D. Watson and P. C. White, *Analytical Chemistry*, 1997, **69**, 4703-4707.

109. C. McHugh, F. Docherty, D. Graham and W. E. Smith, *Analyst*, 2004, **129**, 69-72.

110. K. Faulds, R. Jarvis, W. E. Smith, D. Graham and R. Goodacre, *Analyst*, 2008, **133**, 1505-1512.

111. H. Kearns, N. Shand, W. E. Smith, K. Faulds and D. Graham, *Physical Chemistry Chemical Physics*, 2015, **17**, 1980-1986.

112. T. A. Laurence, G. Braun, C. Talley, A. Schwartzberg, M. Moskovits, N. Reich and T. Huser, *Journal of the American Chemical Society*, 2008, **131**, 162-169.

113. A. M. Schwartzberg, T. Y. Oshiro, J. Z. Zhang, T. Huser and C. E. Talley, *Analytical Chemistry*, 2006, **78**, 4732-4736.

114. S. Lee, H. Chon, J. Lee, J. Ko, B. H. Chung, D. W. Lim and J. Choo, *Biosensors and Bioelectronics*, 2014, **51**, 238-243.

115. S. L. Kleinman, R. R. Frontiera, A. I. Henry, J. A. Dieringer and R. P. Van Duyne, *Physical Chemistry Chemical Physics*, 2013, **15**, 21-36.

116. S. J. Oldenburg, S. L. Westcott, R. D. Averitt and N. J. Halas, *The Journal of Chemical Physics*, 1999, **111**, 4729-4735.

117. S. Lefrant, I. Baltog, M. Baibarac, J. Mevellec and O. Chauvet, *Carbon*, 2002, **40**, 2201-2211.

118. N. Leopold and B. Lendl, *The Journal of Physical Chemistry B*, 2003, **107**, 5723-5727.

119. L. Hirsch, J. Jackson, A. Lee, N. Halas and J. West, *Analytical Chemistry*, 2003, **75**, 2377-2381.

120. L. R. Hirsch, R. Stafford, J. Bankson, S. Sershen, B. Rivera, R. Price, J. Hazle, N. Halas and J. West, *Proceedings of the National Academy of Sciences*, 2003, **100**, 13549-13554.

121. D. P. O'Neal, L. R. Hirsch, N. J. Halas, J. D. Payne and J. L. West, *Cancer Letters*, 2004, **209**, 171-176.

122. H. Xie, I. A. Larmour, K. Faulds and D. Graham, *The Journal of Physical Chemistry C*, 2012, **116** 8338-8342.

123. E. Boisselier and D. Astruc, *Chemical Society Reviews*, 2009, **38**, 1759-1782.

124. A. Bashkatov, E. Genina, V. Kochubey and V. Tuchin, *Journal of Physics D: Applied Physics*, 2005, **38**, 2543.

125. M. Culha, B. Cullum, N. Lavrik and C. K. Klutse, *Journal of Nanotechnology*, 2012, **2012,** 1-15.

126. A. McLintock, N. Hunt and A. W. Wark, *Chemical Communications*, 2011, **47**, 3757-3759.

127. M. Instruments, *Zetasizer Nano Series User Manual*, 2009.

128. K. F. Gibson, D. Correia-Ledo, M. Couture, D. Graham and J. F. Masson, *Chemical Communications*, 2011, **47**, 3404-3406.

129. S. Abalde-Cela, S. Ho, B. Rodríguez-González, M. A. Correa-Duarte, R. A. Álvarez-Puebla, L. M. Liz-Marzán and N. A. Kotov, *Angewandte Chemie*, 2009, **121**, 5430-5433.

130. B. Nikoobakht, J. Wang and M. A. El-Sayed, *Chemical Physics Letters*, 2002, **366**, 17-23.

131. I. Khan, D. Cunningham, S. Lazar, D. Graham, W. E. Smith and D. W. McComb, *Faraday Discussions*, 2006, **132**, 171-178.

132. G. Ku, M. Zhou, S. Song, Q. Huang, J. Hazle and C. Li, *Acs Nano*, 2012, **6**, 7489-7496.

133. J. Hu, B. Zhao, W. Xu, B. Li and Y. Fan, *Spectrochimica Acta Part A: Molecular and Biomolecular Spectroscopy*, 2002, **58**, 2827-2834.

134. A. Michota and J. Bukowska, *Journal of Raman Spectroscopy*, 2003, **34**, 21-25.

135. Z. Zhuang, J. Cheng, X. Wang, Y. Yin, G. Chen, B. Zhao, H. Zhang and G. Zhang, *Journal of Molecular Structure*, 2006, **794**, 77-82.

136. Z. Zhuang, J. Cheng, H. Jia, J. Zeng, X. Han, B. Zhao, H. Zhang, G. Zhang and W. Zhao, *Vibrational Spectroscopy*, 2007, **43**, 306-312.

137. X. Wang, B. Zhao, Y. Wang, Y. Wu, W. Xu and Y. Fan, *Materials Science and Engineering: C*, 1999, **10**, 3-6.

138. W. H. Yang, J. Hulteen, G. C. Schatz and R. P. Van Duyne, *The Journal of Chemical Physics*, 1996, **104**, 4313-4323.

139. A. Kim, F. S. Ou, D. A. Ohlberg, M. Hu, R. S. Williams and Z. Li, *Journal of the American Chemical Society*, 2011, **133**, 8234-8239.

140. T. Lou, Y. Wang, J. Li, H. Peng, H. Xiong and L. Chen, *Analytical and Bioanalytical Chemistry*, 2011, **401**, 333-338.

141. W. E. Doering, M. E. Piotti, M. J. Natan and R. G. Freeman, *Advanced Materials*, 2007, **19**, 3100-3108.

142. Z. Zhuang, X. Shang, X. Wang, W. Ruan and B. Zhao, *Spectrochimica Acta Part A: Molecular and Biomolecular Spectroscopy*, 2009, **72**, 954-958.

143. Z. Zhuang, X. Shi, Y. Chen and M. Zuo, *Spectrochimica Acta Part A: Molecular and Biomolecular Spectroscopy*, 2011, **79**, 1593-1599.

144. D. Sikdar, I. D. Rukhlenko, W. Cheng and M. Premaratne, *Biomedical Optics Express*, 2013, **4**, 15-31.

145. M. M. Harper, K. S. McKeating and K. Faulds, *Physical Chemistry Chemical Physics*, 2013, **15**, 5312-5328.

146. K. Gracie, E. Correa, S. Mabbott, J. A. Dougan, D. Graham, R. Goodacre and K. Faulds, *Chemical Science*, 2014, **5**, 1030-1040.

147. S. McAughtrie, K. Lau, K. Faulds and D. Graham, *Chemical Science*, 2013, **4**, 3566-3572.

148. A. Samanta, K. K. Maiti, K. S. Soh, X. Liao, M. Vendrell, U. Dinish, S. W. Yun, R. Bhuvaneswari, H. Kim and S. Rautela, *Angewandte Chemie International Edition*, 2011, **50**, 6089-6092.

149. K. K. Maiti, U. Dinish, A. Samanta, M. Vendrell, K. S. Soh, S. J. Park, M. Olivo and Y. T. Chang, *Nano Today*, 2012, **7**, 85-93.

150. J. M. Schmitt, A. Knuttel, M. Yadlowsky and M. Eckhaus, *Physics in Medicine and Biology*, 1994, **39**, 1705-1720.

151. M. Balu, T. Baldacchini, J. Carter, T. B. Krasieva, R. Zadoyan and B. J. Tromberg, *Journal of Biomedical Optics*, 2009, **14**, 010508-010503.

152. I. H. Chen, S. W. Chu, C. K. Sun, P. C. Cheng and B. L. Lin, *Optical and Quantum Electronics*, 2002, **34**, 1251-1266.

153. C. L. Zavaleta, B. R. Smith, I. Walton, W. Doering, G. Davis, B. Shojaei, M. J. Natan and S. S. Gambhir, *Proceedings of the National Academy of Sciences*, 2009, **106**, 13511-13516.

154. X. M. Qian and S. Nie, *Chemical Society Reviews*, 2008, **37**, 912-920.

155. A. McLintock, H. J. Lee and A. W. Wark, *Physical Chemistry Chemical Physics*, 2013, **15**, 18835-18843.

156. C. Brouillette, H. Huang, W. E. Smith and S. Farquharson, *Applied Spectroscopy*, 2011, **65**, 561-563.

157. H. Huang, C. Shende, A. Sengupta, F. Inscore, C. Brouillette, W. E. Smith and S. Farquharson, *Journal of Raman Spectroscopy*, 2012, **43**, 701–705.

158. K. A. Lynn, G. McNay, D. A. Eustace, N. C. Shand and W. E. Smith, *Analyst*, 2010, **135**, 1904-1905.

159. M. Donahue, H. Huang, C. Brouillette, W. E. Smith and S. Farquharson, *http://www.spectroscopyonline.com/detecting-explosives-portable-raman-analyzers-comparison-785-976-1064-and-1550-nm-retina-safe-laser,* Accessed 16th May, 2015.

160. J. Barton, A. Welch and J. Izatt, *Optics Express*, 1998, **3**, 251-256.

161. B. Bouma, G. Tearney, I. Bilinsky, B. Golubovic and J. Fujimoto, *Optics Letters*, 1996, **21**, 1839-1841.

162. D. Kobat, M. E. Durst, N. Nishimura, A. W. Wong, C. B. Schaffer and C. Xu, *Optics Express*, 2009, **17**, 13354-13364.

163. D. H. Kim, R. M. Jarvis, Y. Xu, A. W. Oliver, J. W. Allwood, L. Hampson, I. N. Hampson and R. Goodacre, *Analyst*, 2010, **135**, 1235-1244.

164. S. Mabbott, A. Eckmann, C. Casiraghi and R. Goodacre, *Analyst*, 2013, **138**, 118-122.

165. G. W. T. M. J. Frisch, J. R. Cheeseman, G. Scalmani, M. Caricato, H. P. Hratchian, X. Li, V. Barone, J. Bloino, G. Zheng, T. Vreven, J. A. Montgomery, Jr., G. A. Petersson, G. E. Scuseria, H. B. Schlegel, H. Nakatsuji, A. F. Izmaylov, R. L. Martin, J. L. Sonnenberg, J. E. Peralta, J. J. Heyd, E. Brothers, F. Ogliaro, M. Bearpark, M. A. Robb, B. Mennucci, K. N. Kudin, V. N. Staroverov, R. Kobayashi, J. Normand, A. Rendell, R. Gomperts, V. G. Zakrzewski, M. Hada, M. Ehara, K. Toyota, R. Fukuda, J. Hasegawa, M. Ishida, T. Nakajima, Y. Honda, O. Kitao and H. Nakai., *Gaussian 09 Software, http://www.gaussian.com/g_tech/g_ur/m_citation.htm,* Accessed 16th May, 2015.

166. F. Weigend and R. Ahlrichs, *Physical Chemistry Chemical Physics*, 2005, **7**, 3297-3305.

167. F. Weigend, *Physical Chemistry Chemical Physics*, 2006, **8**, 1057-1065.

168. A. D. Becke, *The Journal of Chemical Physics*, 1993, **98**, 5648-5652.

169. C. Lee, W. Yang and R. Parr, *Physical Review B*, 1994, **98**, 11623-11627.

170. S. Vosko, L. Wilk and M. Nusair, *Canadian Journal of Physics*, 1980, **58**, 1200-1211.

171. P. Stephens, F. Devlin, C. Chabalowski and M. J. Frisch, *The Journal of Physical Chemistry*, 1994, **98**, 11623-11627.

172. M. R. Detty and B. J. Murray, *The Journal of Organic Chemistry*, 1982, **47**, 5235-5239.

173. M. R. Detty, J. McKelvey and H. Luss, *Organometallics*, 1988, **7**, 1131-1147.

174. M. Bedics, H. Kearns, J. Cox, S. Mabbott, F. Ali, N. Shand, K. Faulds, J. Benedict, D. Graham and M. Detty, *Chemical Science*, 2015, **6**, 2302-2306.

175. P. L. Stiles, J. A. Dieringer, N. C. Shah and R. P. Van Duyne, *Annual Review of Analytical Chemistry*, 2008, **1**, 601-626.

176. A. Dube, A. R. Chadeayne, M. Sharma, P. T. Wolczanski and J. R. Engstrom, *Journal of the American Chemical Society*, 2005, **127**, 14299-14309.

177. T. Nakamura, R. Kimura, F. Matsui, H. Kondoh, T. Ohta, H. Sakai, M. Abe and M. Matsumoto, *Langmuir*, 2000, **16**, 4213-4216.

178. F. K. Huang, R. C. Horton, D. C. Myles and R. L. Garrell, *Langmuir*, 1998, **14**, 4802-4808.

179. S. Y. Lee, E. Ito, H. Kang, M. Hara, H. Lee and J. Noh, *The Journal of Physical Chemistry C*, 2014, **118**, 8322-8330.

180. J. A. Dougan and K. Faulds, *Analyst*, 2012, **137**, 545-554.

181. I. Khan, D. Cunningham, R. E. Littleford, D. Graham, W. E. Smith and D. W. McComb, *Analytical Chemistry*, 2006, **78**, 224-230.

182. W. Haiss, N. T. K. Thanh, J. Aveyard and D. G. Fernig, *Analytical Chemistry*, 2007, **79**, 4215-4221.

183. E. C. Le Ru and P. G. Etchegoin, *Principles of Surface-Enhanced Raman Spectroscopy: and Related Plasmoni Effects*, Elsevier Science, 2008.

184. S. L. Kleinman, E. Ringe, N. Valley, K. L. Wustholz, E. Phillips, K. A. Scheidt, G. C. Schatz and, R. P. Van Duyne *Journal of American Chemical Society*, 2011, **133**, 4115-4112.

185. X. Qian, J. Li and S. Nie, *Journal of the American Chemical Society*, 2009, **131**, 7540-7541.

186. S. Moreton, K. Faulds, N. Shand, M. Bedics, M. Detty and D. Graham, *Nanoscale*, 2015, **7**, 6075-6082.

187. L. Quaroni and G. Chumanov, *Journal of the American Chemical Society*, 1999, **121**, 10642-10643.

188. D. Craig, J. Simpson, K. Faulds and D. Graham, *Chemical Communications*, 2013, **49**, 30-32.

189. L. Rocks, K. Faulds and D. Graham, *Chemical Communications*, 2011, **47**, 4415-4417.

190. T. Donnelly, W. E. Smith, K. Faulds and Duncan Graham, *Chemical Communications*, 2014, **50**, 12907-12910.

191. X. Huang, P. K. Jain, I. H. El-Sayed and M. A. El-Sayed, *Lasers in Medical Science*, 2008, **23**, 217-228.

192. J. Kopeček, *Biomaterials*, 2007, **28**, 5185-5192.

193. A. K. A. S. Brun-Graeppi, C. Richard, M. Bessodes, D. Scherman and O. W. Merten, *Progress in Polymer Science*, 2010, **35**, 1311-1324.

194. J. Y. Sun, X. Zhao, W. R. Illeperuma, O. Chaudhuri, K. H. Oh, D. J. Mooney, J. J. Vlassak and Z. Suo, *Nature*, 2012, **489**, 133-136.

195. K. Y. Lee and D. J. Mooney, *Chemical Reviews*, 2001, **101**, 1869-1879.

196. I. Molina, S. M. Li, M. B. Martinez and M. Vert, *Biomaterials*, 2001, **22**, 363-369.

197. M. Zhou, A. M. Smith, A. K. Das, N. W. Hodson, R. F. Collins, R. V. Ulijn and J. E. Gough, *Biomaterials*, 2009, **30**, 2523-2530.

198. J. Wang, M. Gu, J. Di, Y. Gao, Y. Wu and Y. Tu, *Bioprocess and Biosystems Engineering*, 2007, **30**, 289-296.

199. D. T. Eddington and D. J. Beebe, *Advanced Drug Delivery Reviews*, 2004, **56**, 199-210.

200. J. L. Drury and D. J. Mooney, *Biomaterials*, 2003, **24**, 4337-4351.

201. G. Graziano, *International Journal of Biological Macromolecules*, 2000, **27**, 89-97.

202. L. C. Dong and A. S. Hoffman, *Journal of Controlled Release*, 1991, **15**, 141-152.

203. C. Alvarez-Lorenzo, L. Bromberg and A. Concheiro, *Photochemistry and Photobiology*, 2009, **85**, 848-860.

204. R. Zhang, M. Tang, A. Bowyer, R. Eisenthal and J. Hubble, *Biomaterials*, 2005, **26**, 4677-4683.

205. H. Meng and J. Hu, *Journal of Intelligent Material Systems and Structures*, 2010, **21**, 859-885.

206. S. B. Leeb, E. C. Lupton, X. Yu and G. Hovorka, Google Patents, 1998.

207. R. A. Alvarez-Puebla and L. M. Liz-Marzán, *Chemical Society Reviews*, 2012, **41**, 43-51.

208. T. Tanaka, I. Nishio, S. T. Sun and S. Ueno-Nishio, *Science*, 1982, **218**, 467-469.

209. A. Suzuki and T. Tanaka, *Nature*, 1990, **346**, 345 - 347.

210. T. Tanaka, *Physica A: Statistical Mechanics and its Applications*, 1986, **140**, 261-268.

211. D. Schmaljohann, *Advanced Drug Delivery Reviews*, 2006, **58**, 1655-1670.

212. M. A. Ward and T. K. Georgiou, *Polymers*, 2011, **3**, 1215-1242.

213. M. N. T. Okano and F. M. Winnik, *Material Matters*, 2010, **5**, 56-61.

214. D. Nisbet, K. Crompton, S. Hamilton, S. Shirakawa, R. Prankerd, D. Finkelstein, M. Horne and J. Forsythe, *Biophysical Chemistry*, 2006, **121**, 14-20.

215. D. R. Nisbet, A. E. Rodda, M. K. Horne, J. S. Forsythe and D. I. Finkelstein, *Tissue Engineering Part A*, 2010, **16**, 2833-2842.

216. A. K. A. S. Brun-Graeppi, C. Richard, M. Bessodes, D. Scherman, T. Narita, G. Ducouret and O. W. Merten, *Carbohydrate Polymers*, 2010, **80**, 555-562.

217. T. Law, T. Whateley and A. Florence, *International Journal of Pharmaceutics*, 1984, **21**, 277-287.

218. A. L. Clutterbuck, C. A. Cochrane, J. Dolman and S. L. Percival, *Annals of Clinical Microbiology and Antimicrobials*, 2007, **6**, 2, 1-10.

219. S. S. Stalling, S. O. Akintoye and S. B. Nicoll, *Acta Biomaterialia*, 2009, **5**, 1911-1918.

220. F. A. Aouada, Z. Pan, W. J. Orts and L. H. Mattoso, *Journal of Applied Polymer Science*, 2009, **114**, 2139-2148.

221. M. J. Caicco, T. Zahir, A. J. Mothe, B. G. Ballios, A. J. Kihm, C. H. Tator and M. S. Shoichet, *Journal of Biomedical Materials Research Part A*, 2013, **101**, 1472-1477.

222. J. M. Dang, D. D. Sun, Y. Shin-Ya, A. N. Sieber, J. P. Kostuik and K. W. Leong, *Biomaterials*, 2006, **27**, 406-418.

223. H. T. Ta, C. R. Dass and D. E. Dunstan, *Journal of Controlled Release*, 2008, **126**, 205-216.

224. C. Wei, C. Hou, Q. Gu, L. Jiang, B. Zhu and A. Sheng, *Iranian Polymer Journal*, 2009, **18**, 355-364.

225. D. L. Nettles, A. Chilkoti and L. A. Setton, *Advanced Drug Delivery Reviews*, 2010, **62**, 1479-1485.

226. M. K. McHale, L. A. Setton and A. Chilkoti, *Tissue Engineering*, 2005, **11**, 1768-1779.

227. H. Betre, S. R. Ong, F. Guilak, A. Chilkoti, B. Fermor and L. A. Setton, *Biomaterials*, 2006, **27**, 91-99.

228. Y. Wu, J. A. MacKay, J. R. McDaniel, A. Chilkoti and R. L. Clark, *Biomacromolecules*, 2008, **10**, 19-24.

229. L. Guo, J. Nie, B. Du, Z. Peng, B. Tesche and K. Kleinermanns, *Journal of Colloid and Interface Science*, 2008, **319**, 175-181.

230. M. Q. Zhu, L. Q. Wang, G. J. Exarhos and A. D. Li, *Journal of the American Chemical Society*, 2004, **126**, 2656-2657.

231. R. A. Álvarez-Puebla, R. Contreras-Cáceres, I. Pastoriza-Santos, J. Pérez-Juste and L. M. Liz-Marzán, *Angewandte Chemie International Edition*, 2009, **48**, 138-143.

232. Y. Lu, S. Proch, M. Schrinner, M. Drechsler, R. Kempe and M. Ballauff, *Journal of Materials Chemistry*, 2009, **19**, 3955-3961.

233. S. Wu, J. Dzubiella, J. Kaiser, M. Drechsler, X. Guo, M. Ballauff and Y. Lu, *Angewandte Chemie International Edition*, 2012, **51**, 2229-2233.

234. J. H. Kim and T. R. Lee, *Chemistry of Materials*, 2004, **16**, 3647-3651.

235. X. Liu, X. Wang, L. Zha, D. Lin, J. Yang, J. Zhou and L. Zhang, *Journal of Materials Chemistry C*, 2014, **2**, 7326-7335.

236. J. H. Kim and T. R. Lee, *Drug Development Research*, 2006, **67**, 61-69.

237. P. G. Yin, Y. Chen, L. Jiang, T. T. You, X. Y. Lu, L. Guo and S. Yang, *Macromolecular Rapid Communications*, 2011, **32**, 1000-1006.

238. R. Contreras-Cáceres, S. Abalde-Cela, P. Guardia-Girós, A. Fernández-Barbero, J. Pérez-Juste, R. A. Alvarez-Puebla and L. M. Liz-Marzán, *Langmuir*, 2011, **27**, 4520-4525.

239. N. Singh and L. A. Lyon, *Chemistry of Materials*, 2007, **19**, 719-726.

240. H. Kearns, N. Shand, K. Faulds and D. Graham, *Chemical Communications*, 2015, **51**, 8138-8141.

241. W. Agut, A. Brulet, D. Taton, S. Lecommandoux, *Langmuir*, 2007**, 23,** 23, 11526-11533.

242. G. Mocanu, D. Mihai, V. Dulong, L. Picton, D. Le Cerf, *Carbohydrate Polymers*, 2012**, 87**, 2, 1440-1446.

7. Appendices and Publications

Appendix I: SEM image for HGNs with an LSPR at 814 nm and the associated histogram detailing the frequency-size of the HGNs in the SEM image.

Appendix II: Extended peak assignment tables for NIR active HGNs plus AZPY, BPE and MPY; tables a-c respectively.

Appendix III: Extinction spectra for a selection of the chalcogenopyrylium dyes.

Appendix IV: 1064 nm SERS of silver and gold nanoparticles with chalcogen dye 252 and potassium chloride; figures a and b respectively.

Appendix V: Structures of all chalcogenopyrylium dyes tested.

Appendix VI: Bar chart containing error bars for PNIPAM coated HGNs and citrate capped HGNs; figures a and b respectively.

Appendix VII: Publications and Patent.

Appendix I:

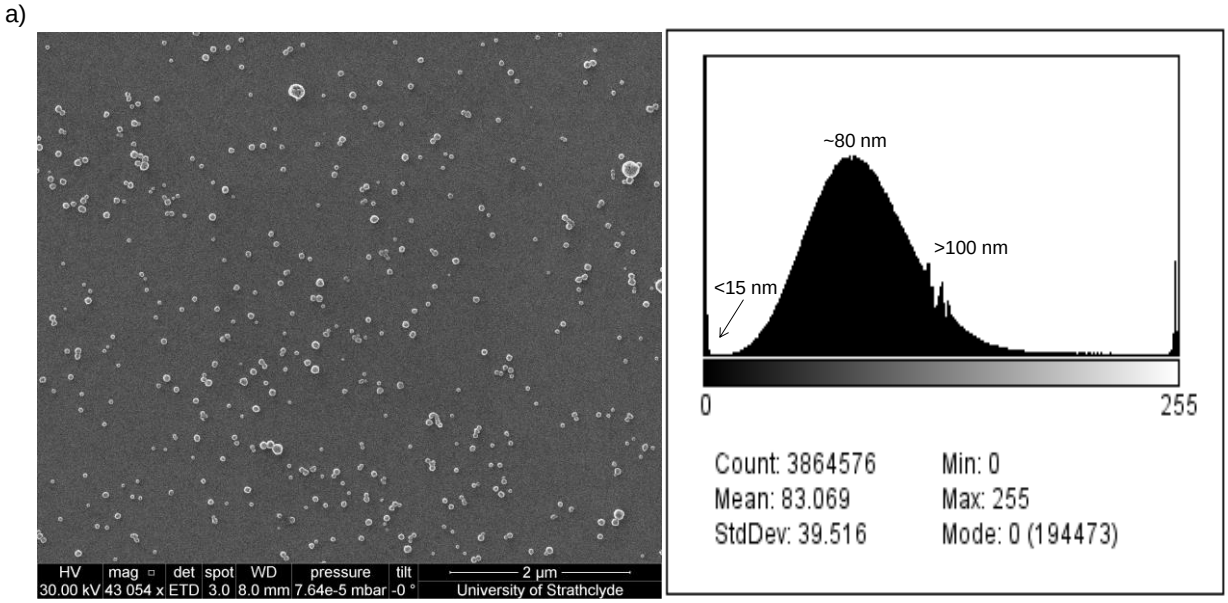

Figure – a) SEM image for HGNs with an LSPR at 814 nm and b) histogram detailing the frequency-size of the HGNs in the SEM image. Histogram was processed in imageJ.

Appendix II:

Table a) - Raman shifts (cm^{-1}) and peak assignments for AZPY (solid), HGN + AZPY + KCl (SERS-HGN) and Zhuang's silver foil + AZPY (SERS-Ag).[111, 135, 137, 142]

Raman	SERS-HGN	SERS-Ag	Assignments for AZPY
661	668	-	δ(C-C–C)py, δ(C-N–C)py, δ(C-N=N)
928	930	-	ν(C–C)py, δ(C-N–C)py, δ(C-N=N)
990	1015	1010	Ring breathing
1167	1162	1163	Ring breathing, ν(C–Nazo), δ(C–H)py
1232	-	1235	δ(C–H)py, ν(C–Nazo), ν(C–C)py
1333	1325	1326	ν(C–C)py, δ(C–H)py
1413	1415	1415	δ(C–H)py, ν(C-C)py, ν(N=N)
1465	1463	1466	ν(C–C)py, ν(C–N)py, δ(C–H)py
1493	1491	1497	ν(C–C)py, ν(N=N)
1587	1597	1597	ν(C–N)py, ν(C–H)py, ν(N=N)

ν = stretch, δ = bend, py = pyridyl ring.

Table b - Raman shifts (cm^{-1}) and peak assignments for BPE (solid), HGN + BPE + KCl (SERS- HGN) and Zhuang's silver foil + BPE (SERS-Ag). [111, 136, 139, 143]

Raman	SERS-HGN	SERS-Ag	Assignments for BPE
670	-	684	Ring breathing
883	-	879	δ(C=C), ring breathing
995	1017	1011	Ring breathing
1198	1202	1205	ν(C–C)py, δ(C–N)py, δ(C–H)py
1232	1245	1268	δ(C–H)py
1275	-	-	ν(C–C)py, ν(C–N)py
1341	1335	1329	δ(C–H)py, δ(C=C)
1415	1424	1425	δ(C–H)py
1546	1541	1553	ν(C–C)py, ν(C–N)py, δ(C–H)py
1595	1603	1600	δ(C–N)py, δ(C–H)py,, ν(C–C)py
1635	1635	1635	ν(C=C)

ν = stretch, δ = bend, py = pyridyl ring.

Table c – Raman shifts (cm^{-1}) and peak assignments for MPY (solid), HGN + MPY + KCl (SERS-HGN) and Hu's silver foil + MPY (SERS-Ag).[111, 133]

Raman	SERS-HGN	SERS-Ag	Assignments for MPY
645	-	-	δ(C-C-C) py
721	715	707	ν(C–S), ring breathing
990	1006	1010	Ring breathing
1044	-	-	δ(C–H)py
1080	1096	1061	δ(C–H)py
1106	1113	1098	ν(C–S), ring breathing
1205	-	1220	δ(C–H)py, δ(N-H)py
1249	-	-	δ(C–H)py
1394	-	-	ν(C–C)py
1478	-	-	ν(C=C)py, ν(C=N)py
1595	1587	1580	ν(C–C)py
1612	-	-	ν(C–C)py

ν = stretch, δ = bend, py = pyridyl ring.

Appendix III:

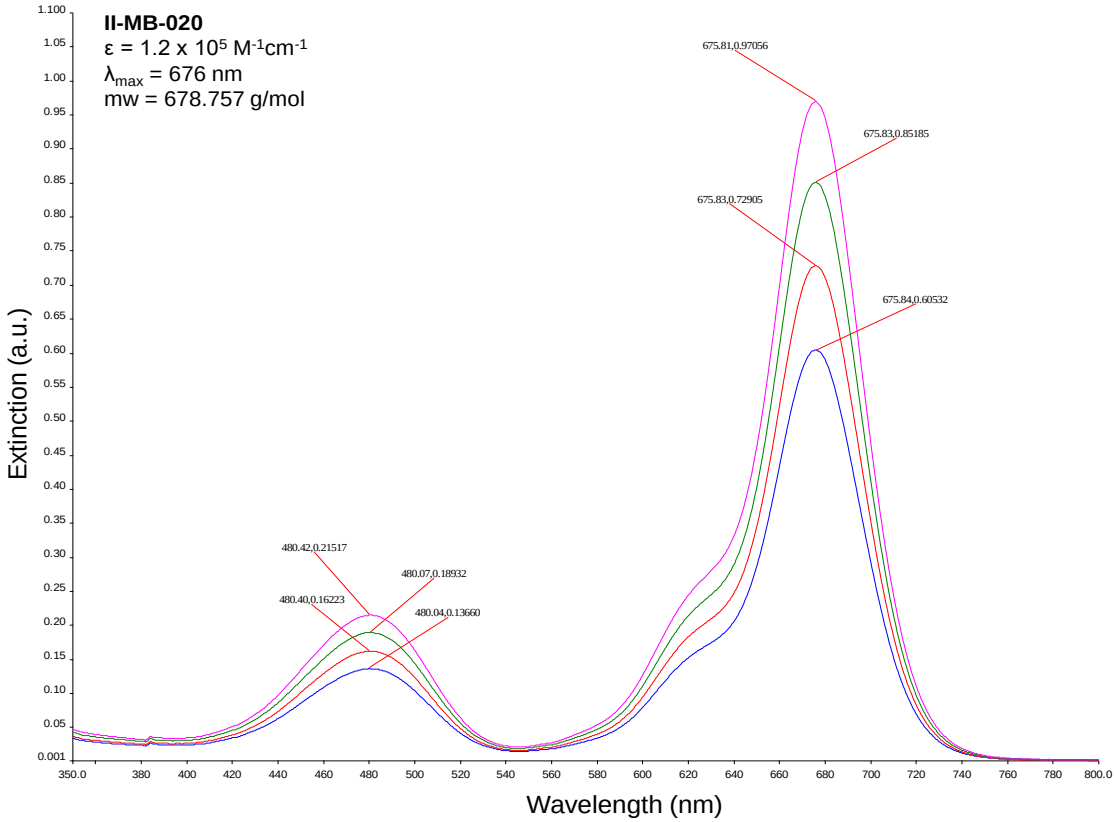

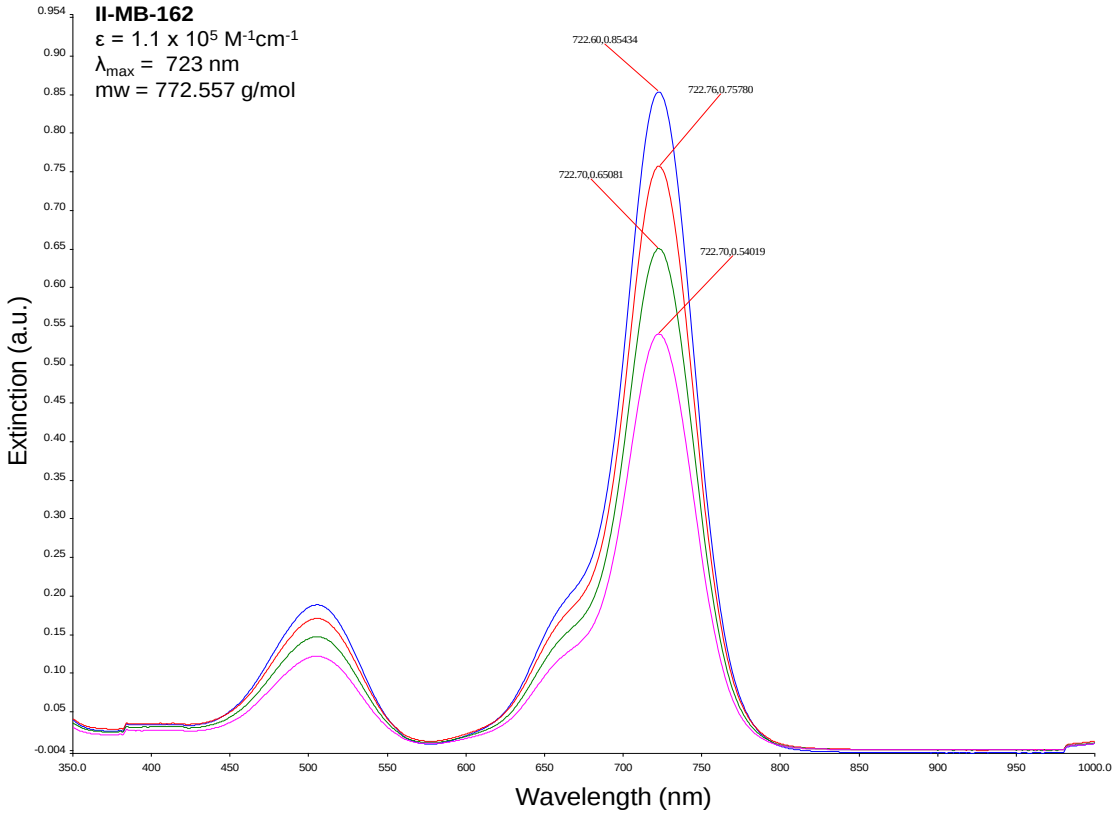

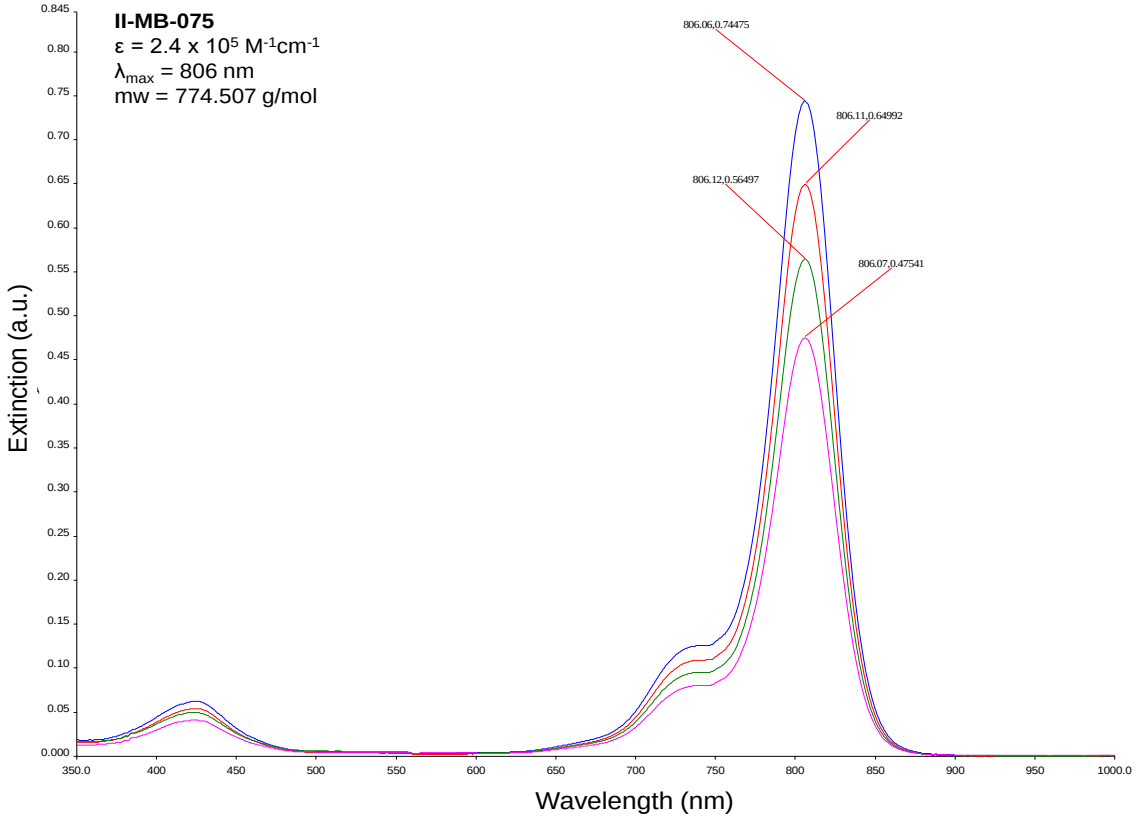
II-MB-075
ε = 2.4 x 10^5 M^-1cm^-1
λmax = 806 nm
mw = 774.507 g/mol
806.06,0.74475
806.11,0.64992
806.12,0.56497
806.07,0.47541
Extinction (a.u.)
Wavelength (nm)

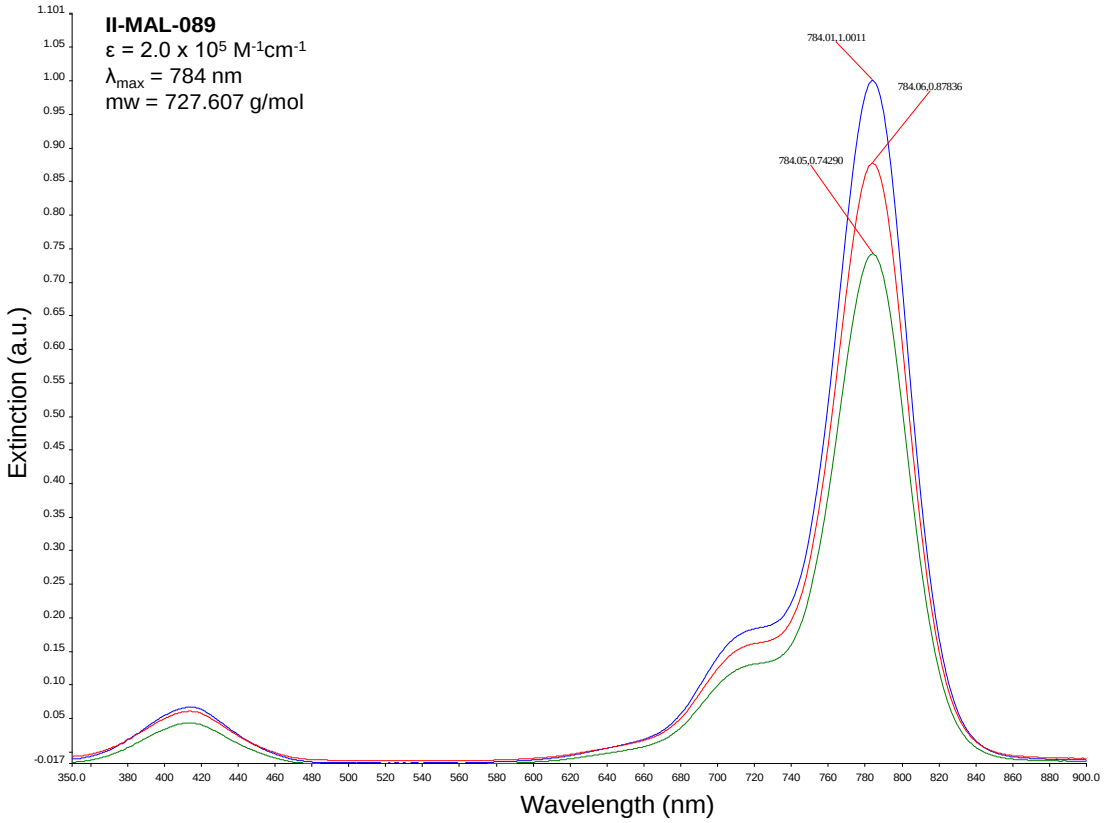
II-MAL-089
ε = 2.0 x 10^5 M^-1cm^-1
λmax = 784 nm
mw = 727.607 g/mol
784.01,1.0011
784.06,0.87836
784.05,0.74290
Extinction (a.u.)
Wavelength (nm)

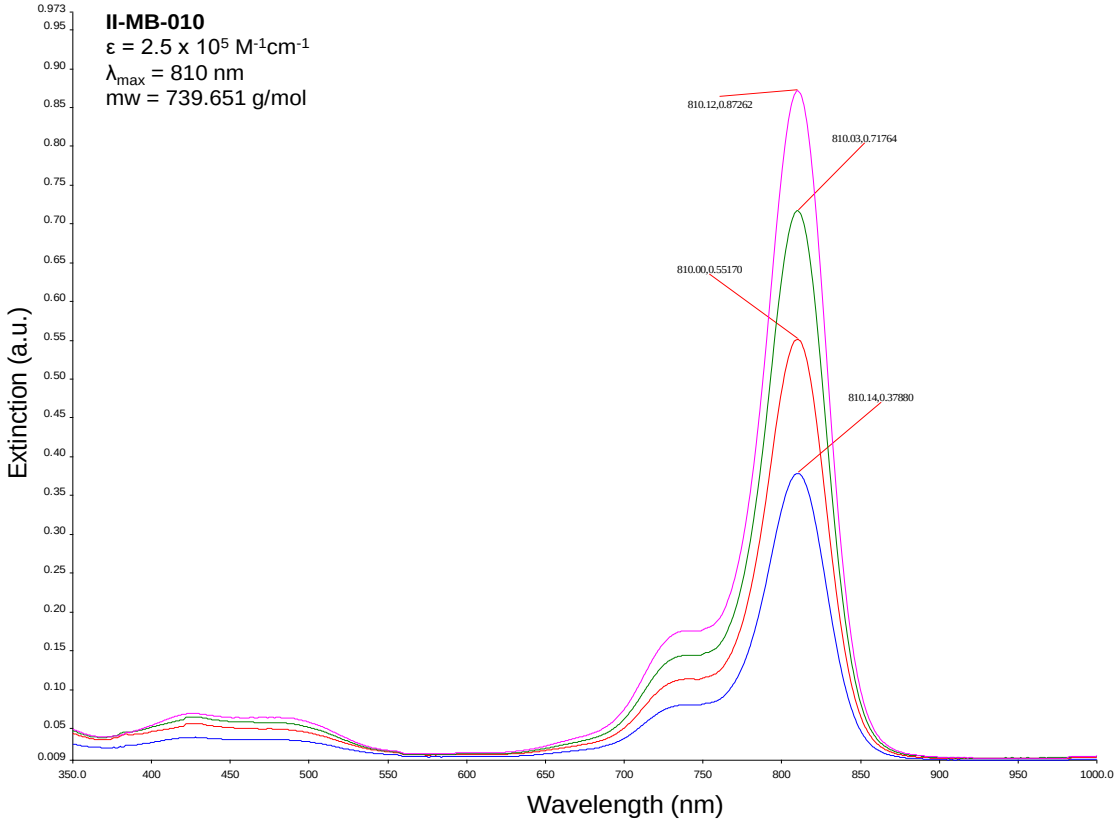
II-MB-010
ε = 2.5 x 10^5 M^-1cm^-1
λmax = 810 nm
mw = 739.651 g/mol
810.12,0.87262
810.03,0.71764
810.00,0.55170
810.14,0.37880
Extinction (a.u.)
Wavelength (nm)

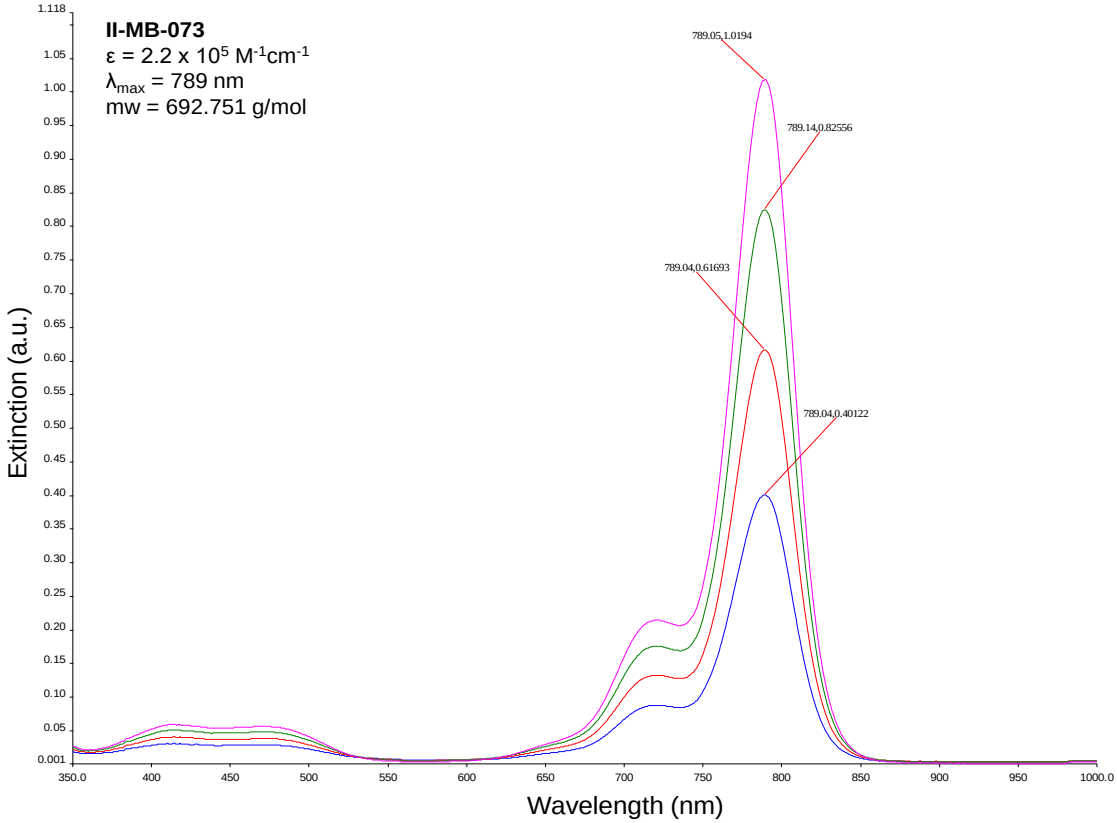
II-MB-073
ε = 2.2 x 10^5 M^-1cm^-1
λmax = 789 nm
mw = 692.751 g/mol
789.05,1.0194
789.14,0.82556
789.04,0.61693
789.04,0.40122
Extinction (a.u.)
Wavelength (nm)

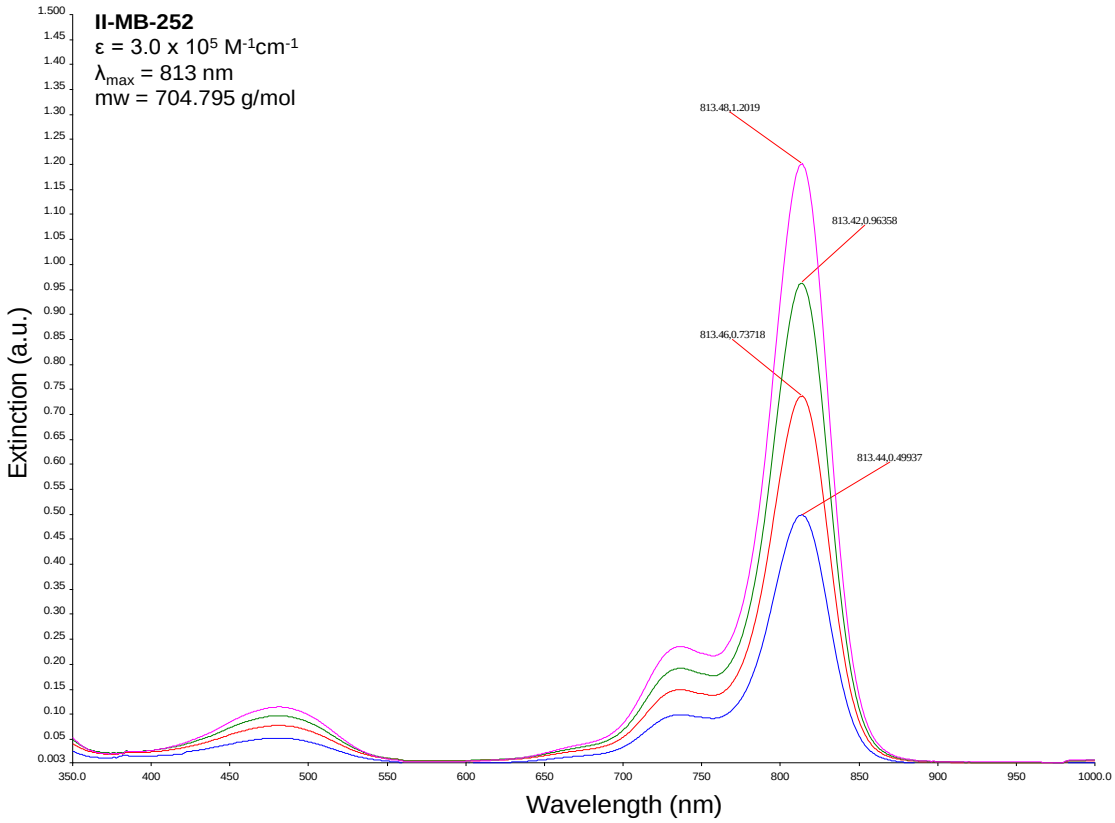

Figure – Extinction spectra for a selection of the chalcogenopyrylium dyes. The spectra were obtained by Matthew Bedics, (PhD student in Professor Michael Detty's group at the University at Buffalo).

Appendix IV:

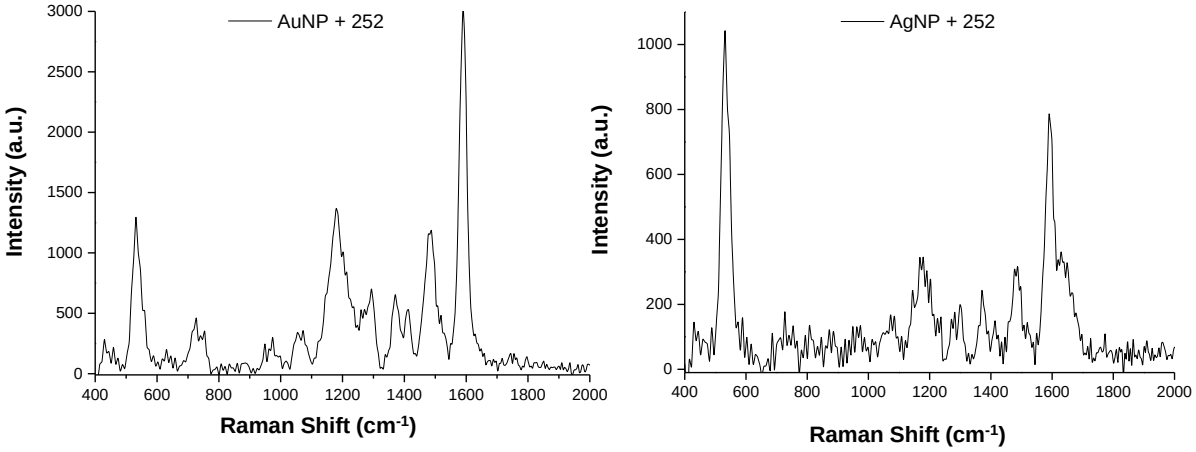

Figure - SERS spectra for dye 252 with a) gold and b) silver nanoparticles of and aggregated with KCl. These nanoparticles have an average size of 40 -60 nm. A laser excitation of 1064 nm and an exposure time of 3 seconds were employed in this analysis. All spectra have been background corrected.

Appendix V:

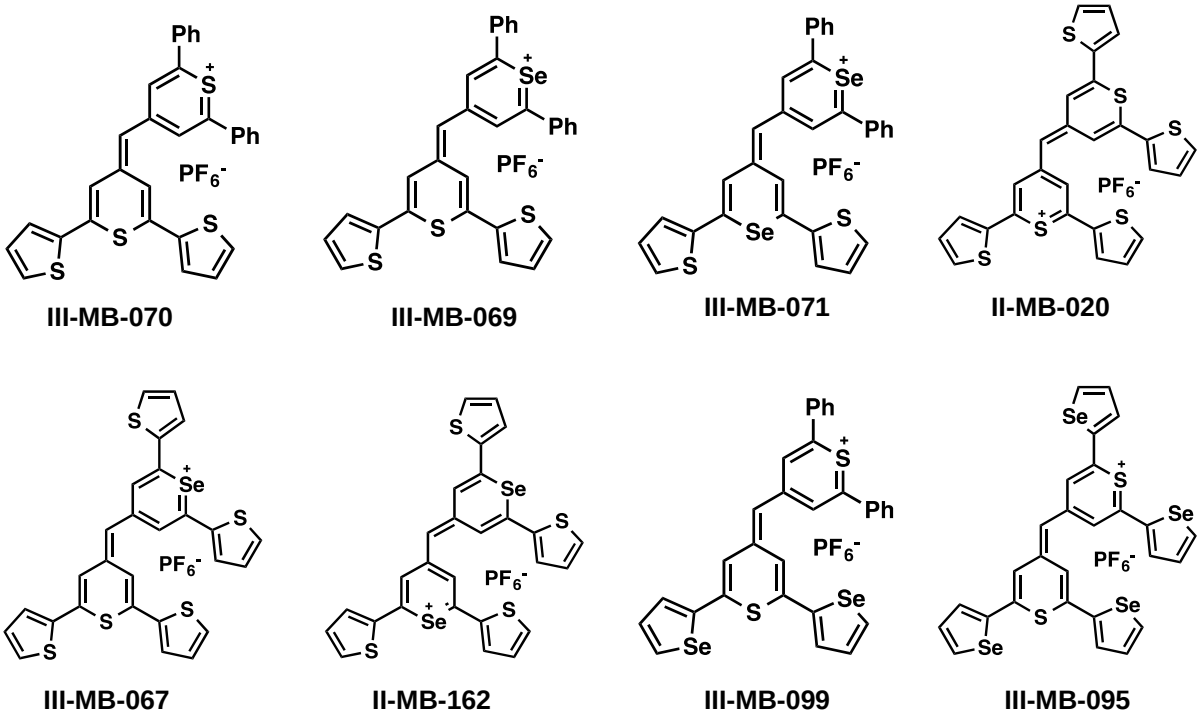

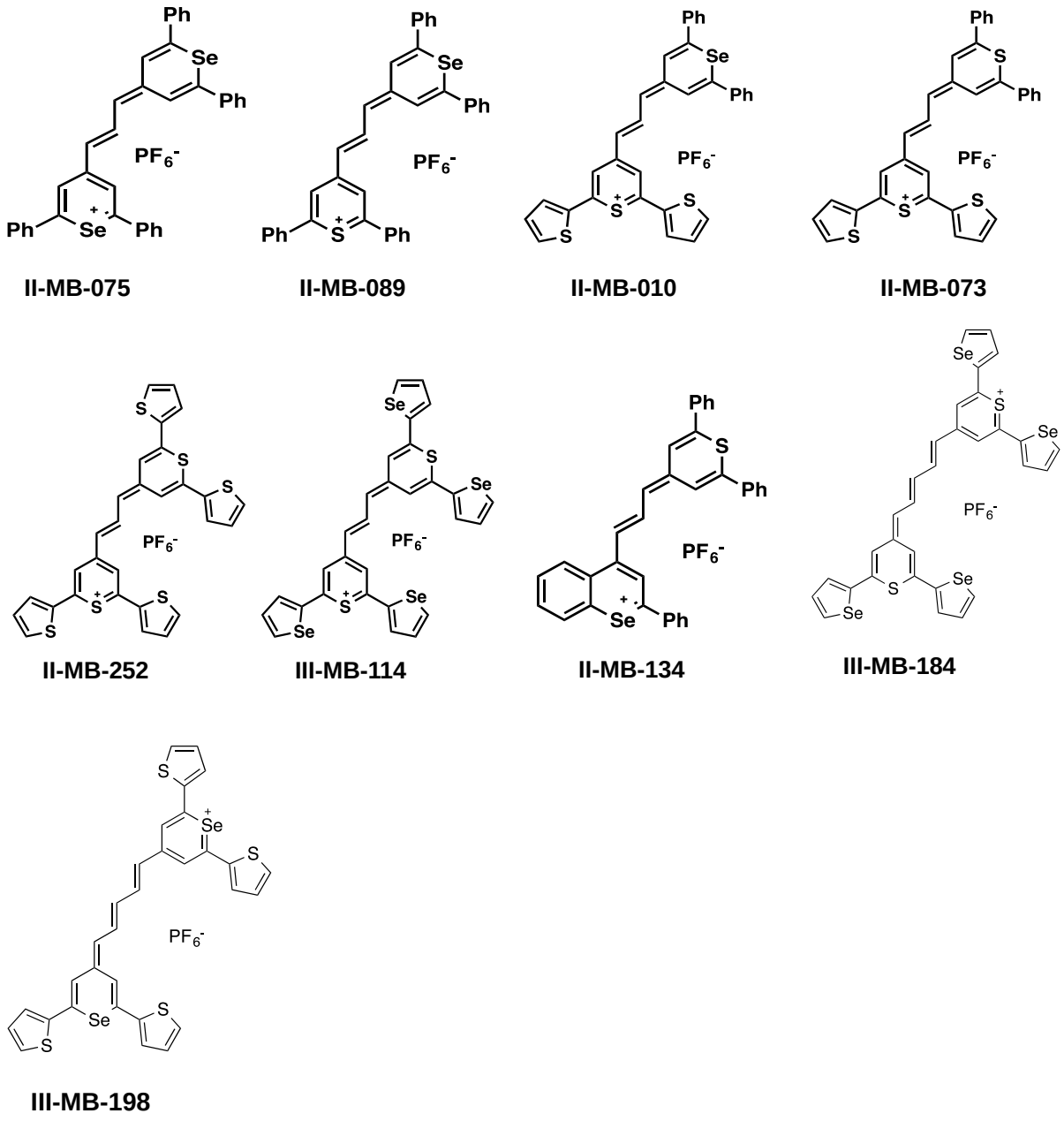

Figure - Structures of all chalcogenopyrylium dyes tested.

Appendix VI:

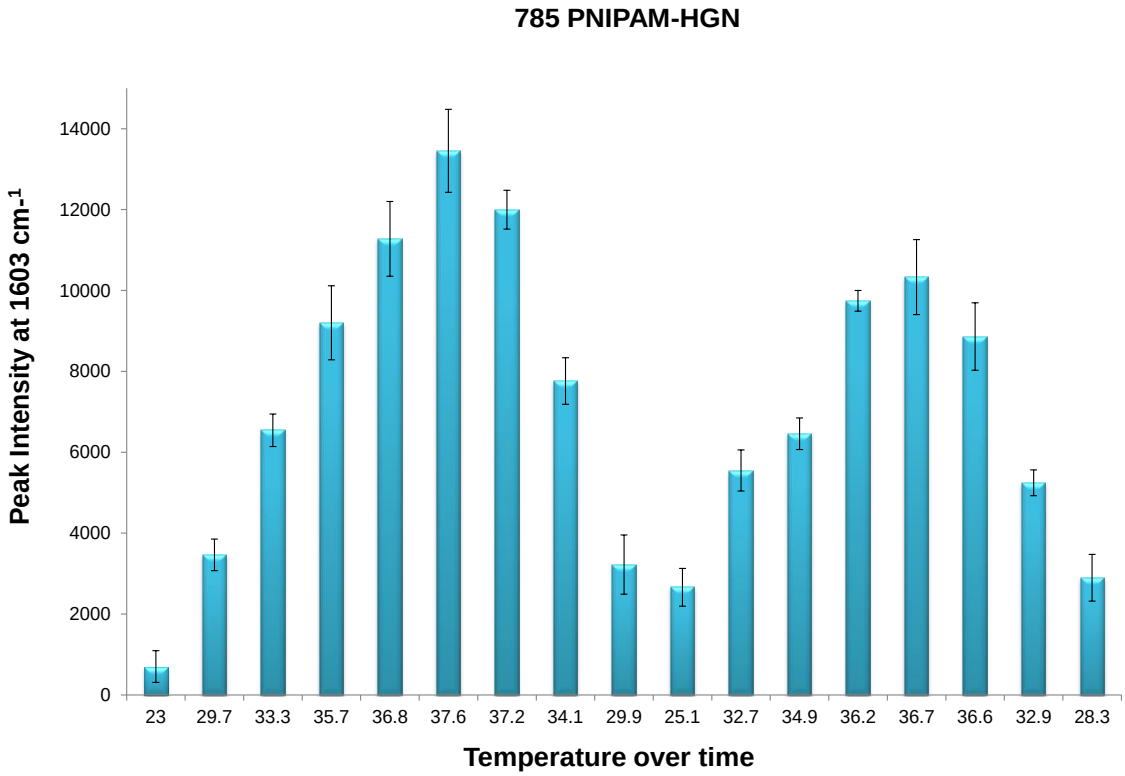

Figure a) - Bar chart showing the change in SERS signal of PNIPAM coated HGNs + BPE (0.1 mM) resonant at 785 nm over two cycles of heating and cooling past the LCST of 32 ^{o}C. The SERS spectra and temperature readings were taken every 5 minutes. A laser excitation of 785 nm was used to induce plasmonic heating of the HGNs and a secondary portable Deltanu 785 nm spectrometer was used to collect the SERS data. The peak intensity values shown in the bar chart are from the C-C stretch of BPE at 1603 cm^{-1} and the error bars represent one standard deviation resulting from 5 scans at each time interval. The heating and cooling cycles were over the temperature ranges 23 ^{o}C to 40 ^{o}C, with the largest temperature increase being 14.6 ^{o}C.

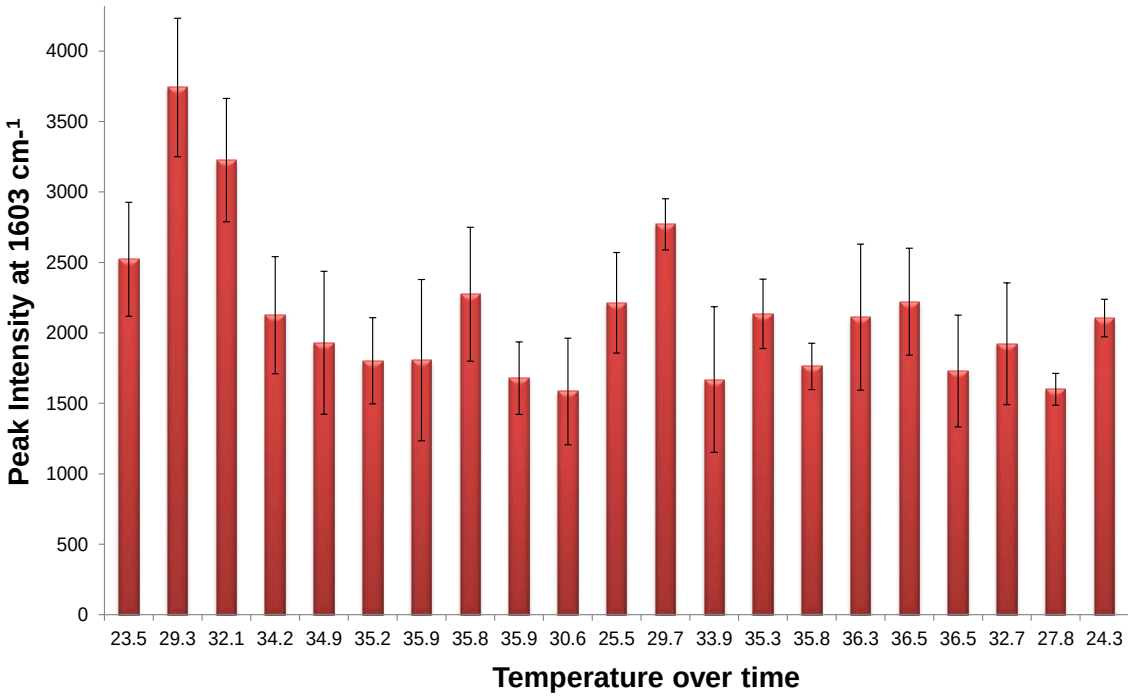

Figure b) - Bar chart showing the change in SERS signal of citrate capped HGNs + BPE (0.1 mM) resonant at 785 nm over two cycles of heating and cooling past the LCST of 32 ^{o}C. The SERS spectra and temperature readings were taken every 5 minutes. A laser excitation of 785 nm was used to induce plasmonic heating of the HGNs and a secondary portable Deltanu 785 nm spectrometer was used to collect the SERS data. The peak intensity values shown in the bar charts are from the C-C stretch of BPE at 1603 cm^{-1}. Error bars represent one standard deviation resulting from 5 scans at each time interval. The heating and cooling cycles were over the temperature ranges 23 ^{o}C to 36 ^{o}C, with the largest temperature increase being 13 ^{o}C.

Appendix VII:

1. "1064 nm SERS of NIR Active Hollow Gold Nanotags," H. Kearns, N. C. Shand, W. E. Smith, K. Faulds, D. Graham, **Physical Chemistry Chemical Physics**, 2015, 17, 1980-1986.

2. "Extreme Red Shifted SERS Nanotags," M. A. Bedics, H. Kearns, J. M. Cox, S. Mabbott, F. Ali, N. C. Shand, K. Faulds, J. B. Benedict, D. Graham, M. R. Detty, **Chemical Science**, 2015**,** 6, 2302-2306**.**

3. "Laser Induced SERS Switching using Plasmonic Heating of PNIPAM coated HGNs," H. Kearns, N. C. Shand, K. Faulds, D. Graham, **Chemical Communications**, 2015, 51, 8138-8141.

4. "Sensitive SERS Nanotags for use with 1550 nm (Retina-Safe) Laser Excitation," H. Kearns, M. A. Bedics, N. C. Shand, K. Faulds, M. R. Detty, D. Graham, **Analyst**, 2016, DOI:10.1039/c5an02662h.

5. "Elucidation of the Bonding of a Near Infrared Dye to Hollow Gold Nanospheres – A Chalcogen Tripod," H. Kearns, S. Sengupta, I. Ramos-Sasselli, L. Bromley, III , K. Faulds, T. Tuttle, M. A. Bedics, M. R. Detty, L. Velarde, D. Graham, W. E. Smith. (under review)

6. "Novel Chalcogenopyrylium Dyes Useful as Reporter Molecules on Noble Nanoparticles for Surface Enhanced Raman Scattering," M. R. Detty, D. Graham, K. Faulds, H. Kearns, M. A. Bedics. (patent pending)